HAL
open science

Experimental characterization of the combustion dynamics at micro-scale

Annalisa Di Stazio

To cite this version:

Annalisa Di Stazio. Experimental characterization of the combustion dynamics at micro-scale. Reactive fluid environment. Orléans, 2016. English. NNT : . tel-01994718

HAL Id: tel-01994718

https://theses.hal.science/tel-01994718v1

Submitted on 25 Jan 2019

HAL is a multi-disciplinary open access archive for the deposit and dissemination of scientific research documents, whether they are published or not. The documents may come from teaching and research institutions in France or abroad, or from public or private research centers.

L'archive ouverte pluridisciplinaire **HAL**, est destinée au dépôt et à la diffusion de documents scientifiques de niveau recherche, publiés ou non, émanant des établissements d'enseignement et de recherche français ou étrangers, des laboratoires publics ou privés.

UNIVERSITÉ D'ORLÉANS

ÉCOLE DOCTORALE
ÉNERGIE, MATÉRIAUX, SCIENCES DE LA TERRE ET DE L'UNIVERS

Institut de Combustion Aérothermique Réactivité et Environnement
UPR 3021 du CNRS

THÈSE présentée par :

Annalisa DI STAZIO

Soutenue le : **16 décembre 2016**

pour obtenir le grade de : **Docteur de l'Université d'Orléans**

Discipline : **Énergétique, Thermique, Combustion**

Caractérisation expérimentale de la dynamique de la combustion à micro-échelle

THÉSE dirigée par :

Christian CHAUVEAU	Directeur de Recherche, CNRS–ICARE
Guillaume DAYMA	Professeur des Universités, Orléans

RAPPORTEURS :

Guillaume RIBERT	Maître de Conférences, HDR, INSA de Rouen
Guillaume LEGROS	Maître de Conférences, HDR, Université Pierre & Marie CURIE (Paris IV)

JURY :

Christian CHAUVEAU	Directeur de Recherche, CNRS–ICARE
Francesco CONTINO	Assistant Professor, Vrije Universiteit Brussel
Philippe DAGAUT	Directeur de Recherche, CNRS–ICARE
Guillaume DAYMA	Professeur des Universités, Orléans
Guillaume LEGROS	Maître de Conférences, UPMC (Paris IV)
Guillaume RIBERT	Maître de Conférences, INSA de Rouen

Contents

List of Figures **5**

Nomenclature **15**

Study Context **17**

1 Background on Micro Combustion **23**

1.1 Micro Combustion and quenching diameter 24

1.2 The excess enthalpy principle and its application 27

1.3 Micro-combustion: theoretical and numerical approach 29

1.3.1 Phenomenological and theoretical approach 29

1.3.2 Numerical interpretation: issues and perspectives 29

1.4 Micro-combustion: experimental 32

1.4.1 Experimental setups 32

1.4.2 Stable flame regime 33

1.4.3 FREI regime 34

1.4.3.1 Quenching mechanism 36

1.4.4 Weak flame regime 39

1.4.4.1 Auto-ignition temperature (AIT) 39

1.4.5 Transitional regimes 40

1.5 Parameters effect 43

1.5.1 Inlet velocity 43

1.5.2 Equivalence ratio 44

1.5.3 Reactor dimension 45

1.5.4 Fuel type 47

1.6 Conclusions 49

2 Experimental setup 51

2.1 Part I: Experimental Setup 51

2.1.1 Mixture preparation equipment and micro-flow reactor 51

2.1.2 External heating system 54

2.1.3 Data acquisition system 56

2.1.3.1 EMCCD camera 58

2.1.3.2 Infrared camera and emissivity correction 58

2.2 Part II: Operating configuration 63

2.2.1 EMCCD camera configuration 63

2.2.2 Temperature profile 66

2.2.2.1 Distance between the blowtorches and the reactor . . 66

2.2.2.2 Blowtorches distance from the reactor outlet 69

2.2.2.3 Uniformity of the temperature profile 71

2.2.2.4 Temperature measurements via thermocouple 76

2.3 Fuel Type 78

2.4 Summary 79

3 Experimental results: Methane/Air 81

3.1 Effect of the inlet velocity 81

3.1.1 Stable flame regime 86

3.1.2 FREI regime 89

3.1.2.1 Frequency and characteristic time 91

3.1.2.2 Evolution of CH* intensity and quenching mechanism 93

3.1.3 Weak Flames 94

3.1.4 Transitional regimes: oscillating FREIs and weak flames . . . 95

3.2 Comparison with previous studies 98

3.3 Effect of the equivalence ratio 100

3.3.1 Stable flame regime 101

3.3.2 FREI regime 103

3.3.2.1 Characteristic times and frequency 104

3.3.2.2 Evolution of CH* intensity 107

3.3.3 Weak flame regime 110

3.3.4 Transitional regimes 111

3.3.5 Summary 113

3.4 Effect of the reactor diameter 115

3.4.1 Stable flame regime 116

3.4.2 FREI regime 119

3.4.2.1 Frequency and characteristic times 120

3.4.2.2 Evolution of CH* intensity 122

3.4.3 Weak flame regime 124

3.4.4 Transitional regimes 125

3.4.5 Summary 129

3.5 Conclusions 131

4 Experimental results: Ethylene/Air and Acetylene/Air 133

4.1 Ethylene/air mixtures 133

4.1.1 Effect of the inlet velocity 134

4.1.1.1 FREI regime 136

4.1.2 Effect of the equivalence ratio 140

4.1.2.1 Flames with equivalence ratio of 0.3 141

4.1.2.2 Overview and Stable Flames 143

4.1.2.3 FREI and oscillating flames 146

4.1.3 Summary 150

4.2 Acetylene/air mixtures 152

4.2.1 Effect of the inlet velocity 152

4.2.1.1 FREI and transitional regimes 154

4.2.2 Effect of the equivalence ratio 160

4.2.2.1 Flames in very-lean condition 160

4.2.2.2 Overview and Stable Flames 162

4.2.2.3 FREI and oscillating flames 164

4.2.3 Summary 169

4.3 Conclusions 171

5 Numerical study of the ignition points 173

5.1 Numerical models 173

5.1.1 2D model 173

5.1.2 0D model 174
5.2 Reaction mechanisms 176
5.2.1 2D model: discretization and parameters effect 176
5.2.1.1 Spatial discretization 176
5.2.1.2 Radial discretization 177
5.2.1.3 Axial discretization 178
5.2.1.4 Temperature and transport effect 178
5.3 Results 180
5.3.1 Methane/Air 180
5.3.2 Comparison between the numerical models 182
5.3.3 Ethylene/Air and Acetylene/Air 184
5.4 Conclusions 185

Conclusions and Recommendations **187**

Bibliography **191**

Appendices **201**

A Emission Spectroscopy Diagnostic **203**

B Post-processing procedure **207**

C Numerical Simulation with non-reactive mixtures **215**

D Results: Methane/Air mixtures **219**

E Results: Ethylene and Acetylene/Air mixtures **221**

List of Figures

1.1 Comparison of the energy density of several batteries with fuels. . . . 24

1.2 Quenching distance as a function of the equivalence ratio. 26

1.3 Variation of quenching diameter d_T with φ and T [15]. 26

1.4 Schematic of excess-enthalpy combustion. 27

1.5 Flammable domain as a function of Q_f, T, and φ [26]. 28

1.6 Swiss Roll combustor in operation. 28

1.7 Sketch of a flame reacting in a heated micro-channel. 29

1.8 Results obtained by Gauthier et al. [39]. 31

1.9 Scheme of the experimental set-up used by Maruta et al. [38]. 32

1.10 Configuration with a single plate heater [42]. 32

1.11 Flame positions with the mixture velocity (Fig. 5, [38]). 33

1.12 Schematic of the flame shapes (Fig. 1, [45]). 34

1.13 Map of the different flame regimes of fuel-rich H_2/O_2 flames [87] . . . 42

1.14 Time fluctuation in the maximum reaction rate [91]. 43

2.1 Schematic of the experimental setup. 52

2.2 MFCs installation. 53

2.3 Tube rifling used to set the origin. 54

2.4 Heating system components. 55

2.5 Wall temperature profile obtained 55

2.6 Not slated flames obtained 56

2.7 Schematic of the data acquisition system and micro-reactor. 57

2.8 Wall temperature profiles recorded 57

2.9 Example of pixel binning. 59

2.10 Fused silica emissivity with wavelengths and temperature. 60

2.11 Fused silica emissivity as a function of temperature. 62

2.12 Temperature correction. 63

2.13 Configuration 1. 64

2.14 Configuration 2. 64

2.15 Flame position for different configurations 65

2.16 CH^* progression obtained with the two configurations employed. . . . 66

2.17 Schematic of the tube and the blowtorches. 67

2.18 Temperature profiles. 68

2.19 Flame position obtained with different temperature profiles. 68

2.20 Layout. 69

2.21 Water formation in the configuration A. 70

2.22 Periodic drop formation in the configuration B. 70

2.23 Spatially integrated CH^* signal 70

2.24 Frequencies obtained in each configuration. 71

2.25 Schematic of the experimental layout. 72

2.26 Temperature measurement at the initial tube section. 72

2.27 Temperature profiles obtained on the inner and outer tube side. . . . 73

2.28 Temperature distribution of the tube outer side. 74

2.29 Temperature distribution of the tube inner side. 74

2.30 Line selected on the reactor side. 75

2.31 Extrapolated temperature on the tube thickness. 75

2.32 Temperature profile along the wall thickness. 76

2.33 Moving stage used during experiments. 77

2.34 Temperature measured with Inconel-sheated thermocouple. 78

3.1 Flame position for CH_4/air, $\varphi = 1$, d = 1.85 mm. 82

3.2 Flames images with the inlet velocity (CH_4/air, $\varphi = 1$, d = 1.85 mm). 83

3.3 Temporal evolution of CH^* intensity during FREI progression 84

3.4 Evolution of an oscillating FREI. 85

3.5 Centerline temperature profiles at 1 and 0.5 m/s. 87

3.6 Flame positions defined at the wall and axial temperature. 87

3.7 Spatially integrated CH^* signal of stable flames and CH^* profiles. . . 89

3.8 Extinction positions defined at the wall and axial temperature. 90

3.9 FREI frequency variation with inlet velocity, d = 1.85 mm, $\varphi = 1$. . . 91

3.10 Comparison between τ_{IE} and τ_{EI} for a 1.85 mm diameter reactor. . . . 92

3.11 Maximum CH^* progression at different inlet velocity. 93

3.12 Temporal evolution of CH^* signal with inlet velocity. 96

3.13 Frequency variation as a function of the inlet velocity. 97

3.14 Comparison with the results obtained by Tsuboi et al. [42]. 98

3.15 Comparison between the temperature profiles. 99

3.16 Flames obtained with three and two heat sources. 99

3.17 Effect of equivalence ratio on the flame positions. 101

3.18 Stable flame positions at the centerline temperature. 102

3.19 Correlation between T_{ad}/T and S_l/v_{unb}. 103

3.20 τ_{IE} and τ_{EI} at different equivalence ratios. 104

3.21 Equivalence ratio effect on FREI frequencies. 105

3.22 Strouhal Number for methane/air FREI flames. 106

3.23 Progression of the maximum CH^* for methane/air FREI flames. . . . 108

3.24 CH^* signals at successive instants at $v = 0.4\,m/s$ and $\varphi = 1.5$. 109

3.25 Weak flames obtained varying the equivalence ratio 110

3.26 Temporal evolution of CH^* signal with inlet velocity at $\varphi = 0.5$. . . . 112

3.27 Frequency variation as a function of the inlet velocity. 113

3.28 Map of different flame regime. 114

3.29 Diameter effect on the flame position. 115

3.30 Images of stable flames at $d = 1.0$ and $2.5\,mm$. 116

3.31 Centerline temperature for 1.0 and 2.5 mm i.d. 117

3.32 Flame positions plotted at the centerline temperature. 118

3.33 FREI extinction positions. 119

3.34 τ_{EI} obtained for stoichiometric mixtures changing the reactor size. . . 120

3.35 τ_{IE} obtained for stoichiometric mixtures changing the reactor size. . . 121

3.36 Frequencies obtained changing the reactor size. 122

3.37 Maximum CH^* progression 124

3.38 Stabilization temperatures of the weak flames. 125

3.39 Temporal evolution of CH^* signal for $d = 2.15\,mm$. 126

3.40 Temporal evolution of CH^* signal for $d = 2.50\,mm$. 127

3.41 Temporal evolution of CH^* signal for d = 1.0 mm. 128

3.42 FREI frequencies for different reactor inner diameters. 129

3.43 Map of different flame regimes. 130

4.1 Flame position for C_2H_4/air, $\varphi = 1$, d = 1.0 mm. 134

4.2 Oscillating weak flame observed at v = 0.14 m/s. 135

4.3 FREI frequency variation with the inlet velocity, d = 1.0 mm, $\varphi = 1$. 136

4.4 Comparison between τ_{EI} and τ_{IE} for 1.0 mm diameter tube. 137

4.5 Maximum CH^* progression for stoichiometric ethylene/air flames. . . 138

4.6 Spatially resolved CH^* emission signals at v = 0.69 m/s. 139

4.7 Spatially resolved CH^* emission signals at v = 0.20 m/s. 140

4.8 Ultra-lean ($\varphi = 0.3$) ethylene/air flame position. 141

4.9 Frequencies of weak oscillating ethylene/air flames ($\varphi = 0.3$). 142

4.10 Temporal evolution of the CH^* signal (v = 0.43 m/s, $\varphi = 0.3$). 142

4.11 Ethylene/air flame position. 144

4.12 Correlation between T_{ad}/T and S_l/v_{unb} for ethylene/air mixtures. . . 145

4.13 Maximum CH^* progression high and low v. 147

4.14 Flame frequencies. 148

4.15 Characteristics times of ethylene/air mixtures. 149

4.16 Oscillating flames observed at v = 0.5 m/s and $\varphi = 0.4$. 149

4.17 Strouhal Number for ethylene and methane/air mixtures. 150

4.18 Map of different flame regimes for ethylene/air mixtures. 151

4.19 Flame position for C_2H_2/air, $\varphi = 1$, d = 0.7 mm. 153

4.20 FREI frequency variation. 154

4.21 Comparison between τ_{IE} and τ_{EI}. 155

4.22 Maximum CH* progression. 156

4.23 CH* emission at successive instants at v = 1.12 m/s. 157

4.24 CH* emission at successive instants at v = 0.30 m/s. 158

4.25 Integrated CH* signal for v = 1.12 and 0.30 m/s. 159

4.26 Integrated CH* signal of oscillating flames. 159

4.27 Flame position for $\varphi = 0.1$ and 0.3. 161

4.28 Integrated CH* signals at $\varphi = 0.3$. 161

4.29 Frequencies of FREI and oscillating FREIs obtained at $\varphi = 0.3$. . . . 162

4.30 Flame position for different equivalence ratios. 163

4.31 Correlation between T_{ad}/T and $Le \times S_l/v_{unb}$ for acetylene/air mixtures. 164

4.32 Maximum CH* progression at $\varphi = 1.7$. 165

4.33 CH* signals at successive instants. 166

4.34 Oscillating flames at different equivalence ratios. 167

4.35 Flame frequencies. 168

4.36 Strouhal number progression. 169

4.37 Map of different flame regimes. 170

5.1 Effect of multicomponent transport and Soret effect. 174

5.2 Sketch of the temperature profile extraction. 175

5.3 Time-varying temperature profiles. 175

5.4 Results obtained varying the number of radial points. 177

5.5 Results obtained with varying the axial refinement. 178

5.6 Effect of the temperature profile. 179

5.7 Transport properties effect on the ignition temperatures. 180

5.8 Ignition points obtained for methane/air mixtures (d = 1.85 mm). . . 181

5.9 Ignition points obtained with changing the reactor diameter. 182

5.10 Comparison between the 0D and the 2D model. 183

5.11 Results obtained with the 2D model for C_2H_4/air mixture. 184

5.12 Results obtained with the 2D model for C_2H_2/air mixture. 185

A1 He spectrum. 204

A2 Emission spectrum of an oxygen-enriched methane/air flame. 204

A3 Bandwidth of the filter used in the present work. 205

B1 Example of averaged cross-section on a 2×2 domain. 207

B2 Example of cross-section on 1000 frames. 208

B3 Determination of characteristic times. 209

B4 Example of post-processing applied on a single instant. 210

B5 Temporal evolution of maximum CH^* peaks. 210

B6 Point selected during propagation phase. 211

B7 Points selected during the propagation phase over several cycles. . . . 212

B8 Progression of a stoichiometric ethylene/air flame. 213

B9 Example of spatially integration on the CH^* signal (grey area). 213

B10 Spatially integrated CH^* signal at v = 0.32 m/s. 214

C1 3D model. 216

C2 Temperature profile at the wall. 217

C3 Temperature contours for methane/air mixture. 217

C4 Evolution of v/v_0 with the wall temperature. 218

D1 Temporal evolution of CH_4/Air unstable flames at $\varphi = 0.7$. 219

D2 Temporal evolution of CH_4/Air unstable flames at $\varphi = 1.5$. 220

E1 Characteristic times of C_2H_4/Air unstable flames. 222

E2 Characteristic times of C_2H_2/Air unstable flames. 223

E3 Temporal evolution of C_2H_4/Air unstable flames at $\varphi = 0.7$. 224

E4 Temporal evolution of C_2H_4/Air unstable flames at $\varphi = 0.9$. 224

E5 Temporal evolution of C_2H_4/Air unstable flames at $\varphi = 1.1$. 225

E6 Temporal evolution of C_2H_4/Air unstable flames at $\varphi = 1.3$. 225

E7 Temporal evolution of C_2H_4/Air unstable flames at $\varphi = 1.5$. 226

E8 Temporal evolution of C_2H_2/Air unstable flames at $\varphi = 0.5$. 226

E9 Temporal evolution of C_2H_2/Air unstable flames at $\varphi = 0.7$. 227

E10 Temporal evolution of C_2H_2/Air unstable flames at $\varphi = 0.9$. 228

E11 Temporal evolution of C_2H_2/Air unstable flames at $\varphi = 1.1$. 229

E12 Temporal evolution of C_2H_2/Air unstable flames at $\varphi = 1.3$. 230

E13 Temporal evolution of C_2H_2/Air unstable flames at $\varphi = 1.5$. 231

E14 Mamimum CH^* progression for C_2H_4/Air flames. 232

E15 Mamimum CH^* progression for C_2H_2/Air flames. 233

Nomenclature

Dimensionless Numbers

Symbol	Description	Definition
Le	Lewis number	$\frac{\alpha}{D}$
Nu	Nusselt number	$\frac{h \times d}{k}$
Pe	Peclet number	$\frac{d_T \times S_{lq}}{\alpha}$
St	Strouhal number	$\frac{f \times d}{v}$

Greek Symbols

Symbol	Description	Units
α	Thermal diffusivity	$m^2\ s^{-1}$
λ	Wavelength	μm
ρ	Density	kg m^{-3}
τ	Transmission	–
τ_{EI}	Time between the FREI extinction and ignition	s
τ_{IE}	Time between the FREI ignition and extinction	s
τ_{opt}	Transmission of the external optic	–
ε	Emissivity of a real body	–
ε_λ	Spectral emissivity at a specific wavelength	–
φ	Equivalence ratio	–

Roman Symbols

Symbol	Description	Units
c_p	Specific heat capacity	J kg^{-1} K^{-1}
d_T	Quenching diameter	m
D	Mass diffusivity	m^2 s^{-1}
d	Reactor inner diameter	m
f	Frequency	Hz
h	Heat transfer coefficient	W m^{-2} K^{-1}
k	Thermal conductivity	W m^{-1} K^{-1}
L_0	Reactor Length	m
M_λ	Spectral radiance	W m^{-2} μm^{-1}
M_λ^{BB}	Spectral radiance of a perfect blackbody	W m^{-2} μm^{-1}
M	Molar mass	kg mol^{-1}
N	Number of species	–
RH	Relative humidity	–
S_{lq}	Laminar burning velocity at the quenching limit	m s^{-1}
S_l	Laminar burning velocity	m s^{-1}
T_w	Wall temperature	K
T_{ad}	Adiabatic flame temperature	K
T_{gas}	Gas temperature	K
T_{opt}	Temperature of the external optic	K
T_q	Flame temperature at the quenching limit	K
T_{room}	Room temperature	K
T	Temperature	K
v_{unb}	Unburned gas velocity	m s^{-1}
v	Inlet velocity	m s^{-1}
W	Molecular weight	kg mol^{-1}
X	Mole fraction	–

Study Context

This thesis is a part of the European project ERC 2G-CSafe (Combustion of Sustainable Alternative Fuels for Engines used in aeronautics and automotive, FP7/2007-2013/ERC grant agreement n°291049) funded by the European Research Council (ERC).

The ERC 2G-CSafe project

The 'Seventh framework program' is a European research programme that runs from 2007 to 2013. The aim is to consolidate the European research in several scientific fields. This programme is divided into four specific programmes which correspond to four goals (http://cordis.europa.eu/fp7/home_en.html):

- The specific program 'Cooperation' supports all types of research activities carried out by various research organizations in transnational cooperation. The aim is to gain or consolidate the leadership in scientific and technological areas.
- The objective of the specific programme 'Ideas' is to reinforce excellence, dynamism and creativity in European research by funding innovative proposals, judged by peers, and independently of the thematic priorities. By doing so, the ERC intends to make Europe a pole of attraction for researchers from all Europe and third countries. The goal is also to offer investments in industrial research, providing a competitive funding structure for the frontier of knowledge research. This funding is attributed to individual teams at the European level in addition to national funding without substituting it. Communication and dissemination of research results represent an important aspect of this programme.
- The overall objective of the specific programme 'People' is to strengthen, quantitatively and qualitatively, the human potential and the technology development. It intends to make research more appealing and stimulating, to en-

courage European researchers to stay in Europe, and to make Europe more attractive for top researchers from all around the world. The coherent set of Marie Curie actions will be implemented under the 7th Framework Programme (PC) and will build on the successful experience of the Marie Curie actions in previous framework programs. Especially it will take into account the benefits of these actions regarding the structuring the European Research Area. These actions will cover all stages of the professional life of researchers, whether they are from the public or private sector, from the initial research training, specifically dedicated to young researchers, to career development and training throughout their career. Efforts will also be made to increase the participation of women researchers by encouraging equal opportunities in all the Marie Curie actions. These actions will guarantee for all researchers a balance between private and professional life, and facilitate a return to work after a career break.

- The 'Capacities' programme aims to support the coherent development of policies, to complete the Cooperation program and to contribute to EU policies and initiatives. The objective is to improve the coherence and the impact of Member States' policies, to find synergies between regional policies, structural funds, education, training programs as well as the Competitiveness and Innovation Framework Programme (CIP).

The 2G-CSafe research project aims to promote sustainable combustion technologies for the transport through the validation of combustion kinetics models using new and sophisticated laboratory scale experiments, measurements in engine and theoretical calculations. This project focuses on the kinetics of the combustion of 2nd generation biofuels and conventional fuels. The motivation of this work is that no specific kinetic models for the ignition, oxidation and burning of 2nd generation biofuels are available, even though they are necessary for the control of new compression-ignition engines. Currently there is a crucial lack of information, *i.e.*, of data from well-characterized experiments on pollutants (unburned, soot) and of data on key intermediates of combustion (radicals and other unstable species). The control of the combustion by active species is studied and interpreted with the help of the detailed models in order to develop new control engine techniques. The project is organized into five tasks, as described in the following paragraph.

Overview of Tasks

Figure 1 summarizes the organization of the 2G-CSafe project. The different tasks (WP1 to WP5) are detailed above.

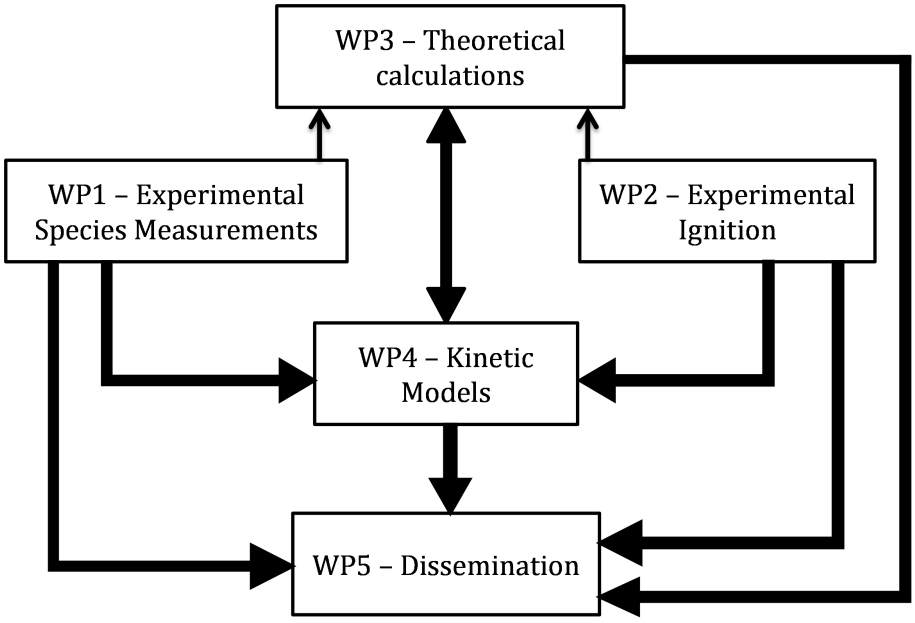

Figure 1: Organization of the 2G-CSafe project.

- **WP1: Acquisition of new data for 2nd generation fuel combustion and pollutant formation.** Kinetic oxidation mechanisms of 2nd generation biofuels must be validated by the confrontation with experimental results in well-characterized conditions (concentration profiles of reactants, intermediates, and final products measured in different conditions). In addition to the measurement of stable species, we need to measure concentration profiles of labile species. The measurement of the combustion key species HO_2 is targeted. New techniques are developed to achieve these measurements. Experiments on the engines are performed to assess the advantages or disadvantages of new fuels according to their combustion behavior and pollutant formation.

- **WP2: Determination of self-ignition characteristics of biofuels and conventional fuels, and control of self-ignition.** The first part concerns the development of a small-scale reactor in order to study the ignition modes of different fuels. The second aspect concerns the control of the combustion of an engine by the injection of active species (NO, NO_2, O_3). The kinetic modeling in these two configurations is used to interpret the results.

- **WP3: Generation of thermochemical and kinetic parameters by theoretical calculations.** Currently the thermodynamic properties and the kinetics of many reactions of 2nd generation biofuels are unknown. Using *abinitio* calculations and RRKM (Rice-Ramsperger-Kassel-Marcus) theory, this information can be available for the development of new kinetic models.

- **WP4: Development of kinetic models and generalization.** While the

oxidation mechanisms of conventional fuels are well known, extending to components of 2nd generation biofuels is difficult. The success of this task strongly depends on the results of tasks 1 and 3.

- **WP5: Dissemination** of results is achieved through articles and thesis publications, conferences, and public interventions with students, as well as dispatching the results on the Web.

The work presented in this manuscript is part of the task 2 (WP2.1) which is described in detail below.

WP2 - Determination of ignition characteristics of 2G biofuels and conventional fuels

With the development of new engine technologies and combustion strategies (HCCI, LTC, etc.), the knowledge of the ignition characteristics of fuels is critical. Research octane number (RON) and motor octane number (MON) have been widely used to represent ignition characteristics of fuels as ignition index. But these indexes represent more knocking tendencies than fuels' ignition characteristics. Moreover, these indexes were established for petroleum-derived fuels, and their application to reformulated fuels and biofuels is questionable.
Shock Tubes (ST) and Rapid Compression Machines (RCM) have been the preferred experimental platform for the measurement of Ignition Delay Times over the last decades. While these two setups have been considered as perfectly homogeneous systems and thus modeled as 0D constant volume batch reactors, recent works have reported that ST and RCM measurements may be strongly affected by uncontrollable disturbances such as combustion-gas dynamics coupling or fluid dynamic non-idealities. Other complications also exist in RCM: heat loss to the combustion chamber wall and vortices generated by the piston movement. It is therefore preferable to investigate the fuel ignition characteristics in a better-suited and characterized reactor (WP2.1). Moreover, to overcome difficulties in the tuning of new engine technologies, the use of active species to control the ignition could be useful. To assess the interest of this approach, engine studies combined with kinetic modeling are required (WP2.2).

WP2.1 - Fuel ignition

It was chosen to use a micro-flow reactor with a well-controlled temperature profile for mapping the ignition characteristics of fuels and their perturbation by EGR

components.
We planned to build a micro-flow reactor with advanced diagnostics (IR and intensified camera) to characterize well, in real time, its operating conditions. It consists of a quartz capillary reactor with external heating by three H_2/Air blowtorches.
This set-up could be useful for studying the effect of pressure on ignition. To determine the ignition characteristics, an intensified EMCCD camera with appropriate filters are used to monitor the emission of radicals during single and two-stage ignition. We planned to initially monitor CH^* emission at 431 nm. Moreover the recent developments of the fast multispectral thermographic systems should allow the characterization of the flame position, thanks to the CO_2 emission (4.2 µm). The ignition processes will be investigated by computations with detailed kinetics. One can expect that this new technique will represent a powerful means to better characterize ignition than classical ignition indexes (ON, CN).

The present work thesis focuses on the first part of the task WP2.1. As detailed in Chapter 2, a new platform has been developed and characterized to this end. It consists of micro-reactors of different sizes with a controlled temperature profile. EMCCD camera has been used to detect the CH^* emission at 431 nm, while an infrared camera has been employed to measure the reactor temperature continuously. This system has allowed the study of the combustion characteristics of different fuels at ambient pressure; as detailed in Chapter 1, despite the huge effort made in the last decade, the knowledge of the combustion dynamics at micro-scale is still lacking. The experimental results achieved are presented in Chapters 3 and 4 for the fuels investigated: methane, ethylene and acetylene. Then, a numerical study has been carried out to investigate the ignition points and presented in Chapter 5.
Then the conclusion and perspectives will conclude this manuscript.

Chapter 1

Background on Micro Combustion

The recent successful development of small devices, known as MicroElectroMechanical Systems (MEMS), has favored the fast miniaturization of technologies in all fields, such as electronics, manufacturing, biology, medicine, chemistry [1]. These devices are characterized by a long lifetime and a reduced weight and cost, but their potential is significantly hampered by the low energy density and the charge time of modern batteries [2, 3].
This need for high-specific-energy miniaturized systems has stimulated the interest of combustion applications towards small-scale technologies because of the high energy density of hydrocarbon fuels. Figure 1.1 compares the energy density of several modern batteries with iso-octane and methanol. Even with a 10% efficiency, a miniaturized liquid-fueled combustor would still have a higher energy density than the most powerful battery currently available [4–7].
The expected primacy of micro combustors has thus led a growing interest and many studies have been carried out over the past decade in the field of micro combustion.

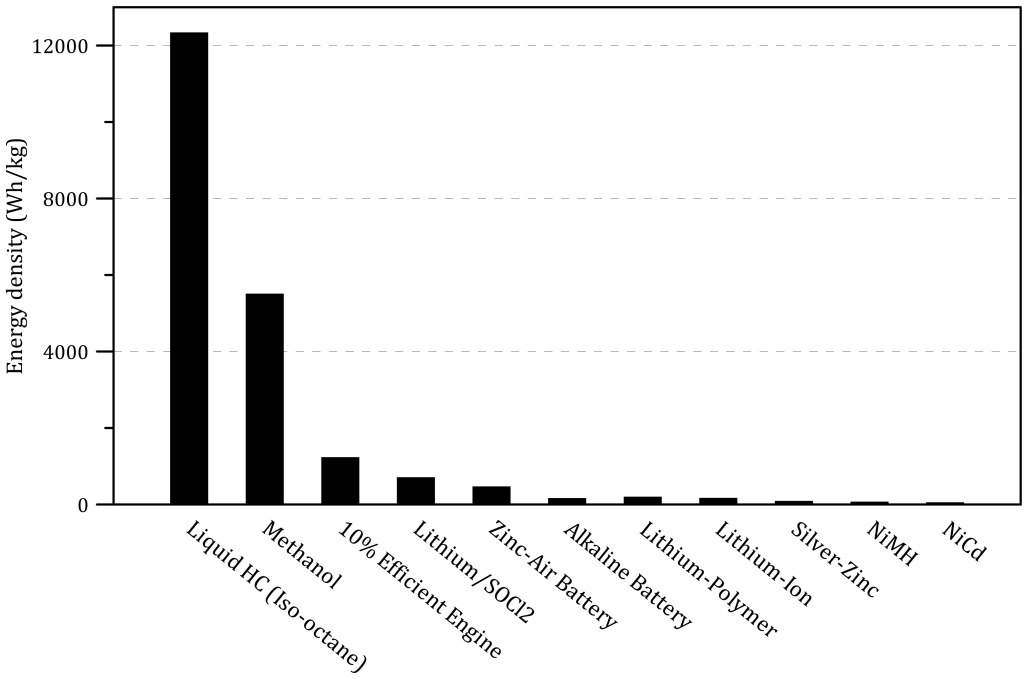

Figure 1.1: Comparison of the energy density of several batteries with fuels [5].

1.1 Micro Combustion and quenching diameter

A combustor is defined 'micro' if its characteristic size is smaller than the quenching diameter [2]. This quenching diameter is the smallest tube diameter which allows a flame to propagate. It is an important parameter that characterizes the interaction between a laminar flame and the wall. Indeed, when the combustor size approaches the quenching diameter, the heat loss to the wall equals the flame heat release rate [8–10].

The distance at which a flame is quenched strongly depends on several parameters, such as the fuel type and its concentration [11, 12], the wall material, the tube geometry [13], the initial temperature and pressure [14]. As the tube diameter shrinks down, the volumetric heat losses are enhanced because of a higher surface-area-to-volume ratio (S/V) while the number of collisions between active radical species increases. These aspects greatly depend on the operating conditions and thus prevent a specific analytical determination of the quenching diameter [15].

As a consequence, extensive experimental studies were carried out to measure the quenching distances over several conditions. Different experimental methods were proposed to determine this parameter and the most used are the burner method (also called the Holm's method [16]), the tube method, and the flange electrode method.

Although no specific analytical approach can be considered, the quenching phe-

nomenon can be investigated from a theoretical perspective. The greatest contribution was achieved by Zeldovich [17], who linked the laminar burning velocity S_{lq} and the flame temperature T_q at the quenching limit to their adiabatic counterparts S_l and T_{ad} through the two relations [18]:

$$\frac{S_{lq}}{S_l} = \exp^{-1/2}$$

$$(T_q - T_{ad}) = \frac{T_{ad}^2 \times R}{E}$$

with:
R = universal gas constant,
E = activation energy.

Moreover, Zeldovich has demonstrated that the Peclet number (Pe), defined as the ratio of advective transport rate to the thermal diffusivity, remains constant at the flame quenching limit [17] and proposed the following expression that relates the quenching diameter d_T [m], the laminar burning velocity S_l [m/s] and the mixture thermal diffusivity α [m^2/s]:

$$Pe = \frac{d_T \times S_{lq}}{\alpha} = \frac{d_T \times S_l \times \exp^{-1/2}}{\alpha}$$

The proportionality expressed by the Peclet number indicates that there is an inverse relation between the burning velocity (S_l) and the quenching diameter (d_T). This explains the U-shape dependence of the quenching distance on the equivalence ratio measured experimentally (Fig. 1.2).

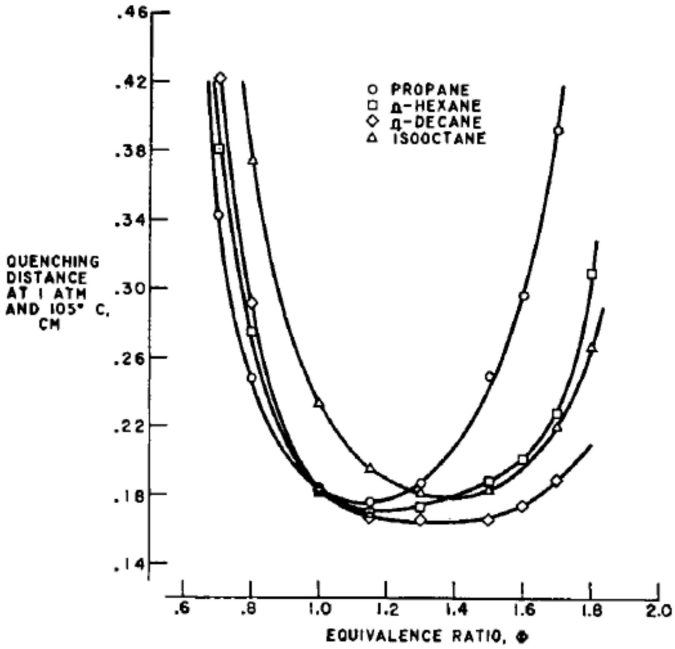

Figure 1.2: Quenching distance as a function of the equivalence ratio for different fuel/air mixtures [16].

The values of quenching diameters available in literature are usually for Standard Ambient Temperature and Pressure (SATP) as a temperature of 298.15 K (25°C, 77°F) and an absolute pressure of exactly 100 kPa (1 bar). However, it was found experimentally [19] that an increase of the initial temperature reduces the heat losses and thus the quenching diameter decreases, as illustrated in Fig. 1.3.

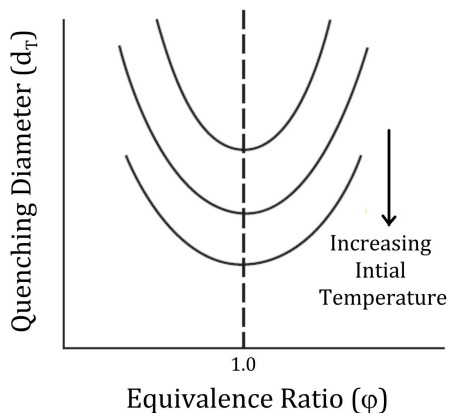

Figure 1.3: Variation of quenching diameter d_T with equivalence ratio φ and temperature [15].

This suggests that by heating the vessel walls, the flame can propagate for a diameter which is smaller than the conventional (SATP conditions) diameter. Moreover, if

the temperature is high enough, a thermal spontaneous ignition may also occur. This has led to the conception of a new regime of combustion, called the 'excess enthalpy' combustion [20].

1.2 The excess enthalpy principle and its application

Weinberg [20] has first introduced the expected advantages of high combustion temperatures, also called 'excess enthalpy' (or superadiabatic) combustion [21, 22]. Through heat recirculation from exhaust gases using high-efficiency heat exchangers [23], the reactants are preheated resulting in a speed up of the reaction rates and thus an enhancement of the burner performances. Hardesty and Weinberg [23] have showed experimentally that preheating the reactants enables reducing pollutant formation and burning low grade fuels. A schematic of such a burner is shown in Fig. 1.4.

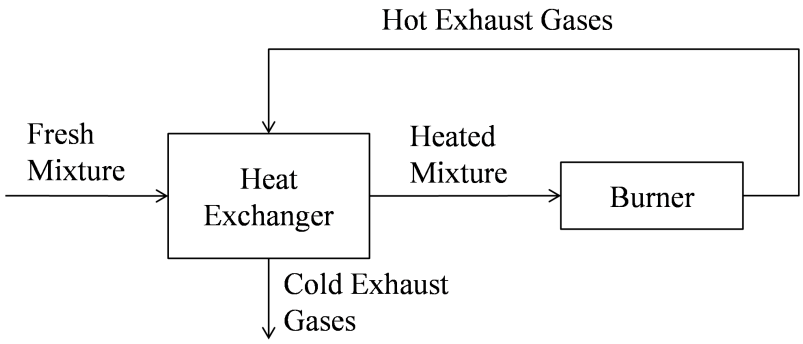

Figure 1.4: Schematic of excess-enthalpy combustion [24].

However, the high temperatures encountered in these burners put constraints on the device walls, the properties and the strength of which can be affected. For instance, Kim et al. [25] have observed that the surface characteristics of the micro-combustor inner walls were strongly impacted by the high temperatures, promoting the flame quenching through an enhancement of radical effects [25].
Later Katsuki et al. [26] have shown that the flammability limits are extended at high temperatures (Fig. 1.5), hence allowing the combustion of low-calorific value fuels or in extremely fuel-lean conditions. This combustion mode, for which the temperature of the fuel-lean reacting mixture is over the auto-ignition temperature, is referred as MILD (Moderate or Intense Low-oxygen Dilution) combustion (also called flameless combustion) and nowadays is a very promising technology for clean and efficient combustion [27].

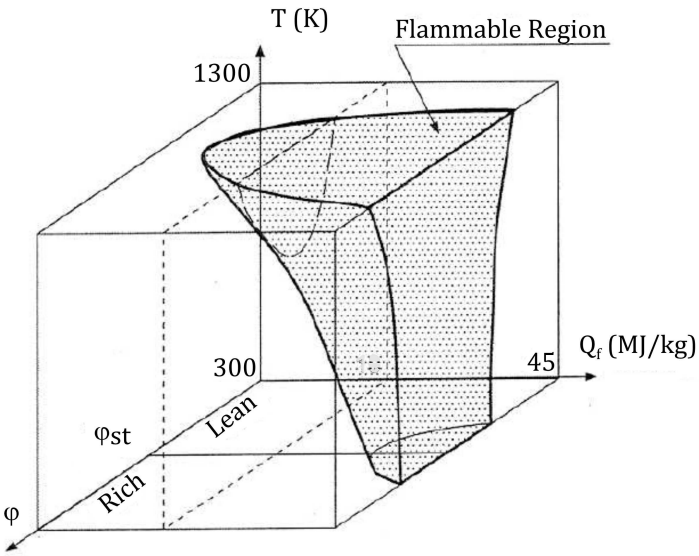

Figure 1.5: Flammable domain as a function of calorific value of fuel, Q_f, initial temperature of mixture, T, and mixture equivalence ratio, φ [26].

Thanks to these studies, the 'excess enthalpy' concept has been adopted to conceptualize a high efficiency micro-combustor. This burner is known as the 'Swiss Roll' burner [28, 29] the reactants are preheated by the burned gases while the combustion zone is located at the center of a pair of spiral channels (Fig. 1.6). With the heat recirculation, notably high temperatures at the reaction zone can be achieved, thus leading to a superadiabatic combustion [30, 31]. With the increase of the flame temperature, standard flammability limits are extended and the quenching phenomena through the heat losses are lessened.

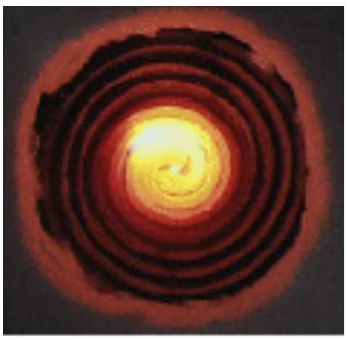

Figure 1.6: Swiss Roll combustor in operation [2].

Furthermore, channels smaller than the conventional quenching diameter have been recently used with this configuration. The experimental results showed that this design is a promising structure for the development of small-scale combustors [32, 33]. However, a thermal management is required to sustain a stable combustion.

Nevertheless, in order to improve the current design and to achieve the highest energy conversion efficiency, a deep fundamental understanding of the effect of all the physical (heat loss, flow mixing, wall-flame thermal coupling) and chemical (oxidation chemistry, radical quenching) aspects involved in the propagation of a flame in micro-channels is mandatory.

1.3 Micro-combustion: theoretical and numerical approach

1.3.1 Phenomenological and theoretical approach

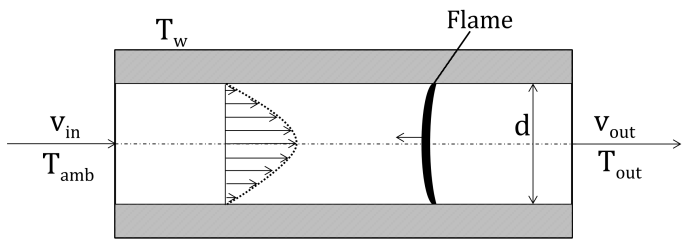

Figure 1.7: Sketch of a flame reacting in a heated micro-channel.

In Fig. 1.7 a schematic of a flame is presented, reacting in an open micro-channel (ambient pressure) heated externally at the temperature T_w. The fresh gases flow inside the tube with a Poiseuille profile and are heated by the tube wall. If the temperature T_w is high enough, a spontaneous ignition occurs and a flame is established inside the tube. As the ratio S/V is high, the heat flux to the wall, described by Fourier's law ($q=-k\nabla T$, where k is the material conductivity and ∇T is the temperature gradient), is particularly enhanced. Moreover, the interfacial heat transfer between the gas and the wall is described by Newton's law of cooling:

$$q = h(T_w - T_{gas})$$

where h is the convective heat transfer coefficient. The value of this term is crucial for modeling the heat transfer inside the reaction zone. As detailed in the next section, many formulations have been proposed, that are not always accurate.

1.3.2 Numerical interpretation: issues and perspectives

As mentioned above, flame propagation in channels is a complex phenomenon which involves gas dynamic, heat transfer, detailed chemistry, etc. Modeling such a system

requires considering all these aspects simultaneously, which is challenging. Over the last decade, several attempts have been made to propose modeling tools to simulate and rationalize the experimental observations. These models have adopted different strategies to solve each aspect of the phenomenon.
Although most of the experimental configurations have a 2D-axisymmetric geometry, early models have proposed, in order to reduce the computational cost, to further simplify the modeling by adopting a 1D geometry where the radial component is neglected and the radial variables are averaged. However, Bianco [34, 35] showed that the choice of the model dimension can play an important role in the predictions. He concluded that the 1D model can provide qualitative information, but the validity of the results is limited. Moreover, the 1D assumption makes difficult to represent the wall-flame heat transfer. This heat transfer is in fact controlled by the thermal boundary layer, *i.e.* the temperature gradient at the wall, which is totally omitted in 1D calculation. Newton's law of cooling is thus reformulated using a Nusselt number when modeling the heat transfer between the reaction zone and the wall. A constant value of $\mathrm{Nu} = 4$ is usually assumed [2].
Norton and Vlachos [36] have performed 2D Computational Fluid Dynamic simulations of stoichiometric propane/air mixtures with an elliptic 2D model for internal heat transfer and a one-step chemistry model. Then they carried out a Nusselt number analysis on the simulated results. They found a strong non-monotonic behavior of this Nusselt number along the channel axis, with large variations around the flame location, thus precluding the assumption of a constant Nu. Later, Veeraragavan and Cadou [37] have demonstrated that a fixed Nusselt number is inaccurate for predicting heat transfer, especially in the reaction zone. However, in the weak flame regime, for which the temperature rise is smooth and limited, the assumption of a constant Nusselt number can hold. Thus, the 1D-model with a fixed Nu employed by the Japanese group headed by Maruta [38] can be used for qualitative interpretation of the experimental results but cannot be used for quantitative predictions.
Recently, in order to elucidate the effect of the model dimensionality and the wall-flame heat transfer description, Gauthier et al. [39] have performed numerical simulations on a stoichiometric methane/air mixture in a 1 mm diameter tube. They employed three different models: a 2D detailed model used as the reference case, a 1D-volumetric with constant Nusselt model, and a modified 1D-volumetrically averaged model that recovers the thermal boundary layer. The three models used a semi-detailed kinetic mechanism (DRM19) [40]. Only flat stable flames were investigated.
The main observation was that the flame position strongly depends on the model that is used: the 1D constant Nusselt model computes much lower stabilization temperatures than the 2D detailed model, while the modified 1D-model shows improved predictions, with deviations lower than 4.2% with the detailed model (Fig. 1.8). Furthermore, the analysis of species distribution showed that, although radially average mole fractions of stable species are in good agreement between the 2D and 1D-simulations, a stronger discrepancy exists for the chain carriers (H, OH, and

HCO) [39].

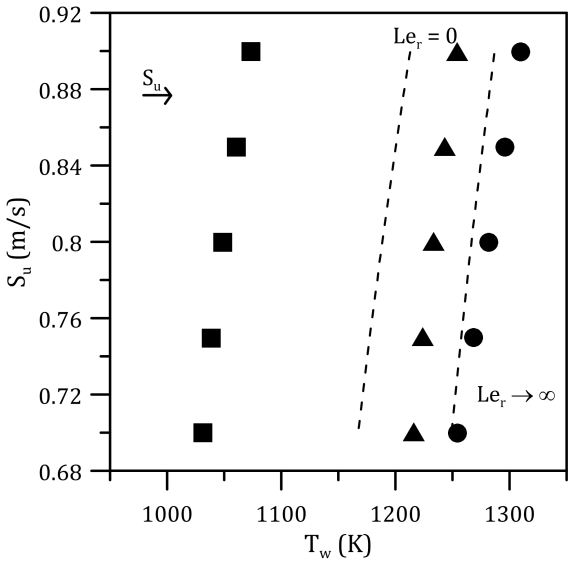

Figure 1.8: Results obtained with the 1D model with Nu = 4 (squares), the volumetrically averaged model (triangles) and the detailed model (circles) [39].

Actually, 1D models cannot capture the radial diffusion of these species, which play a critical role in dictating the mass burning rate and thus the spatial energy profile. The study of Gauthier et al. demonstrates the importance of accurately modeling the interfacial heat exchange at the wall-flame interface. As claimed in [41], only a 2D model with an elliptic formulation of heat transfer can capture the exact topography of heat release in a Poiseuille flow field, but at an expensive cost. Further efforts are still necessary to propose a one-dimensional model that could provide quantitative information.
The aim of this work is to provide experimental data and details about the combustion dynamics that may be used for the development of micro-reactors and also for the improvement of numerical models.
Indeed, the small-scale combustion implies the presence of combustion modes that are not present at meso-scale. With the reduction of the combustor's size, the Damköler number, defined as the ratio of the residence time of a packet of fluid in advective flow to the characteristic chemical reaction time, is smaller; the heat losses reduce the reaction rate, increasing the reaction time, while the residence time is reduced due to the channel's size [5]. This implies a 'weak combustion' where either the flame is quenched or new instabilities appear. In the next sections the combustion modes observed until now, experimentally and numerically, are detailed.

1.4 Micro-combustion: experimental

1.4.1 Experimental setups

In 2005 Maruta et al. [38] have published the first experimental study on micro scale combustion. They used a micro-channel heated up by an external source. The experimental set-up, displayed in Fig. 1.9, consisted of a quartz tube with a 2 mm inner diameter located between two parallel plate heaters. In later works, this experimental configuration was modified by substituting the two heaters by one flat flame burner fed with a hydrogen/air mixture (Fig. 1.10) [42, 43].

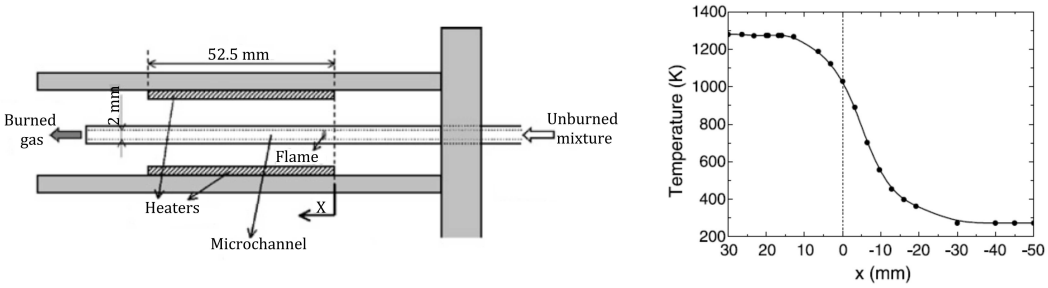

Figure 1.9: Scheme of the experimental set-up used by Maruta et al. (Fig. 1, [38]) and the temperature profile obtained (Fig. 2, [38]).

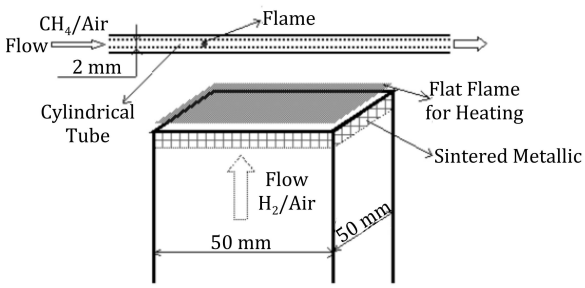

Figure 1.10: Configuration with a single plate heater (Fig. 1b, [42]).

These systems ensure a continuous heating, as well as a controlled temperature gradient along the channel inner wall since the upstream section of the reactor is maintained at room temperature. By setting downstream temperature around 1300 K, the flowing mixture can auto-ignite. The temperature profiles along the channels were measured by a K-type thermocouple with and without an air stream; the flow cooling effect was found negligible.
Methane/air mixture ($\varphi = 0.85$) at atmospheric pressure was studied and the flow rate of the incoming stream was varied. Depending on the inlet velocity, different flame behaviors were identified (Fig. 1.11).

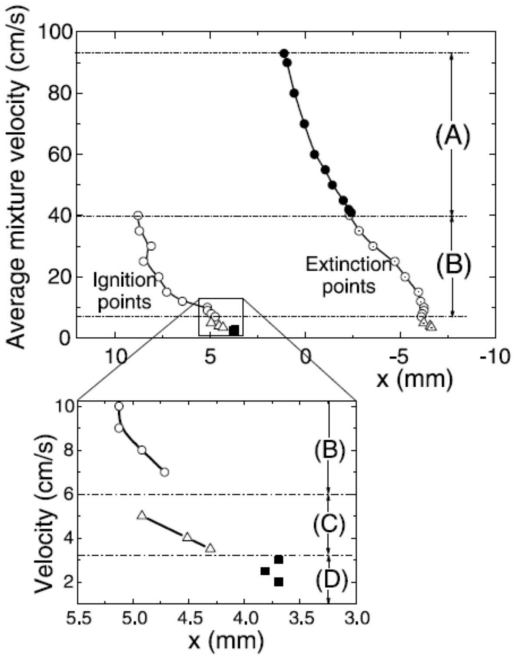

Figure 1.11: Flame positions with the mixture velocity (Fig. 5, [38]).

In the high velocity region (v > 0.4 m/s), stable stationary flames were observed (region A). They stabilize at a specific and well-defined position in the temperature gradient. Decreasing the inlet speed (0.07 ≤ v (m/s) ≤ 0.06), the flame behavior changes and a new regime appears (region B). These flames were called FREI (Flames with Repetitive Extinction and Ignition) and are characterized by a repetitive ignition and extinction of the mixture. For slow inlet velocities, stable flames were once again detected (region D, v < 0.03 m/s), but they exhibited a very low luminosity and were thus called weak flames. These weak flames stabilize at locations that are close to the extrapolated line of the ignition positions of FREI in the moderate velocity regime (ignition points, region B). In the transition between the FREI and weak flame regimes, a combined regime was observed (region C, 0.03 ≤ v (m/s) ≤ 0.06), in which the flames result from the association of the fluctuation of pulsating flames with small amplitude, and repetitive ignition and extinction with large amplitude. In the next sections each flame regime is described in more details.

1.4.2 Stable flame regime

After the downstream auto-ignition (hot channel side), the flame moves upstream and stabilizes at a certain position [38, 43, 44]. The knowledge of such flames is essential for the development of micro-reactors.

Daou and Matalon [45] have studied analytically the propagation of a flame in narrow channels, subject to a Poiseuille flow field and conductive heat losses to the wall. Their results showed that the flame sensibility to the heat losses depends on its shape (Fig. 1.12).

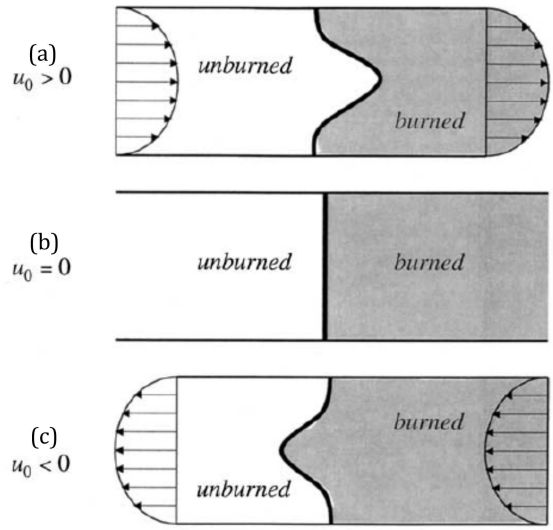

Figure 1.12: Schematic of the flame shapes (Fig. 1, [45]).

When directed from the unburned towards the burned gas (at high inlet velocity, Fig. 1.12a), the flame is more vulnerable to heat losses and thus the quenching diameter increases, as already observed in [46]. Moreover, the flame temperature decreases with the inlet velocity and the heat transfer to the wall is affected [30]. This aspect is more evident when increasing the tube diameter: the Poiseuille profile is increased and simultaneously the axial convection is promoted, resulting in lower temperatures on the channel centerline. As a consequence, if the inlet velocity is high enough the flame temperature is lowered [30].
Furthermore, different velocity profiles affect the flame itself [47], resulting in different propagation velocities and flame structures. As explained by Norton and Vlachos [31], increasing the inlet velocity requires a longer distance to preheat the incoming gases: the flame is therefore stabilized further downstream. The wall temperature at the flame location is higher and the heat losses are lower, thus resulting in higher reaction rates and higher flame temperatures (also over the adiabatic flame temperature) [30].

1.4.3 FREI regime

In the FREI region, the flame ignites downstream, then propagates towards the fresh gases, and is finally quenched in the upstream region. After some time, the flame reignites at the same location as previously and the phenomenon repeats itself, on

a regular basis.
In the last decade, many studies have attempted to elucidate the behavior of these unstable flames in straight channels [38, 48] and curved ducts [49]. Fan et al. [50] investigated methane/air FREI flames in planar quartz combustors of different heights (0.7, 1.0, and 1.5 mm) using laser diagnostics. They monitored the temporal evolution of the CH^* and OH^* signals. In a later study [51], the experimental setup was upgraded with a Nd-YAG pumped dye laser which allowed performing phase-locked OH-PLIF measurement in spite of the transience of the phenomenon of interest. They observed that the CH^* emission signal increases at the ignition, reaches a maximum during the propagation phase, and drops down as the flame gets quenched. The FREI frequencies were measured and found to be dependent on the channel height (from 30 to about 70 Hz).
Fan et al. [52] have investigated numerically and experimentally the FREI of stoichiometric propane/air mixtures in a 2 mm inner diameter channel. The objective of this study was to propose a detailed analysis of the dynamic of each FREI phase (ignition, propagation and extinction). Experimentally, the flame dynamic was recorded with a high-speed digital video camera. The pictures revealed the existence of two luminous regions of different brightness after auto-ignition for an inlet velocity between 20 and 30 cm/s. The brightest kernel is the ordinary flame, and it propagates upstream, while the second moves downstream. Thereafter, the main flame front splits again during propagation: three reaction zones coexist simultaneously, but the second and third extinguish first. The numerical model used to interpret this phenomenon was a global one-step Arrhenius-type reaction, with temperature-independent transport properties and constant-density approximation. The simulation could predict the first splitting observed experimentally: a larger and bright peak, corresponding to the main flame, and a weaker one, as shown also in [53]. However the model could not capture the second splitting, most likely because of the simplified chemistry scheme employed.
Nakamura et al. [54] refined the flame splitting analysis by using a 1D plug flow model with detailed transport properties and chemical kinetics for a stoichiometric methane/air mixture. The presence of several heat release rate (HRR) peaks was confirmed. Before auto-ignition, a weak HRR peak is computed and arises because of the presence of unburned gases (mostly CO) of the previous FREI cycle. Then the flame appears and propagates upstream at a velocity faster than the local mixture speed. As a consequence, while CH_4 is completely consumed, significant amounts of CO and O_2 remain behind the flame front. These unburned species then react, generating a second HRR peak that appears behind the main peak and propagates downstream. Finally, during the extinction/quenching phase, a third HRR peak is observed, that may result from the oxidation of unburned CO at the end of the cycle.
The existence of multiple HRR peaks was also confirmed through numerical simulations by Alipoor and Mazaheri [55], for lean H_2/O_2 mixtures in a 1 mm internal diameter channel. Alipoor and Mazaheri reused the five phases classification of a

FREI cycle proposed by Nakamura et al. [54]: initiation, ignition, propagation, weak reaction and flowing phase. During the initiation phase, the high temperatures in the wall vicinity initiate the reactions and thus leads to a release of small radicals that remain near the wall (consistently with the results obtained by Norton and Vlachos [31]). With the increase of the bulk temperature, the radical pool moves to the channel center and the mixture auto-ignites. Then the flame propagates both upstream and downstream. The main flame advances against the flow and burns the fresh gases, while a secondary and weaker flame consumes the remaining unburned gases at downstream. The main HRR decreases during the propagation phase and a second weak flame is observed right before the extinction. Between extinction and re-ignition, the fresh mixture is heated up again, and a new cycle begins.
Recently, Miyata et al. [56] have investigated the effect of the temperature gradient on the ignition and extinction temperatures of FREI flames. The simulations showed that these temperatures were dependent on the imposed temperature profile. In particular the use of larger wall temperature gradients moves the extinction positions of the flame towards higher wall temperatures region whereas ignition locations are slightly affected.
Although the models of Fan et al., Minaev et al., Nakamura et al., and Alipoor and Mazaheri [52–55] are able to capture qualitatively some key aspects of the FREI propagation, they overlook a critical aspect of the propagation of a flame in a micro-channel, that is to say the wall-flame interaction. This aspect cannot be neglected in order to understand the FREI dynamics, as it will be explained in the next section.
The knowledge of the FREI regime is currently very limited with scarce information available on the dynamics of these flames, such as frequencies and characteristic times. Therefore, it is crucial to gain further insights into the underlying physics of this combustion mode not only to advance our scientific knowledge, but because these FREI flames may help in operating small-scale combustors. Indeed, the repetitive ignition-extinction process could be used as a source of controlled temperature fluctuations. However the temperature variation may induce thermal stress to the reactor walls that should not be overlooked when designing micro-reactors.

1.4.3.1 Quenching mechanism

Unlike in macro-scale systems, the wall is an important part of the system and can affect the flame quenching through two mechanisms, either thermal and/or chemical. The thermal quenching has been widely studied and refers to the heat loss to the wall [57].
On the contrary, the radical quenching mechanism has received much less attention. It refers to the heterogeneous reaction at the wall and includes radical adsorption, desorption, and recombination. The effect of these reactions is negligible in macro-scale devices, but in small-scale combustors, for which the surface-over-volume ratio

is larger, the effect of flame-surface interaction may become dominant. In the past years several studies have been conducted on this topic.
Bai et al. [58] studied theoretically the flame propagation in a micro-channel using a quasi-one-dimensional model that included thermal and kinetic quenching at the wall. The model considers a two-step chain-branching mechanism for the gas phase chemistry and one surface reaction. The influence of several parameters, such as the initial temperature and the tube diameter, on the thermal and radical quenching limits has been investigated. The results show that increasing the initial temperature widely extends the thermal quenching limit and that the flame is mainly quenched by radical depletion, while a decrease of the tube diameter promotes the radical quenching which slows down the flame speed and thus favors extinction. Furthermore, the wall-flame coupling is stronger at high flow rate, in agreement with the previous conclusions of Ju and Xu [59].
As computed by Popp and Baum [60] with a 1D-model, the wall heat flux increases with the wall temperature but also gets faster. Moreover, with the rise of the wall temperature, the fuel consumption is accelerated, resulting in an increase of the active species concentration (H and OH mainly) and thus in a change of the reactive mixture behavior. The combination of these high temperatures and concentrations of light species near the wall may require the systematic consideration of the Soret effect since it can have a significant influence on the flame propagation speed [61–63], especially if surface reactions for such high temperatures become effective, as suspected by Popp and Baum. This supposition was later confirmed by Kim et al., who studied experimentally the influence of surface reactions on the quenching distance of a stoichiometric methane/air mixture as a function of the initial temperature [25]. They observed that only above $\sim$673 K the flame quenching becomes sensitive to the heterogeneous reactions.
The early approach of Popp and Baum was refined by Raimondeau et al. [64] who used a two-dimensional model with detailed chemistry and multicomponent transport to investigate the propagation of methane/air mixtures in micro-channels. They introduced a Langmuir-Hinshelwood surface kinetics mechanism (Table 1.1) in order to account for radicals surface reactions.
The computations showed that when the channel radius is small enough, both the temperature and the mass fraction radial gradients are negligible. As a result, heat and mass transfer between the bulk and the wall is extremely fast and the flame stability is strongly sensitive to the radical pool depletion at the wall.
However, the radical recombination reactions at the wall are exothermic, and thus can help stabilizing the flame. Aghalayam et al. [65] studied numerically the stability of H_2/air flames impinging on a flat surface, by coupling surface reactions and gas-phase chemistry in a 1D-model. Unlike previous modeling attempts, desorption of stable species generated at the wall along with the associated heat release was implemented in the mass and energy conservation equations. For weak fuel-lean and fuel-rich flames, the wall-gas interaction appears to be crucial. Indeed, in these conditions, the exothermicity of the surface reactions increases the wall heat flux, thus

counteracting the sole kinetic quenching effect and resulting in more stable flames. In particular, H atoms were found to most strongly affect flame stability at ignition, while the extinction phase is affected by H, O and OH radicals to a similar extent. Gubernov et al. [66] also studied numerically the effect of radical depletion on freely propagating hydrogen flames: their result confirm that the flame propagation and stability is affected by the radical recombination at the wall.

Reactions
$CH_3 + * \rightarrow CH_3^*$
$H + * \rightarrow H^*$
$OH + * \rightarrow OH^*$
$O + * \rightarrow O^*$
$2CH_3^* \rightarrow C_2H_6 + 2*$
$2H^* \rightarrow H_2 + 2*$
$2OH^* \rightarrow H_2O + O^* + *$
$2O^* \rightarrow O_2 + 2*$
$CH_3^* + H^* \rightarrow CH_4 + 2*$
$OH^* + H^* \rightarrow H_2O + 2*$

Table 1.1: Radical quenching mechanism [64]. $*$ denotes a vacant surface site and X^* a surface adsorbed species.

The radical quenching mechanism shown in Table 1.1 was also employed by Kizaki et al. [67] in a 2D numerical simulation considering gas-phase and surface reactions to describe stable methane/air flames in micro-channels. Comparing experimental data with their model predictions, they observed that at 1.0 and 0.5 atm, although the flame position was well captured by the model, this latter overestimated the amount of CO in the exhaust gases for fuel-rich cases while the quenchless wall simulations provided a much better agreement. They concluded that the Langmuir-Hinshelwood model proposed by Raimondeau et al. overestimates the radical quenching effect, which appears to be negligible around atmospheric pressure, in disagreement with the results obtained in [25, 58, 64, 65]. However, by decreasing the pressure further down (0.05 atm), a strong effect of the radical quenching mechanism was observed which, surprisingly, enhances the overall reactivity in fuel-lean conditions by promoting the production of the OH radical.
Saiki et al. [68] investigated the influence of the wall material (fused silica, alumina, chromium, and platinum) in the quenching mechanism with methane/air flames. They measured by PLIF the distribution of OH radicals in the reactor and used numerical modeling to interpret the experimental observations. They found that below 873 K the wall thermal effect is dominant, as demonstrated by comparable measured OH concentrations in the wall vicinity, but is overtaken by the chemical effect at higher temperatures. Furthermore, the chemical quenching effect depends on the wall material: alumina exhibited the best inertness while fused silica and

chromium showed significant kinetic quenching effect [69, 70].
Although many studies were dedicated to the experimental and numerical investigation of the wall-flame interaction, the mechanisms involved are still unclear. However, undoubtedly, this phenomenon strongly depends on the wall and mixture properties. Consequently, without suitable quantitative data it will remain impossible to compare and pin down the processes responsible for the flame extinction in different conditions.

1.4.4 Weak flame regime

In the low velocity region (region D, v $< 3\,\mathrm{cm/s}$ in Fig. 1.11), stationary flames are again observed. They have a very weak luminosity, and thus an image-intensified camera was required to track their chemiluminescence. These weak flames stabilize at locations that are close to the extrapolated line of the ignition positions of FREI in the moderate velocity regime (ignition points, region B in Fig. 1.11).
The preliminary numerical work of Maruta et al. [38] with a 1D constant Nusselt model showed that the HRR associated with these flames was weak, resulting in a small increase of the temperature ($\sim$15 K), and that they were also characterized by a broad distribution of intermediate species (such as CO and CH) because of prominent mass diffusion favored by a slow overall reactivity. For these reasons, weak flames have been readily associated with the mild combustion regime [27, 71, 72].
Theoretical predictions by Minaev et al. [73] with a 1D nonlinear evolutionary equation of the flame front showed that such weak flames stabilize close to the ignition point and with a small temperature increase. Tsuboi et al. [42] studied the stability of premixed methane/air flames in meso-channels, with special attention to the lower limit of the weak flame regime. Regardless the equivalence ratio, no flame was detected for inlet velocities lower than 0.02 m/s. At this velocity, the flame temperature, measured by introducing a thermocouple in the system, was nearly identical (within 2 K) to the wall inner surface, around 1225 K. From their measurements and the numerical predictions of Minaev et al., Tsuboi et al. concluded that the flame temperature, thus the stabilization wall temperature, at the lower limit of the weak flame could be considered as the minimum ignition temperature of the mixture. From this conclusion, several experimental studies [74–78] using the experimental setup employed by Tsuboi et al. have been undertaken to access the ignition temperatures of several fuels.

1.4.4.1 Auto-ignition temperature (AIT)

The Auto-Ignition Temperature (AIT) of a given mixture is the minimum temperature required for the mixture to ignite spontaneously, that is to say without an

external ignition source. Several standardized methods exist to determine the AIT at atmospheric pressure: EN 14522, DIN 51794, IEC 60079-4, BS 4056-66, ASTM E 659-15, ASTM D2155-12, ASTM D2883-95. Even if the difference between the setups is small (as vessel volume or material), the measured AITs change greatly according to the method used, as shown in Table 1.2 for methane/air mixtures:

AIT (K)	Method
793	DIN 14011 [79]
813	ASTM D-2155 [80]
868	DIN 51794 [81]
893	EN 14522 [82]
923	DIN 14011 [83]

Table 1.2: Comparison of methane/air auto-ignition temperatures obtained with different test methods.

The large discrepancy between the AITs measured for methane/air mixtures indicates that this temperature is influenced by several parameters, such as the vessel volume, material and geometry.
In 1954 Setchkin [84] measured the AIT of several fuels in spherical vessels of different sizes. He observed that the AIT decreases as the vessel volume increases. Actually, the ignition occurs only if the heat release rate of the reaction is greater than the external heat losses. Thus a decrease in the vessel diameter increases the surface-to-volume ratio, enhancing heat losses and increasing the energy required to ignite the mixture [83]. This volume dependency is described by the Semenov theory of thermal ignition [85]. Beside the vessel volume, the influence of the vessel material cannot be neglected. Like the quenching mechanism, the material can promote or inhibit the ignition process via heterogeneous reactions at the wall or through its thermal capacity. While several studies are available in literature regarding the effect of different metals on the AIT, the influence of inorganic material such as fused silica on the AIT has never been investigated. The values reported in Table 1.2 are thus specific to the operating conditions adopted for the measurements, as long as detailed information on the effects of the vessel size and material are not available. Therefore the conclusion drawn in [42], that the wall temperature at which the weak flame stabilizes is the minimum ignition temperature must be considered cautiously since no clear comparison with literature values is possible.

1.4.5 Transitional regimes

In the first experimental study of Maruta et al. [38], the FREI and the weak flame regimes were separated by a peculiar regime, described by the authors as a combination of periodical motions of pulsating flames with small amplitude and repetitive

ignition and extinction with large amplitude (region C, Fig. 1.11). However, they did not observe pulsating flames with a regular oscillatory motion in the condition investigated (stoichiometric methane/air flames, cylindrical quartz 2 mm inner diameter channel). This combined regime was not mentioned in the experimental works that followed. For instance, Tsuboi et al. [86] detected a transitional flame between stable flame and FREI regimes, labeled 'FREI + pulsating'. However, further details were not provided in the paper.

While experimentally accessing and investigating these transitional regimes is tricky, numerical simulations have widely contributed to the knowledge of these transitional regimes. Getting further insights into such transitional regimes is crucial for the development of small-scale reactors. Their existence has important safety and efficiency implications for industrial applications.

Minaev et al. [73] (with a 1D nonlinear evolutionary equation of the front flame) theoretically predicted the existence of flames with small oscillation amplitude between the weak flames and FREI regimes, but also another oscillating regime in the transition between the FREI and stable flames. This new regime, never experimentally observed before but already predicted by Norton and Vlachos [31] (with a 2D, one-step chemistry CFD model), was named 'FREI with oscillations' as the flame oscillates before extinction. Norton and Vlachos [31] explained this periodic oscillatory behavior near extinction as the results of pressure waves associated with the fluid density variation.

Further examinations were carried out by Miroshnichenko et al. [87] using a thermal-diffusion model with a two-step reaction scheme for fuel-rich H_2/O_2 flames ($\varphi > 7.0$). The simulations showed that three different oscillating regimes exist depending on the inlet velocity. Starting from a stable stationary flame and decreasing the inlet velocity, a 'chaotic regime', that results from thermo-diffusive instabilities, emerges. In these conditions the radical concentration remains finite and oscillates around an average value that corresponds to radical concentration computed for the stable flame [87]. Further decreasing the inlet flow makes the oscillation amplitude increases until a period-doubling bifurcation is detected; the flame now pulsates before extinction due to diffusive-thermal instabilities. Under a critical value of flow inlet velocity, the thermo-diffusive instabilities vanished and the FREI regime, characterized by the flame extinction, is observed. Miroshnichenko et al. derived the existence diagram of these transition regimes in terms of inlet velocity versus equivalence ratio (Fig. 1.13).

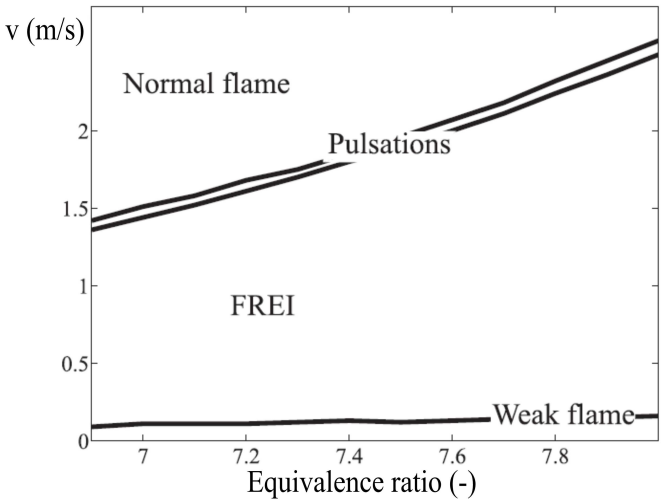

Figure 1.13: Map of the different flame regimes of fuel-rich H_2/O_2 flames proposed by Miroshnichenko et al. [87].

However Gurbenov et al. [88] and Karsakova et al. [89] studied numerically the thermo-diffusive instabilities of rich hydrogen/air flames and demonstrated that the prediction of such instabilities strongly depends on the reaction mechanism employed.
Miyata et al. [56] performed Direct Numerical Simulation (DNS) with a detailed chemistry (GRI-Mech. 3.0 [90]) scheme for a stoichiometric methane/air mixture in a 1 mm internal diameter channel. Calculations show the existence of oscillating flames with small amplitude in the transition from stable to FREI flames. These flames exhibit a lower temperature and thus evolve in a narrower wall temperature domain than the FREI flames, which can propagate towards cooler wall temperatures (1150 against 1300 K) before extinction. Moreover, these two types of flames behave differently regarding the heat transfer through the wall, which plays a crucial role in their dynamics. While the oscillating flame constantly loses heat to the wall, the FREI flame in its flowing phase gains energy from the wall.
Jackson et al. [91] have proposed a 1D, one-step one-reactant chemistry model with thermal wall-flame coupling to qualitatively investigate flames in micro-channels. They were able to capture the experimental observations of Maruta et al. [38] regarding the existence of two transitional regimes connecting the FREI regime with the stable and the weak flame regimes. The different oscillating behaviors –that depend on the inlet velocity– were unveiled by monitoring the temporal evolution of the reaction rate, as illustrated in Fig. 1.14.
These oscillations were associated with instabilities generated by the heat flux within the wall reactors. Recently, Bucci et al. [92], with the help of 2D numerical simulations have attributed these instabilities to the emergence of a phase shift between the heat production and the heat radial diffusion, which display an oscillating behavior

in phase opposition as soon as the flame enters the FREI.

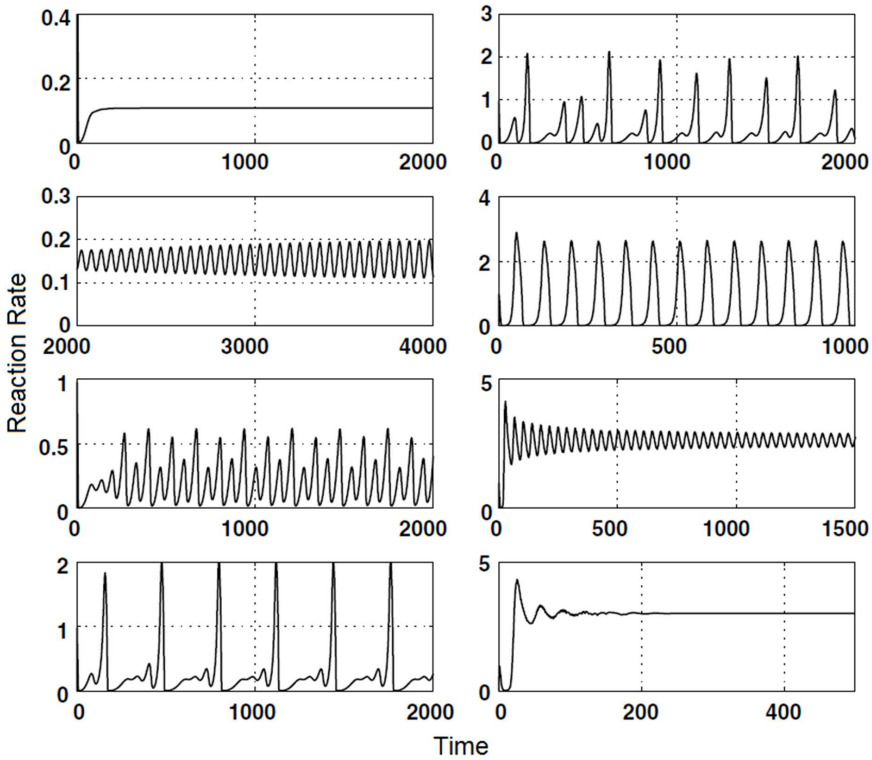

Figure 1.14: Time fluctuation in the maximum reaction rate increasing the inlet velocity (ordered by columns) [91].

1.5 Parameters effect

1.5.1 Inlet velocity

As detailed in the Section 1.4.1, three main flame regimes exist with respect to the inlet velocity: stable, FREI, and weak flames.
The high flow speed region is the domain of stable flames. In this regime, for increasing velocities, the convective timescale decreases leading to cooler gas phase temperatures (less efficient heat conductivity from the wall to the gas) and thus to a displacement of the flame downstream, towards hotter wall temperature regions, in order to reach thermal equilibrium. Conversely, decreasing the mixture speed the residence time becomes higher and the convective timescale becomes long compared to the axial conductive timescale. The reactor temperature is higher, although the heat generated by the reaction decreases. When the heat losses to the wall are sufficiently high, the FREI regime appears. The velocity value at which the flame

switches from the stable combustion mode to extinction strongly depends on the operating conditions and the wall thermal conductivity [36]. Minaev et al. [73] have demonstrated that the flame inertia is crucial for the study and the interpretation of unstable regimes. Omitting the flame acceleration and the temperature variations in the numerical models, flame extinction and oscillatory behaviors, that are particularly sensitive to the heat losses, become difficult to predict.
Pizza et al. [93] have studied the behavior of H_2/O_2 flames in planar channels using DNS focusing their analysis on the FREI regime. They deduced from their simulations that the FREI characteristic frequency, that is associated to one initiation-ignition-propagation-extinction-flowing cycle, increases with the inlet velocity. Alipoor and Mazaheri [94] relate this dependency to the increase in flame temperature (resulting from the reaction heat release) and thus in the subsequent higher burning velocities. As a consequence the flame propagates faster towards the fresh mixture, but the low temperature of the incoming unburned gases causes a sudden drop in flame temperature and its consequent extinction. Therefore the flame is quenched in a shorter time whereas a fast re-ignition occurs leading to the observed higher frequency. However, experimental works focusing on the FREI frequencies and characteristic times (time required for flame ignition and extinction during each cycle) are not currently available in the literature, precluding the assessment of the above interpretation.

1.5.2 Equivalence ratio

Most of the previous experimental studies have been carried out with stoichiometric mixtures, therefore overlooking the effect of the equivalence ratio on the dynamics of flames in heated micro-channels. Tsuboi et al. [42] have looked at the effect of the mixture composition on the characteristics of methane/air weak flames. They observed that the lowest inlet velocity allowing the stabilization of a weak flame was independent of the equivalence ratio, as well as the wall stabilization temperature for this weakest flame. However, within the weak flame regime, the measured flame front temperature was observed to increase with both the inlet velocity and the equivalence ratio. This latter observation must nevertheless be cautiously considered, since 1.2 was the highest equivalence ratio studied. Indeed, the weak flame temperature may behave similarly as the adiabatic flame temperature decrease for the fuel-richest compositions.
Nakamura et al. [95] have investigated the propensity of methane/air flames to produce PAHs (polycyclic aromatic hydrocarbons) and soot in a micro-channel and its dependence on the equivalence ratio and inlet velocity (U_0). A response map to these two parameters was derived: soot formation could only be observed for very–fuel rich mixtures ($\varphi \geq 2$) and moderate inlet velocities (0.05 – 0.30 m/s), either in the existence of a flame front ($\varphi = 2$ and $U_0 \geq 0.2$ m/s) or not ($\varphi > 2$ and $U_0 \leq 0.525$ m/s). Dubey et al. [96] and Nakamura et al. [95] have later extended

this study to ethane/air and cetane/air mixtures, respectively.
Sànchez-Sanz et al. [97] have investigated analytically the effect of equivalence ratio on flame stability employing a 2D-model within the thermo-diffusive approximation and with a global one-step chemistry scheme. In the case of equi-diffusional mixtures (Lewis number = 1), fuel-lean and fuel-rich mixtures behave similarly (all other parameters being identical) and symmetrically with respect to the stoichiometric mixture, which is the most stable. Furthermore, a new unstable behavior, identified by a change in the oscillating frequency and amplitude shortly after the flame ignition, is predicted for non-stoichiometric mixtures in a specific inlet velocity range (which depends on the equivalence ratio).
Regarding the dependence of AIT, which has been associated with the weak flame regime, to the equivalence ratio, the strong effect of the experimental device on the measurements results in large discrepancies between the scarce data [98, 99] available. However, it seems that the AIT is minimum for equivalence ratios around 0.7 (for methane) and then increases along with the equivalence ratio, in contradiction with the most recent numerical study by Ye et al. [100] who found that the AIT of fuel/air mixtures decreases with decreasing the fuel mole fraction.

1.5.3 Reactor dimension

The flame response to the channel dimensions, namely the length, the inner diameter and the wall thickness, has not been the subject of any previous experimental study. However, the choice of the appropriate dimensions is fundamental to develop micro and meso-scale reactors. Indeed, the reactor dimensions affect the flame stability and the quenching mechanisms; the extent of this effect remains an open question from an experimental perspective.
Although no experimental data are available as mentioned above, several computational studies have tackled the influence of the reactor characteristics, such as reactor length, wall thickness and channel diameter. Kaisare and Vlachos [101] have studied numerically, amid other parameters, the effect of the reactor length on the stabilization of methane/air and propane/air flames with a 1D, constant Nusselt, one-step chemistry model. Increasing the channel axial dimension enhances external heat losses. Consequently the inlet velocity range that allows achieving stable self-sustained flame shrinks down with the increase of the channel length, whereas the blow-off limit is weakly affected. Moreover, the flame location is almost independent on the reactor length, due to the localized nature of homogeneous combustion at micro-scale.
Norton and Vlachos [31] explained that increasing the wall thickness was equivalent to increase the wall conductivity. Their 2D computations clearly demonstrated that the wall thermal conductivity/thickness plays an important role in flame stability by governing axial heat recirculation or heat losses. A low thermal conductivity results in a poor heat recirculation through the walls and thus in a large axial tem-

perature gradient. Then the flame stabilizes far downstream (hot region) and as a result is very sensitive to the inlet velocity regarding the blow-off limit. Conversely, large thermal conductivity favors uniform but elevated wall temperatures. Then, heat losses are large and affect the entire reactor length, rendering the flame less stable while enhancing its sensitivity to extinction. Furthermore, a high thermal conductivity enhances the radial gradient, and thus the thermal extinction limits are extended compared to the radical quenching limits [64, 102]. Norton and Vlachos determined the optimum wall thermal conductivity range (3 – 5 W/m/K) to achieve combustion in micro-channel combustion. According to their work, ceramic materials such as high-temperature silica and alumina are to be preferred.
Norton and Vlachos [31], Pizza et al. [93], Bai et al. [58], and Gauthier et al. [103] have studied the influence of the channel diameter on flame stability. As the channel diameter decreases, radial heat transfer is favored, resulting in higher wall temperatures although the gas phase temperature remains controlled by axial heat convection [30]. Thanks to heat recirculation via the wall, the preheating capacity of the reactor improves and enhances the burning rate. Then, the quenching diameter decreases and operating conditions are extended. However, when the diameter becomes excessively small, this promoting effect disappears. The centerline is strongly affected by the heat transfer to the wall, and the gas phase temperature decreases [31, 93] while radical quenching effect gets enhanced by both the higher wall temperatures [58] and the negligible radial mass gradient [64]. As a result incomplete combustion is observed: the flame becomes less stable and more sensitive to extinction. Ultimately, there is a channel diameter below which no flame can exist.
Pizza et al. [93] additionally derived a map of the different flame regimes with respect to the inlet velocity and the channel diameter. Interestingly, they observed that the transition speeds (velocities for which a change of flame regime is observed) increase with the diameter. Bianco et al. [34] extended recently this observation to methane/air flames. Paying special attention to the FREI regime, Pizza et al. also noticed that the FREI frequencies decrease with the tube diameter. This observation can be rationalized by considering that as the channel diameter decreases, the heating efficiency of the reactor increases (because of better radial heat transfer) and fresh mixture travels through a shorter distance before reaching the auto-ignition temperature, resulting in higher frequencies. Adopting a similar approach than Richecoeur et al. [49], the Strouhal number (St), which relates the FREI frequency, f, the channel diameter, d, and the inlet velocity, v, was calculated with the following formulation:

$$St = \frac{f \times d}{v}$$

It is generally used to describe oscillating flow mechanism [104], in particular for the

vortex shedding. Surprisingly the Strouhal number was found constant for channel diameter greater than 0.5 mm.
In the above discussion, the relative effect of each parameter was discussed mostly based on theoretical/numerical considerations. However, the quantitative influence depends on the fuel as demonstrated by Kaisare et al. [3], which suggests that there will be as many optimized reactors as they are potential fuels for micro-combustion.

1.5.4 Fuel type

After the successful observation of methane flames in a micro-channel, Maruta et al. [38] have investigated the micro-scale combustion of more complex fuels, with a strong focus on the characterization, both experimentally and numerically, of the weak flame regime.
Yamamoto et al. [78] have performed experiments with stoichiometric n-heptane/air mixtures. As before, three flame regimes were identified (stable, FREI, weak flames) with respect to the inlet velocity. However, differently from the observations of Tsuboi et al. [42] for a stoichiometric methane/air stream, a clear temperature gap was detected between the stabilization temperature of the last stable flame (T = 960 K at 0.31 m/s) and the extinction temperature of the first FREI (T = 780 K at 0.29 m/s). Nevertheless, the FREI regime exhibits a similar behavior as that reported for methane: the oscillating frequency decreases with the inlet velocity, from 70 Hz at 0.30 m/s to 4 Hz at 0.04 m/s. Conversely, the weak flame regime displayed some unique particularities. Indeed, three luminous zones were detected while only one could be observed for methane. The first spot, located in the cold section of the micro-channel, is characterized by a very weak luminosity. Further downstream, there is a broad luminous zone containing two distinct reaction fronts. Numerical computations with a 1D, constant Nusselt model with detailed n-heptane chemistry confirmed the existence of a three-stage oxidation process, while path flux analysis combined with sampling experiments allowed delineating the chemical processes involved in each reaction zone. In the first reaction zone, a cool flame occurs ($T_w \sim 800$ K), CH_2O and H_2O_2 are produced through reactions relevant to n-heptane low temperature chemistry. The low-temperature products are then conveyed to a second zone ($T_w \sim 950$ K) where they are oxidized into CO and CH_4. Finally, CO, CH_4 and other unburned species are completely oxidized to CO_2 and H_2O in a third flame ($T_w \sim 1150$K). The multistage weak flame structure was previously [78] proposed to be a characteristic of fuels with strong low-temperature chemistry, as demonstrated by experiments with DME [74], n-cetane [75], and gasoline surrogates [76, 77]. In these studies, the influence of the pressure on the weak flames was also investigated. Pressure as high as 6 atm was achieved, without altering significantly the weak flame structure. The three-stage structure was still observed, but with a shift towards lower temperatures associated to a stronger intensity of the first and the second reaction zones, while the third reaction front got weakened.

Hori et al. have investigated the effect of blending n-heptane with toluene [77] or iso-octane [76], known to be rather unreactive at low temperature, on the weak flame characteristics. They observed that the cool flame weakens with the amount of additive, and is cut off above some threshold (less than 50% for iso-octane and more than 50% for toluene). Otherwise, the hot flame is slightly impacted, except that it is shifted downstream *i.e.* towards higher wall temperatures. Ultimately, neat toluene and iso-octane/air flames exhibited one and two-stage structure, respectively, and toluene flames stabilized at higher wall temperatures than iso-octane flames (1220 vs. 1150 K).
Kamada et al. [105] have compared the micro-combustion of natural gas components (methane, ethane, propane, and n-butane) in the weak flame regime, at the stoichiometry and atmospheric pressure. It was surprisingly found that ethane was more reactive (the reactivity criterion being the wall temperature stabilization) than the larger alkanes (T_w = 1145, 1175, and 1170 K for ethane, propane, and n-butane, respectively) despite its higher RON (Research Octane Number) (115, 112, and 94 for ethane, propane, and n-butane, respectively). However, numerical simulations showed that this unexpected observation was an artefact caused by the different thermodynamic conditions (pressure mainly) between the micro-channel and the RON measurements. At higher pressures, the simulations recover a monotonic relationship between RON and wall temperature stabilization. A similar comparative study was performed by Kikui et al. [106] regarding the weak flames of linear 1-alkenes, from ethylene to 1-pentene. Ethylene was identified as the most reactive fuel, which was attributed to its higher propensity to producing H_2O_2.
Li et al. [107] have studied the influence of the bath gas, by substituting nitrogen by CO_2. The wall temperature-inlet velocity flame regime diagram was experimentally determined. The velocities at which the transitions between the different regimes are observed are lower for the CO_2 diluted mixture than for the air mixture: 0.40 vs. 0.25 m/s and 0.05 vs. 0.025 m/s for the stable-FREI flames and the FREI-Weak flames transition, respectively. The weak flame was also observed to stabilize at slightly higher temperatures (+10 K) in the presence of CO_2. Supporting numerical simulations (1D, constant Nusselt model) showed that CH_4/air and $CH_4/O_2/CO_2$ stoichiometric flame structures did not present remarkable differences but similar stabilization temperatures (1203 and 1205 K).
Besides the experimental work of Maruta and his team, Norton and Vlachos [36, 38] have investigated numerically the influence of two fuel characteristics, namely the heat of combustion and the global one-step reaction rate constant, on the micro-combustion stability using methane and propane as prototypical fuels. They concluded that the most sensitive parameter was the kinetics, and especially the activation energy. Therefore fuels with lower ignition temperature would be more robust regarding micro-combustion.
Despite the remarkable efforts made over the last decade, there is still a lack of information about the fuel effect on flame dynamics at micro-scale. The stable flame and FREI regimes have been widely neglected, such as the equivalence ratio and the

diameter effects.
Experiments with ethylene [108] and acetylene [109], both fuels studied in the present work, have been never carried out earlier. A different apparatus was used to study the flame propagation speed of acetylene/air mixtures at micro-scale [110], but the authors do not provide details about the combustion dynamics in micro-reactors.

1.6 Conclusions

Nowadays the fast miniaturization of technologies in all fields has suggested the combustion application in small-scale device, promoted by the high energy density of hydrocarbon fuels. The micro-combustion concept is to burn fuels in reactors of size smaller than the conventional quenching diameter. Spontaneous ignition is possible if the reactor is heated externally, resulting in a reduction of the quenching diameter. This has led to the concept of the 'excess enthalpy' combustion: the flammability limits are extended, allowing the combustion under very lean conditions (MILD combustion).
However, combustion at micro-scale is a far from trivial problem: the small scale enhances the heat losses and increases the reaction time, while the residence time is reduced. This implies the presence of new combustion modes, not present at macro-scale. Three main flame regimes have been observed: stable flames, FREI (flames with repetitive extinction and ignition) and weak flames. Between these regimes, transitional flames are present.
In the last decade huge efforts have been made to understand the dynamics of these combustion modes, more numerically than experimentally. However, in the numerical models developed the approximations used to simulate the heat transfer strongly affect the reliability of the results obtained. On the other side, the experimental works carried out until now mainly focused on the study of the weak flame regime. The other flame regimes have been mostly neglected, as well as the effect of parameters like equivalence ratio and reactor size.
The aim of this work is thus to provide deeper insights into all the combustion modes present at micro-scale because this is fundamental for their future application in micro-reactors. Moreover the data provided may be used for the improvement of numerical models currently available as well as kinetic mechanisms.
To this end, a deep analysis of each flame regime was carried out and the influence of different parameters was investigated: inlet velocity, equivalence ratio, reactor size, and fuel (nature). Particular attention has been devoted to the study of the unstable flames, for which frequencies and characteristic times are provided. Furthermore a detailed analysis of the transitional regimes, studied experimentally for the first time is presented.

Chapter 2

Experimental Setup

2.1 Part I: Experimental Setup

The micro-combustion experiments were conducted in the ICARE laboratory. This chapter describes the device developed during this thesis work in detail. A schematic of the experimental setup is shown in Fig. 2.1. It consists of three major parts: (i) the mixture preparation equipment and the micro-flow reactor, (ii) the external heating system and (iii) the data acquisition system.
The aim of this system is to provide further details to understand the flame dynamics on micro-combustion. As seen in Chapter 1, despite the remarkable progress achieved during the last decade [2], there is still a lack of detailed information. To this end, a spectroscopic high frequency camera is employed to study the dynamics of flames. Furthermore a new heating configuration is developed to achieve a homogeneous temperature for a given reactor section.

2.1.1 Mixture preparation equipment and micro-flow reactor

The components of the gas mixture (fuel, oxygen and nitrogen) are supplied from high-pressure cylinders followed by three in-line filters (Swagelok, series 4TF). Each gas line is equipped with two Mass Flow Controllers (Brooks GF40), the operating flow ranges of which overlapped, in order explore all the flow rate ranges (Fig. 2.2). Shut-off valves (Springless Diaphragm Valves) are used before and after the MFCs. The downstream pressure is set at atmospheric pressure.
The MultiFlo configurator application is used to choose and calculate the operating range of each MFC according to the inlet gas. A digital control is used to change

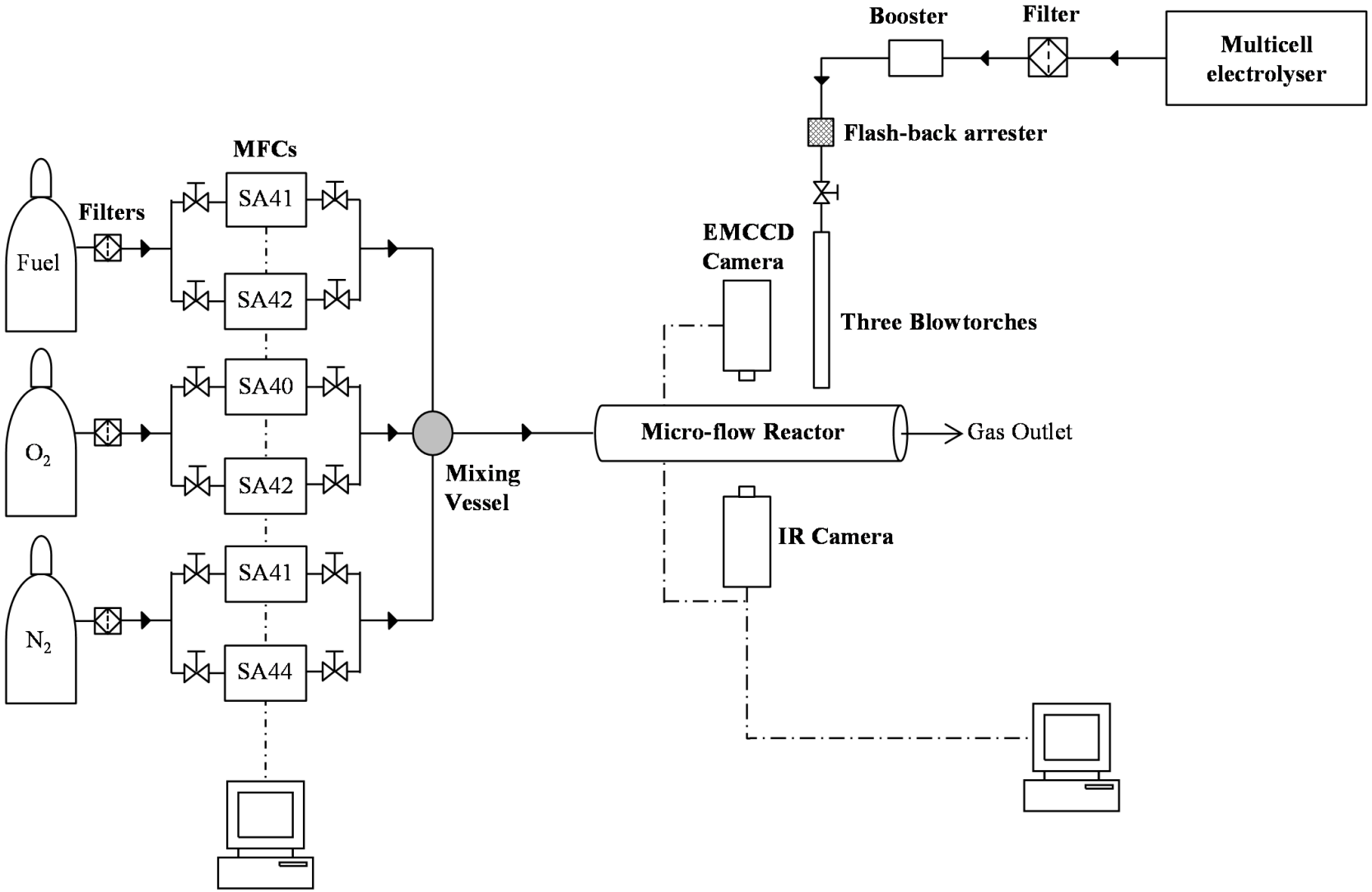

Figure 2.1: Schematic of the experimental setup.

the flow rate during experiments. The accuracy is ± 1% for flow rate within 35 to 100% of full scale (FS) and ± 0.35% for lower flow rate (< 35% of FS). In Table 2.1 the operating ranges are detailed.

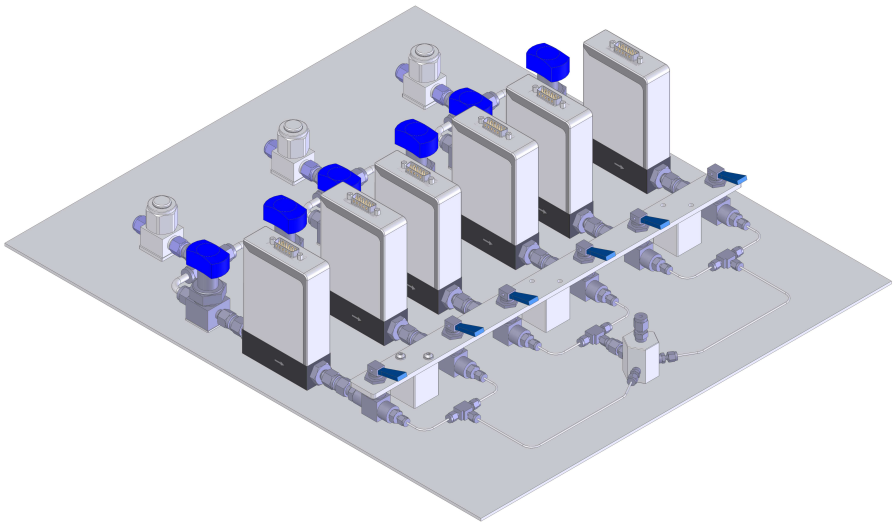

Figure 2.2: MFCs installation.

Gas	MFC Model	Operating range (sccm)
CH_4	SA41	0 – 23
	SA42	0 – 71
C_2H_4	SA41	0 – 10
	SA42	0 – 30
C_2H_2	SA41	0 – 7
	SA42	0 – 20
O_2	SA40	0 – 10
	SA42	0 – 92
N_2	SA41	0 – 30
	SA44	0 – 860

Table 2.1: Flow rate range of the different mass flow controllers.

The gases delivered by the MFCs are then mixed inside a 20 mL vessel and this homogeneous mixture is sent to the reactor.
The micro-flow reactor consists of a transparent tube. Fused silica was chosen because of its good transparency and high resistance to temperature (melting point around 2000 K). It also has a near zero thermal expansion (10^{-6}/K) and a good inertness, although previous studies have shown that the chemical inertness may not be ensured at high temperature (T > 873 K) [15, 68, 69].
The tubes employed have a high optical quality to prevent any flame signal distortion that may be caused by the presence of inhomogeneity. While the external diameter

is fixed by mechanical constraints and set to 6 mm, the internal diameter is varied according to the fuel used during the experiments. Table 2.2 lists the tube diameters employed for each fuel.

Fuel	Internal tube diameter (mm)
CH_4	1, 1.85, 2.15, 2.5
C_2H_4	0.7, 1
C_2H_2	0.7

Table 2.2: Internal tube diameter used during experiments.

Rifling on the external tube surface is used as a physical reference and as common reference for the cameras employed in the present work (zero position, Fig. 2.3).

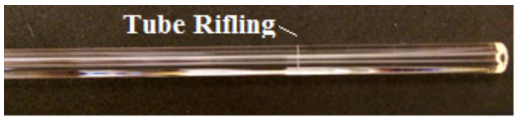

Figure 2.3: Tube rifling used to set the origin.

2.1.2 External heating system

The micro-flow reactor is heated externally by three micro-flames (Fig. 2.4).
A stoichiometric H_2/O_2 stream is generated by a multicell electrolyzer (Spirflame, model 250 HP, Fig. 2.4a) from distilled water. Several parts compose the heating system:

- an external filter (Fig. 2.4b), installed between the booster and the electrolyzer, to retain impurities that could have been present in water;

- twin-boosters (Fig. 2.4c), filled with distilled water, to prevent a flame flash-back;

- three blowtorches tips (internal diameter 0.35 mm, Fig. 2.4d), each one is equipped with a flashback arrester and a gas flow regulation valve. The blow-torches are placed around the reactor, separated from each other by a 120° angle. A moving stage allows modifying the tube separation distance and the angulation.

This novel heating system ensures a stationary temperature profile that goes from ambient temperature at the upstream side (gas inlet) to a maximum of about 1600 K with a smooth temperature slope allowing the mixture auto-ignition (Fig. 2.5).

(a) Electrolyzer

(b) Filter

(c) Booster

(d) Blowtorch

Figure 2.4: Heating system components.

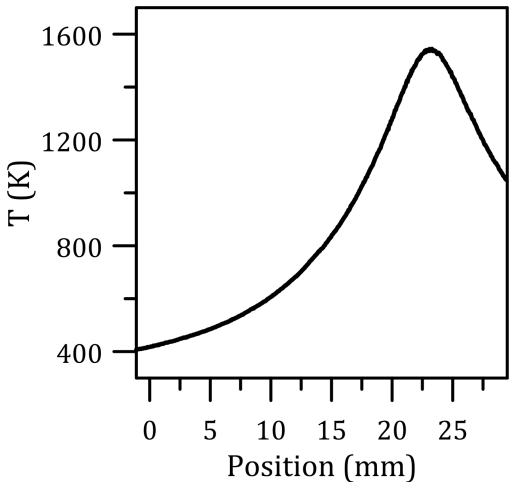

Figure 2.5: Wall temperature profile obtained with a 2.15 mm inner diameter tube.

This circumcentric heating system is one of the main novelties of this device over other available micro-combustion experimental setups. It allows a homogeneous temperature distribution along the tube radius, as explained in Section 2.2.2.3. This differs from the heating system used by Tsuboi et al. [42], in which the reactor is heated from below by a flat flame, resulting in slated flames (Fig. 2.6a). Our system ensures the formation of straight flames which reduces uncertainty in the detection of the flame position (Fig. 2.6b).

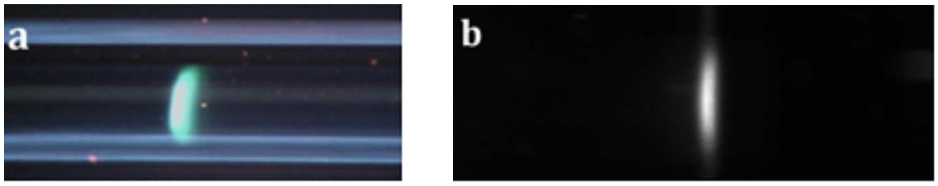

Figure 2.6: a) Flame obtained by Tsuboi et al. [42] with a flat flame burner; b) flame obtained in the present work.

A study was carried out in order to determine the optimal setup configuration, *i.e.* the separation distances between (i) the blowtorches and the tube and (ii) the blowtorches and the reactor outlet (Sections 2.2.2.1 and 2.2.2.2).

2.1.3 Data acquisition system

The data acquisition system consists of a Princeton Instrument spectroscopy EM-CCD camera (ProEM 1600) and a FLIR A655sc thermal camera facing each other, with the tube in between (Fig. 2.7).
The CCD camera is equipped with a 105 mm Nikkor lens (f/2.8D) and two auto extension tubes (Nikon PK–11A). A band-pass filter (20BF10–430) is used to detect the signal at 430 nm. This optical wavelength is related to CH^*, a radical characteristic of the flame front in hydrocarbon flames (see Annex A).
The infrared camera equipped with a standard 25° lens and a microscope 50 µm/pixel lens is used to measure the temperature distribution along the outer wall of the reactor. The operating conditions and the emissivity correction are detailed in the Section 2.1.3.2.
Unlike the previous studies [2], the spectroscopic camera used in the present work allows tracking and recording the flame at high frequency. High frequency recording permitted the exploration of unstable flames regime, with the determination of flame frequencies and characteristic times. Furthermore, the temperature profile is measured continuously by the infrared camera. The measurements show that the heat released by the flame inside the tube cannot be neglected, as can be seen in Fig. 2.8.

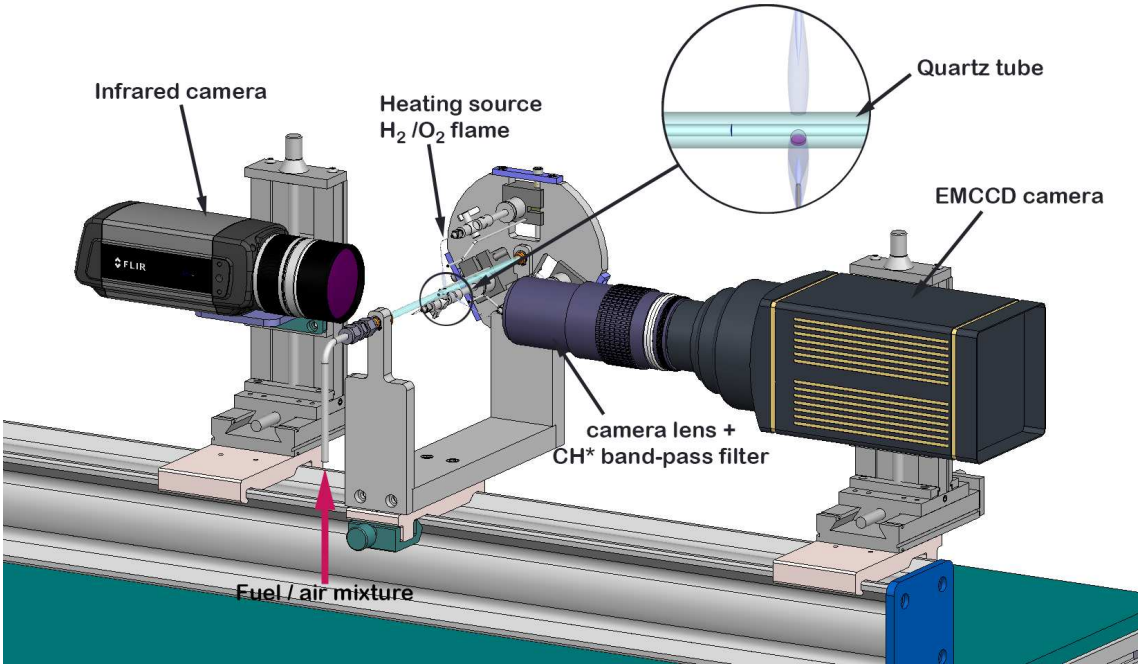

Figure 2.7: Schematic of the data acquisition system and micro-reactor.

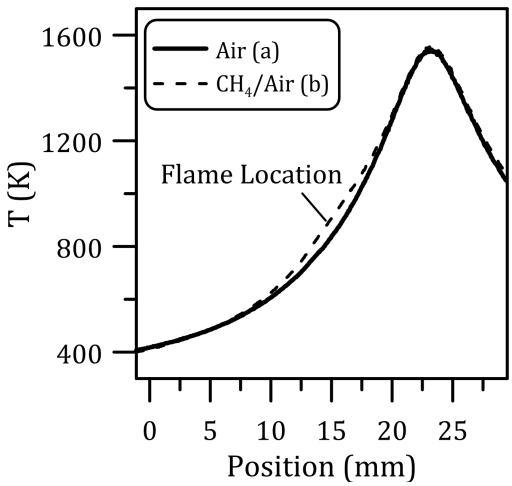

Figure 2.8: Wall temperature profiles recorded with (a) non-reactive and (b) reactive flow at 0.35 m/s in a 2.15 mm diameter tube.

2.1.3.1 EMCCD camera

The flame chemiluminescence is tracked by the ProEM 1600 spectroscopy camera. It operates with a 1600×200 pixels matrix and a 16-bit output digitalization. The spatial resolution is 72 pixels/mm. The resolution was determined during each experimental campaign by introducing a target inside the micro-flow reactor at the exact focus point.
Two sources of noise are present when operating with EMCCDs camera: one thermal and one electronic. The dark charge (or dark current) is the thermally induced buildup of charges in the CCD over time. The values of this source of noise vary widely from one CCD array to another and are temperature dependent. Thus, to minimize dark-charge effects, the default CCD temperature is set at -60°C.
On the other hand, Clock-Induced Charge (CIC) is a noise source that is independent of exposure time and weakly dependent on the temperature. CIC creates an error in photon estimation. The ProEM+ camera used in automatic mode minimizes spurious charges by optimizing clock voltages and timing edges [111].
In the present work, we employed pixels binning and high avalanche gain on the CH^* signal to study the flame dynamics. Pixel binning is a clocking scheme that combines the charge collected by several adjacent CCD pixels into one super pixel in a defined region of interest (ROI). It is designed to reduce the noise and improve the signal-to-noise ratio and frame rate, albeit at the expense of a reduced spatial resolution.
The Figure 2.9 shows an example of 2×2 binning. Pixels can be binned vertically by shifting two image rows into the horizontal register, without reading it after the first shift. They can also be binned horizontally by summing two adjacent pixels in the line and reporting out as a single pixel. Horizontal binning cannot be done on the image sensor, but it can be performed during the image processing. Vertical binning, however, can be done on the sensor level and is used in this work.
Avalanche gain (EM gain) refers to the magnitude of amplification that the system will produce. Gain is reported in terms of electrons/ADU (analog-to-digital unit). A gain of 8 means that the camera digitizes the CCD signal so that each ADU corresponds to 8 photoelectrons. When the multiplication is sufficiently high, it is possible to see extremely low emission events.

2.1.3.2 Infrared camera and emissivity correction

The temperature distribution along the tube outer side is measured by a FLIR A655sc thermal camera. The camera operates in a 640×480 pixels matrix with a 16-bit output digitization. The accuracy is ±2% of reading. Calibration was done by exposing the camera to a 1500 kW transmitter. The spatial resolution is 19 pixels/mm and is determined before each experimental campaign by placing a target near the focus point. The temperature measurements are collected at a

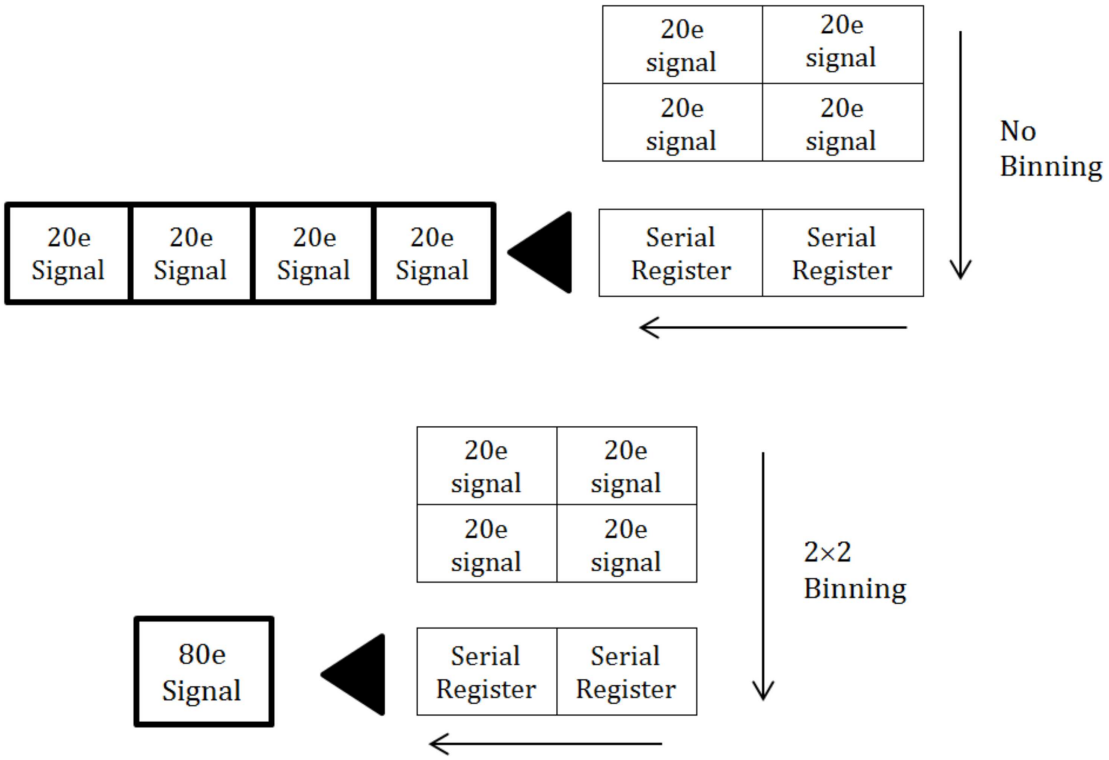

Figure 2.9: Example of pixel binning.

frequency of 10 Hz, which ensures a continuous recording of the temperature imposed on the micro reactor.
The operating range of the camera is selected between 300 and 2000°C. Several parameters are required to compute more accurately the temperature profile: the room temperature (T_{room}) and the relative humidity (RH), transmission (τ) and distance (l) from the measured object, transmission (τ_{opt}) and temperature (T_{opt}) of the external optic, and the object emissivity (ε).
The room temperature parameter is set as to the temperature measured with a K-type thermocouple. The humidity parameter has little impact on the measurements: changing the RH from 0 to 100% results in only a 0.1% change in temperature, thus a mean humidity factor of 50% is adopted. The distance is set at 0.1 m, as the camera is placed at about 10 cm from the object. Like the humidity parameter, the distance factor has little impact on the final result: varying the distance from 0 to 0.1 m results in a 0.1% temperature change. The transmission correction is then computed automatically from the distance, atmospheric temperature and relative humidity inputs.
The parameters for the external optic are set at 20°C and 0.9 for the temperature and the transmission, respectively.
The last parameter, the fused silica emissivity, varies with the temperature and

the wavelength (Fig. 2.10) in the operating spectral range of the camera (7.5 – 14 µm) [112].

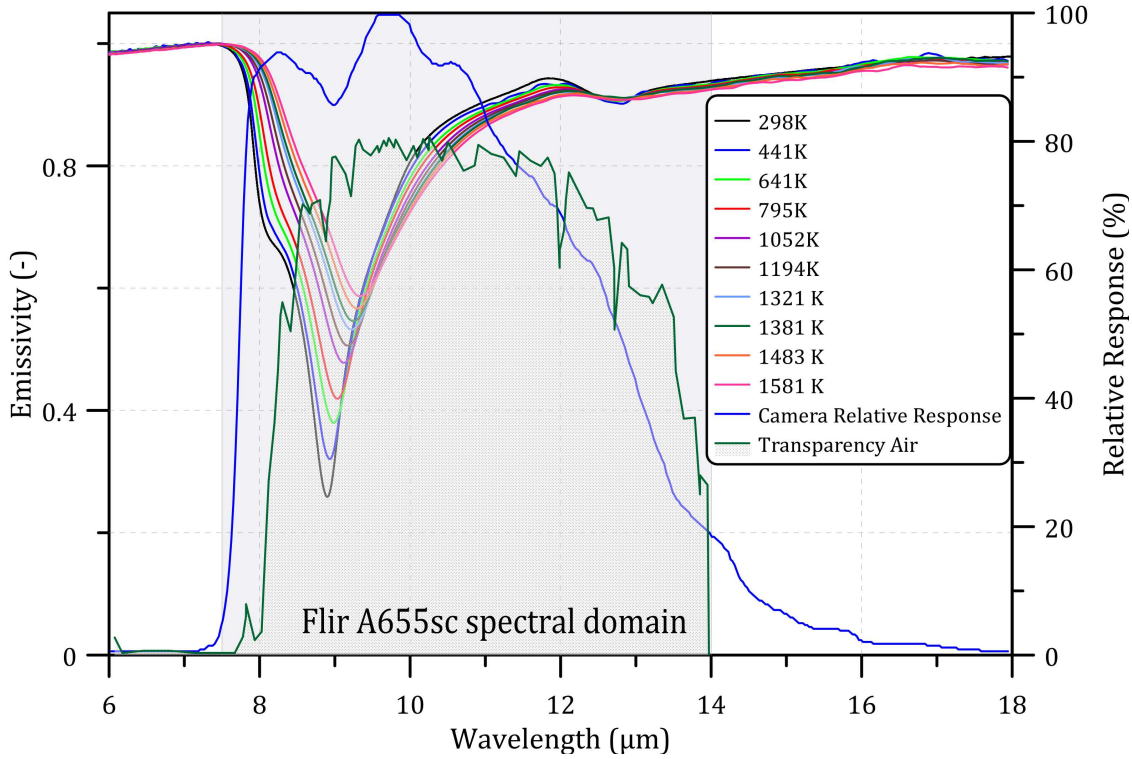

Figure 2.10: Fused silica emissivity with wavelengths and temperature.

In order to provide the camera software with the correct emissivity factor, the study described below is carried out.
The amount of radiant energy emitted by a black body at a specific wavelength is a function of its temperature, according to the Planck's law (equation 2.1):

$$M_{\lambda}^{BB} = \frac{C_1 \lambda^{-5}}{\exp \frac{C_2}{\lambda T} - 1} \tag{2.1}$$

With:

$$C_1 = 2\pi h c^2 \tag{2.2}$$

$$C_2 = \frac{hc}{k} \tag{2.3}$$

Where M_λ^{BB} is the spectral radiance of a perfect blackbody [W m^{-2} µm^{-1}], *i.e.* the power emitted from a unitary surface emitting per wavelength, $h = 6.62 \times 10^{-34}$ [J s] is the Planck constant, $c = 2.99792 \times 10^8$ [m s^{-1}] is the speed of light in vacuum, $k = 1.38 \times 10^{-23}$ [J K^{-1}] is the Boltzmann constant, λ is the wavelength [µm], and T is the temperature [K].
Planck's law is used to calculate the spectral radiance flux per unit area and per unit wavelength generated by a real body (characterized by a spectral emissivity ε_λ) at a specific temperature [113]:

$$M_\lambda = \varepsilon_\lambda \times \frac{C_1 \lambda^{-5}}{\exp \frac{C_2}{\lambda T} - 1} \tag{2.4}$$

In order to compute the power emitted over a specific spectral interval between two wavelengths λ_1 and λ_2, the equation 2.4 is integrated in the interval:

$$M_{\lambda_1 - \lambda_2} = \int_{\lambda_1}^{\lambda_2} \varepsilon_\lambda \times \frac{C_1 \lambda^{-5}}{\exp \frac{C_2}{\lambda T} - 1} d\lambda \tag{2.5}$$

where $M_{\lambda_1 - \lambda_2}$ is the total energy emitted [W m^{-2}].
Hence we can define the emissivity ε for a real body as:

$$\varepsilon = \frac{M_{\lambda_1 - \lambda_2}}{M_{\lambda_1 - \lambda_2}^{BB}} = \frac{\int_{\lambda_1}^{\lambda_2} \varepsilon_\lambda \times \frac{C_1 \lambda^{-5}}{\exp \frac{C_2}{\lambda T} - 1} d\lambda}{\int_{\lambda_1}^{\lambda_2} \frac{C_1 \lambda^{-5}}{\exp \frac{C_2}{\lambda T} - 1} d\lambda} \tag{2.6}$$

From the literature [112] we know the values of emissivity as a function of wavelengths at different temperatures (ε_λ): equation 2.6 provides the emissivity progression with temperature (Fig. 2.11) in the operating spectral range of the camera. From this progression, a mean emissivity factor of 0.8086 is computed.
Since we know the temperature $T_{measured}$ from the camera's measurements and the surface emissivity progression with temperature, we can calculate the real body temperature T_{real} using the Stephan-Boltzmann law:

$$T_{real} = \frac{T_{measured}}{\varepsilon^{1/4}} \tag{2.7}$$

Figure 2.12 depicts the results obtained after operating the post-correction with either the polynomial function or with the mean emissivity (equal to 0.8086) on the temperature profile acquired by the infrared camera at emissivity 1 (in black).

These three profiles are also compared to the temperature profile measured by the camera with an emissivity of 0.8086 (in blue).

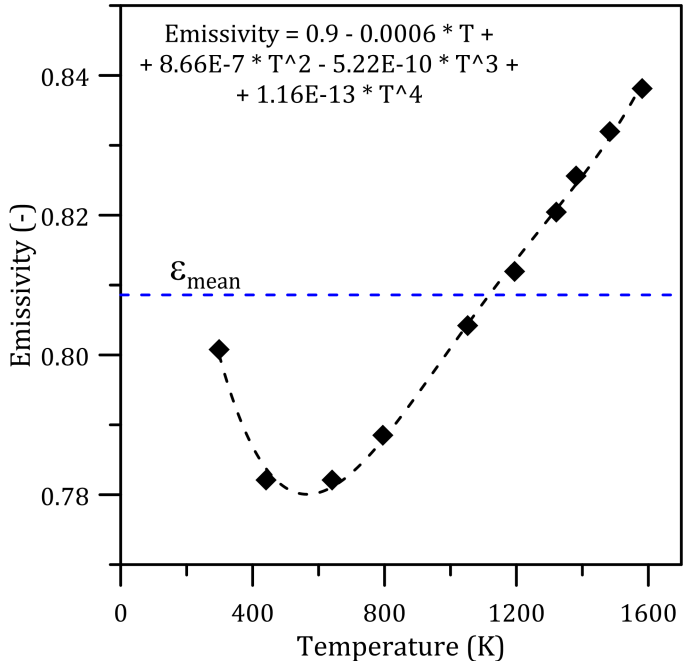

Figure 2.11: Fused silica emissivity as a function of temperature.

Post-processing the data with either the polynomial function or the mean emissivity results in very close temperature profiles (error less than 1.2%). However, these profiles differ significantly from the temperature profile obtained by the infrared camera with mean emissivity, especially at high temperature. Actually, the temperature measured by the camera is computed from the total radiation power (W_{tot}) received. IR camera software provides the computation of this quantity as a combination of several factors [114]:

$$W_{tot} = (1-\tau) * W_{obj} + (1-\varepsilon) * \tau * W_{amb} + (1-\tau) * W_{atm} \tag{2.8}$$

Where ε is the object emissivity, τ the transmission through the atmosphere , W_{obj}, W_{amb} and W_{atm} the total radiation emitted respectively by the object, the ambient sources and the atmosphere. Since the correction made by the IR software is issued from the quantities W_{obj}, W_{amb}, W_{atm} and τ (computed from several parameters) the result obtained is different from that achieved with a simple post-processing with the Stefan-Boltzmann law (Fig. 2.12).
Based on these observations, it is thereafter chosen to perform the measurements with an average emissivity factor (0.8086) while the temperature correction is made through the IR software (blue profile in Fig. 2.12).

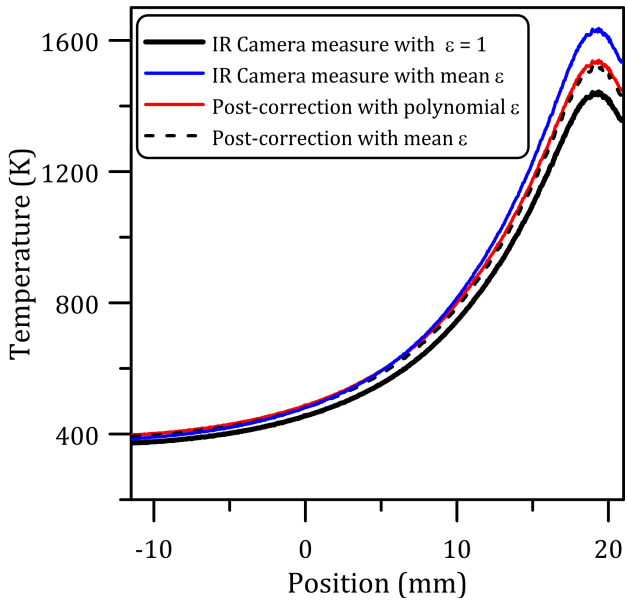

Figure 2.12: Temperature correction.

2.2 Part II: Operating configuration

In order to confirm the reliability of the measurements taken by the infrared and spectroscopic cameras, several test experiments were carried out. The aim of these experiments was to verify the uniformity of the temperature distribution along the inner wall circumference and to find the EMCCD camera operating configuration.

2.2.1 EMCCD camera configuration

As described in Section 2.1.3.1, the EMCCD camera operates a pixel binning on a user-defined region of interest (ROI). As a consequence, the experimental results depend strongly on this ROI. The chosen ROI must be representative of the analyzed flame while providing with a sufficient luminosity. To this end, two display configurations were tested: 8-pixel window centered on the flame center (Configuration 1), and 30-pixel window centered on the flame center (Configuration 2). These configurations are illustrated in Figs. 2.13 and 2.14. A 1×8 binning is performed to improve the observation of the frame rate and a 700 EM gain is set to increase the flame chemiluminescence. With these settings, the maximum recording speed is 4260 Hz. The ROI was selected by moving a black plate placed between the CCD camera and the reactor, so as to cover the undesired flame section. A background subtraction is operated to reduce noise.

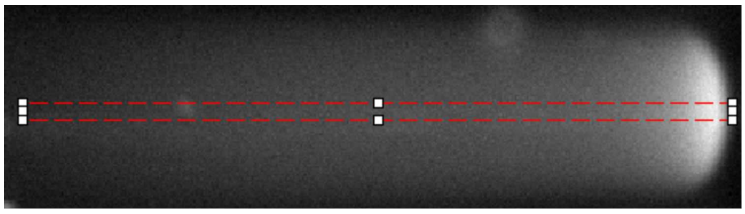

Figure 2.13: Configuration 1.

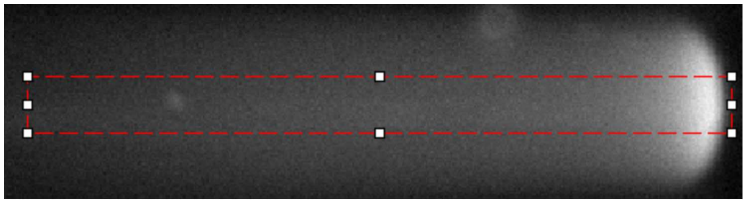

Figure 2.14: Configuration 2.

Figure 2.15 depicts the flame position for different flame regimes as a function of the inlet mixture velocity. The points, at which the flame stabilizes (or ignites and extinguishes), are reported in terms of wall temperature.Three regimes were identified (i) stable flames (crosses), (ii) unstable flames (stars) characterized by ignition and extinction points at the hot and cold sides respectively, and (iii) weak flames (diamonds). The temperatures reported in Fig. 2.15 were not corrected for non-unity emissivity.

First, one can notice that the positions of the stable flames and the extinction points for unstable flames do not change significantly (error less than 2%). On the other hand, the ignition points of unstable flames and the weak flames show a higher dependence on the configuration adopted (error of about 6%). This stronger dependence on the configuration adopted is mostly related to the intensity of the CH^* signal: the smaller the display window, the weaker the collected signal as illustrated in Fig. 2.16. Indeed, the flame position is determined from the CH^* signal, as discussed thoroughly in Chapter 3. The aim of these profiles is to show qualitatively the differences obtained between the flame progressions with the configuration adopted. Therefore, collecting the signal on a larger window gives a better precision as well as a higher signal-to-noise ratio, thus allowing a more accurate location of the flame and the identification of important phenomena in the flame extinction (see Chapter 3).

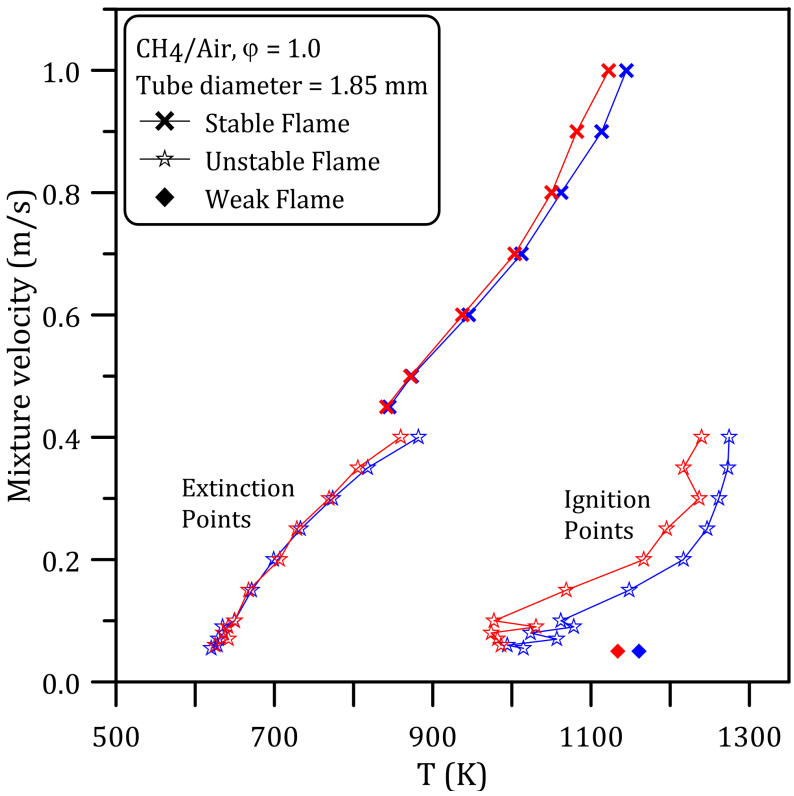

Figure 2.15: Flame position defined at the wall temperature as a function of the mixture flow velocity. Configuration 1 = red, Configuration 2 = blue.

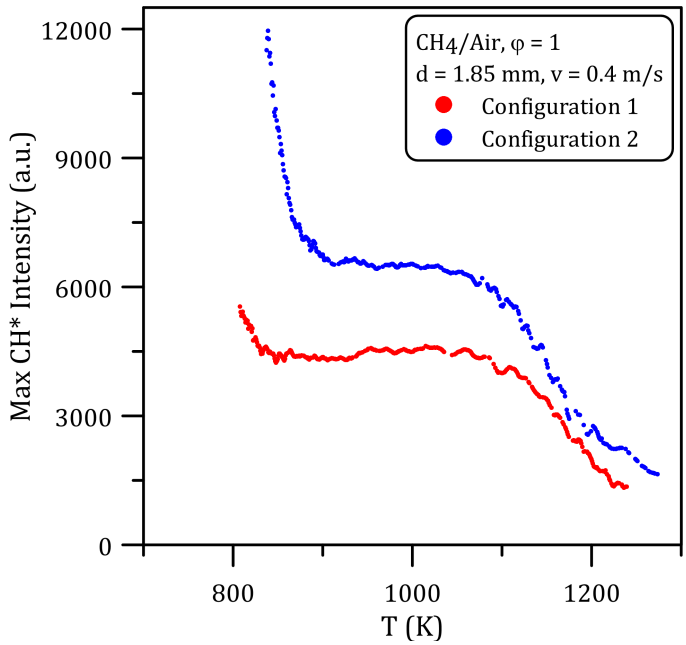

Figure 2.16: CH* progression obtained with the two configurations employed.

2.2.2 Temperature profile

Experiments were carried out to assess the impact of the temperature profile on the results and to choose the optimal setup configuration. The aim of these experiments was to find a homogeneous and sufficiently high temperature profile, in order to prevent uneven circular temperature distribution and quenching issues. Furthermore, a high temperature profile allows using smaller reactors, as the quenching diameter decreases with increasing temperature (see Chapter 1).
Two parameters regulate the temperature profile: (i) the distances between the blowtorches and the reactor outer wall, and (ii) the distance between the blowtorches and the reactor outlet. These two parameters have been optimized independently, and the methodology employed is described below.
The temperature homogeneity was thus checked along the tube section, as described in Section 2.2.2.3, and experiments with thermocouples were conducted to confirm the emissivity correction detailed in Section 2.2.2.4.

2.2.2.1 Distance between the blowtorches and the reactor wall

Although the separation angle between the three blowtorches could have been varied, an even 120° angle around the reactor was chosen based on geometric considerations to obtain a uniform temperature distribution. Thus, only the separation distances between the blowtorch tips and the reactor outer surface were optimized. The top

blowtorch was considered independently from the two side torches, providing us with two optimization variables: 'Distance 1' (d_1) the distance between the top blowtorch and the reactor, and 'Distance 2' (d_2) the distance between the side blowtorches and the reactor. Figure 2.17 shows a schematic representation of this system while Table 2.3 details the three configurations investigated: in the Configuration 1, d_1 and d_2 were set to the minimum mechanically accessible distance (3 mm) whereas the Configuration 2 adopts the maximum distance available (6 mm). The Configurations 3 was used as an intermediate configuration. These three configurations resulted in three different temperature profiles, mainly characterized by different temperature maxima, depicted in Fig. 2.18. As expected, Configuration 1 leads to the highest temperature peak whereas the peak is minimal with Configuration 2.

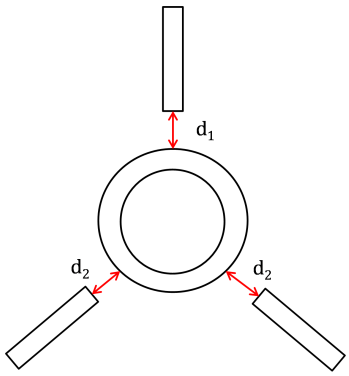

Figure 2.17: Schematic of the tube and the blowtorches.

	Config. 1	**Config. 2**	**Config. 3**
Distance 1 (mm)	3.0	6.0	4.0
Distance 2 (mm)	3.0	6.0	3.2

Table 2.3: Distance between the blowtorches and the channel in the three configurations used.

Although Configuration 1 appears to be the most favorable because of its highest temperature peak, it was discarded because of an overheating of the top blowtorch. Indeed, this blowtorch is heated by the side blowtorches, which could have resulted over time in deformation or fusion of the top-blowtorch tip. Thus, the results obtained with the Configuration 1 were used as reference, but this configuration could not be used for experimental campaigns and the blowtorches were further moved away and the Configurations 2 and 3 were tested.
In order to compare the reliability of the configuration employed, the flame position was used as a benchmark. Figure 2.19 depicts the flame positions (stable flames (closed diamonds) and the unstable flames (open diamonds)) obtained with the three configurations; they are plotted in terms of stabilization temperature.

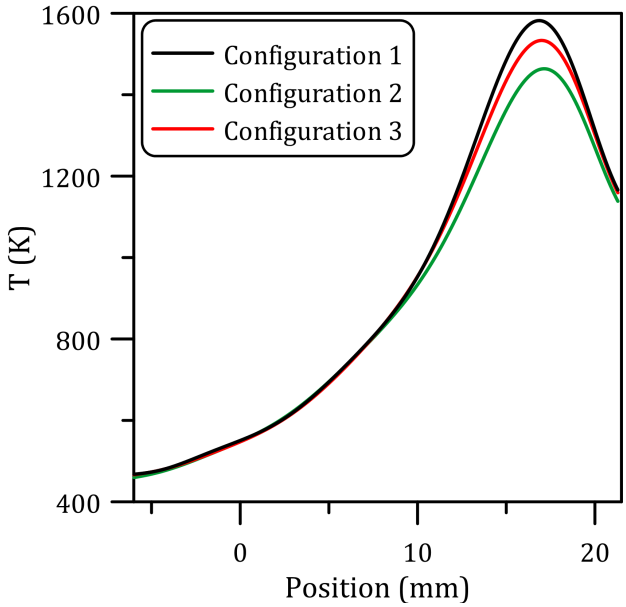

Figure 2.18: Temperature profiles.

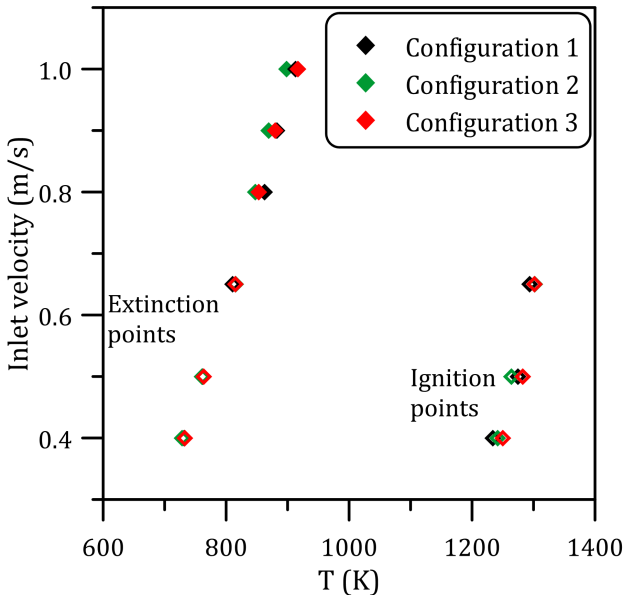

Figure 2.19: Flame position defined at the wall temperature as a function of the mixture flow velocity. Closed diamonds = stable flames, open diamonds = unstable flames.

First, one can observe that the flame stabilization temperatures of stable ($0.65 \leqslant$ v (m/s) $\leqslant 1$) and unstable (v < 0.65 m/s) flames are almost identical

regardless of the configurations adopted. However, a closer look at the stable flame region shows that the deviation between the results obtained with Configurations 1 and 2 increases with the inlet velocity. Therefore, using a lower temperature profile could affect the flame position, especially at high velocity. Since it is preferable to have a higher temperature to avoid flame quenching, Configuration 2 was discarded and Configuration 3 was preferred as it prevents overheating of the top blowtorch while exhibiting a negligible impact on the experimental results.

2.2.2.2 Blowtorches distance from the reactor outlet

After setting up the distances between the blowtorches and the reactor wall, the impact of the separation length (Lo) between the blowtorches and the reactor outlet was investigated. To do so, the blowtorches were positioned as far as possible from the outlet, and the reactor (25 cm long) was then moved to gradually lower Lo (Fig. 2.20 and Table 2.4). The fresh gases inlet velocity was kept at 0.2 m/s, and the flame observed was unstable. Such unstable flames, called FREI (Flame with Repetitive Extinction and Ignition), consist of a repetitive ignition-propagation (towards the fresh gases)-extinction cycle characterized by a well-defined frequency. Further details on FREIs are provided in Chapter 3. The aim of these experiments is to test the dependency of the flame dynamics on the blowtorches-reactor outlet distance, and the FREI frequency is an appropriate physical parameter for this purpose.

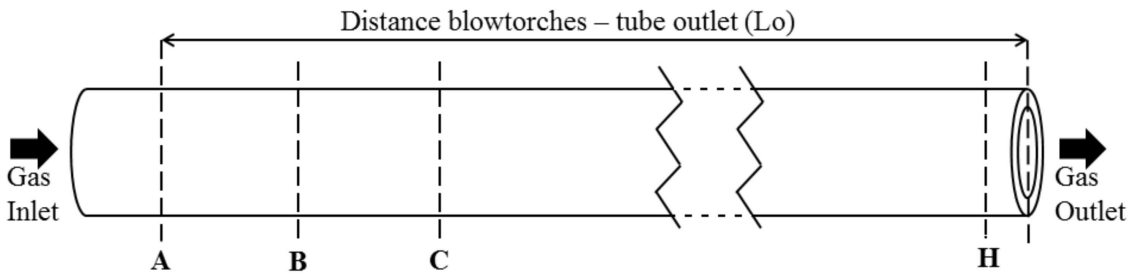

Figure 2.20: Layout.

First, it is noteworthy that water condensation was observed for positions A and B with the formation and evacuation of drops on the tube inner wall (Fig. 2.21) and a periodic drop formation at the reactor outlet (Fig. 2.22) respectively. The formation of water drops at the reactor exit perturbs the flame progression as illustrated in Figure 2.23, in which the spatially integrated CH^* signal is depicted. In this figure, one can see that the flame does not exist anymore as the combustion products condense and obstruct the reactor outlet, conversely to the signal obtained in the configuration E where water condensation is not observed.

Position	Distance between the blowtorches and the tube outlet (mm)
A	116
B	91
C	65
D	51
E	36
F	20
G	13
H	6

Table 2.4: Configurations used during experiments.

Figure 2.21: Water formation in the configuration A.

Figure 2.22: Periodic drop formation in the configuration B.

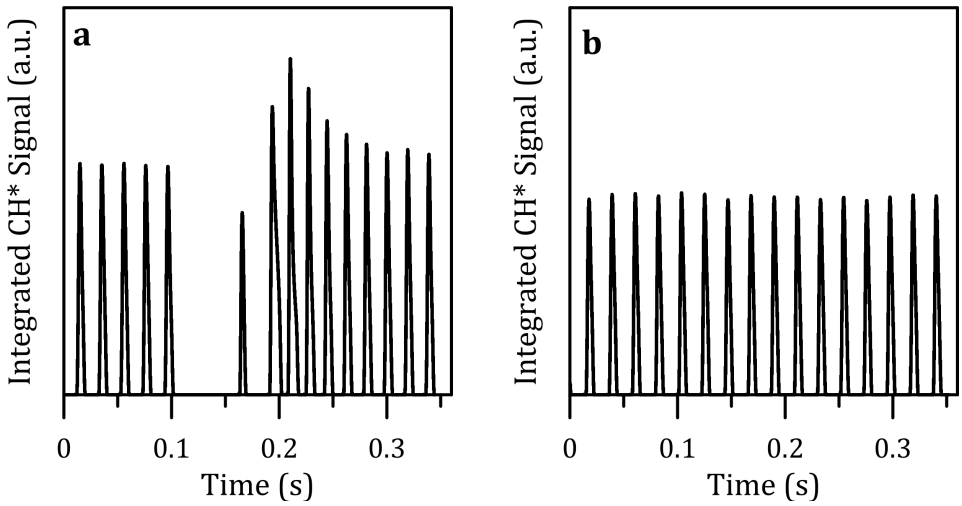

Figure 2.23: Comparison between the spatially integrated CH* signal obtained in the configurations (a) B and (b) E.

Unlike the configuration B, configurations A and C to H exhibit a uniform and regular CH* signal. Operating a Fourier transform on the spectral-cross section of this CH* signal, the frequency of the unstable flame can be extracted. Figure 2.24 shows the FREI frequencies obtained in each configuration. The highest frequency

is recorded in the configuration A, in which the water condensation was observed, while it is minimum in the configuration E. As the distance is further decreased, the frequency rises again (up to 5%). This last frequency increase may be due to an interaction between the burned expanded gas at the reactor exit and the blowtorches.

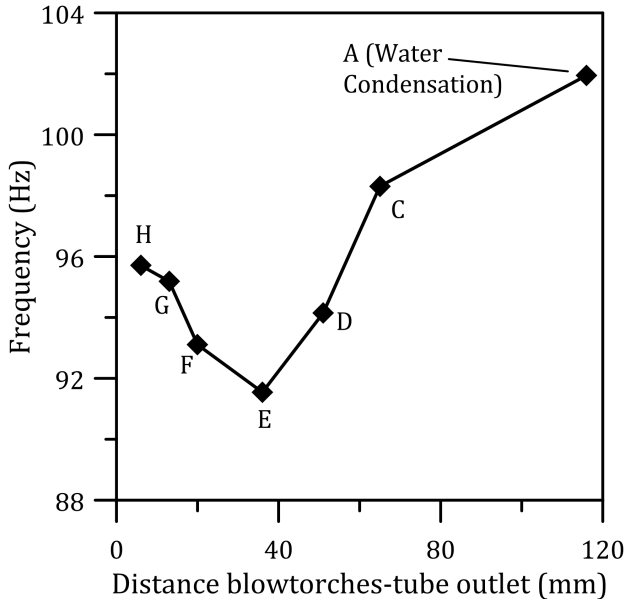

Figure 2.24: Frequencies obtained in each configuration.

From these results, we can conclude that a too large distance between the reactor exit and the heat sources results in the formation of liquid water that impacts the flame dynamics, while a too short distance leads to a possible interaction between outflowing hot gases and the heat sources. It is not to exclude also the presence of acoustic effects that may impact the flame oscillation frequencies. To avoid these drawbacks, all the experiments thereafter were conducted with an intermediate distance of $\backsim$36 mm.

2.2.2.3 Uniformity of the temperature profile

After the optimal blowtorches configuration has been established, experiments were performed to check the homogeneity of the temperature profile along the reactor inner and outer walls. To this end, a tomography approach was adopted in order to reconstruct the reactor temperature spatial profile. Indeed, since only the reactor outlet section is accessible and the temperature profile obtained by the heating system is symmetric, the IR camera was positioned facing the reactor outlet (Fig. 2.25). Then, the temperature measurements of the tube section were collected while moving step-wisely (0.5 mm steps) the reactor along its longitudinal axis so as to increase the separation distance between the blowtorches and the reactor outlet. For these

experiments, a 2.15 mm inner diameter reactor was employed and an air flow at 0.5 m/s was imposed.

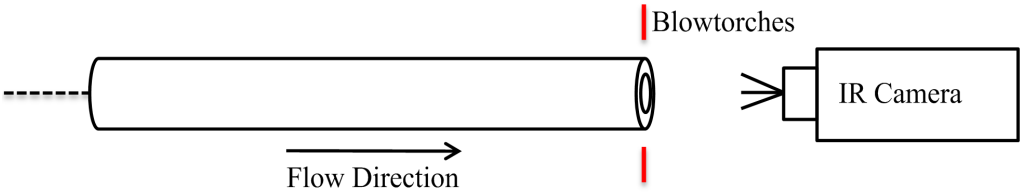

Figure 2.25: Schematic of the experimental layout.

Figure 2.26 shows the temperature surface obtained at the initial position, *i.e.* when the blowtorches are aligned with the reactor outlet. The impact areas of the three heat sources are clearly visible: they correspond to the three higher temperature spots. These temperature plots were then processed to extract the temperature along the reactor inner and outer contours (displayed with black dots in Fig. 2.26). The reference for the angular coordinate is indicated in Fig. 2.26, and a clockwise rotation direction was adopted.

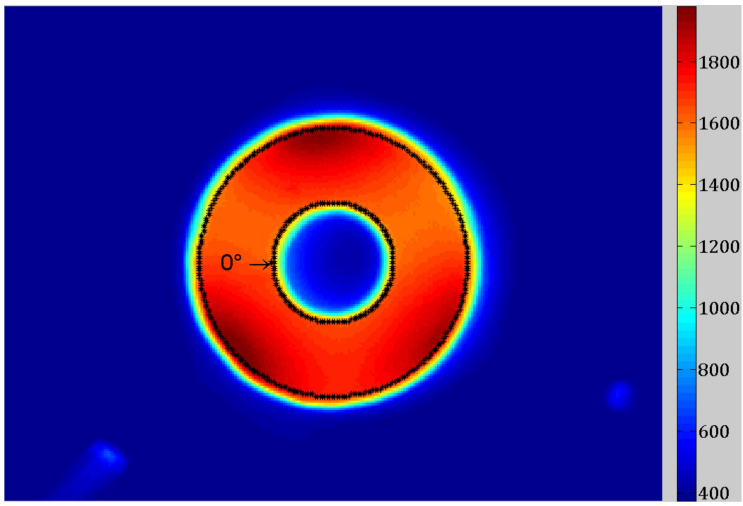

Figure 2.26: Temperature measurement at the initial tube section. The tube contours are displayed on the external and internal circumference.

The temperature contours extracted from Fig. 2.26 are plotted in Fig. 2.27. Three temperature peaks can be observed on the outer wall temperature profile (R_{ext}, in red), which correspond respectively to the top and the two side blowtorches. The temperature profile obtained on the inner circumference (R_{int}, in black) is more uniform: the average temperature is 1593 K with a standard deviation of 34 K. This means that, although there are hot spots on the outer wall due to the presence of the three blowtorches, the temperature profile is smoothed down by heat diffusion through the fused silica, resulting in a sufficiently uniform temperature distribution along the reactor inner wall for a given section.

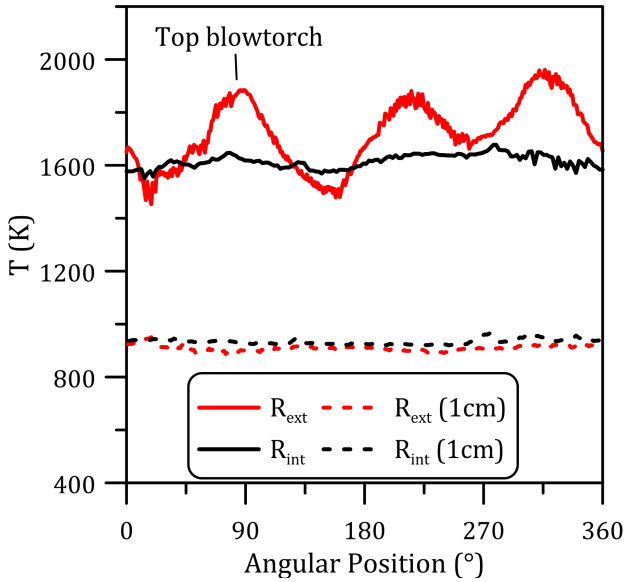

Figure 2.27: Temperature profiles obtained on the inner and outer tube side.

Figure 2.27 also depicts the temperature profiles collected for a blowtorches-reactor outlet distance of 1 cm (dashed lines). The hot spots that could be observed initially are not visible anymore: the temperature distribution is uniform on both the inner and outer walls. Unlike in the initial position, the internal temperature is slightly higher than the external one: the reactor is also heated from the inside by the gas flow.

By assembling all the contours obtained for each blowtorches-reactor outlet distance, it is possible to reconstruct a 3D profile representative of the temperature distribution along the reactor outer and inner side as a function of the distance blowtorches-reactor outlet and the angular position. Those profiles are depicted in Fig. 2.28 and Fig. 2.29.

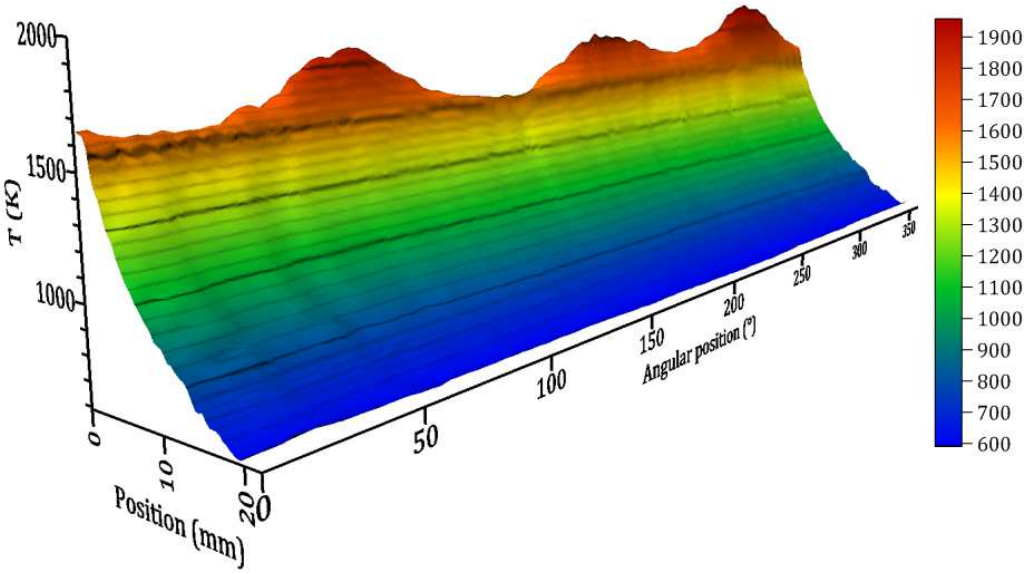

Figure 2.28: Temperature distribution of the tube outer side.

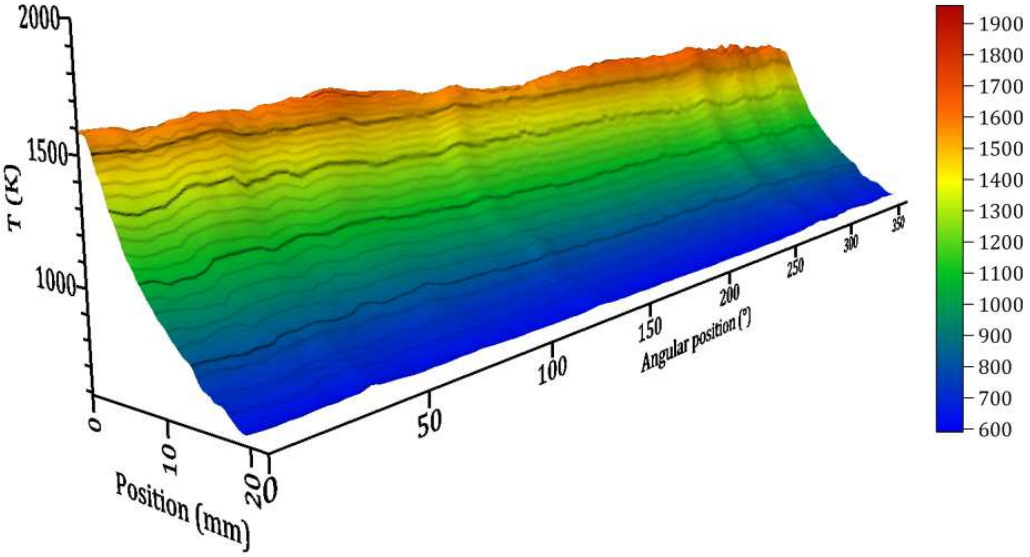

Figure 2.29: Temperature distribution of the tube inner side.

The results obtained show that, despite the presence of three heat sources and thus a non-homogeneous temperature distribution along the reactor outer side, the temperature measured on the inner side is sufficiently homogeneous to avoid the presence of hot spots that may impact the flow dynamic inside the reactor.
After checking the homogeneity of the temperature distribution inside the reactor, tests were carried out to make sure that the temperature profile measured by the infrared camera along the reactor external wall is representative of the temperature

inside the reactor.
When performing regular experiments, the infrared camera is positioned on the reactor side, as explained in Section 2.1.3, in order to collect continuously the temperature distribution along the tube; the exposure time is 6 s with a recording frequency 10 Hz. The temperature profile is extracted from one single line along the reactor longitudinal axis which must ideally capture the coldest region between the two blowtorches (visualized as two hot spots in Fig. 2.30).

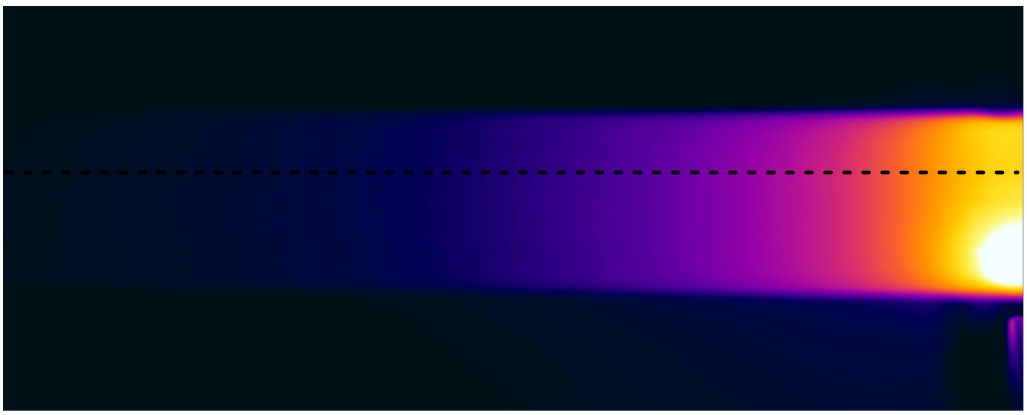

Figure 2.30: Line selected on the reactor side.

One may then wonder if the temperature profile obtained is representative of temperature on the reactor inner wall. To check this, the temperature contours collected above are employed, and the temperature along the reactor wall thickness is extracted for the angular position relevant to the temperature profile selected in Fig. 2.30 (∼25°) (see Fig. 2.31).

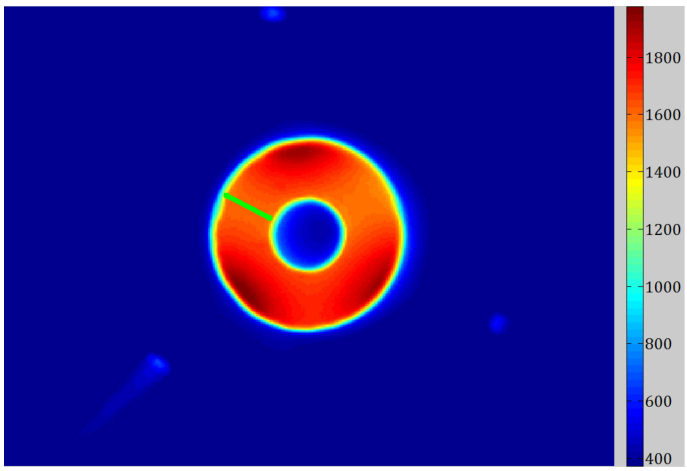

Figure 2.31: Extrapolated temperature on the tube thickness.

Representative temperature profiles along the wall reactor thickness are shown in Fig. 2.32. As previously, two tube sections are here considered: when the blowtorches

are aligned with the reactor outlet and when the blowtorches-reactor outlet distance is equal to 1 cm (dashed lines).

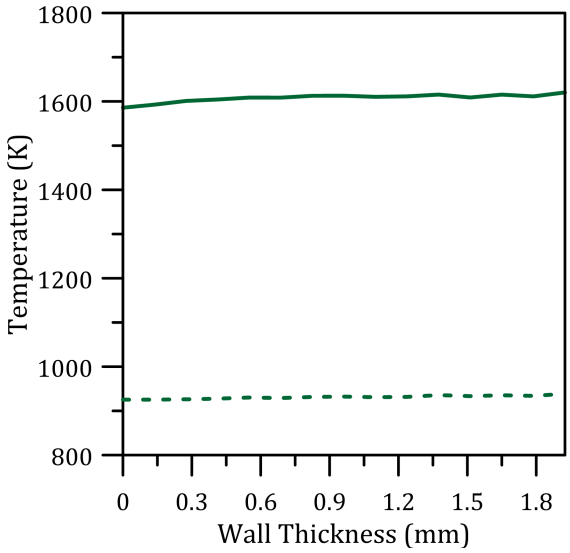

Figure 2.32: Temperature profile along the wall thickness.

One can notice that for the angular position selected in Fig. 2.31, the temperature is indeed homogeneous throughout the wall thickness, and thus that the temperature measured on the outside (at 0 mm) is really representative of the temperature in the inside (at 1.925 mm), with a difference less than 2%. As shown earlier in Fig. 2.27, temperature along the inner wall is not dependent on the angular position, and one can thus claim that the temperature measured along the line displayed in Fig. 2.30 is really representative of the temperature inside the reactor.

2.2.2.4 Temperature measurements via thermocouple

In order to further assess the reliability of the temperature measurements carried out with the infrared camera and to validate our emissivity correction, thermocouples were employed to check the temperature inside the micro-channel. The procedure adopted is comparable to that used by Maruta et al. [38] to determine the reactor temperature profile.
The thermocouple employed was an Inconel-sheated, K-type miniaturized thermocouple (diameter 0.25 mm, insulation material Inconel 600, length 10 cm). A USB data acquisition system (Iotech, PersonalDaq/55) was used, and the measurements were displayed in real time using the software Personal DaqView. A secondary thermocouple was connected to the acquisition system to measure the room temperature and compensate the temperature measurements.
The thermocouple was then inserted in a reactor of 1.85 mm internal diameter so

that the junction touched the wall. The thermocouple was then fixed on a 3D moving stage and inserted into the reactor (Fig. 2.33). The moving stage allowed precise control of the thermocouple position, ensuring that the TC junction was in contact with the inner reactor wall. During the measurements, a constant flow of nitrogen at 0.4 m/s was used.

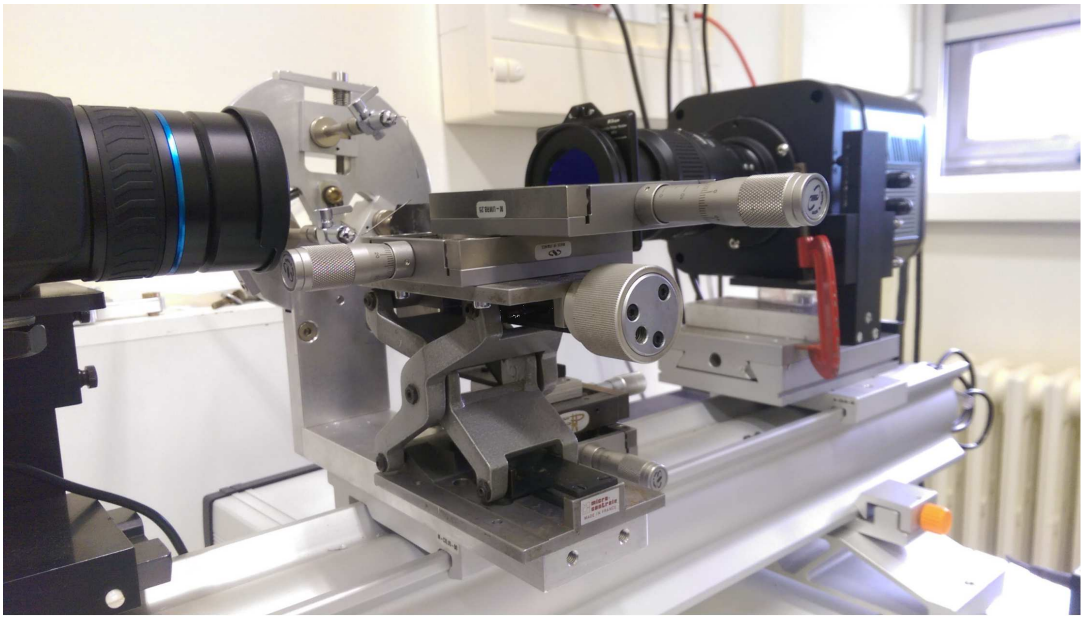

Figure 2.33: Moving stage used during experiments.

The thermocouple was inserted in the reactor from the gas outlet, and first positioned at a temperature of about 300°C. Once the temperature was stabilized, the thermocouple was shifted towards the fresh gases and the temperature measured every 0.5 mm. The initial position of the thermocouple is recorded by the EMCCD camera; the rifling on the tube was chosen as the initial reference for the recordings. Three experimental profiles were collected, and the measurements were found to be reproductive within 1%. In Fig. 2.34 a representative temperature profile is compared to that obtained with the infrared camera using a mean emissivity factor of 0.8086.

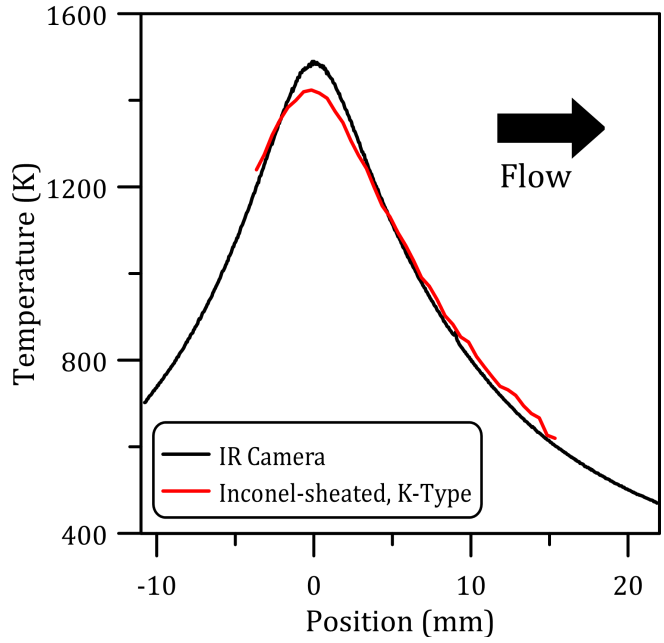

Figure 2.34: Temperature measured with Inconel-sheated thermocouple.

The two temperature profiles are in good agreement with each other. The maximum peak temperature measured with the thermocouple is 66 K lower than that measured with the camera. This difference is due to the conduction through the wall thickness, the presence of a fresh-gas flow, and the thermocouple dragging along the reactor inner wall.
These results therefore confirm the reliability of the temperature measurements through the infrared camera and the mean-emissivity correction ($\varepsilon = 0.8086$).

2.3 Fuel Type

The fuels used in this study are methane (CH_4), ethylene (C_2H_4) and acetylene (C_2H_2). The experiments were performed with pure fuels to avoid the influence of other unknown components. They are supplied in high-pressure cylinders with a purity of 99.95% for methane (N35) and ethylene (N35), and of 99.7% for acetylene (AAS27). The pressure cylinders are 75, 70 and 15 bar for CH_4, C_2H_4 and C_2H_2 respectively. A specific pressure regulator (Air Liquide, model BS–A) is used for acetylene cylinder. The pressure at the regulator outlet is 5 bar for CH_4 and C_2H_4 and 1.5 bar for C_2H_2.
As explained in Section 2.1.1, the micro-reactor size is chosen according to the quenching diameter of the fuel used [8–10], reported in Table 2.5. All data are for stoichiometric fuel-air mixture, at 25°C and 1 atm [11, 12, 16].

Fuel	Internal tube diameter (mm)
CH_4	2.50
C_2H_4	1.25
C_2H_2	0.85

Table 2.5: Quenching distances for fuels used during experiments [11, 12, 16].

Preliminary work was also carried out with n-butane gas (C_4H_{10}). The gas cylinder was at 1 bar (N25, 99.5% pure) and a specific pressure regulator was used (Air Liquide, model BS–GL). The results obtained were not reliable and the MFCs calibration showed and high uncertainty (up to 25%). This is due to an insufficient pressure difference between the MFCs inlet (1 bar) and outlet (1 bar): the flow rates obtained were too low to ensure a continuous and controlled flow.

2.4 Summary

A new experimental device was designed to investigate the combustion in narrow channels with premixed fuel/air blends at atmospheric pressure. The micro reactor used here consists of a cylindrical quartz tube, in which the gaseous mixture flows. This tube is heated externally by three blowtorches placed on a perpendicular plane around the tube and separated from each other by 120°. Experiments were performed to set the distance between the blowtorches and the reactor, and their distance from the tube outlet. This heating system ensures a stationary and homogeneous temperature profile starting from ambient temperature on the upstream side (gas inlet) to a maximum of 1600 K downstream. This smooth temperature gradient allows the mixture to auto-ignite, overcoming quenching issues. The three external heat sources are fed by a hydrogen/oxygen mixture. Thus these heating flames are free of CH^* species, which allows a better visualization of CH^* chemiluminescence from the flame inside the microchannel.
The fuel/air mixtures are premixed in a small tank and six thermal mass flowmeters Brooks GF40 are used to feed the reactor. Each gas line (fuel, oxygen and nitrogen) has two flowmeters with overlapping flow rate ranges, allowing a good exploration of all flame regimes.
The temperature distribution along the outer side of the tube is measured by a FLIR A655sc thermal camera with a 640×480 pixels matrix. The operating range is selected between 300 and 2000°C. The temperature measurements are collected in real time at a frequency of 10 Hz, which ensures a continuous recording of the temperature imposed on the micro reactor. An emissivity correction is carried out because in the operating spectral range of the camera, fused silica emissivity varies with temperature. In order to confirm the accuracy of our measurements, the temperature profile along the inner surface of the tube wall was measured

with an inconel-sheated K-type thermocouple. The uniformity of the temperature profile along the wall thickness was also confirmed by carrying out temperature measurements on the tube section.
A Princeton Instrument spectroscopy EMCCD camera (ProEM 1600), equipped with a 105 mm Nikkor lens, is used to detect the CH^* signal at 430 nm. The CCD camera operates in a 1600×200 pixels matrix with a 16-bit output digitization. A band-pass filter is used to observe the flame chemiluminescence through the quartz tube. In order to increase sensitivity and frame rate, binning operation and adapted exposure time are performed. The spatial resolution is 62 pixels/mm. For unstable flames the maximum recording frequency of 4260 Hz is used.

Chapter 3

Experimental results: Methane/Air

In this chapter the results regarding methane/air mixtures reacting in narrow channels are presented. This mixture has been chosen as a benchmark to ensure the reliability of the new device described in Chapter 2 as well as to provide new experimental insights into the flame dynamic at micro-scale.
To do so, a detailed analysis of each flame regime was carried out. Especially, important aspects of unstable flames were investigated experimentally for the first time, *i.e.* frequencies, characteristic times and the presence of multiple zones of reactivity. Moreover, the effect of several parameters was studied. The response of the flame behavior to the inlet velocity is first discussed and the present results are compared to data from the literature. Then, the effects of the equivalence ratio and the reactor size are considered and are investigated experimentally for the first time to the author's knowledge.

3.1 Effect of the inlet velocity

When a fuel/air stream is flowed through the micro-reactor, the mixture auto-ignites where the temperature is high enough. Then the flame propagates upstream and finally stabilizes at a location for which the equilibrium between the flame propagation speed and the fresh gas velocity is obtained. In line with the previous work of Maruta et al. [38], three main flame regimes were detected in the present study depending on the inlet velocity [44]: Stable Flames, Flames with Repetitive Extinction and Ignition (FREI), and Weak Flames. Furthermore, oscillating flames were observed experimentally for the first time in the transition between these main flame regimes.

The flame behavior distribution according to the inlet velocity is shown in Fig. 3.1 for a stoichiometric methane/air mixture in a 1.85 mm internal diameter reactor. This figure is a state mapping where the flame position at each inlet velocity is reported in terms of wall temperature.
The crosses correspond to the stable flame regime (1.0 – 0.45 m/s). The open stars indicate the FREI regime: ignition occurs at high temperatures (right-hand side) and extinction occurs at lower temperatures (left-hand side). Weak flames are represented by open diamonds (v = 0.04 m/s). The transition region between stable flames and FREI is clearly shown in this figure, with a discontinuity in the evolution corresponding to the oscillating FREI (closed stars, 0.415 – 0.413 m/s) while the oscillating weak flames, between FREI and weak flame regimes, are represented by closed diamonds (v = 0.05 m/s).

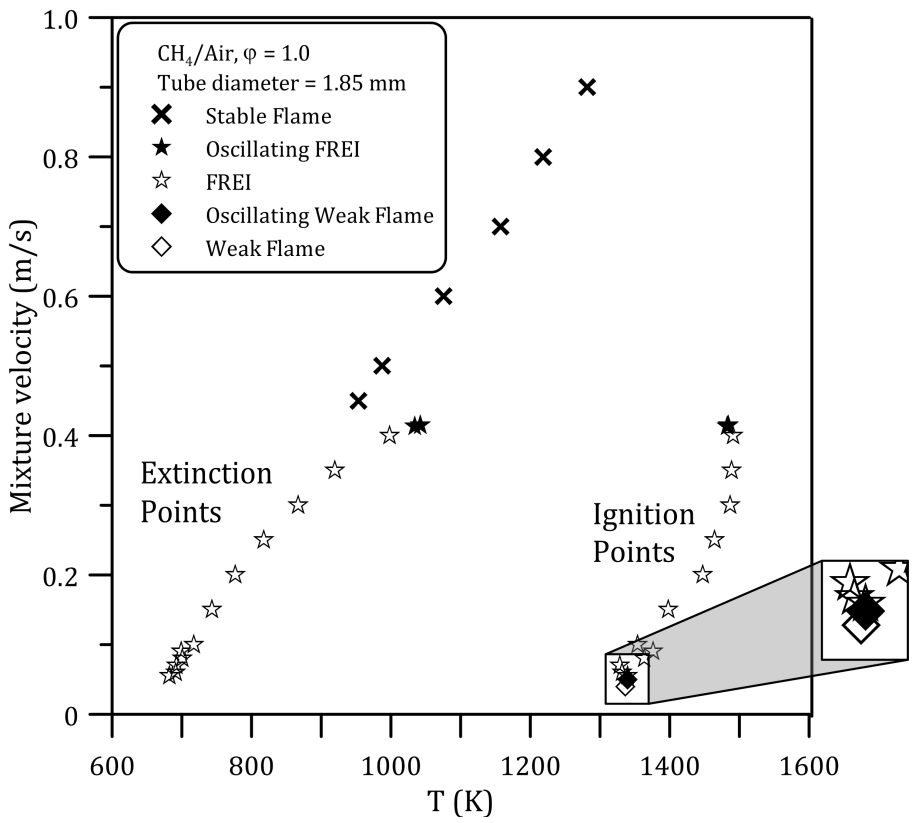

Figure 3.1: Flame position defined at the wall temperature as a function of the mixture flow velocity.

The evolution of the flame shape and features with the inlet velocity is presented in Fig. 3.2. It is noteworthy that at low flow rate (v < 0.415 m/s) the contrast has been adjusted to enhance the flame brightness.

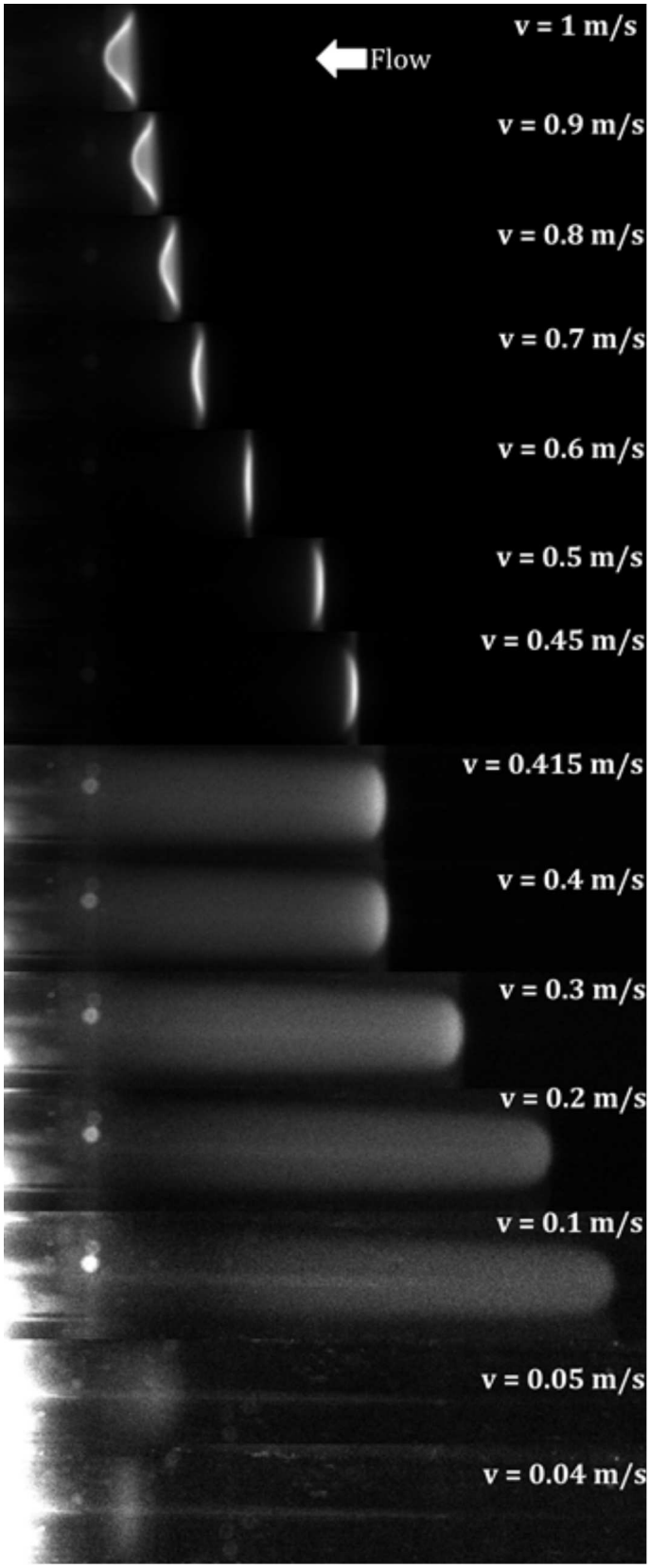

Figure 3.2: Flames images with the inlet velocity (CH_4/air, $\varphi = 1$, d = 1.85 mm).

In the stable flame regime the flame front evolves from a convex to a concave shape as the inlet velocity decreases and its position shifts toward cooler regions. Indeed, the flame shape is driven by the flow field, issued from the parabolic nature of the Poiseuille flow and the flame curvature. As described by Daou and Matalon [45], when oriented toward the burned gases, the flame is more vulnerable to heat losses. For FREI flames three main phases are observed during a cycle: ignition, propagation towards the fresh gas and extinction. Figure 3.3 depicts the time evolution of the CH* signal for a typical FREI. The flame ignites downstream (hot side) with a time delay after the previous cycle. A bright and broad CH* emissivity peak is observed while the flame propagates upstream. Then the emission zone gets thinner until collapsing onto a sharp peak. During the extinction phase, the peak intensity decreases and the flame finally extinguishes. This phenomenon is repetitive with a fixed and well-defined frequency, consistent with previous observations [50, 51].

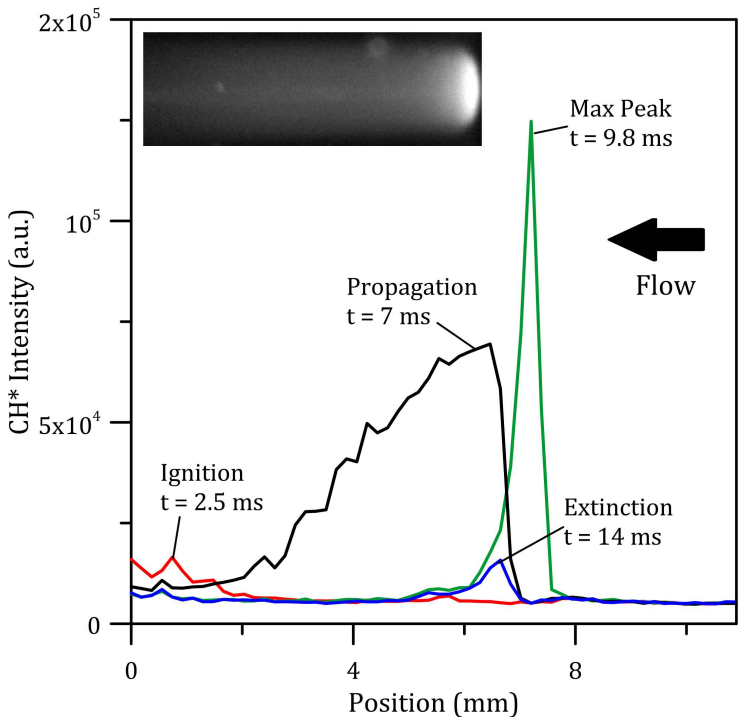

Figure 3.3: Temporal evolution of CH* intensity obtained during FREI progression.

The post-processing methodologies employed to extract the flame frequencies, the related characteristic times and the progression of the maximum CH* signal during the propagating phase are presented in Annex B.
The knowledge of FREI dynamics is fundamental for the application of this combustion mode in small-scale reactors. Since the repetitive ignition-extinction process leads to temperature variation at the reactor wall, they can be used as a source of controlled temperature fluctuations in devices operating at high temperature, such as thermo-photovoltaic devices. On the other side, the temperature variation may

produce thermal stress to the reactor walls that cannot be overlooked when designing micro-reactors. Furthermore, the flame/wall coupling plays an important role during FREI as it can dramatically affect the flame structure and its dynamics. While at macro-scale these effects can be neglected, they affect the burning efficiency or quenching at micro-scale.
Between the stable flame and the FREI regimes oscillating FREIs, with a brighter flame front due to periodical fluctuations, are observed. In this case the flame ignites, propagates upstream, reach the extinction point and oscillates before extinction. This phenomenon reported previously by Tsuboi et al. [43] and called 'oscillating FREI', is highlighted on Fig. 3.4, where the evolution of the CH* signal is displayed. In Fig. 3.4a the flame propagation over time is presented. One can notice the flame oscillation over several cycles before its extinction. In Fig. 3.4b the spatially integrated CH* signal is shown: in this specific case, the number of peaks before extinction does not follow any pattern.

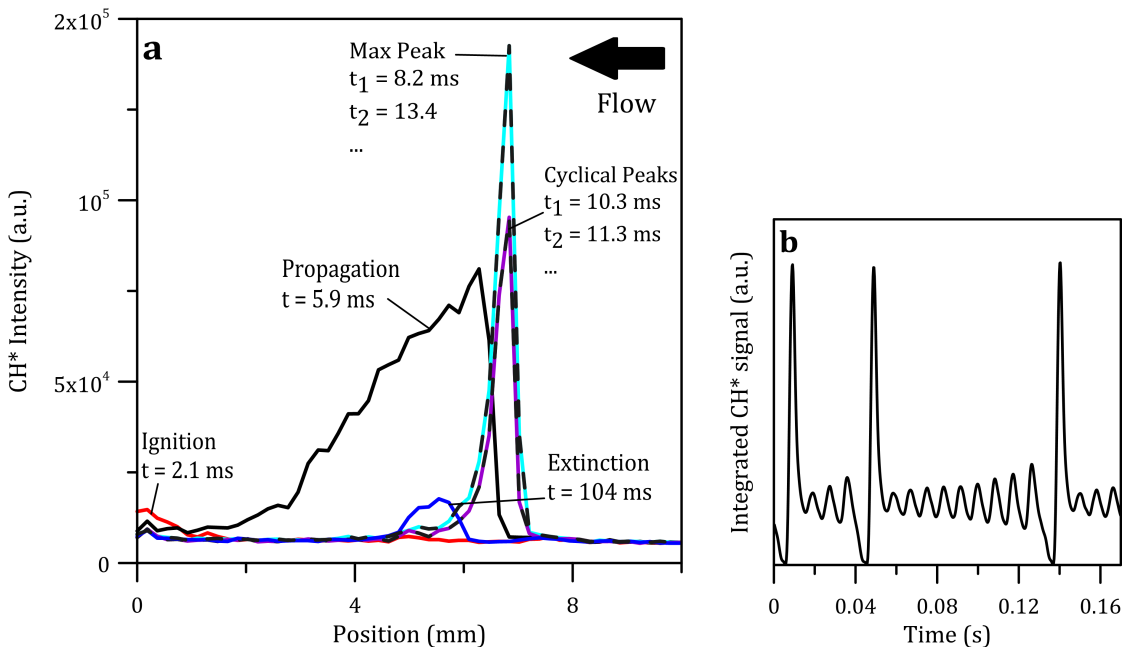

Figure 3.4: Evolution of an oscillating FREI. (a) Temporal evolution of FREI and (b) the correspondent spatially integrated CH* signal.

A weak flame, typical of mild combustion [27], is observed at v = 0.04 ms. This flame has a very low CH* intensity and the luminous zone is broader compared to the stable flames region. High EM gain ($\geq$ 700) is therefore required to visualize the flame chemiluminescence. As shown in [42], the weak flames stabilize at high temperature, close to the extrapolated line on the FREI ignition position and with a small temperature increase [71, 72].
Tsuboi et al. [42] have proposed to consider the wall temperature at which the weak flame anchors as the minimum ignition temperature of the inlet mixture for the given

conditions (fuel, reactor size, equivalence ratio). For this reason, many works [74, 75, 77, 78, 105, 107] have been devoted to this flame regime. Understanding the ignition characteristics of fuels is essential for many applications. However, up to now, only the influence of the fuel on the weak flame characteristics has been investigated, both experimentally and numerically. The goal here is thus to study the response of weak flames to the operating conditions in order to validate, or not, the assumption made by Tsuboi et al. [42].
In the transition region between FREI and weak flame regimes, another oscillating behavior is observed: an oscillating weak flame, with a broader luminous zone, is present at 0.05 m/s. This oscillating regime, though observed experimentally for the first time during this study, has been predicted numerically by Jackson et al. [91] and has been described in [38] as a 'combination' flame with small amplitude.
The existence of oscillatory behavior during the combustion process could have important safety and efficiency implications for industrial application. Indeed, local oscillations may lead to the wall overheating, thus affecting the mechanical resistance of micro-combustors. Therefore, understanding the underlying dynamics behind the transitional regimes is an important issue for the further development of micro-reactors.
In the following sections we detail the behavior of each flame regime as a function of the inlet velocity.

3.1.1 Stable flame regime

The stabilization temperatures discussed above are the temperatures at the wall where the flame stabilizes. However in [30, 31] it is reported that the gas phase temperature is correlated to the inlet velocity: for a same wall temperature profile, the higher the flow rate, the lower the axial temperature. This statement can be clearly observed in Fig. 3.5, where the centerline temperature profiles are depicted for 1.0 and 0.5 m/s. Such profiles are obtained through the numerical simulations detailed in Annex C. By increasing the inlet velocity the gas temperature profile shifts downstream, *i.e.* towards the reactor exit. Thus, mapping the flame location as a function of the wall temperature may be misleading. Therefore Fig. 3.6 displays the flame positions within the stable region (0.45 – 1.0 m/s) in terms of both wall and centerline temperatures. In addition, direct pictures of these stable flames are reported in order to highlight the change in the flame shape with the inlet velocity. It can be observed that, while the difference between the maximum (at 1.0 m/s) and the minimum (at 0.4 m/s) stabilization temperature at the wall is about 460 K, the centerline gas phase stabilization temperature is nearly independent of the inlet velocity (difference of ± 30 K at most).

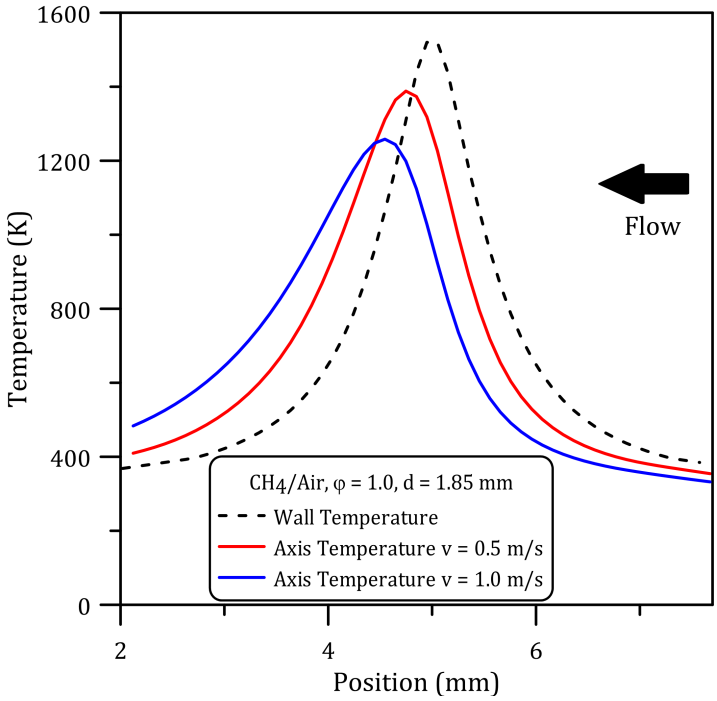

Figure 3.5: Centerline temperature profiles at 1.0 and 0.5 m/s.

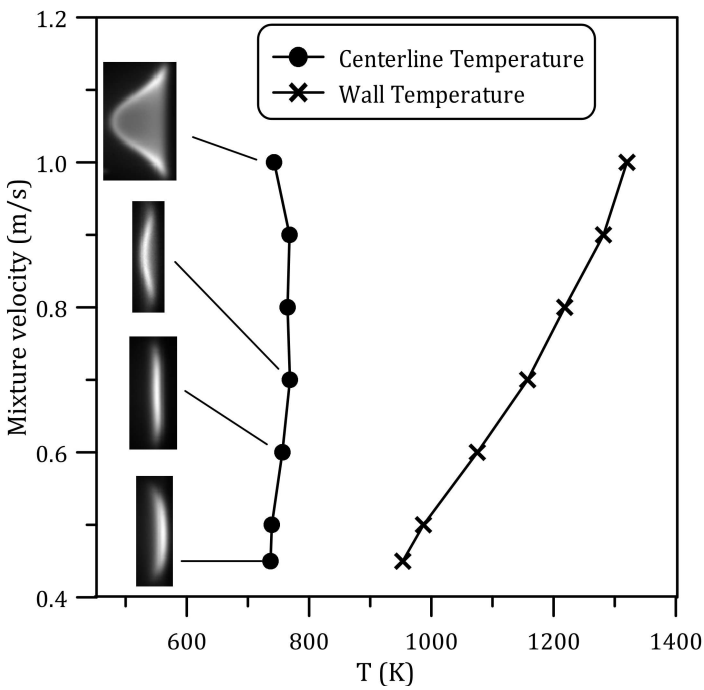

Figure 3.6: Flame positions defined at the wall and axial temperature as a function of the mixture flow velocity.

As demonstrated numerically in [30, 31, 36, 94], the higher the flow rate the faster the chemicals rate and thus the higher the heat release rate and the flame temperature. Conversely, lower inlet velocities result in a lesser power generation in which case the heat losses become greater relative to the heat generated. One could thus think that by decreasing the reacting mixture inlet velocity, the flame would stabilize at higher temperatures to compensate the greater heat losses. However, Fig. 3.6 clearly shows that the stabilization temperature for a stoichiometric methane/air mixture is on average 750 K regardless of the flow rate, and that the thermal equilibrium is therefore always achieved for this temperature. This suggests that the heat loss increases with the inlet velocity, which may be related to the shape of the flame. Indeed Daou and Matalon [45] demonstrated that the geometry of the front flame strongly affect the flame sensitivity to the external heat losses. When the flame is directed toward the burned gases (convex shape), the heat losses to the wall are enhanced since there is a larger flame surface in contact with the walls and the fresh gases, which are not warmed up by the reactor walls because of the short residence time. On the other side, when the flame exhibits a concave shape (at 0.45 m/s for example), it is less vulnerable to the heat losses since the flame surface is smaller and the fresh gases are heated up by the reactor walls because of the longer convective time scale. The wall temperature measured at the flame position at v = 0.45 m/s is 953 K, while the axis temperature is 736 K, only 6 K lower compared to 1.0 m/s (742 K). At 0.7 m/s, a higher centerline temperature is observed (769 K).
Experimentally, the chemical reactivity in our experimental setup is monitored by collecting the CH^* chemiluminescence. The evolution of the spatially integrated CH^* signal as a function of the inlet velocity is displayed in Fig. 3.7. One can notice that the signal decreases with the inlet velocity: the lower the flow rate is, less CH^* is produced. Nevertheless, the spatially resolved CH^* profiles for each flow rate, provided in the insert of Fig. 3.7, behave differently. Although, at first, the flame gets brighter with increasing the inlet velocity (the signal reaches a maximum for 0.7 m/s) when the flame becomes convex (Fig. 3.2), and then decreases while the peak gets broader. This spreading of the CH^* signal is most likely caused by the higher flow rates that spread the reaction zone rather than any chemical or thermal effects.

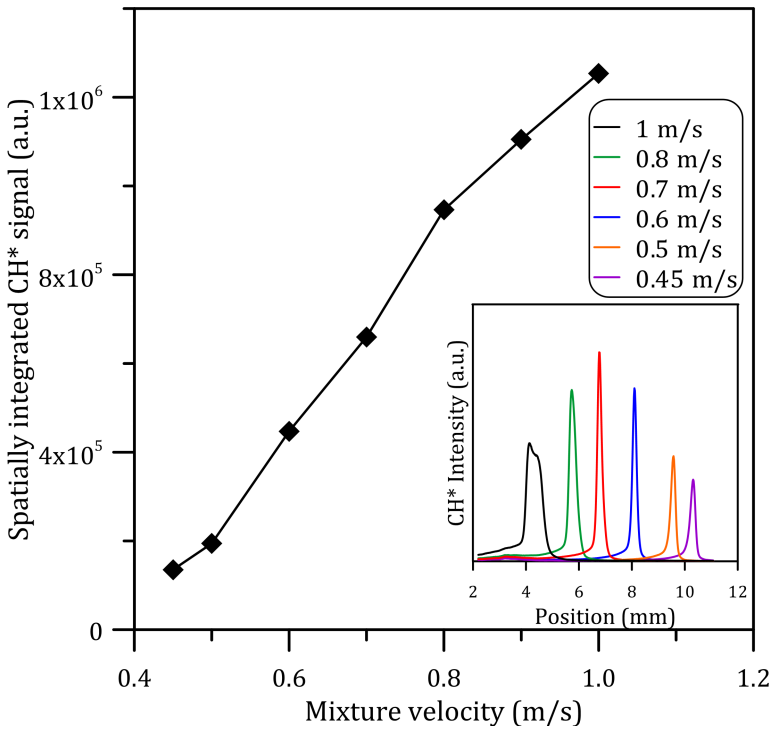

Figure 3.7: Spatially integrated CH* signal of stable flames and CH* profiles.

To summarize, at high flow speed, the total CH* signal is intense but spread on a large spatial domain while the flame stability is strongly impacted by fluid dynamics effects: the convective time scale is short, and the internal reactor temperature remains low, thus enhancing the heat losses. In order to compensate for this energy loss, the flame stabilizes at higher temperatures. For lower inlet velocity, heat conduction from the flame front to the reactor walls dominates because of the longer residence time, although the heat release rate and the CH* emission are weaker. Nevertheless, the temperature of the unburned gases is high, which, in combination with the nearly flat flame shape, limit the heat losses and allows the flame stabilizing at centerline temperatures close to those encountered for higher flow rates.

3.1.2 FREI regime

The FREI regime is observed for inlet velocities between 0.412 and 0.06 m/s. Similarly to the stabilization temperature of the stable flames, the ignition and extinction temperatures at the wall in the FREI regime depend on the flow rate.
From Fig. 3.1 it can be observed that the ignition occurs at lower temperatures as the velocity decreases, because of a longer residence time leading to hotter fresh gases.
Several experimental attempts were done to study the ignition phenomenon, and

determine whether the flame ignites near the wall or at the center of the reactor. Unfortunately, those experiments were not conclusive because of an extremely low signal-to-noise ratio, preventing a clear visualization of the ignition position. Nevertheless, the ignition characteristics have been studied numerically, and the details and conclusions of this study are presented in Chapter 5.
Regarding the extinction, a clear and strong dependence of the quenching temperature to the flow velocity is observed. This dependence remains when reporting the gas phase temperature instead of the wall temperature (Fig. 3.8): the lower the inlet velocity, the lower the extinction temperature.

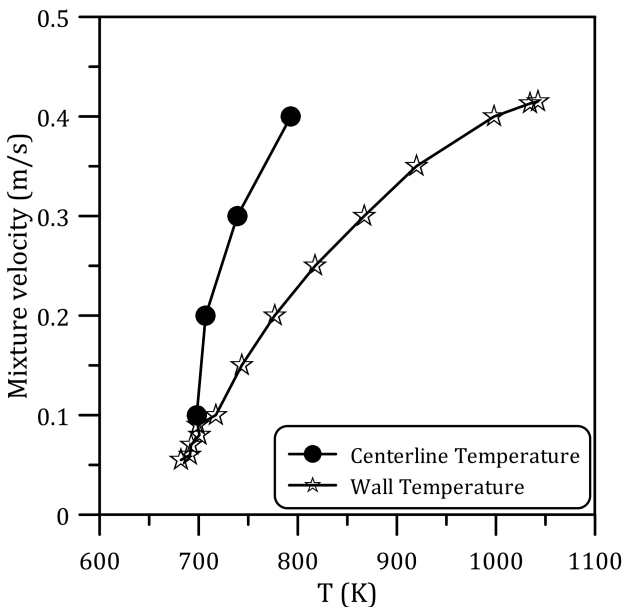

Figure 3.8: Extinction positions defined at the wall and axial temperature as a function of the mixture flow velocity.

This extinction phenomenon has been numerically investigated by Norton and Vlachos [31] and Minaev et al. [73]. From their works, the following qualitative explanation of the FREI regime can be proposed: at moderate inlet velocity (0.20 – 0.40 m/s) the residence time is short, and therefore the convective time scale is small in comparison with the axial conductive time scale. This has a twofold effect. First, heat transfer from the wall to the unburned mixture is limited, and the reacting mixture must travel over a long distance to get preheated. The flame thus ignites at high temperatures. Conversely, heat losses to the wall are negligible, which result in high flame temperatures [30, 31, 94] and a sharp and intense reaction zone. Once the flame exists, the fresh gases are warmed up through heat conduction from the flame front and the flame thus propagates upstream, *i.e.* towards cooler regions. Ultimately, the flame gets thermally quenched [57]. This explanation is supported by the time tracking of the spatially resolved CH^* signal displayed in Fig. 3.3. The CH^* signal appears at high temperatures, then increases and broadens as the flame

propagates before narrowing into a sharp and intense peak.
As the inlet velocities get lower (0.05 to 0.2 m/s), the residence time increases, and the fresh gases are heated up by the reactor walls. Moreover, the convective time scale becomes longer, which enhances axial heat conduction and results in, nearly isothermal conditions inside the reactor. Hence, although the flame generates less power, decreasing the heat transfer to the unburned mixture, thanks to the high reactor temperature the reaction zone can still travel upstream over longer distances in comparison with higher flow rates flames. Furthermore, the lower extinction temperatures observed for these low inlet velocities may also partially be explained by the radical pool depletion. The wall temperature ($T > 700\,K$) and the slow flow speed enhance the wall-gas interactions, boosting radicals recombination, which are exothermic [65] and thus releasing enthalpy that can help to sustain the flame and postpone its extinction. The influence of the chemistry on the flame quenching is further discussed in Section 3.1.2.2, where the CH^* evolution is presented.

3.1.2.1 Frequency and characteristic time

The frequencies and the characteristic times of FREI flames have been determined by using the procedure described in Annex B. In Fig. 3.9 frequencies for a stoichiometric methane/air mixture in a 1.85 mm internal diameter reactor are presented.

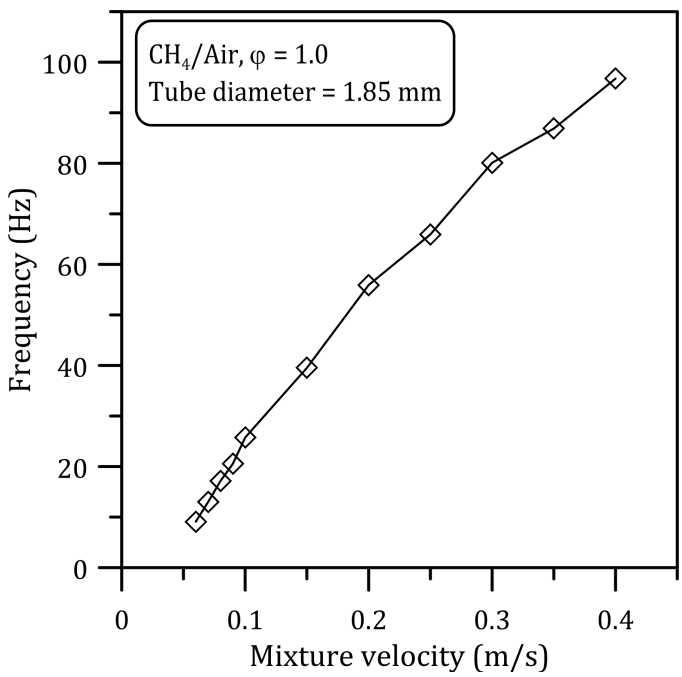

Figure 3.9: FREI frequency variation with inlet velocity, $d = 1.85\,mm$, $\varphi = 1$.

The frequency increases almost linearly with the inlet velocity, confirming the results reported in [93, 94]. This behavior can be rationalized by considering the explanation

of the FREI phenomenon discussed above. As shown in [30, 31], the maximum flame temperature increases with the inlet velocity, leading to higher burning velocities, whereas the temperature of the fresh gases quickly decreases as the reaction zone travels upstream. Consequently, the flame propagates quickly but for short distances before getting quenched. The time of one FREI cycle time is thus short (higher frequency).

At low flow rate the residence time is longer and more time is required for the mixture to reach the ignition zone. Furthermore, the flame is weaker (lower power generation) and propagates on a longer distance (since the fresh gases are warmer because of a better conductive heat transfer): the period of each cycle is high and the frequency is low.

In order to better understand the frequency dependence with the inlet velocity, the characteristic times of FREI flames, τ_{IE} the time between ignition and extinction and τ_{EI} the time between extinction and ignition, have been determined as described in Annex B and are depicted in Fig. 3.10.

During the oscillating flame regime, at 0.415 and 0.413 m/s the trend of τ_{IE} changes: the time required for the flame propagation is higher due to the presence of multiple oscillations. Excluding the times measured for the oscillating FREI (detailed in Section 3.1.4), both characteristic times decrease with the mixture velocity: the time required for the fresh gas to reach the ignition point and the time required for the flame to get quenched decrease with the flow rate. Since the FREI frequency is the inverse of the sum of these two characteristic times, it implies that the frequency increases with the inlet velocity, as seen in Fig. 3.9.

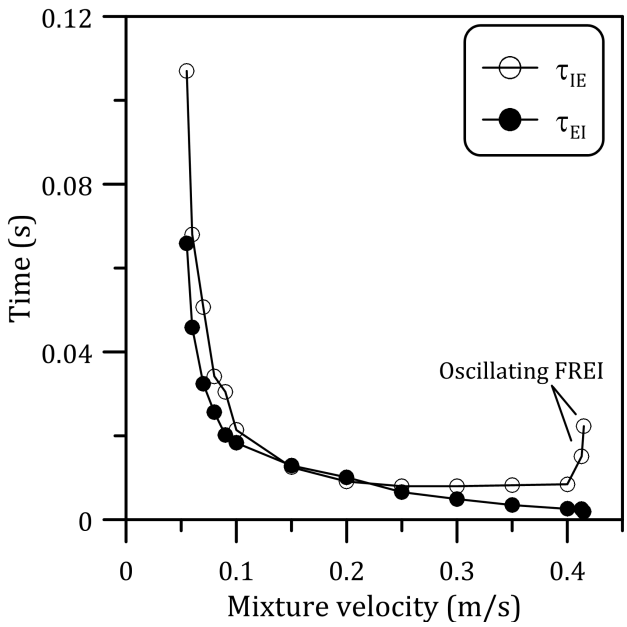

Figure 3.10: Comparison between τ_{IE} and τ_{EI} for a 1.85 mm diameter reactor, $\varphi = 1$.

For inlet velocities higher than 0.2 m/s, the flames propagate fast and the time required to heat up the mixture is small compared to the low velocity region.
On the other hand, for inlet velocities ranging from 0.1 to 0.2 m/s, the two characteristic times are comparable. Further decreasing the mixture velocity, the flame lifetime becomes once more longer, especially for the lowest inlet velocity (0.055 m/s) for which a FREI could be observed. In this latter case, the Reynolds number is very low (Re < 1) and the viscous forces are strongly enhanced, causing a high transport time (high τ_{EI}). At the same time the reactions are particularly weak and thus the flame propagation is very slow.

3.1.2.2 Evolution of CH* intensity and quenching mechanism

Monitoring the evolution of the maximum of CH* intensity may be useful to get further insight into the flame dynamic behavior. Figure 3.11 displays these traces, computed through the methodology detailed in Annex B, for all the inlet velocities leading to the existence of FREI flames with a stoichiometric methane/air mixture:

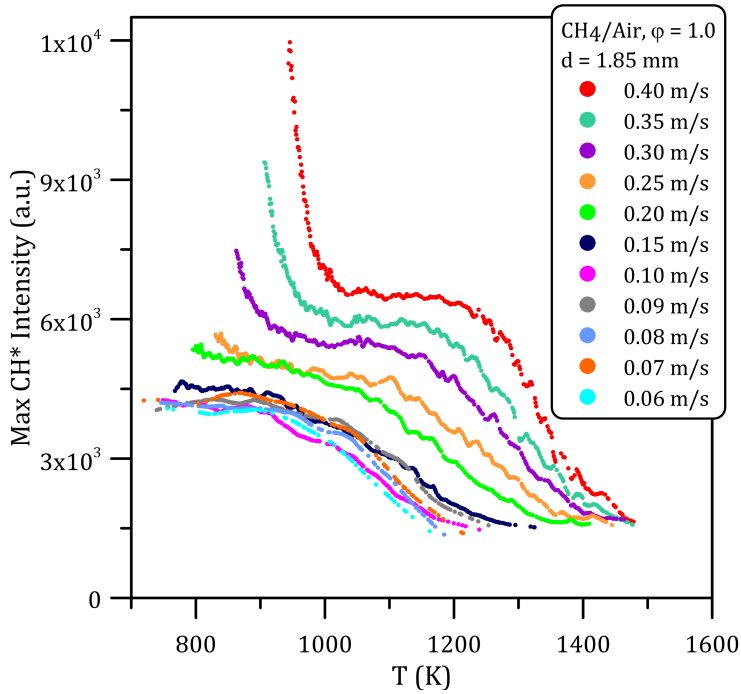

Figure 3.11: Maximum CH* progression in the FREI region at different inlet velocity.

Regardless of the flow rate, the flame ignites in the high temperature region (1350 – 1500 K). At ignition, the CH* emission is weak but increases as the flame propagates upstream, until the flame extinction. For a stoichiometric methane/air mixture, a single CH* peak was detected.
Looking at Fig. 3.11, a change in the maximum CH* progression (flame propaga-

tion) can be noticed for an inlet velocity around 0.2 m/s. Above this threshold, a sharp increase in the CH^* signal is detected right before the flame extinction while below this threshold the signal stays constant through the cool region. From a phenomenological point of view, and considering the results obtained by numerical simulations [31, 73], we can provide the following explanation.
At high inlet velocity, the fresh gases promptly reach the hot region and thus quickly ignite (short τ_{EI}, Fig. 3.10). After ignition, the flame rapidly propagates toward the cooler region, resulting in a built-up of the CH^* radical pool as illustrated by the sharp increase in the light intensity in the early stages of the flame propagation. However, during the propagation phase, the flame is widely spread along the reactor axis (Fig. 3.3) but gets thinner while advancing to the quenching region: the flame 'bumps on a barrier' of gases that are too cold to be warmed up by the flame front and cannot advance further until it vanishes because of heat losses. As the flame width decreases, the production of CH^* gets localized in a narrower region. The local concentration of this active species increases, which rationalizes the rise of the signal intensity before the flame extinction.
On the other hand, when the fresh gas speed decreases (0.1 m/s), the CH^* intensity is significantly reduced. The time devoted to heat up the fresh gas (τ_{EI}, Fig. 3.10) increases, *i.e.* the conduction time between the hot walls and the fresh gas is increased. As compared to high flow speed, for a given position,the centerline temperature is higher; even if the reaction is weak and the heat generated is low, the heat lost relative to heat generated decreases.
Furthermore at lower velocity the radial gradients (mass fraction and temperature versus radius) become negligible. As demonstrated by Raimondeau et al. [64] the heat and mass transfer between the bulk and the wall are faster and the effect of radical reactions at the wall becomes significant. As said before, in this case the extinction cannot be associated with a thermal effect. The radical depletion effect becomes dominant [64, 65] resulting in a more stable flame that extinguishes at lower temperature.

3.1.3 Weak Flames

When the inlet velocity becomes lower than 0.05 m/s, the FREI regime disappears and weak flames are observed. At 0.05 m/s, an oscillating weak flame is detected. This peculiar flame type is described in Section 3.1.4. At 0.04 m/s, a stable weak flame appears: it stabilizes in the hot region, at temperatures close to the extrapolated line of the ignition position of FREI (see Fig. 3.1). Although weak flames may exist for inlet velocities below 0.04 m/s, it was not possible to experimentally achieve such low flow rates because of the range of tolerance of the MFCs.
The emission signal collected by the EMCCD camera shows a broad CH^* profile with a very low intensity, in line with the earlier work of Maruta et al. [38]. These flames are characterized by a broader distribution of intermediate species (CO, CH,...)

than flames observed at higher inlet velocities. Chemical reactions are slow, and the heat release is small, resulting in very low flame temperatures [43]. As a consequence, weak flames are mostly governed by mass diffusion [38].
As detailed in Chapter 1, theoretical predictions [73] indicate that weak flames stabilize close to the ignition point. Indeed, the temperature increase resulting from the flame existence is small. The wall temperature at which the weak flame anchors can thus be considered as the minimum ignition temperature of the mixture, at the given conditions.
With standard methods the Auto-Ignition Temperature (AIT) of a stoichiometric methane/air mixture at atmospheric pressure varies from 793 to 923 K according to the operating conditions [79–83]. The AIT increases with the surface-to-volume ratio and is affected by the vessel material [84, 85] which can either promote or prevent/inhibit ignition. Tsuboi et al. [42] reported an AIT of 1225 K for a stoichiometric methane/air mixture in a 2.0 mm inner diameter reactor flowing at 0.02 m/s, although the plot (Fig. 3, [42]) supporting their discussion indicates an AIT of 1253 K. For the same mixture, we obtained an AIT of 1336 K but for an inlet velocity of 0.04 m/s. However, the inner diameter of the reactor employed in the present study is smaller (1.85 mm). The relative effect of the reactor dimensions on the AIT remains unclear, and thus prevents a direct comparison of the different AITs values with stoichiometric mixtures. This aspect is further investigated in Section 3.3.3, where the effect of the equivalence ratio is studied.

3.1.4 Transitional regimes: oscillating FREIs and weak flames

As mentioned earlier, two transitional regimes have been detected. The first one, called oscillating FREIs, is observed for inlet velocities ranging from 0.413 to 0.415 m/s and connects the stable flame and FREI regimes. Similarly, the second oscillating regime lies between the FREI and weak flame region and exists for an inlet velocity around 0.055 m/s.
In order to explore these oscillating regimes, the time evolution of the spatially integrated CH^* signal for different flow rates is presented in Fig. 3.12. Significantly different behaviors are observed according to the inlet velocity. At v = 0.050 m/s (Fig. 3.12a) an oscillating weak flame is present: the integrated CH^* signal is very low but rapidly fluctuates. By increasing the velocity to 0.055 m/s, the flame switches to a conventional FREI (Fig. 3.12b). Small variations of the CH^* signal are detected before a sharp and fast increase. The system behaves as if a pulsating weak flame slowly oscillates before evolving to a flame that quickly propagates upstream. This behavior, mentioned in [38] as 'combination' flames, is similar to that predicted by the 1D thermo-diffusive model of Minaev et al. [73] and by Jackson et al. [91]. At low flow rates, the conductive time scale is longer than the convective one, leading

to nearly isothermal conditions along the reactor radius [44]. Furthermore, despite the fact that fused silica is considered as an inert surface, high temperatures along with the small channel width favor radical depletion [58]. The initial weak flame, which is characterized by exothermic radical recombinations at the wall [64, 65], can thus provide, considering that the inlet enthalpy flow rate is large enough, the energy required to initiate the main flame which then propagates quickly upstream thanks to the high temperature of the fresh gases heated up by the reactor walls.

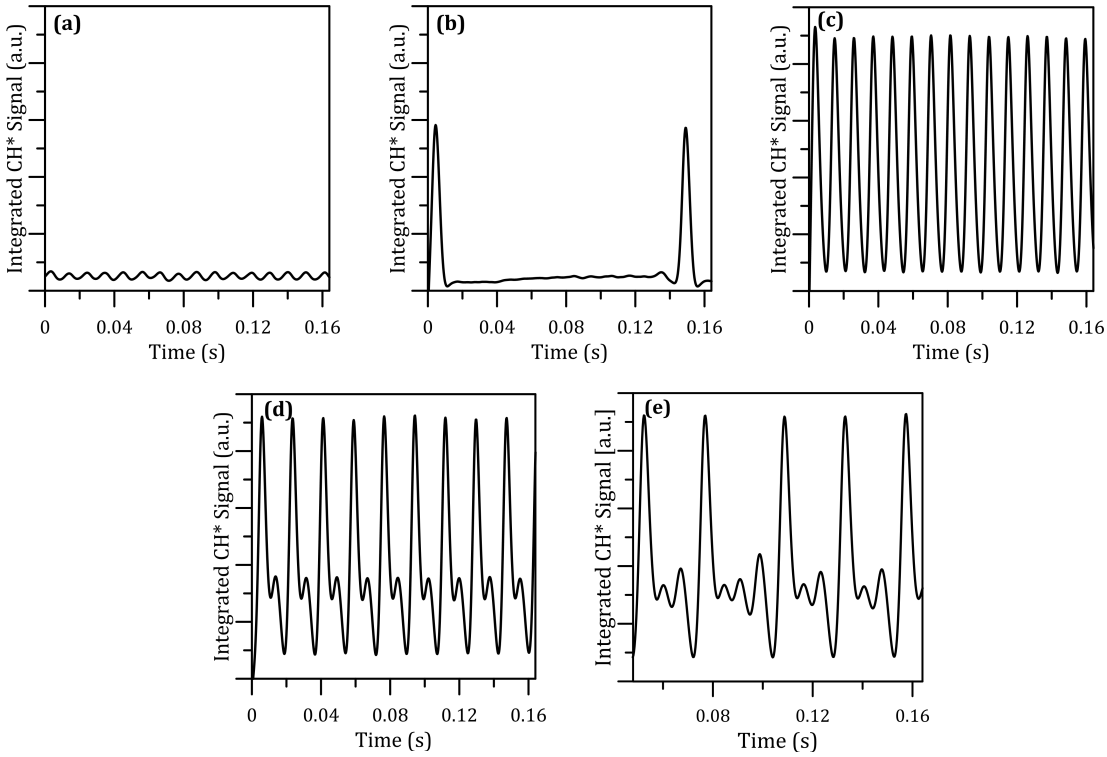

Figure 3.12: Temporal evolution of CH^* signal with inlet velocity: a) v = 0.05 m/s (oscillating weak flame) Fr = 94.7 Hz, b) v = 0.055 m/s Fr = 9 Hz, c) v = 0.40 m/s Fr = 96.8 Hz, d) v = 0.413 m/s (oscillating FREI) Fr = 57.2 Hz, e) v = 0.415 m/s (oscillating FREI).

At v = 0.40 m/s (Fig. 3.12c) a typical FREI is also observed, but with a stronger CH^* signal emission and frequency. By slightly increasing the inlet velocity to 0.413 m/s (Fig. 3.12d), the system switches to an oscillating flame with a singular and regular pattern. The flame oscillates near the extinction point within a distance of 0.6 mm, which corresponds to a wall temperature variation of 20 K. Before reaching the stable flame region, the oscillations become irregular (v = 0.415 m/s, Fig. 3.12e): no regular pattern (amplitude, number of second order peaks) is detected. This oscillatory behavior near extinction has been studied by Norton and Vlachos [31] who described it as the outcome of the pressure waves coupled to fluid density variations. Likewise, Miroshnichenko et al. [87] predicted numerically this transitional regime

using a 1D-thermal-diffusive model for fuel-rich hydrogen/air mixtures. This behavior corresponds to the 'mixed-mode oscillations'. A decrease in the inlet velocity changes the number of oscillations until the FREI regime. The presence of unburned gases, resulting from an incomplete combustion, behind the main flame where the temperature is high and the exothermic reactions at the wall are enhanced, may also explain the existence of these multiple peaks. Miyata et al. [56] also observed numerically the presence of an oscillating behavior between the FREI and stable flame regime by performing DNS calculations. As can be seen from in Fig. 3.1, the extinction of these oscillating flames occurs at higher wall temperature than typical FREI flames because of a lower temperature in the center of the tube, thus preventing the flame to propagate further.
The frequencies associated with the different oscillating flames observed (FREI and weak) are compared to the FREI characteristic frequencies in Fig. 3.13. The oscillating FREI flames have moderate frequencies, due to the multiple oscillations, that increase as the inlet velocity decreases. Then, as the mixture inlet velocity is further reduced, the frequency of the FREI flames also decreases. At the lowest velocity (at v = 0.05 m/s), an oscillating weak flame was observed and is characterized by a high frequency (95 Hz): the flame is trapped in the high temperature zone presumably because, unlike the case at v = 0.055 m/s, the radical recombination does not provide the energy required for the flame propagation.

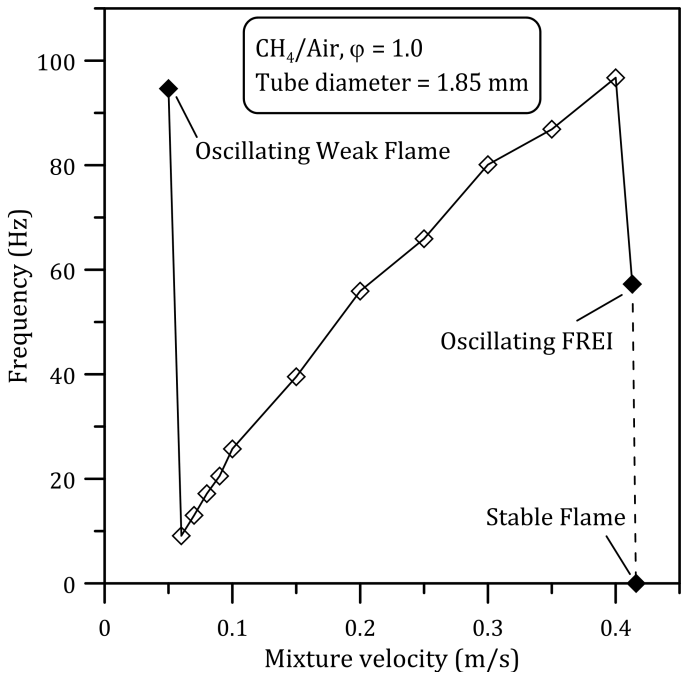

Figure 3.13: Frequency variation as a function of the inlet velocity.

The experimental observation of these oscillating flames confirms the work of Jackson et al. [91], whose mathematical model predicted those oscillating behaviors as well as some instabilities observed at higher inlet velocity.

3.2 Comparison with previous studies

Figure 3.14 compares the results presented in Fig. 3.1 with those obtained by Tsuboi et al. [42, 43] for stoichiometric CH_4/air mixtures in a 2.0 mm internal diameter reactor:

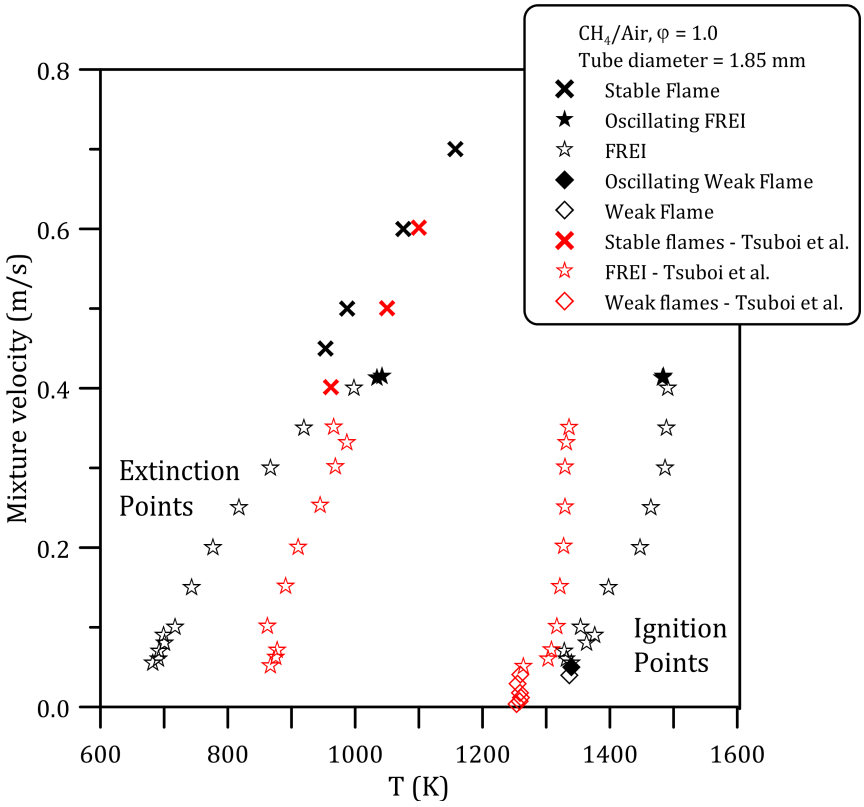

Figure 3.14: Comparison between the present work and that of by Tsuboi et al. [42].

Although a qualitative agreement (similar trends) between the two sets of data can be observed, significant temperature shift is observed. These differences are mainly due to the different experimental setups, especially in the heat sources employed. First, the temperature gradient in the present experimental configuration is steeper and heat is distributed evenly around the reactor because of the use of three blowtorches. Furthermore, the temperature profile along the tube wall is measured continuously with an infrared camera which allows accounting for non-negligible heat release by the flame (see Chapter 2). Conversely, in the experiments carried out by Tsuboi et al. [42, 43], the reactor was heated from below by a flat flame burner, and the temperature profile was measured prior to any experiment thus neglecting inner flame contributions. The temperature profiles used in [42, 43] and in the present work are compared in Fig. 3.15.

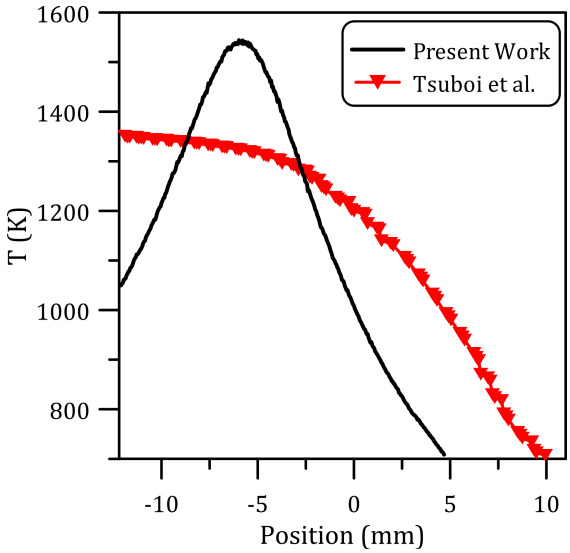

Figure 3.15: Comparison between the temperature profiles used in the present work and by Tsuboi et al. [42].

In order to mimic the experimental setup of Tsuboi et al. [42, 43], and then understand the differences observed in Fig. 3.14, experiments were repeated with only two heat sources, removing the top blowtorch. Direct pictures of the stable flames are compared for the two configurations (three or two blowtorches) in Fig. 3.16.

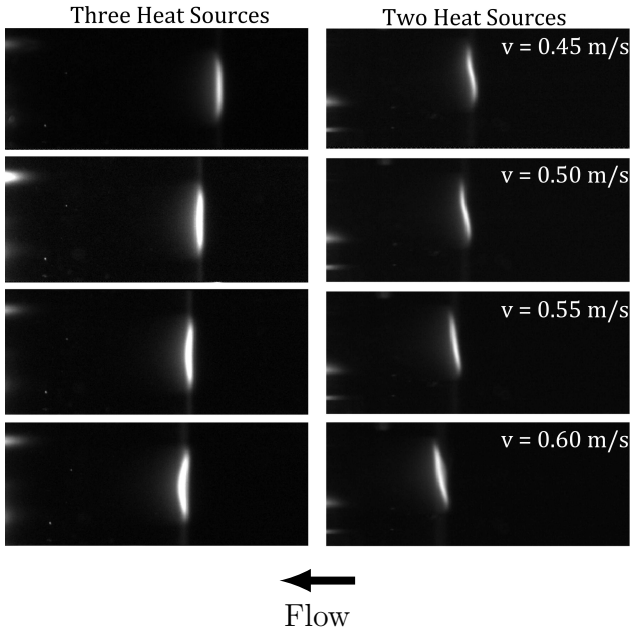

Figure 3.16: Flames obtained with three and two heat sources at different flow velocities in a 2.15 mm diameter tube.

The shape of the flame is strongly affected by the non-symmetric distribution of heat sources: with two heating sources, the flames are bent and less bright, which brings uncertainty in the flame localization and consequently in the temperature determination. Regarding the higher FREI extinction temperatures reported by Tsuboi et al. [42, 43], this disagreement can be assigned to the different shape of the temperature profile and to the non-uniformity of the temperature distribution inside the reactor. Indeed, the upper section of the reactor is colder than the lower half, the latter being used for the temperature measurement. As a consequence the thermal quenching is most likely initiated by the upper wall (colder) and the extinction temperature is overestimated. On the other hand, the lower ignition temperatures measured by Tsuboi et al., especially at high flow rates, are the consequence of (i) the lower temperature peak when using a flat flame burner and (ii) the temperature plateau measured downstream: while the fresh gases must travel further into the reactor to be warmed up, the temperature reading remains almost the same ($\sim$1350 K) because of the low gradient.
Miyata et al. [56] performed numerical simulations using step temperature profiles with different maxima. The results showed that the extinction temperatures in the FREI regime were affected by the profile used, while the ignition steps and the stable flames were little affected. It also impacts the transition between the different flame regimes. One can notice in Fig. 3.14 that the transition between stable and FREI regimes takes place at a lower inlet velocity in the study of Tsuboi et al. [42, 43] than herein: 0.350 m/s vs. 0.412 m/s. From Miyata et al. it could be concluded that the difference in temperature maxima observed in Fig. 3.15 is directly related to the different results.

3.3 Effect of the equivalence ratio

Despite of its inherent practical importance, no experimental work could be found in the literature to study the effect of the equivalence ratio at micro-scale. The aim of this section is to provide some understandings to the influence of the equivalence ratio regarding the flame behavior. The map of the flame stability as a function of the mass flow rate and the equivalence ratio is then provided.
The experiments were conducted over a range of equivalence ratios from 0.5 to 1.5 in a 1.85 mm internal diameter reactor. The results obtained are depicted in Fig. 3.17: stable flames and FREIs which were observed regardless of the equivalence ratio are represented by crosses and open stars, respectively. The points at which the flame stabilizes (or ignites and extinguishes) are reported in terms of wall temperature. For the sake of clarity, the weak flames and the transitional regimes are not reported in Fig. 3.17 but are discussed in Sections 3.3.3 and 3.3.5 respectively.

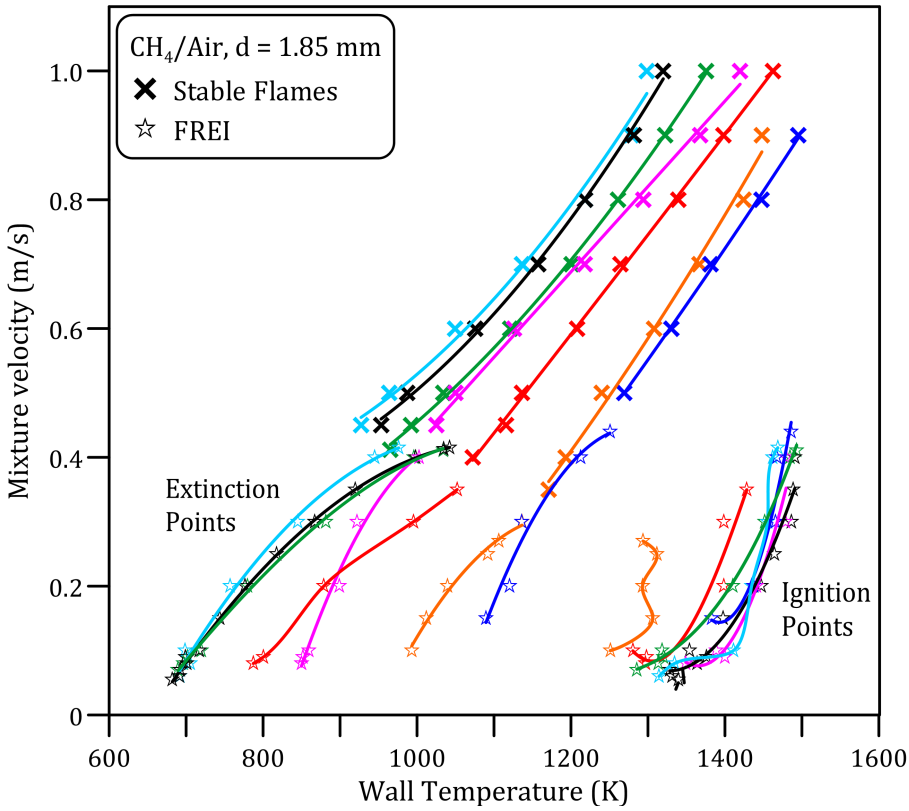

Figure 3.17: Effect of equivalence ratio on the flame positions: 0.5 (orange), 0.7 (red), 0.9 (green), 1 (black), 1.1 (cyan), 1.3 (magenta), 1.5 (blue).

The positions at which stable flames anchor and FREI flames extinguish are observed for higher wall temperatures for both fuel-lean and fuel-rich mixtures. Moreover, the transition velocity between these two regimes changes with the equivalence ratio. While the transition is effective at 0.415 m/s for the stoichiometric condition, it occurs at lower inlet velocities for lean mixtures, 0.270 m/s for $\varphi = 0.5$, but slightly higher velocities for fuel-rich mixture, 0.440 m/s for $\varphi = 1.5$. Likewise the transition between FREI and weak flame regimes occurs at different inlet velocity with respect to the equivalence ratio: 0.050 m/s for $\varphi = 1.0$ but 0.108 m/s for $\varphi = 1.5$. Weak flames were not observed in the lean side due to mechanic limitations.

3.3.1 Stable flame regime

The stable flames obtained for non-stoichiometric mixtures have similar shapes to those observed for stoichiometric mixtures (Fig. 3.2). However, the flame brightness increases with the equivalence ratio (because of a higher fuel concentration) and thus an adapted EM gain was employed during experiments to optimize the flame chemiluminescence recording.
As observed for stoichiometric mixtures, the wall temperature measured at the flame

position increases with the inlet velocity. In order to consider the effect of the flow field on the reactor temperature, in Fig. 3.18 flame positions for each equivalence ratio are plotted at the centerline temperature, obtained through the numerical simulation detailed in Annex C.

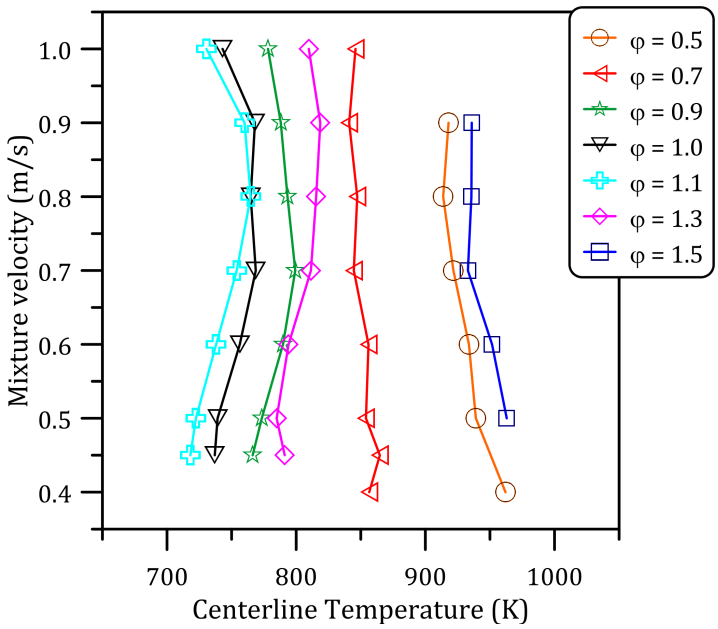

Figure 3.18: Stable flame positions reported in terms of centerline temperature as a function of the mixture flow velocity.

The results obtained at each equivalence ratio confirm the observations of Section 3.1.1: at high speed the flame adopts a convex shape, while upon decreasing the inlet velocity it becomes flat and then has a concave shape.
One can notice that the lowest stabilization temperatures are recorded for the equivalence ratio 1.1, while the highest are for the richest and leanest mixtures. As detailed in Chapter 1, Zeldovich [17] has demonstrated theoretically that it exists a relation between the adiabatic laminar burning velocity and flame temperature and the similar quantities at the quenching limit. Indeed the flame temperature and the flame speed, that are higher near the stoichiometry and lower in the lean and rich side, are directly related to the flame stabilization. To make a clear comparison with the adiabatic conditions, the flame temperature and laminar burning velocity at each equivalence ratio were computed respectively with the EQUIL [115] and PREMIX codes [116] from the CHEMKIN package. The GRI 3.0 mechanism [90] was adopted. For each stable flame reported in Fig. 3.17, the corresponding adiabatic temperature T_{ad} was normalized by the wall stabilization temperature T and the adiabatic laminar flame speed S_l, calculated for the flame centerline stabilization temperature (Fig. 3.18), normalized by the inlet velocity v_{unb}. Plotting the ratio T_{ad}/T as a function of S_l/v_{unb} gives Fig. 3.19.

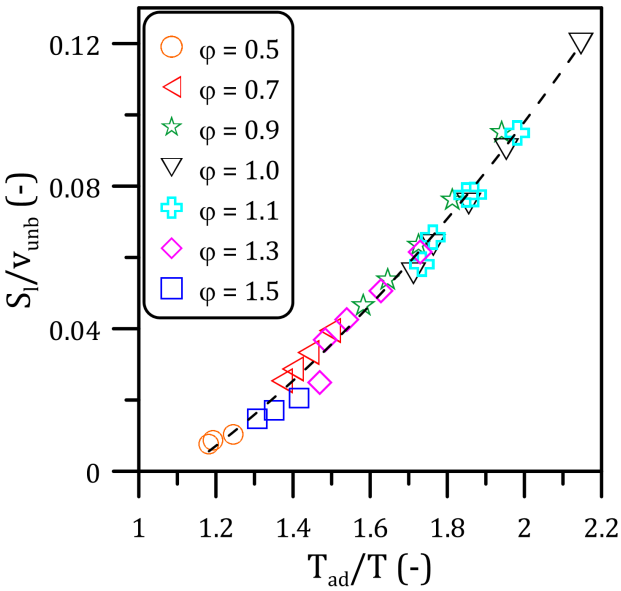

Figure 3.19: Correlation between T_{ad}/T and S_l/v_{unb} for methane/air mixtures at various equivalence ratios.

The fuel-lean and rich data correspond to the region of low T_{ad}/T while mixtures with the highest flame speeds, *i.e.* $\varphi = 1.1$ and 1.0, have the highest T_{ad}/T. For each inlet velocity, the points obtained by changing the equivalence ratio are aligned, which indicates that there is a correlation between the stabilization temperature, the adiabatic temperature and the laminar flame speed.
The flame stabilization dependence on the adiabatic temperature and laminar flame speed is an aspect that must not be neglected during the development of micro-reactors. Operating conditions must achieve high flame temperature and speed to maximize heat exchange through the wall in the Swiss-roll configuration presented in Chapter 1. Indeed the fresh mixture is heated up by the burned gases through heat recirculation if not enough energy is given to the unburned mixture, self-sustained combustion will not be provided.

3.3.2 FREI regime

In the FREI regime the ignition positions for stoichiometric and fuel-rich mixtures (see Fig. 3.17) are found to be insensitive to the equivalence ratio (deviation less than 3%). Nevertheless, for fuel-lean mixtures, the flame ignites at lower wall temperature and with no clear dependence on the inlet velocity, which can be attributed to the difficulty to measure precisely the maximum of the CH^* signal because of a low brightness and signal-to-noise ratio.
Regarding the extinction positions, the flames extinguish at higher temperature for lean and rich mixtures, in line with the observations in the stable flame regime.

Furthermore, in the rich side the transition to the weak flame regime occurs at higher inlet velocity, and thus it was not possible to explore the low velocity region, while in the lean side velocities below 0.08 m/s were not accessible because of experimental limitations.
In order to understand the FREI dependence to the equivalence ratio, in Sections 3.3.2.1 and 3.3.2.2 the flame characteristics are examined in further details.

3.3.2.1 Characteristic times and frequency

In Fig. 3.20 characteristic times are depicted as a function of the inlet velocity for the equivalence ratios investigated. The behaviors obtained follow the trend already observed for stoichiometric mixtures (Fig. 3.10): when decreasing the inlet velocity, the time required for the flame propagation (τ_{IE}) increases. The slow flame propagation promotes the convection towards the fresh gases, leading to the flame extinction at lower wall temperatures. However on the lean ($\varphi \leq 0.7$, Fig. 3.20a-b) and rich ($\varphi > 1.3$, Fig. 3.20e-f) sides the flames propagate over a shorter distance but in a higher temperature region (T > 1000 K). Thus the flame propagation is promoted by the high wall temperatures while the convection time scale is reduced.

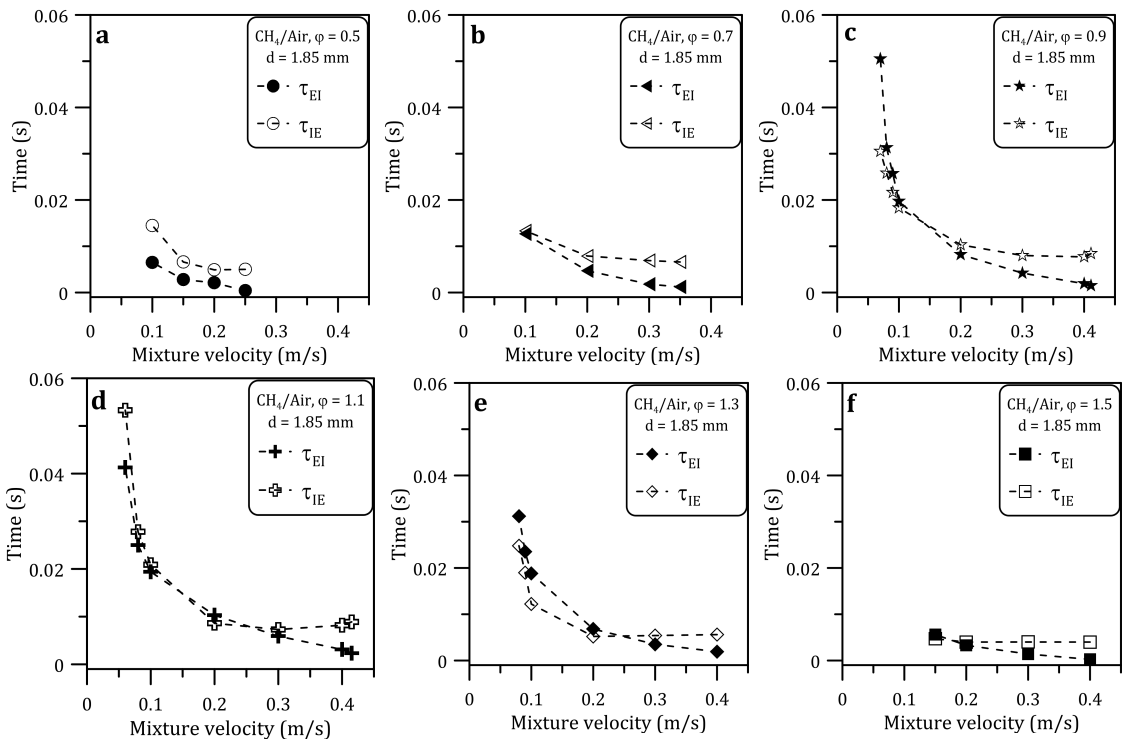

Figure 3.20: τ_{IE} and τ_{EI} at different equivalence ratios in a 1.85 mm internal diameter reactor. a) $\varphi = 0.5$, b) $\varphi = 0.7$, c) $\varphi = 0.9$, d) $\varphi = 1.1$, e) $\varphi = 1.3$, f) $\varphi = 1.5$.

A similar trend is observed for the time required to heat and ignite the fresh mixture (τ_{EI}). However the shortest times are recorded on the lean and rich side, since the fresh gas flows through a high temperature region and thus the time required to heat up the mixture is reduced.
However for $\varphi \geq 0.9$ (Fig. 3.20c-f) and velocity above 0.2 m/s, one can observe that τ_{EI} is smaller than τ_{IE}, while the reverse is true at lower velocity. This progression is not observed for leaner mixtures ($\varphi = 0.7$ and 0.5) for which the τ_{IE} is always higher than τ_{EI} (Fig. 3.20a-b). This suggests that for $\varphi \geq 0.9$ and low inlet velocities (< 0.2 m/s) the flame propagates faster. As a drawback, there is less time for the incoming fresh mixture to heat up: this reduction in the convective time scale leads to an earlier extinction at these low velocities.
The evolution of the measured FREI frequencies with the inlet velocity and the equivalence ratio are depicted in Fig. 3.21. Regardless of the equivalence ratio, the frequency increases with the inlet velocity, consistently with the observations for the stoichiometric mixture. The highest frequencies are obtained for the leanest ($\varphi = 0.5$) and richest ($\varphi = 1.5$) conditions (due to the short characteristic times), whereas the lowest are observed near stoichiometric conditions ($0.9 \leq \varphi \leq 1.1$).

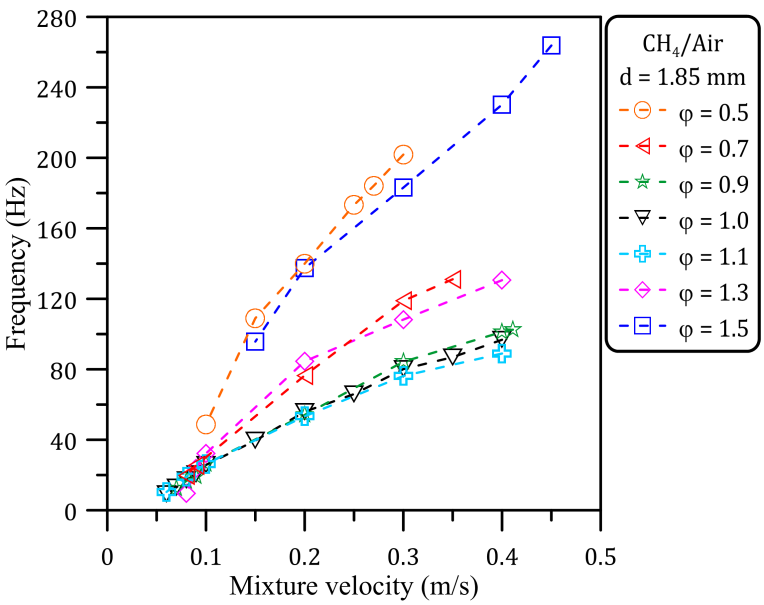

Figure 3.21: Equivalence ratio effect on FREI frequencies.

As pointed out for the stable flame regime, the flame temperature and the combustion speed play a fundamental role during the flame propagation. Near the stoichiometry, the flame has more energy and travels over a longer distance: the characteristic times (τ_{IE} and τ_{EI}) increase. On the lean and rich sides, the effects are reverse: the low temperature and the low flame speed inhibit the flame propagation, thus causing an earlier extinction. These flames are 'trapped' in a high temperature zone.

In their study on flames in curved ducts, Richecoeur et al. [49] brought out the Strouhal number (St) to relate the frequency of the CH_4/O_2 flames and the pipe diameter. A similar approach was adopted in the present work to characterize the effect of the equivalence ratio on the frequency. The Strouhal number is a dimensionless number describing the oscillation frequency within a fluid flow and is often used to represent unstable combustion. Here, St is calculated as $St = f \times d/v$, where f is the characteristic FREI frequency [Hz], d is the inner diameter [m] of the tube and v is the inlet velocity [m/s]. Figure 3.22 shows the evolution of the Strouhal number for the different equivalence ratios. For each mixture composition, the average value over the different inlet velocities is reported and the standard deviation is shown as an uncertainty bar.

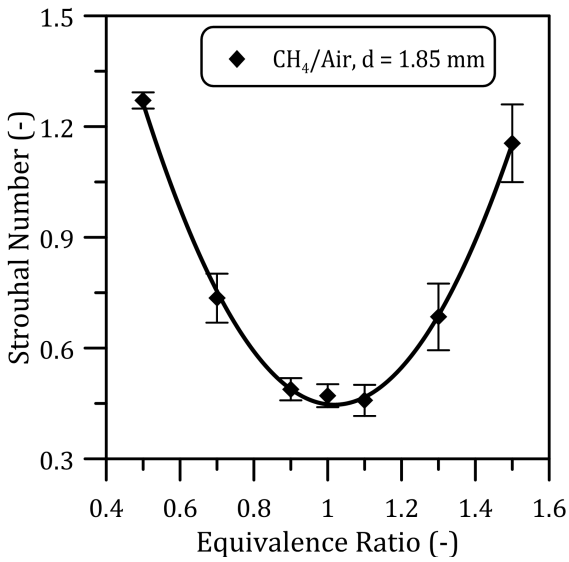

Figure 3.22: Strouhal Number for methane/air FREI flames in a micro-channel of 1.85 mm inner diameter.

Around the stoichiometry ($1 \leq \varphi \leq 1.1$) St = 0.46 which is the minimum value. Richecoeur et al. [49] reported for curved ducts a value of 0.3, which was described by Crow and Champagne [104] as the preferred mode of oscillation of incompressible jets. However, it should be noted that the value of [49] was derived from curved meso-scale ducts (4 mm i.d.), and since the progression St is inversely proportional to the diameter, it is not surprising that the value herein calculated is slightly higher. Furthermore, CH_4/O_2 flames have higher laminar burning velocity and adiabatic flame temperature compared to CH_4/Air flames. Moreover, 0.3 was not presented by Crow and Champagne as a well-defined value but as the average of a broader range of oscillation modes.
However, the existence of a minimum St close to the value reported previously in the literature suggests a coupling between the FREI dynamics at micro-scale and the studies carried in curved ducts. The high frequencies and large St measured in

fuel-lean and fuel-rich conditions indicate the presence of a non-preferred oscillating mode: fast oscillations can lead to local overheating and thus to thermal stress to the wall.

3.3.2.2 Evolution of CH^* intensity

For each methane/air mixtures studied, the evolution of the maximum CH^* intensities is reported in Fig. 3.23 for all the inlet velocities leading to the observation of a FREI flame. Because of the different fuel contents for each equivalence ratio, the EM gain employed by the EMCCD camera was adjusted to increase the signal-to-noise ratio. As a consequence, no quantitative comparison between the signals collected for a same inlet velocity is possible, and the discussion will be limited to qualitative interpretation. As observed for the stoichiometric mixture in Section 3.1.2.2, the trend changes when switching from the moderate to the low inlet velocity region. However, this is not observed for each equivalence ratio.
In the rich side ($\varphi \geq 1.1$, Fig. 3.23a-c) and at velocities over 0.2 m/s, the signal is characterized by a sharp peak before the flame extinction. As shown in Fig. 3.1.2.2, high velocities are associated with short τ_{EI} and τ_{IE}: the time available to warm up the incoming fresh mixture is low while the flame propagates quickly. These two combined effects cause early flame extinction due to a thermal quenching effect [57]. Conversely, at low inlet velocity the two characteristic times are both large, helping the temperature increase of the incoming mixtures through heat recirculation and convection. The flame propagation is therefore promoted by the high temperature and the enhancement of the gas-wall interactions [64, 69].
For lean mixtures, the trend is slightly different, although the profiles displayed in Fig. 3.23d-f must be considered cautiously since the use of high EM gain induced a larger scattering. In Fig. 3.23d-e the peaks observed for fuel-rich mixtures are less noticeable but can be either observed or estimated for velocities over 0.3 m/s. At $\varphi = 0.5$ (Fig. 3.23f), the FREI regime is limited to a short inlet velocity range (0.10 – 0.27 m/s) and the flames have very low luminosity. Even using a high-smoothing coefficient in the Savitzky-Golay filter (Annex B), the profile does not permit reducing the signal dispersion. Under these conditions, the presence of a sharp peak before extinction was not detected.

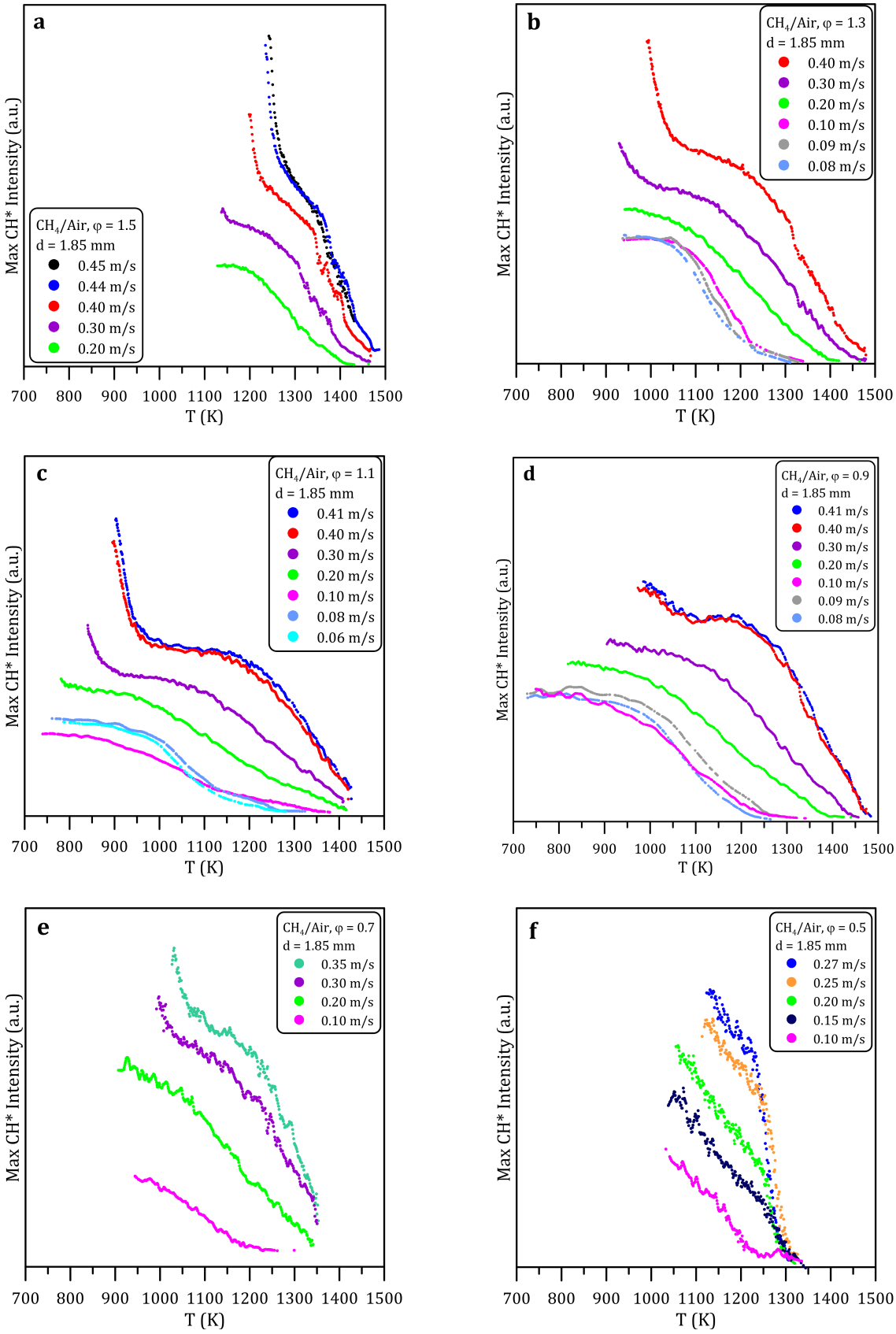

Figure 3.23: Progression of the maximum CH* for methane/air FREI flames as a function of the inlet velocity for different equivalence ratios.

With a closer look at the CH* progression profiles of the richest mixture (Fig. 3.23a), discontinuities can be observed for inlet velocities over 0.3 m/s, indicating the presence of multiple CH* peaks. Stepping back to the time and spatially resolved CH* signals (Fig. 3.24), these multiple peaks are indeed observed in the flame propagation phase.

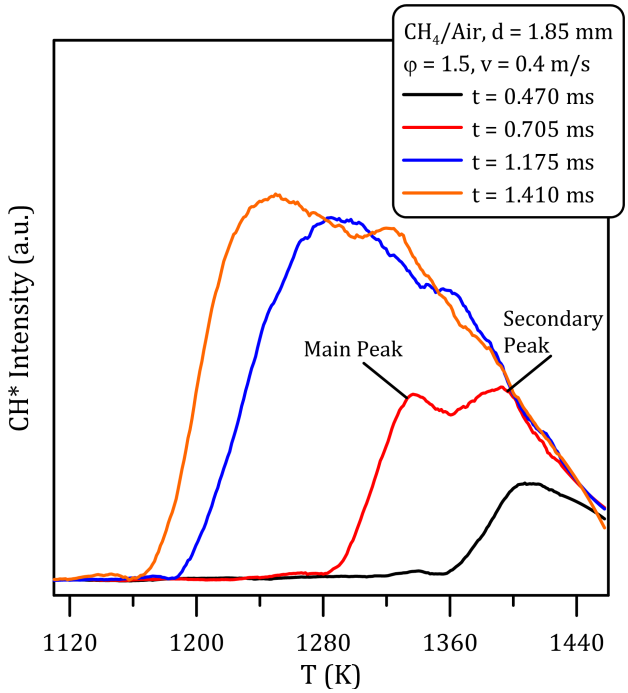

Figure 3.24: CH* signals at successive instants at v = 0.4 m/s and $\varphi = 1.5$.

The flame ignition (in black) occurs at 0.470 ms after the end of the previous FREI cycle. Then the flame propagates and at 0.705 ms (in red) two reactive peaks are visible. The main peak, at lower wall temperature, corresponds to the standard flame that keeps propagating upstream, whereas the second one is probably resulting from the combustion of unburned gases. In fact, at $\varphi = 1.5$ the time between the ignition and the extinction (τ_{EI}, Fig. 3.20) is small, while the flame moves on a large distance. This fast flame propagation may result in an incomplete combustion, leaving unburned species that are later further oxidized with a secondary formation of CH* radicals.
A similar behavior cannot be excluded for leaner mixtures, but is difficult to visualize because of the low luminosity of these methane/air flames.
To sum up, the conclusions derived for the stoichiometric mixture are confirmed by changing the equivalence ratio: at moderate mixture velocities (0.2 – 0.4 m/s) the flame extinction is caused by thermal quenching, while at lower inlet velocities the radical quenching becomes dominant. This means that the propagation of FREI flames is mainly driven by the fluid dynamic effects. The chemical effects are visible in the flame frequencies, as seen in Section 3.3.2.1, where the flame temperature and

flame speed play a crucial role. Furthermore, multiple CH^* peaks could be detected for the richest mixture at $\varphi = 1.5$.

3.3.3 Weak flame regime

Weak flames were observed for stoichiometric and fuel-rich mixtures, but because of experimental limitations (too small flow rate) they were not accessible in the lean side. The wall stabilization temperatures of the weak flames ($1 \leq \varphi \leq 1.5$) are displayed in Fig. 3.25 as a function of the equivalence ratio.
The velocity at which the flame switches from the FREI regime to the weak one depends on the equivalence ratio, and this velocity increases with the fuel mole fraction.

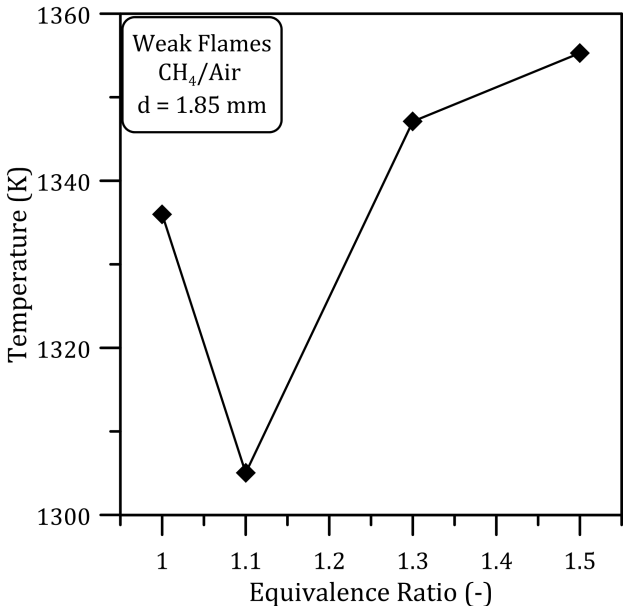

Figure 3.25: Weak flames obtained in the low velocity region varying the equivalence ratio

Tsuboi et al. [42], in their study on methane/air flames at micro-scale, suggested that the stabilization temperature of the weakest flame could be assumed as the minimum auto-ignition temperature. According to the conclusions of Tsuboi et al. [42], temperatures reported in Fig. 3.25 are therefore equivalent to AITs. For equivalence ratios 1.5, 1.3, 1.1, and 1.0, these temperatures are 1355, 1347, 1305, and 1336 K, respectively. The lowest stabilization temperature is thus observed at $\varphi = 1.1$.
As mentioned in Chapter 1, the lack of experimental data regarding the AITs makes arduous any comparison. Nevertheless, Robinson and Smith [98] and Naylor and Wheeler [99] have reported experimental measurements for methane/air mix-

tures, and more important, the dependence of the AIT with the equivalence ratio. Both groups found that the AIT was minimum for φ between 0.8 and 0.9. Ye et al. [100] used numerical simulations to access the AITs of methane/air mixtures ($0.2 \leq \varphi \leq 1.5$), and computed a negative dependence on the equivalence ratio: the higher the equivalence ratio, the lower the AIT.
In the present study, the lowest stabilization temperature is obtained at $\varphi = 1.1$. The location of this maximum is on the fuel-rich side, in disagreement with the conclusions of [98] and [99], while the overall trend is inconsistent with the computations of Ye et al. [100]. It is reasonable to assume that the stabilization temperatures measured in the micro-channel are affected by the flame temperature and heat release. Indeed, the minimum temperature is experimentally found for the flame with the highest adiabatic temperature. This most likely influence of the flame temperature on the weak flame regime significantly tempers the conclusions drawn by Tsuboi et al. [42] and questions the use of micro-channel devices to access the AIT. In any case, further studies with the present apparatus and flow controllers operating over smaller flow ranges are needed in order to explore the region of existence of the weak flames at very small inlet velocities and very fuel-lean conditions.

3.3.4 Transitional regimes

For the stoichiometric condition, two transitional regimes could be identified, namely oscillating FREI (between stable and FREI flames) and oscillating weak flame (between FREI and weak flames). The existence of these two regimes strongly depends on the equivalence ratio. For instance, the oscillating weak flame could not be observed for non-stoichiometric mixtures. Furthermore, the dynamics of oscillating FREIs in the rich and lean side is different of that observed previously for stoichiometric mixture (Fig. 3.12). As a reminder, at the stoichiometry the flame oscillates near the extinction location.
Figure 3.26 displays the time evolution of the spatially integrated CH^* signal for methane/air FREI flames at $\varphi = 0.5$.

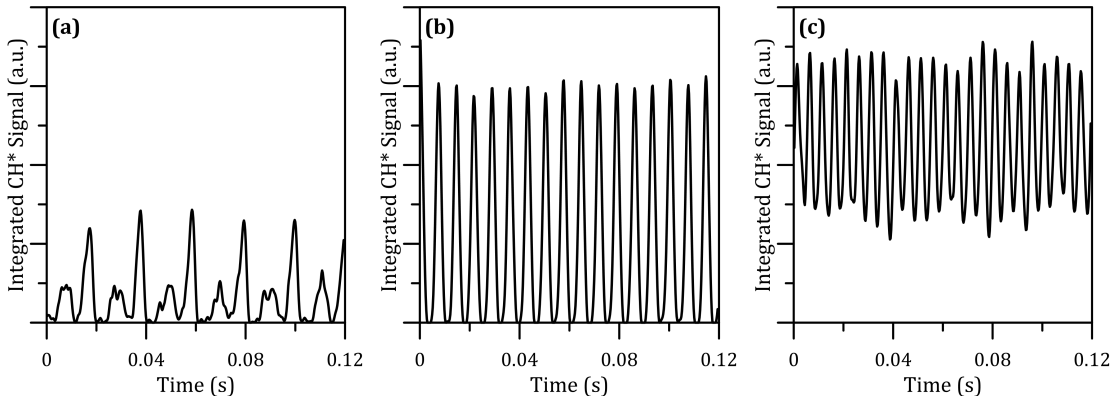

Figure 3.26: Temporal evolution of CH^* signal with inlet velocity at $\varphi = 0.5$: a) v = 0.1 m/s Fr = 48.6 Hz, b) v = 0.2 m/s Fr = 139.0 Hz, c) v = 0.3 m/s Fr = 201.0 Hz (Oscillating FREI).

At 0.1 m/s (Fig. 3.26a), the progression of the CH^* signal is similar to that displayed in Fig. 3.26b for a stoichiometric mixture with a low inlet velocity: there is a small flame (smaller peak) that provides the energy required to initiate the main flame (main peak). Then, increasing the velocity to 0.2 m/s (Fig. 3.26b), the CH^* signal is typical of a FREI flame (periodic oscillations) and the frequency increases. At 0.3 m/s (Fig. 3.26c) an oscillating FREI is observed before the transition to the stable flame regime. Unlike the stoichiometric case, the oscillations that could be observed before the flame extinction (Fig. 3.12d-e) are not present. The flame oscillates at a much higher frequency (201 Hz) and the CH^* signal never goes to zero. Such a pattern was computed by Miroshnichenko et al. [87] for rich H_2/O_2 flames: in the transition from the FREI to the stable flame regime, a diffusive-thermal regime of oscillation emerges. It corresponds to a diffusive-thermal instability, in which the radical concentration remains finite and oscillates around the average value corresponding to the stable flame. The same observations can be made for $\varphi = 0.7$ and 1.5; they are presented in Annex D.
The evolution of the oscillation frequencies as a function of the equivalence ratio and the inlet velocity are displayed in Fig. 3.27 for both normal (open symbols) and oscillating (closed symbols) FREI flames.

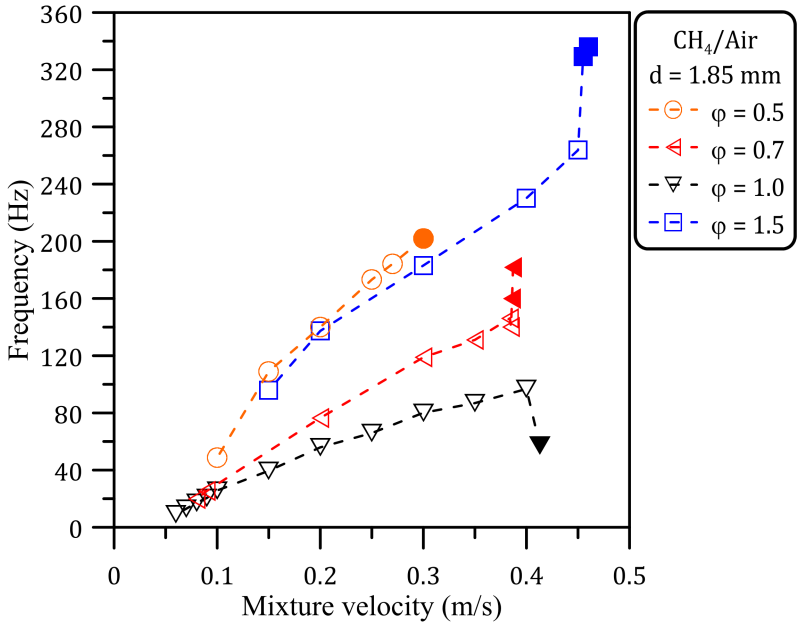

Figure 3.27: Frequency variation as a function of the inlet velocity. The oscillating FREI regime is represented by closed symbols at each equivalence ratio.

While at the stoichiometry the frequency drops down when switching from the normal FREI flame to the oscillating one because of the multiple oscillations before extinction, the opposite behavior is observed for the other equivalence ratios the frequency keeps increasing with the inlet velocity. This type of oscillating behavior has to be carefully considered in designing micro-combustors, as it can lead to hotspots.
It must be noticed that, despite our efforts, not oscillating flames could be detected for $\varphi = 0.9$, 1.1 and 1.3, probably due to the difficulty to detect the transitional regime: it is limited to a very small velocity region.

3.3.5 Summary

The existence diagram of the different flame regimes as a function of the equivalence ratio and the inlet velocity is displayed in Fig. 3.28.

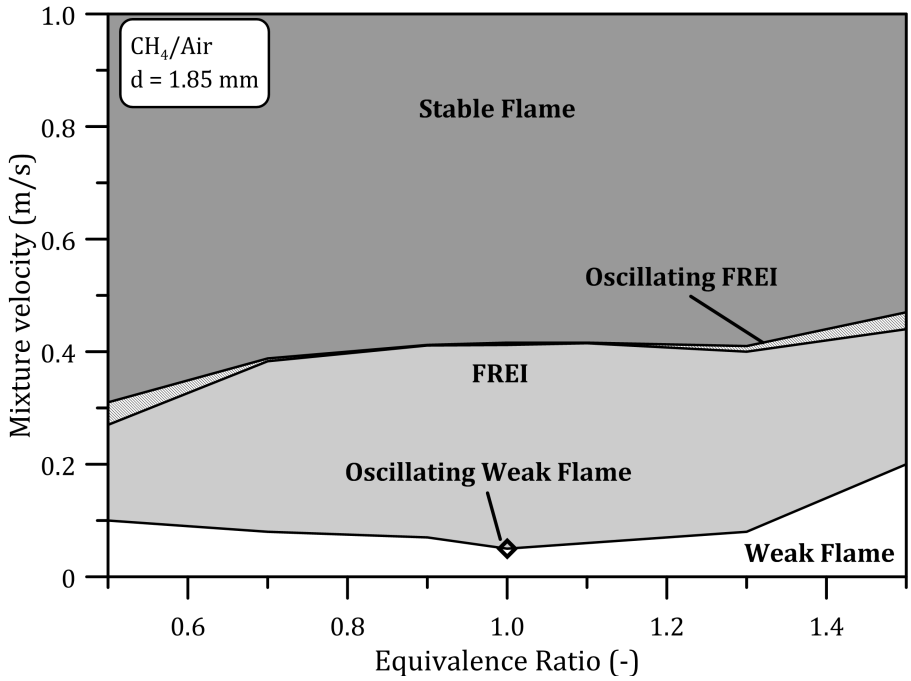

Figure 3.28: Map of different flame regimes with the equivalence ratio as a function of the inlet velocity.

At high velocity, stable flames are observed. These flames are strongly affected by the flame temperature and speed and the lowest wall stabilization temperatures are recorded near the stoichiometry, as detailed in Section 3.3.1.
Decreasing the inlet velocity, a transitional regime is observed before reaching the FREI region. It is spread on a very narrow velocity range. Between equivalence ratios 0.7 and 1.3, the transition occurs almost at the same inlet velocity (∼0.4 m/s). When further increasing or decreasing the equivalence ratio, the oscillating FREI regime appears at higher and lower inlet velocity, respectively, and is extended on a larger velocity range whereas the oscillation frequency increases. These flames are affected by thermo-diffusive instabilities, according to the conclusions of Miroshnichenko et al. [87]. These results do not match those obtained by Sànchez-Sanz et al. [97], in which the flame patterns are symmetrical with respect to the equivalence ratio and hence similar behavior are expected in the rich and lean side.
In the FREI regime, the lowest frequencies are recorded near the stoichiometry, for which the flames extinguish at lower temperature and the lowest St is observed.
The weak flame regime is associated with the low velocity region. These flames are hard to study due to the low flame brightness and to experimental limitations. Nevertheless, it was observed that the transition between this regime and the FREI one occurs at higher inlet velocity when increasing the equivalence ratio. The stability of the weak flames is most likely affected by the flame temperature, and thus may not stabilize at the auto-ignition temperature, in contradiction with the conclusions provided in [42].

3.4 Effect of the reactor diameter

Numerical computations by Norton and Vlachos [31] and Pizza et al. [93] suggested that the channel diameter has an influence on the flame stability. Therefore, we decided to experimentally investigate the effect of the reactor inner diameter on the flame dynamics, in order to get further insights into the coupling between the flame stability and the quenching mechanisms. An accurate knowledge of this coupling is fundamental for the design of micro scale reactors [31].
Based on the experimental determinations of the quenching diameter of methane air-mixtures [11, 12, 16], four micro-channels were employed, with inner diameters of 1.0 (blue), 1.85 (black), 2.15 (red) and 2.50 mm (green), while the external diameter was always 6 mm. The equivalence ratio was held constant and set equal to 1. The flame positions with respect to the inlet velocity and the channel diameter are reported in terms of wall temperature in Fig. 3.29.

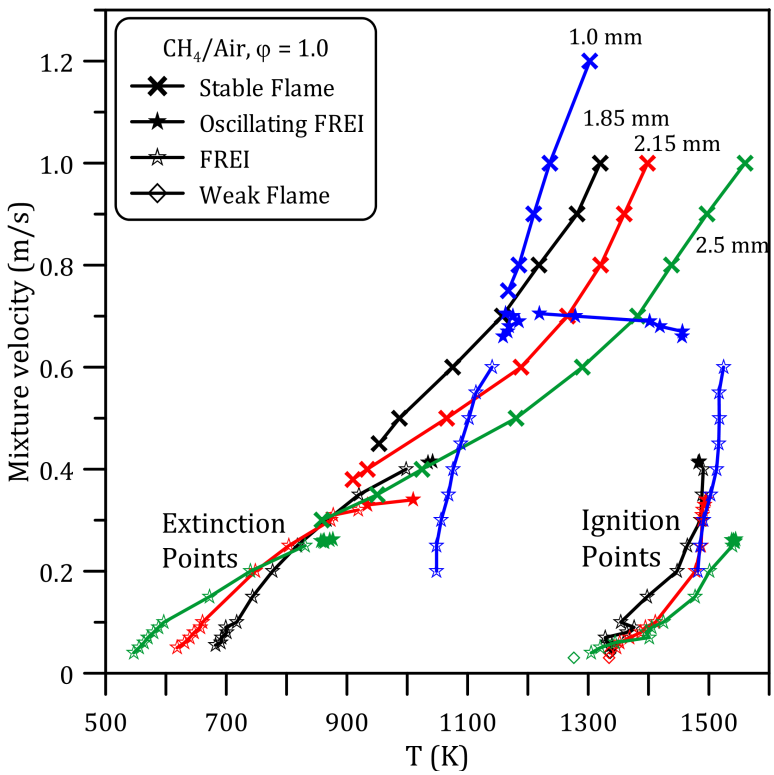

Figure 3.29: Diameter effect on the flame position, reported at the wall temperature. Blue: d = 1.0 mm, black: d = 1.85 mm, red: d = 2.15 mm, green: d = 2.50 mm.

Reducing the reactor diameter results in (a) different wall temperatures for flame stabilization or extinction and (b) transitions between the different regimes at higher inlet velocities. For instance, the transition between the stable and oscillating FREI flame regime occurs at v = 0.705 m/s for 1.0 mm i.d., while the velocity is only

0.262 m/s for the 2.5 mm i.d. channel. It was not possible to investigate the flame regime for inlet velocities below 0.2 m/s for d = 1.0 mm due to the extremely low flow rates required. However, for all other diameters, the transition from the FREI to the weak flame regime is effective for $0.03 \leq$ v (m/s) ≤ 0.05.

3.4.1 Stable flame regime

A change in the reactor diameter directly impacts the flame shape, as the Poiseuille field is enhanced for wider reactors. As shown in Fig. 3.30, at d = 1.0 mm the flames remain almost flat when changing the inlet velocity. Conversely, at d = 2.5 mm, the flame shape is strongly affected by the flow field switching from a convex to a concave shape as the flow rate decreases.

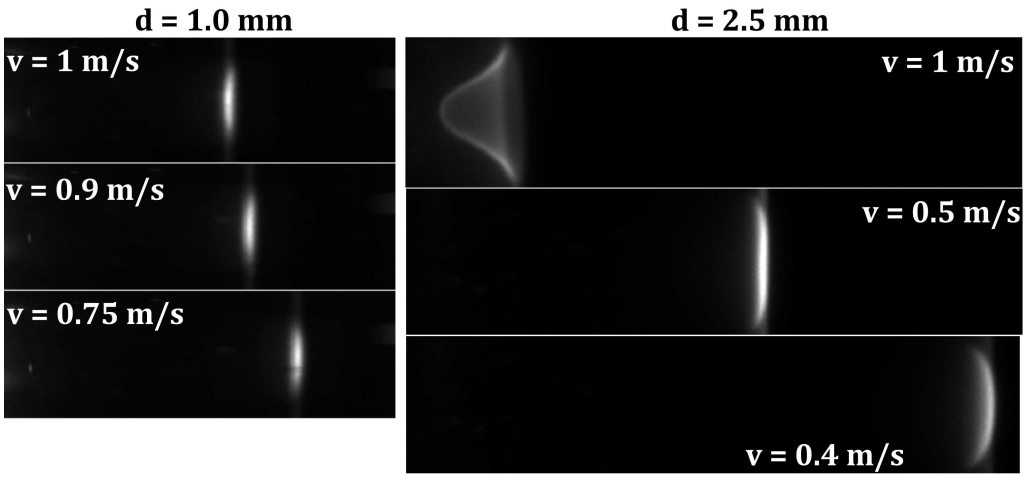

Figure 3.30: Images of stable flames at d = 1.0 and 2.5 mm.

Moreover, the stabilization temperatures at d = 1.0 mm do not change significantly with the inlet velocity (Fig. 3.29). A difference of only 69 K is measured between the first (v = 1.0 m/s) and last (v = 0.75 m/s) stable flames observed, while this difference is as high as 702 K for a diameter of 2.5 mm (velocity between 1.0 and 0.30 m/s). At the same time, the centerline temperature of the fresh gases is deeply affected by the reactor diameter, as illustrated in Fig. 3.31. For larger diameters the profile is shifted downstream, in other words in the flow direction, and the peak temperature is considerably lower.

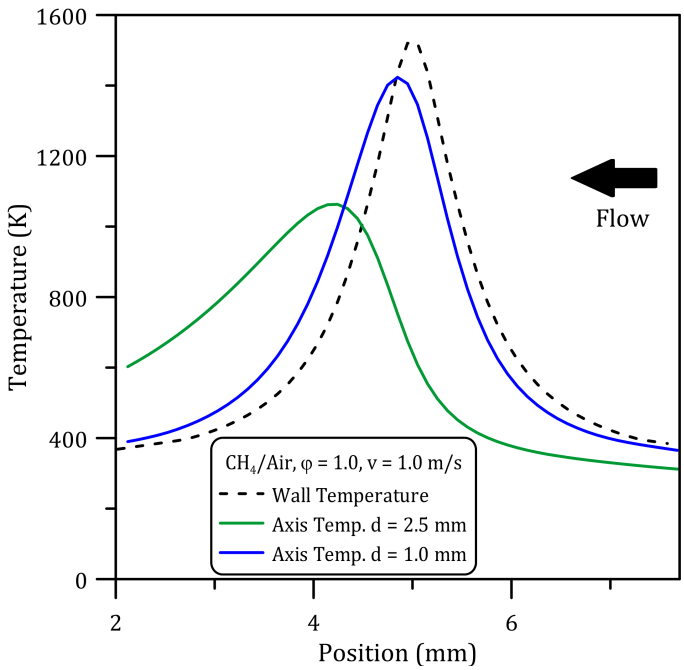

Figure 3.31: Centerline temperature for 1.0 and 2.5 mm internal reactor size at v = 1.0 m/s.

Plotting the stable flame positions as a function of the centerline temperature (Fig. 3.32) confirms that at d = 1.0 mm stabilization temperatures are almost independent of the inlet velocity, which can be explained by the flat flame shape and the weak effect of the flow field on the centerline temperature. Concerning the gas phase temperature, the temperature difference between the flames observed at 1.0 and 0.75 m/s falls down to 11 K (against 69 K with the wall temperature). Regarding the other reactors (d = 2.15 and 2.50 mm), the trends are in line with that obtained for d = 1.85 mm (Section 3.1.1), with the convex and concave stable flames stabilizing at almost similar temperatures. It can be seen in Fig. 3.32 that, regardless of the i.d., the flat flames stabilize at slightly higher temperature than the curved flames.

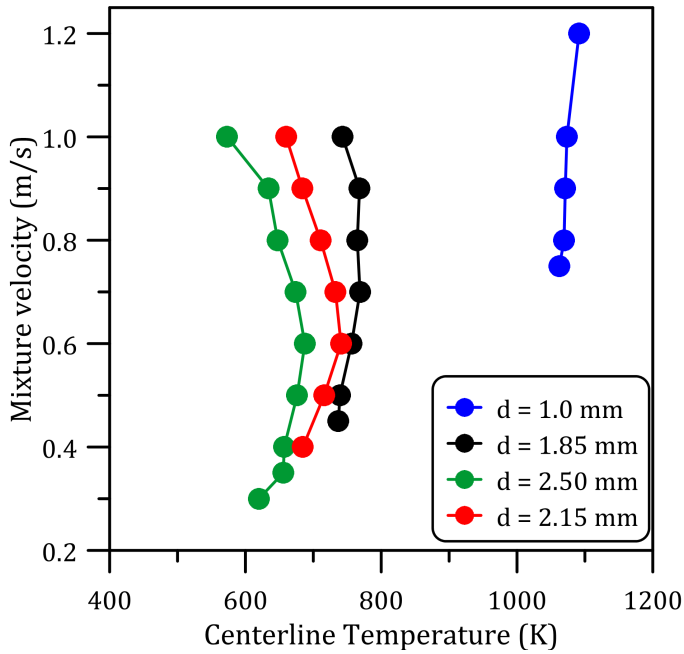

Figure 3.32: Flame positions plotted at the centerline temperature. Blue: d = 1 mm, black: d = 1.85 mm, red: d = 2.15 mm, green: d = 2.5 mm.

One can also notice in Fig. 3.32 that an increase in the reactor size results in flames stabilizing at lower centerline temperature, whereas the reverse is observed for the wall temperature. Indeed, a decrease in the channel width results in an increase of the net transverse heat transfer [101] while the flame-front area decreases. Meanwhile, the surface-to-volume ratio gets larger thus promoting the heat transfer to the wall. Then combustion becomes difficult and the flame front moves to a higher temperature to compensate the extra heat loss.
However, if the gap width is small enough, the radial gradients are negligible and the radical effects between the mixture and the wall are enhanced, as demonstrated in [64]. Indeed, the higher the wall temperature, the higher the fuel consumption rate and the flame-wall interactions. Popp and Baum [60] studied both experimentally and numerically the interaction between a hot wall and a flame, and found that the behavior of the reactive mixture changes at higher wall temperature, as the consequence of a rise of the concentration of light species like H and OH [61, 62]. The rise of those species contributes having higher flame temperatures, also called super-adiabatic flame temperatures [30, 31].
All these effects are crucial when designing very small micro reactors. The radical effects, exothermic and more intense for narrower micro-channel width, can stabilize the flame [65]. Nevertheless a thermal management is required to prevent the flame quenching: insulating materials, such as appropriately prepared ceramic, can be used [64].

3.4.2 FREI regime

Figure 3.29 shows that the ignition temperatures of FREI flames increase slightly with the reactor diameter. This is due to the flow field effects: as seen in Fig. 3.31 the inner reactor temperature is more affected by the flow field when the channel diameter increases. Thus, the mixture ignites further downstream to reach a sufficiently high temperature. The effect of the reactor diameter on the ignition points will be analysed through numerical simulations in Chapter 5.
For the sake of clarity, a zoom on the extinction points of the FREI flames is displayed in Fig. 3.33. One can notice that the slope of the inlet velocity versus the extinction temperature changes with the tube diameter. At d = 1 mm, the flames extinguish at higher temperature and this extinction temperature is nearly independent of the velocity, as indicated by the blue symbols. By increasing the reactor size, the slope decreases and for the same inlet velocity the extinction occurs at a lower temperature.

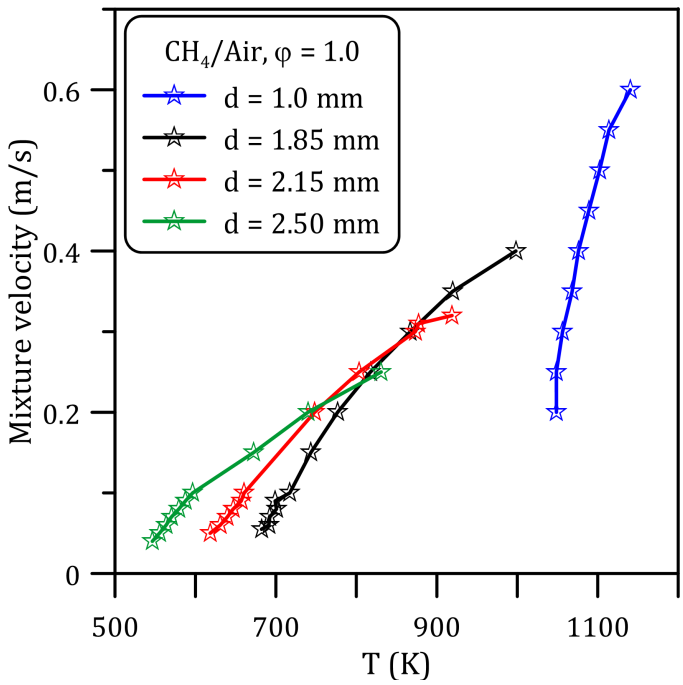

Figure 3.33: FREI extinction positions reported at the measured wall temperature changing the reactor inner diameter.

To understand and rationalize this behavior, a detailed analysis of the characteristic times is required.

3.4.2.1 Frequency and characteristic times

The time required to heat up and ignite the fresh mixture (τ_{EI}) is depicted in Fig. 3.34. For the 1.0 mm i.d. channel, this time is particularly short because of (i) the very efficient radial heat transfer between the wall and the gas due to the narrow section and (ii) the FREI are confined in a short section at very high temperature. Then τ_{EI} increases with the tube diameter. In the moderate velocity region ($v > 0.2$ m/s) the times measured do not change significantly with the channel diameter. In the low velocity region ($v < 0.2$ m/s), the opposite is observed: we measured shorter τ_{EI} as the diameter decreases. Indeed, for velocities slower than 0.2 m/s, the flame extinguishes at lower temperatures as the diameter increases while the ignition locations are pushed downstream, the fresh gases therefore have to travel over a longer distance and in a colder region of the channel: the time required to heat up the mixture increases. The progression does not change during the oscillating FREI regime, in which only τ_{IE} is affected, as shown below.

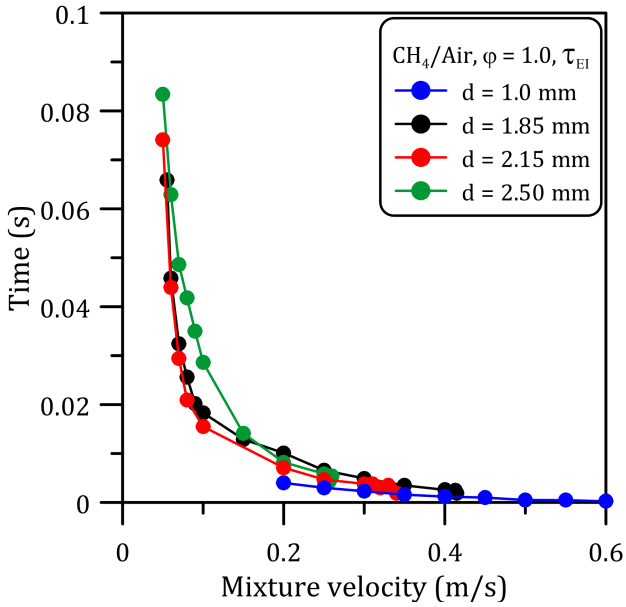

Figure 3.34: τ_{EI} obtained for stoichiometric mixtures changing the reactor inner size.

For velocities above ~0.2 m/s, the time given to the flame to propagate before it extinguishes (τ_{IE}, Fig. 3.35) decreases with the tube diameter. For the narrowest channel employed in this study, τ_{IE} is almost constant with the inlet velocity. The flames propagate over a shorter section and with a higher velocity because of the higher fresh gas temperature. Oscillating FREIs, characterized by multiple oscillations before extinction (closed symbols), are also observed for 1.85, 2.15, and 2.50 mm i.d.. In this regime, which is further analyzed in Section 3.4.4, τ_{IE} rapidly increases for inlet velocities below ~0.2 m/s, similarly to τ_{EI}, an inversion of the

trend is detected, τ_{IE} decreases with the reactor diameter for the reasons provided above. The flames extinguish at lower temperature and thus cover a longer distance, as observed in Fig. 3.33.

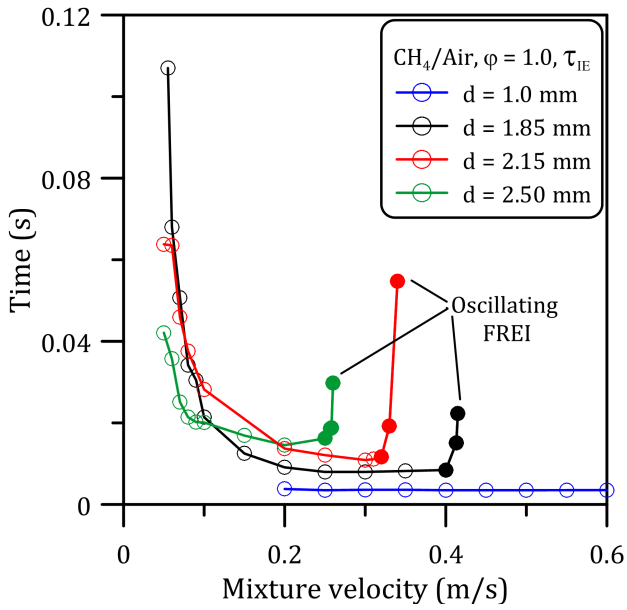

Figure 3.35: τ_{IE} obtained for stoichiometric mixtures changing the reactor inner size.

The frequencies associated with the FREI flames observed for four different micro-reactors are shown in Fig. 3.36.

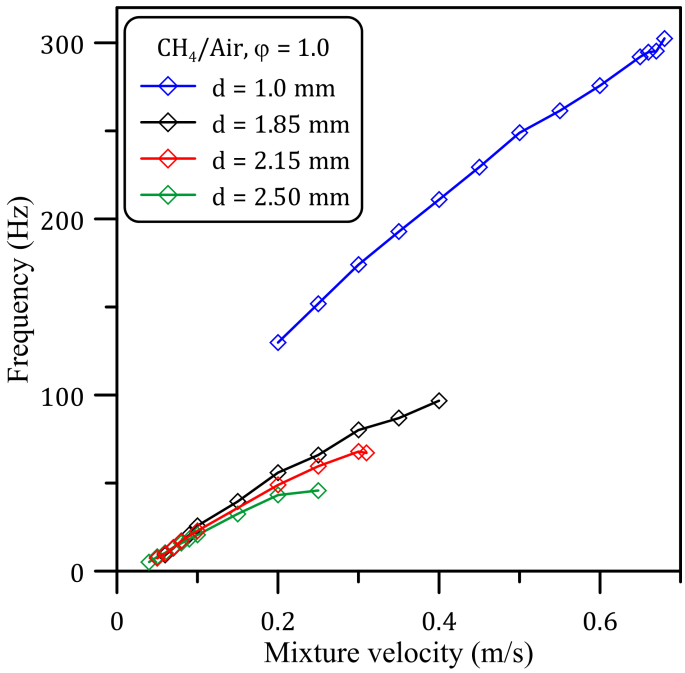

Figure 3.36: Frequencies obtained changing the reactor inner size.

As mentioned before, decreasing the reactor diameter promotes the transversal heat transfer which has a twofold effect: (i) the flame loses more heat and is thus quenched faster and (ii) the fresh gas temperature rises more quickly speeding up the flame propagation and promoting auto-ignition. Therefore, the characteristic times are shorter and the frequencies higher when the channel width increases.

3.4.2.2 Evolution of CH* intensity

As explained earlier, a reduction of the reactor inner diameter strongly affects the flame/wall interaction. The radical effects become dominant and can stabilize the flame due to exothermic recombination reactions [64, 87]. In order to further examine this aspect, the measured maximum CH* evolutions are reported in Fig. 3.37 for the inner diameters considered.
For the largest inner diameter (d = 2.50 mm, Fig. 3.37a), the presence of a sharp rise of the maximum CH* concentration is observed just before extinction for inlet velocity larger than 0.2 m/s. This behavior is similar to that already observed for d = 1.85 mm and discussed in Section 3.1.2.2. However, it is noteworthy that the build-up of the maximum CH* signal is less marked for d = 2.50 mm (Fig. 3.37a) than for d = 1.85 mm (Fig. 3.11). This is probably related to the increase of the flame-front area and the subsequent enhancement of the convection towards the fresh gases, thus avoiding an excessive temperature drop. On the other hand, in the low velocity region, the signal keeps smoothly increasing before the extinction and the

flames propagate further upstream, *i.e.*, to a colder region, compared to the other diameters. For the intermediate reactor diameter, d = 2.15 mm, (Fig. 3.37b) the CH^* traces are qualitatively similar to those at d = 2.50 and 1.85 mm (Fig. 3.11), suggesting the same underlying physical and chemical governing processes. At d = 1.0 mm (Fig. 3.37c), the results obtained are not similar to those observed before: only at high velocity (v > 0.5 m/s), sharp peaks, associated with the thermal quenching, are present before the extinction. For the other inlet velocities the thermal effects are not noticeable. Indeed, for this diameter even at high mixture velocity the radial gradients are negligible and the flames propagate in a high temperature region: it is reasonable to assume that the wall reactions are enhanced during the flame propagation. Only at very high inlet velocity the thermal effects are quite noticeable.

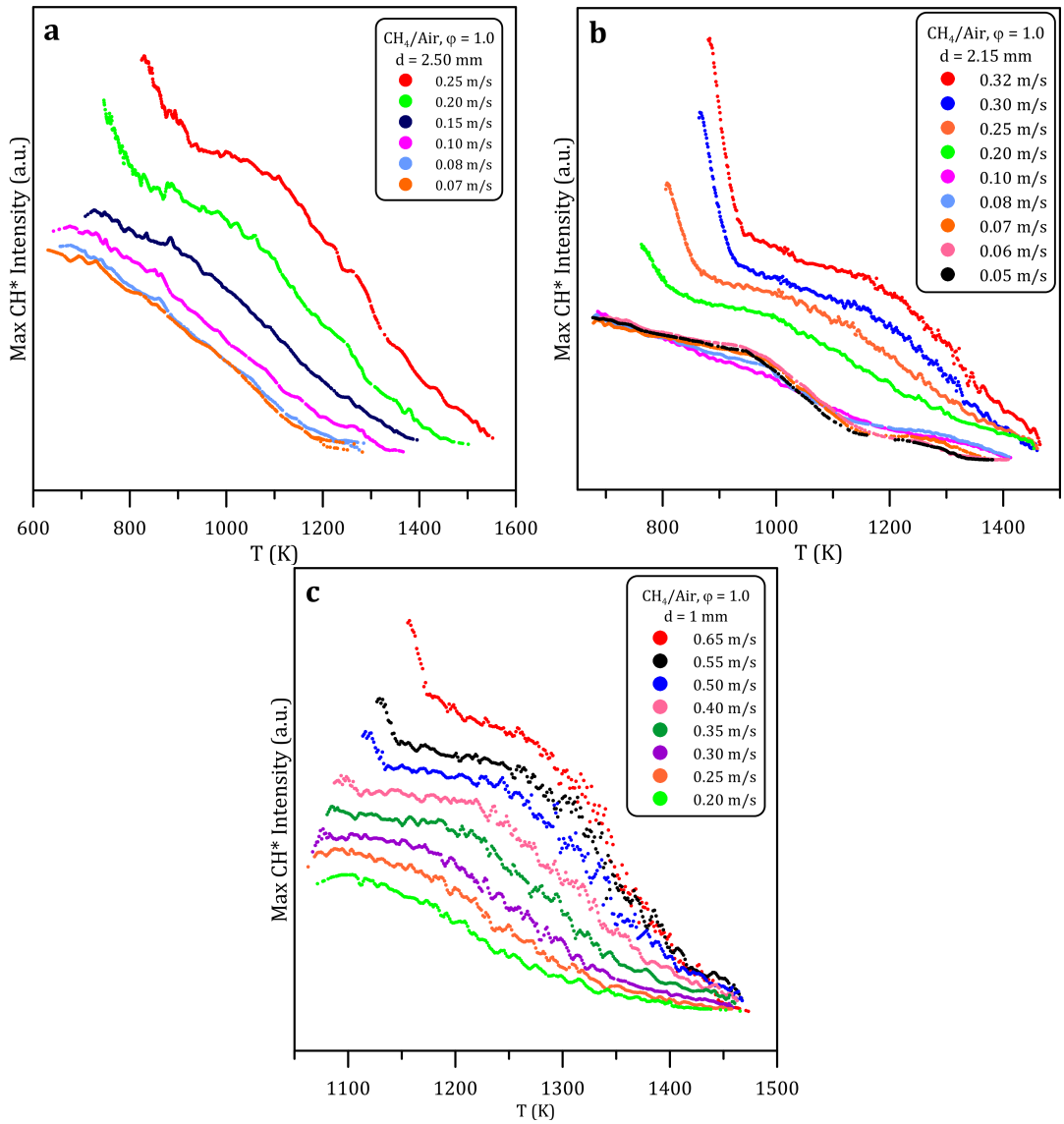

Figure 3.37: Maximum CH* progression in the FREI region for different inlet velocities and reactor inner diameters. a) 2.50 mm, b) 2.15 mm, c) 1.0 mm.

3.4.3 Weak flame regime

The stabilization temperatures of the weak flames are reported in Fig. 3.38 as a function of the channel inner diameter. Weak flames were not accessible with the narrowest channel because of experimental limitations. For all the other diameters investigated, weak flames were observed for velocities lower than 0.05 m/s.

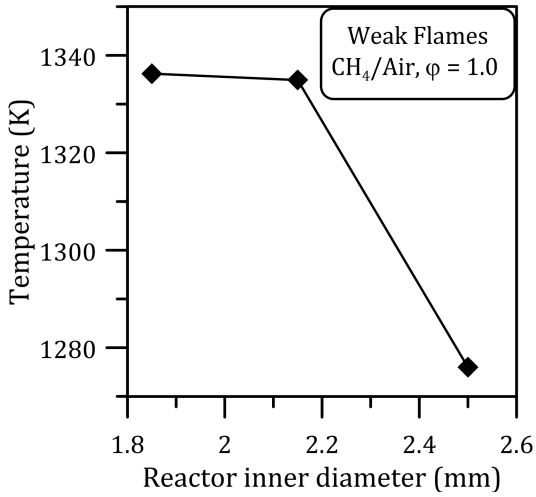

Figure 3.38: Stabilization temperatures of the weak flames as a function of the reactor inner diameter.

The stabilization temperature decreases with the reactor size, which is consistent with the experimental measurements of Affens [83] and Sechkin [84]. Indeed, as the volume of the vessel increases, they observed that the AIT decreases since heat losses are proportional to the surface-to-volume S/V ratio. Nonetheless, the conclusions drawn in Section 3.1.3 prevent any correlation between the weak flame stabilization temperatures and the minimum ignition temperature. In the present case, the stabilization temperature of the weak flames can only be related to the thermal effect: the heat losses decrease with the surface-to-volume ratio and less energy is therefore required to stabilize the flame.

3.4.4 Transitional regimes

As can be seen from Fig. 3.29, the transition between the stable or weak flame to the FREI regime occurs at higher inlet velocity when reducing the reactor inner diameter. This transition is characterized by the presence of oscillating FREI for all the configurations considered. Nevertheless, the oscillating behavior changes with the diameter. In order to illustrate and understand these different behaviors, the time progressions of the spatially integrated CH^* signal are reported below for the diameters 2.50, 2.15, and 1.0 mm and for different inlet velocities.
In Fig. 3.39 are displayed the signals for five flames, covering the transition from the initial oscillating weak flame to the oscillating FREI flames in 2.15 mm i.d.. In this configuration, the observations are similar to those already discussed for the 1.85 mm i.d. reactor (Section 3.1.4).

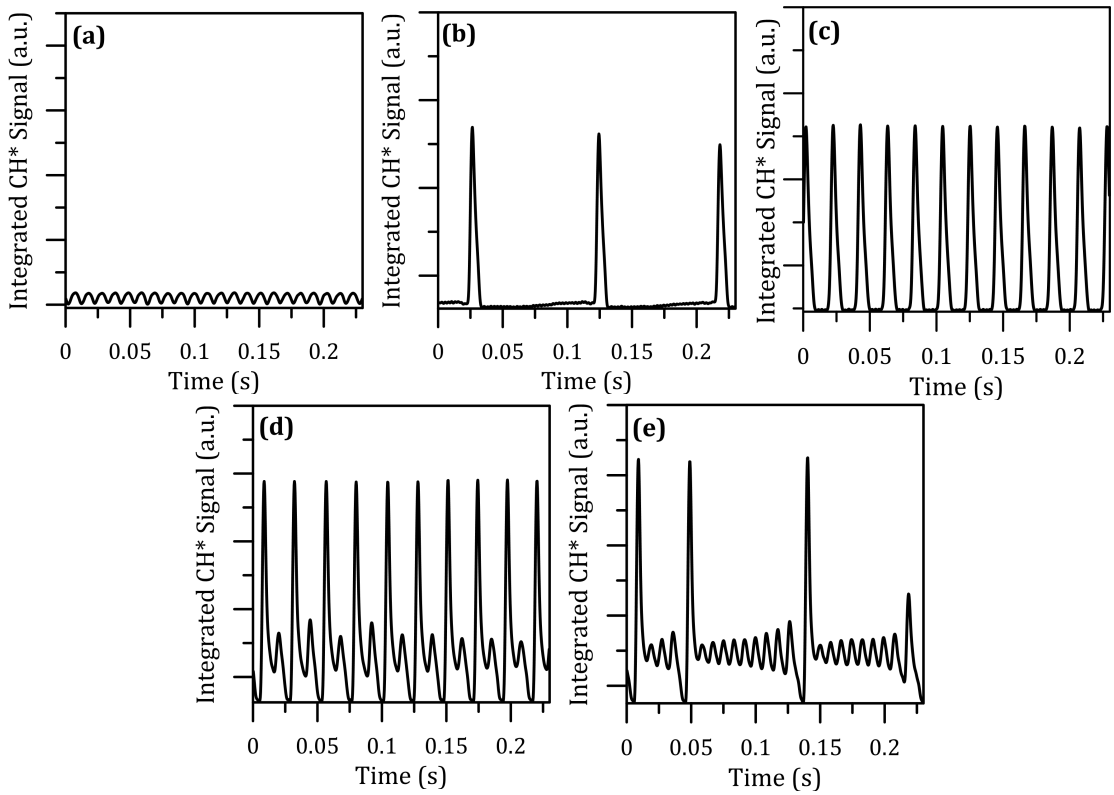

Figure 3.39: Temporal evolution of CH^* signal with inlet velocity for d = 2.15 mm: a) v = 0.04 m/s (oscillating weak flame) Fr = 97.0 Hz, b) v = 0.05 m/s (FREI) Fr = 7.2 Hz, c) v = 0.20 m/s (FREI) Fr = 48.9 Hz, d) v = 0.33 m/s (oscillating FREI) Fr = 43.2 Hz, e) v = 0.34 m/s (oscillating FREI).

At v = 0.04 m/s (Fig. 3.39a) an oscillating weak flame is present. It then switches to a FREI at 0.05 m/s (Fig. 3.39b). As observed for d = 1.85 mm (Fig. 3.12b), a pulsating weak flame oscillates slowly before the propagation of the main flame [64, 65]. At v = 0.2 m/s (Fig. 3.39c) a typical FREI is observed. Increasing further the inlet velocity leads to oscillating flames with regular (at v = 0.33 m/s, Fig. 3.39d) and irregular (at v = 0.34 m/s, Fig. 3.39e) oscillation patterns before reaching the stable flame region. As explained before, this periodic oscillatory behavior near extinction is probably the consequence of pressure waves associated with the fluid density variation [31].

Increasing the reactor inner diameter to 2.50 mm, the oscillating patterns presented in Fig. 3.40 are observed when changing the inlet velocity from 0.060 to 0.262 m/s. In the low velocity region the same flame patterns are observed.

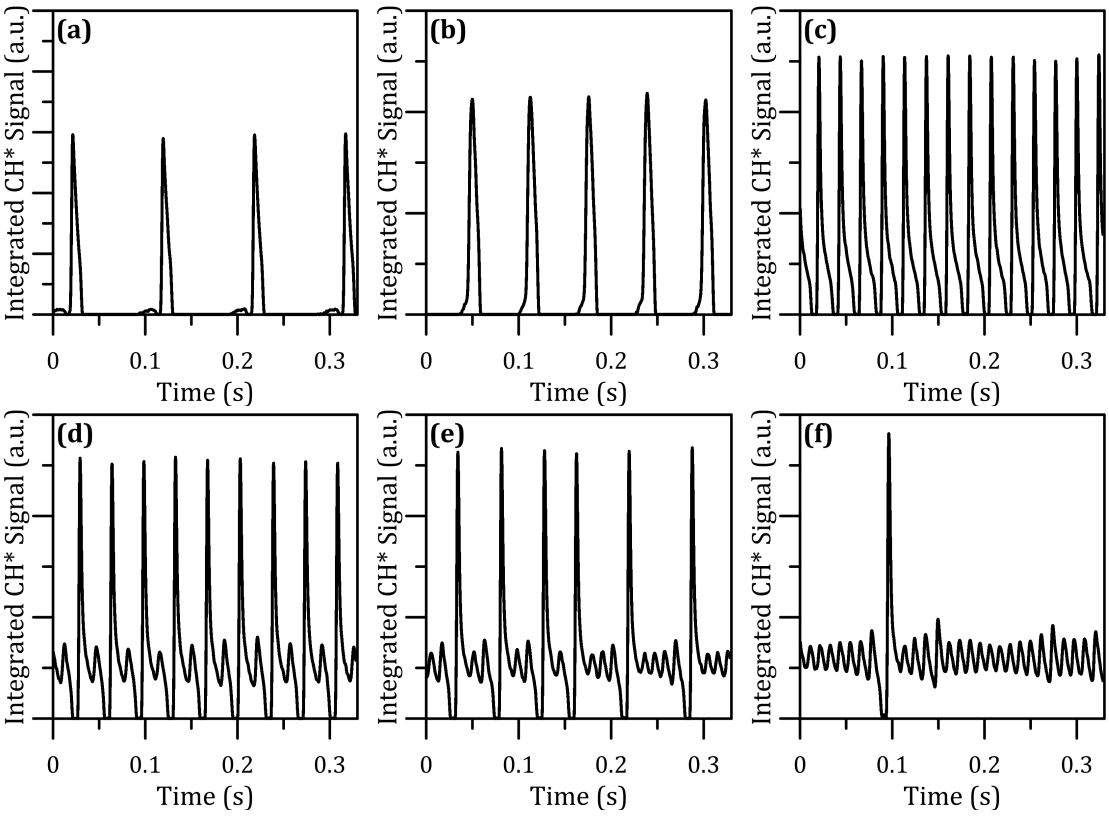

Figure 3.40: Temporal evolution of CH^* signal with inlet velocity for d = 2.50 mm: a) v = 0.06 m/s Fr = 10.4 Hz, b) v = 0.08 m/s Fr = 15.9 Hz, c) v = 0.20 m/s Fr = 43.2 Hz, d) v = 0.259 m/s (oscillating FREI) Fr = 29.4 Hz, e) v = 0.261 m/s (oscillating FREI), f) v = 0.262 m/s (oscillating FREI).

With such a high inner diameter, no oscillating weak flames were observed. However, a pulsating weak flame before the main flame propagation is observed at v = 0.06 m/s (Fig. 3.40a); it switches to a typical FREI at 0.08 m/s (Fig. 3.40b). By further increasing the inlet velocity to 0.20 m/s, the FREI frequency quickly rises and a particular behavior shows up: the extinction phase becomes longer (Fig. 3.40c). This is likely due to the larger flame front that enhances the convection through the fresh gases and thus resulting in a slower flame extinction. At v = 0.259 m/s (Fig. 3.40d) an oscillating FREI appears with a flame oscillation before extinction [31]. A similar flame, but with an irregular oscillation pattern, is observed at 0.261 m/s (Fig. 3.40e). By further increasing the incoming mixture speed, the flame oscillations become dominant: at v = 0.262 m/s (Fig. 3.40f) there is a large irregular number of second order peaks, that are probably due to the high power generated by the flame, then preventing an earlier extinction.

By further reducing the reactor inner diameter to d = 1.0 mm (Fig. 3.41), the flame behavior changes in the transition from weak flames to stable flame, and is more similar to what was observed for fuel-rich and fuel-lean mixtures, as discussed in

Section 3.3.4.

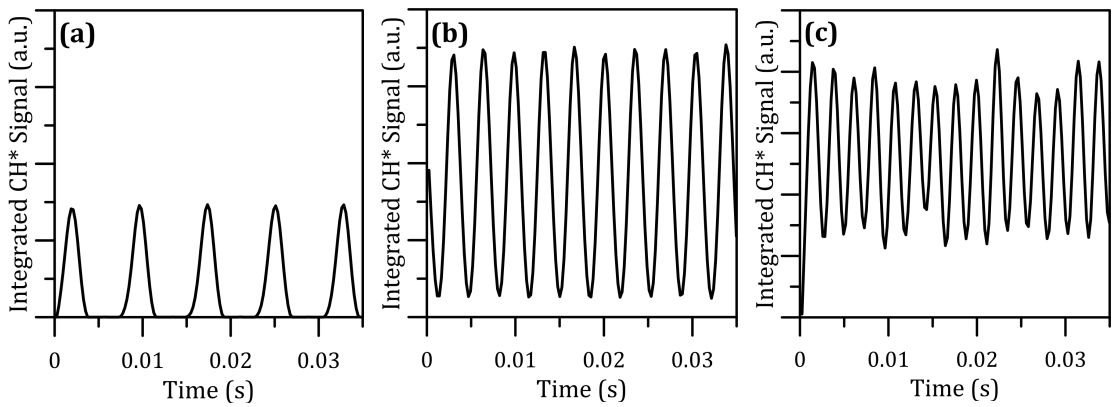

Figure 3.41: Temporal evolution of CH* signal with inlet velocity for d = 1.0 mm: a) v = 0.20 m/s Fr = 129.8 Hz, b) v = 0.65 m/s Fr = 292.1 Hz, c) v = 0.705 m/s Fr = 437.8 Hz (oscillating FREI).

As written before, the lowest inlet velocity accessible was 0.20 m/s. At this speed, a typical FREI, oscillating at high frequency (129.8 Hz), is observed (Fig. 3.41a). Then, with the increase of the inlet velocity, the FREI frequency also increases until v = 0.65 m/s (Fig. 3.41b). Under this condition, the flame oscillates at high frequency but never extinguishes. By keeping increasing the flow rate, the flame oscillates on narrower distances (see Fig. 3.29) while the frequency increases (437.8 Hz at v = 0.705 m/s, Fig. 3.41c). This peculiar behavior is due to diffusive-thermal oscillations, as suggested by the computations of Miroshnichenko et al. [87]. As observed by Jackson et al. [91], heat losses can lead to an oscillatory behavior even if the mixture employed has a unit Lewis number (*e.g.* stoichiometric methane/air mixtures).

The frequencies associated with the FREI and the oscillating weak flames and FREI are depicted in Fig. 3.42. The frequencies of the oscillating regimes are highlighted by the use of closed symbols.

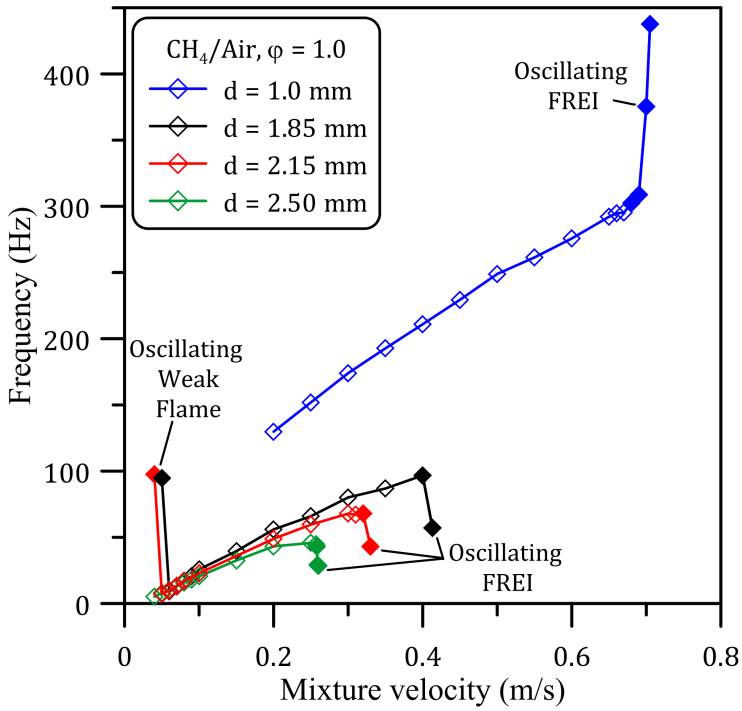

Figure 3.42: FREI frequencies as a function of the inlet velocity for different reactor inner diameters.

The frequency progression with the inlet velocity for the 1.0 mm inner diameter channel is very different from the three others. While a frequency drop due to flame oscillations just before the extinction is observed for the largest diameters when entering the FREI oscillating mode, a sharp rise is detected at d = 1.0 mm as a consequence of the diffusive-thermal instabilities. This means that in narrow reactors the instabilities observed between the main flame regimes may lead to a more unstable and unsafe combustion mode characterized by a flame oscillating at high frequency over a short distance.

3.4.5 Summary

A summary of all the observations made on the effect of the channel diameter enables drawing the velocity-channel diameter stabilization map of a stoichiometric methane/air flame in a micro-channel (Fig. 3.43). Different flame regimes were identified: stable flames, oscillating FREI, FREI, oscillating weak flames, and weak flames.

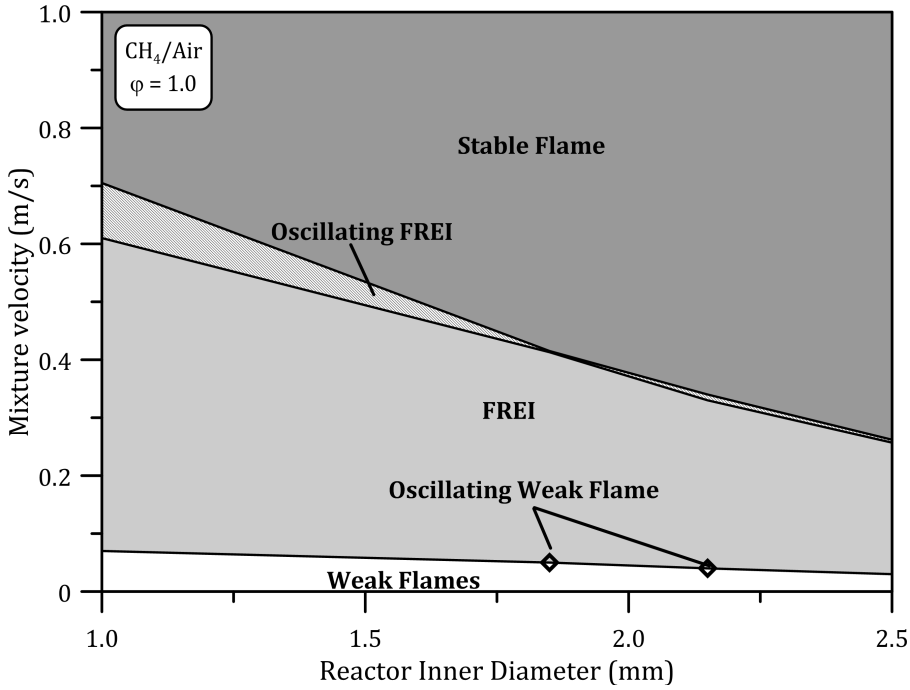

Figure 3.43: Map of different flame regimes with the reactor inner diameter as a function of the inlet velocity.

As the channel diameter is reduced the transition between the stable and the unstable regimes occurs for higher inlet velocities: 0.705 m/s for d = 1.0 mm against 0.262 m/s for d = 2.5 mm. These experimental values are in good agreement with the numerical predictions of Bianco et al. [34] using a 2D axial-symmetric model: 0.78 m/s and 0.30 m/s for d = 1.0 mm and 2.5 mm, respectively.
The transitional region between the stable flame and the FREI regimes spreads over a larger velocity range when the reactor diameter decreases. In narrow reactors, the oscillating flames have high frequencies and may induce thermal stress to the reactor wall. On the other hand, with large inner diameter reactors (1.85 – 2.50 mm), the oscillating flames are characterized by much lower frequencies and the presence of multiple oscillations before extinction. Even if this behavior may lead to the presence of hotspots, the smallest frequencies coupled to the limited velocity range of this transitional regime encourages the use of reactors with larger inner diameter. Furthermore, in these larger inner diameter reactors, the FREI frequencies are lower; the flames propagate over a longer distance because of a reduced heat transfer to the wall and an enhanced convection through the fresh gases.
Oscillating weak flames were observed only for d = 1.85 mm and 2.15 mm. The transition between the FREI and weak flame regimes occurs over a very small range of the flow rate and therefore it is hard to find such a regime experimentally. Therefore, more efforts should be devoted to study the weak flame region.

3.5 Conclusions

Experiments with methane/air mixtures were performed using the experimental set-up developed in this work and described in Chapter 2. The operating conditions were changed in order to study the effect of several parameters.
First, the effect of the inlet velocity was investigated. Our results are consistent with those obtained in previous experimental works [38] and confirm the existence of three main flame regimes, namely stable flames, FREI (flames with repetitive extinction and ignition) and weak flames. The stable flame region is the domain of the high inlet velocity and is strongly affected by the flow field: the higher the flow speed, the higher the heat losses. As a result, in this regime, all flames stabilize at different wall temperature, but the same centerline temperature. In the FREI regime, the wall temperatures of the ignition and extinction points also change according to the inlet velocity. At high flow rate, the conductive and convective time scales are reduced, thus leading to a late ignition and an early extinction due to thermal quenching (cold incoming mixture). On the other hand, at low speed, the heat exchange with the wall is enhanced, the temperature of the incoming mixtures rises and the flame ignites at lower wall temperature. In this case, the flame propagation and extinction are mainly driven by radical effects that are promoted by the high wall temperature. As a result, the oscillation frequency of the FREIs increases with the inlet velocity. The weak flames, characterized by a broad distribution of CH^* radicals, are difficult to observe because of their low luminosity and the low velocities required. However, a study was carried out to determine whether these flames can be associated to the AIT. The new experimental platform has also allowed visualizing transitional flames, namely oscillating FREI and oscillating weak flames, at the transition between the main regimes. The oscillating FREIs feature multiple oscillations before extinction, while the oscillating weak flames fluctuate at high frequency in the high temperature region. The study of such transient flames is crucial to prevent local overheating in micro-reactors.
Secondly, the influence of the equivalence ratio was investigated. In all regimes, the data demonstrated an indisputable dependence of the flame properties to the flame speed and temperature. Near stoichiometric flames, which have higher adiabatic temperature and laminar speed, stabilize or extinguish at lower temperature. Indeed, with the largest heat release, the convection through the fresh gas is enhanced, thus allowing the flames to further propagating or stabilizing downstream. Regarding the FREI regime, the recorded frequencies are particularly high for fuel-rich and fuel-lean mixture. Moreover, a new oscillating mode was detected between the FREI and stable flame regimes. These flames suffer from thermo-diffusive instabilities and thus fluctuate at very high frequency but never extinguish. Then, the observations at low inlet velocity confirmed the disconnection between the weak flames and AITs.
Finally, a study on the dependency of the flame stability to the micro-channel inner diameter was performed for stoichiometric methane/air mixtures. The results show

that the velocities at which the flame switches from one regime to another increases with the reduction of the reactor inner diameter, while the region of the unstable flames (FREI and oscillating FREI) is extended. Indeed, since the flame front area is proportional to the channel width, the net heat transfer is reduced when the channel is broadening, thus strengthening the flame that can propagate further downstream. Moreover, the frequencies associated with these transient flames decreases with the reactor inner diameter. Fluctuating inextinguishable flames, already observed in methane/air mixtures far from the stoichiometry, were confirmed in the narrowest reactor employed but at the stoichiometry. Albeit a unit Lewis number, thermo-diffusive instabilities can be induced by the high heat losses encountered in narrow channels.

To conclude, the use of excessively narrow channel reactors and/or mixtures with low energy content (fuel-lean and fuel-rich mixtures, which have low adiabatic temperature and laminar flame speed) facilitates the emergence of unstable flames that oscillate at very high frequency due to thermo-diffusive instabilities. Such conditions should be avoided in the development and operation of small-scale reactors.

Chapter 4

Experimental results: Ethylene/Air and Acetylene/Air

After successfully exploring the micro-combustion of methane/air mixtures, it was decided to probe different fuels. These fuels are ethylene (C_2H_4) and acetylene (C_2H_2) which were chosen because of their peculiar oxidation behavior and their relevance to the combustion of larger fuels.
Both ethylene and acetylene have smaller quenching diameters than methane [11, 12, 16], and therefore the diameter of the micro-channel was modified accordingly. The effects of the equivalence ratio and the inlet velocity on the flame behavior are investigated. As for methane flames, three main flame regimes are observed with respect to the flow rate: stable flame, FREI, weak flame. For very specific conditions, the presence of transitional regimes, such as oscillating FREI and oscillating weak flames, are also detected. Particular attention is paid to the combustion behavior of ultra-lean mixtures ($\varphi < 0.5$), which is possible because of the high chemiluminescence of C_2 hydrocarbons flames. The experimental results are used to draw stability maps. They are then discussed and compared with similar data already collected for methane.

4.1 Ethylene/air mixtures

Ethylene is the simplest alkene and a key intermediate in the oxidation of larger fuels. It plays a critical role in governing the kinetics of hydrocarbons combustion and heat release [109]. Based on quenching diameters of ethylene/air mixtures available in the literature (d = 1.25 mm, [11, 12, 16]), a micro-channel with an inner diameter of 1.0 mm is selected to conduct the experiments. First, the effect of the inlet velocity on a stoichiometric ethylene/air flame is studied, and the results are compared to

methane/air data in the same conditions. Then the effect of the equivalence ratio is investigated.

4.1.1 Effect of the inlet velocity

Figure 4.1 is a state mapping reporting the stabilization, ignition and extinction points of stoichiometric ethylene/air flames in a 1.0 mm internal diameter channel (in black). For comparison, similar data for a stoichiometric methane/air mixture in the same channel are also displayed (in red).

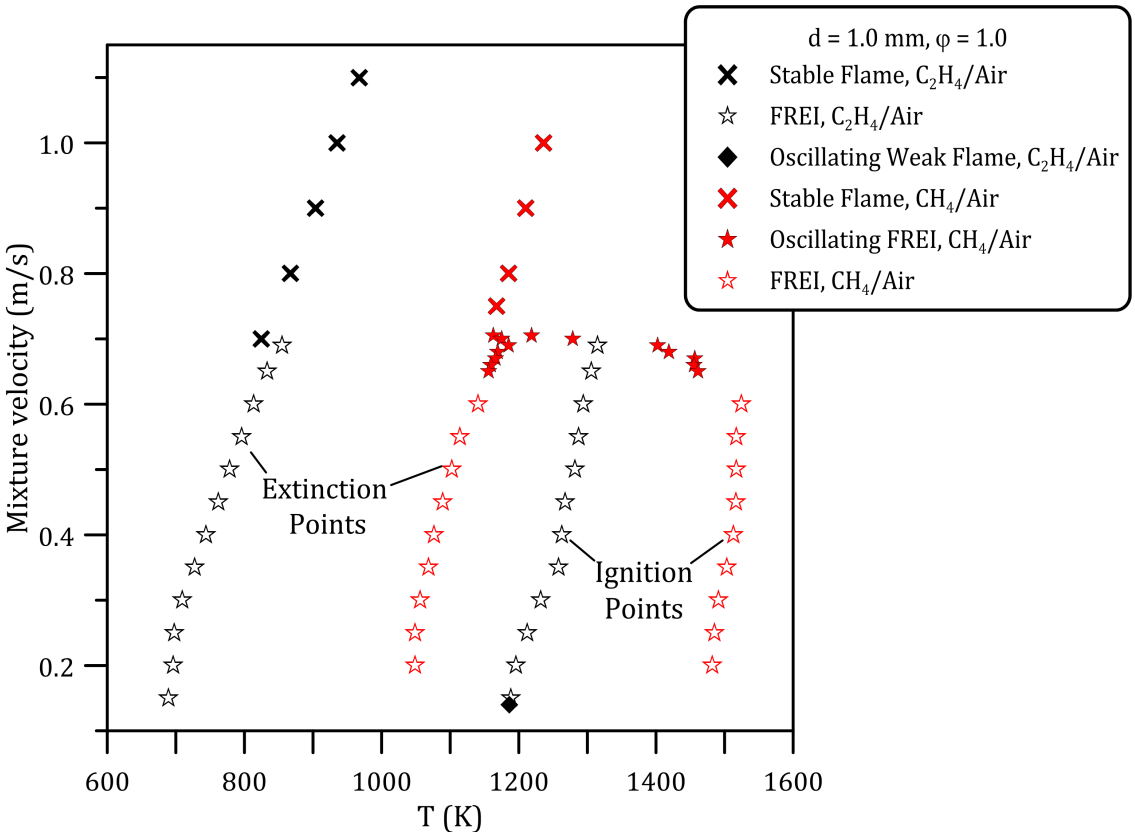

Figure 4.1: Flame position defined at the wall temperature as a function of the mixture flow velocity. Black = ethylene/air, red = methane/air mixtures.

Only three flame regimes are observed for ethylene: stable flames for velocities above 0.70 m/s, FREI for velocities in the 0.69 – 0.15 m/s range, and an oscillating weak flame for a velocity of 0.14 m/s. No flame was observed for lower inlet velocities. No oscillating flames were detected in the transition between the stable flame and the FREI regime, in contrast with the wide oscillating FREI region observed for methane (Chapter 3). Another major difference between the two fuels is the much lower wall temperatures (∼300 K lower) at which the ethylene/air flames stabilize,

ignite or extinguish.
All the stable flames exhibit a flat flame front, due to the small tube diameter, and, moreover, the wall stabilization temperature increases linearly with the inlet velocity. Although the stable flame regime is observed in the same velocity range for both fuels, wall stabilization temperatures are much lower for ethylene than for methane. This observation can be rationalized by looking at the adiabatic temperature and laminar flame speed of both fuels: they are both much higher in the case of ethylene [108] (∼2600 K and ∼60 cm/s for C_2H_4 and ∼2200 K and ∼36 cm/s for CH_4). This is thus possible for the flames to have the energy required to propagate over a longer distance and to anchor at a lower temperature.
The oscillating weak flame observed at 0.14 m/s has a low CH^* emission and pulses with very small amplitude (Fig. 4.2). This flame behavior is identical to that observed for a stoichiometric methane/air mixture flowing at 0.05 m/s in a 1.85 mm reactor diameter (Chapter 3). Radical recombination reactions at the wall are promoted by the locally high wall temperature but do not provide sufficient energy for the flame to propagate. Thus, the flame is trapped in a high temperature region. Although the ethylene oscillating weak flame is located at a wall temperature of 1190 K, about 150 K lower than methane (d = 1.85 mm), the oscillating frequency is much higher: 266.3 Hz versus 100.0 Hz. This large difference can be partially attributed to the higher reactivity of ethylene but also to the higher S/V ratio of the 1.0 mm inner diameter channel.

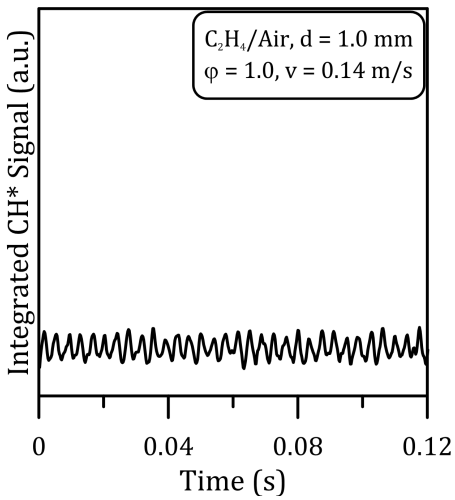

Figure 4.2: Oscillating weak flame observed at v = 0.14 m/s. Fr = 266.3 Hz.

The absence of weak flames for v < 0.14 m/s prevents any comparison with methane and confirms the impossibility to associate this regime to the AIT.
In contrast with the similar behavior between methane and ethylene regarding stable and oscillating weak flames, remarkable differences are observed in the FREI regime.

4.1.1.1 FREI regime

As already observed for the stable flame regime, the extinction and ignition points in the FREI region occur at lower wall temperature for ethylene/air flames than for methane/air flames (Fig. 4.1). While ethylene/air FREIs would be expected to oscillate faster than their methane counterparts (as witnessed for the oscillating weak flame) because of a higher flame temperature and speed, the frequencies are actually on an average 60% lower as it can be seen from Fig. 4.3. However, one can notice that the frequencies still increase with the inlet velocity, in line with previous observations.

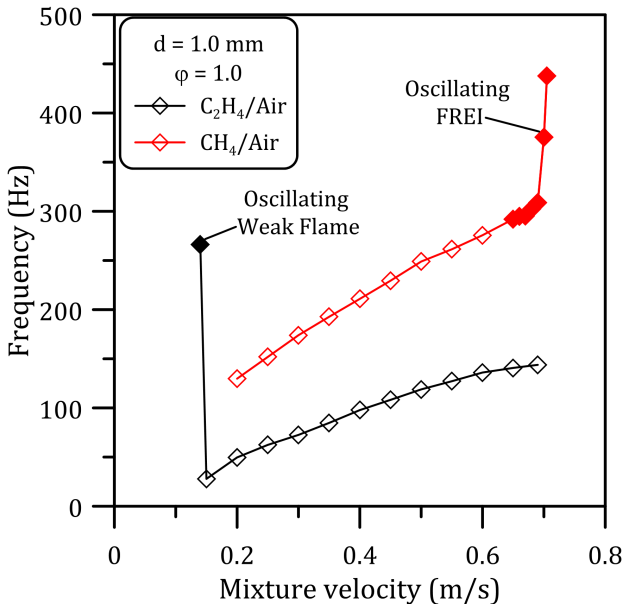

Figure 4.3: FREI frequency variation with the inlet velocity, d = 1.0 mm, $\varphi = 1$.

The lower frequencies of the ethylene/air flames can be explained by comparing the characteristic times obtained for the two fuels (Fig. 4.4).
The time between ignition and extinction, τ_{IE}, does not change significantly between the two fuels. Even if the ethylene flames have, for identical thermodynamic conditions, higher burning velocities than methane, both flames move in the microchannel at similar velocity because ethylene flames are located in colder regions (about 500 K lower): the lower the wall temperatures, the lower the temperature of the unburned gas, thus preventing a fast flame propagation (flame front inertia) [58, 73]. After extinction, the cooler wall temperatures encountered by the ethylene/air stream also affect the time required to heat up the fresh mixture to the auto-ignition point: τ_{EI} is on average 80% higher for the ethylene/air mixture than the methane/air one. Therefore, these larger ignition timings are the cause of the lower frequencies observed for ethylene in Fig. 4.3.

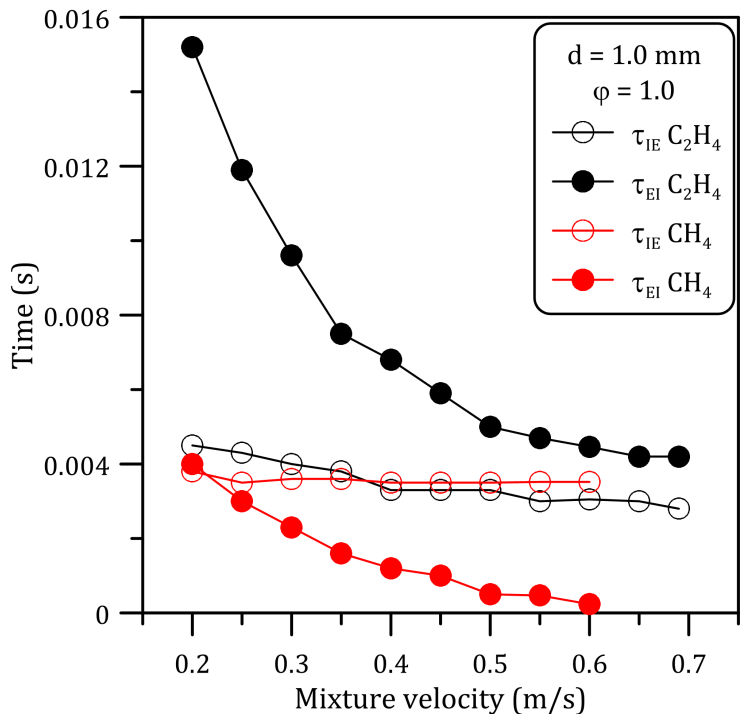

Figure 4.4: Comparison between τ_{EI} and τ_{IE} for 1.0 mm diameter tube.

Another important feature of ethylene FREIs is the presence of multiple CH* peaks. The strong chemiluminescence of ethylene flames allows a clear and unambiguous visualization of multiple peaks during the propagating phase. The formation of multiple reaction fronts has been predicted numerically [52–54, 94] for hydrogen and methane/air flames; it is due to the combustion of unburned/partially oxidized gases behind the main flame front. Figure 4.5 displays the evolution of the maximum of CH* intensity at high (v = 0.69 m/s) and low (v = 0.20 m/s) inlet velocities.

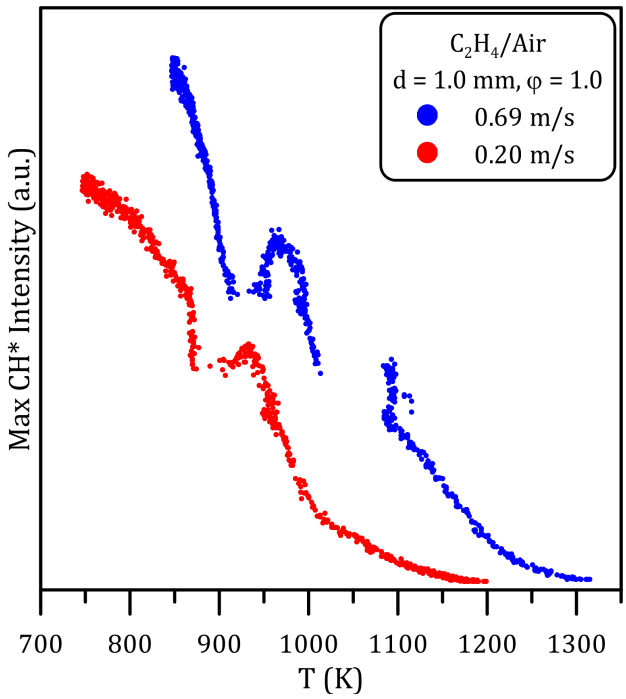

Figure 4.5: Maximum CH* progression for stoichiometric ethylene/air flames in the FREI region at high (v = 0.69 m/s) and low (v = 0.20 m/s) inlet velocity (d = 1.0 mm).

It is surprising to observe on Fig. 4.5 the presence of discontinuities in both CH* profiles. At v = 0.69 m/s a wide gap is present between 1100 and 1000 K. Then a peculiar behavior (decrease of the signal) is observed between 1000 and 950 K, followed by a new, yet narrower, gap between 950 and 910 K. For v = 0.20 m/s, similar characteristics, but less marked, are present: a short gap between 990 and 980 K, a local maximum at 930 K and another gap between 900 and 880 K. Stepping back and visualizing the spatially resolved CH* emission signal at different instants during the propagation phase, (Fig. 4.6 and Fig. 4.7), highlights the presence of multiple CH* peaks.

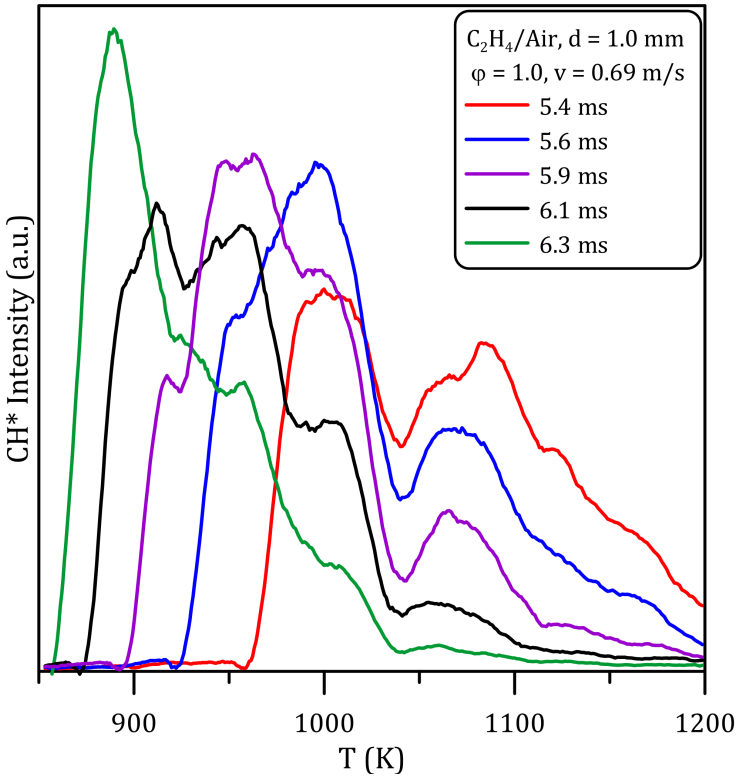

Figure 4.6: Spatially resolved CH* emission signals at successive instants during the propagation of a stoichiometric ethylene/air FREI at v = 0.69 m/s.

At v = 0.69 m/s (Fig. 4.6) the flame ignition occurs 4.2 ms after the end of the previous cycle (τ_{EI}). During the propagation, a first splitting occurs at 5.4 ms (in red) between 1000 and 1100 K. The brightest peak, centered around 1000 K, corresponds to the normal flame that keeps moving upstream, whereas the secondary peak around 1075 K is due to the oxidation of remaining unburned species. While the flame keeps moving forward, the flame brightness increases but the secondary peak intensity decreases, as noticed at 5.6 ms (in blue). Between 5.9 (in purple) and 6.1 ms (in black) a new splitting occurs between 950 – 1000 K and 910 – 950 K, resulting in four oxidation fronts. Then the main flame keeps propagating with higher CH* emission (in green), whereas the secondary peaks disappear.

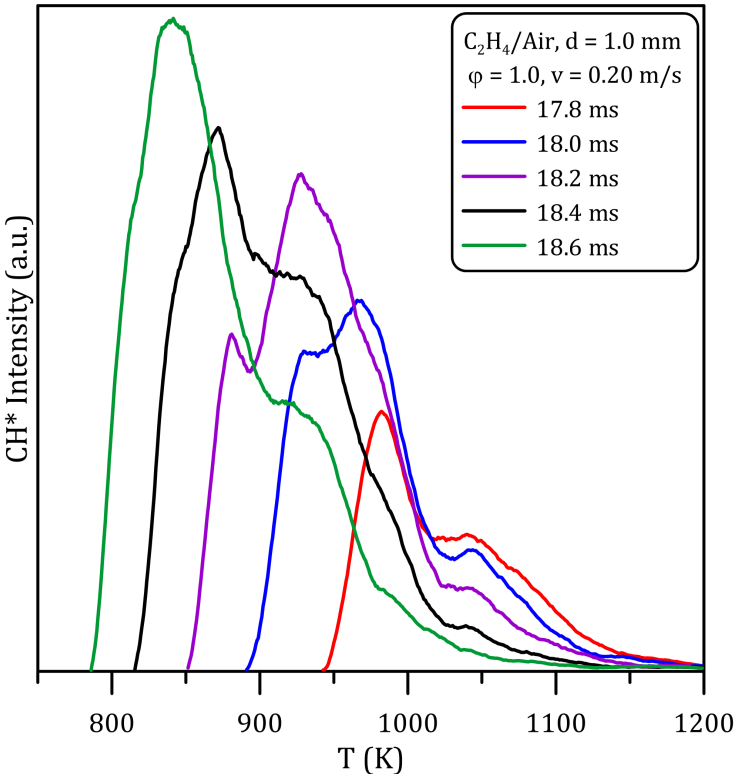

Figure 4.7: Spatially resolved CH* emission signals at successive instants during the propagation of a stoichiometric ethylene/air FREI at v = 0.20 m/s.

As mentioned above, auto-ignition is delayed at v = 0.20 m/s and the flame appears 15.2 ms after the end of the previous cycle. In the propagation phase, the first splitting takes place at 17.8 ms (in red) between 980 and 1030 K. A second splitting follows immediately after, at 18.0 ms (in blue) and 930 K. Meanwhile, the main flame brightness rapidly increases (at 18.2 and 18.4 ms, in purple and black) while the two secondary peaks extinguish (at 18.6 ms, in green).
Unlike methane/air flames, in which the maximum CH* progressions enabled us to distinguish the different quenching mechanisms, either thermal or radical (see Chapter 3), the existence of multiple CH* peaks in ethylene/air flames prevents the clear identification of sharp peaks, which would be the indication of a strong thermal quenching.

4.1.2 Effect of the equivalence ratio

In order to provide a micro-combustion stability map of ethylene/air flames, experiments were performed over an extended range of equivalence ratios (from 0.3 to 1.5). As usual, the three main flame regimes (stable flame, FREI and weak flame) were identified. However, under fuel-lean conditions (φ = 0.4 – 0.7) os-

cillating flames were observed between the different regimes. Moreover, ultra-lean ethylene/air flames ($\varphi = 0.3$) exhibit a unique behavior with the inlet velocity, and more details are provided in the next section.

4.1.2.1 Flames with equivalence ratio of 0.3

At such a low equivalence ratio all the ethylene/air flames present a very low luminosity, which is typical of weak flames. These flames stabilize at high temperatures, in a much warmer region than the stoichiometric stable flames. By decreasing the flow speed (down to v = 0.45 m/s), the wall stabilization temperatures are reduced along with the CH^* emission signal. Then for inlet velocities slower than 0.45 m/s, flames with low luminosity and high frequency oscillations are observed (Fig. 4.8): such flames are associated to the oscillating weak flames.

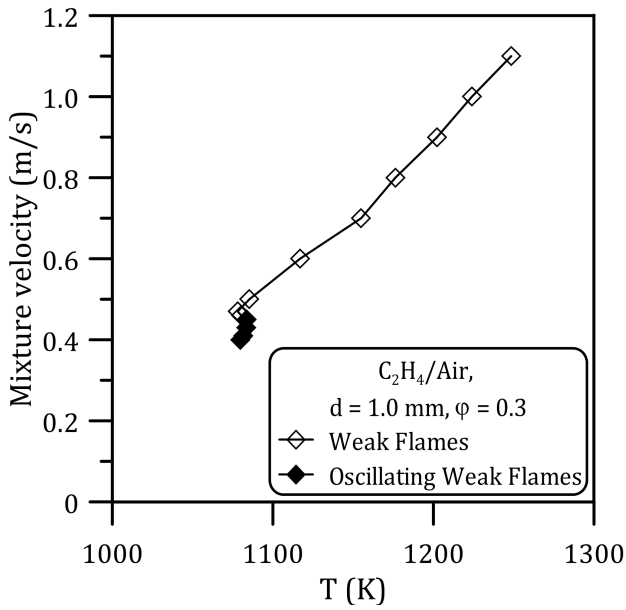

Figure 4.8: Ultra-lean ($\varphi = 0.3$) ethylene/air flame position as a function of the inlet velocity and wall temperature (d = 1.0 mm).

Figure 4.9 shows the frequency of these oscillating flames. They are very high but slightly decrease with the inlet velocity. An example of the time evolution of the spatially integrated CH^* signal for such a flame is displayed in Fig. 4.10. Although a single wall temperature is reported in Fig. 4.8, the oscillating weak flame actually moves around an average position. The amplitude of this motion is about 0.5 mm, which corresponds to a wall temperature difference of 40 K.

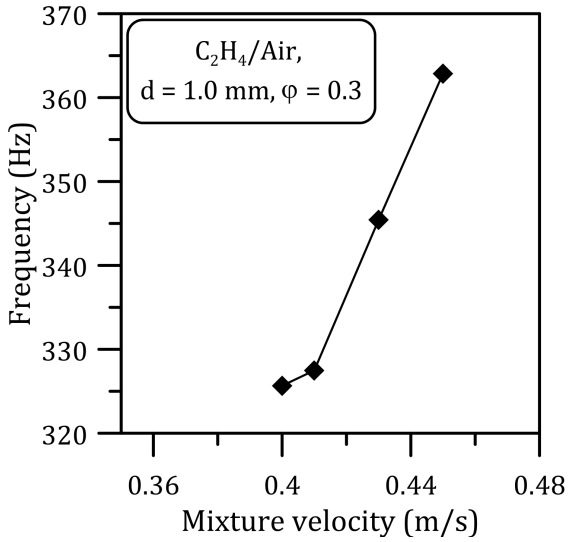

Figure 4.9: Frequencies of weak oscillating ethylene/air flames in ultra-lean conditions ($\varphi = 0.3$) and in a 1.0 mm i.d. micro-channel.

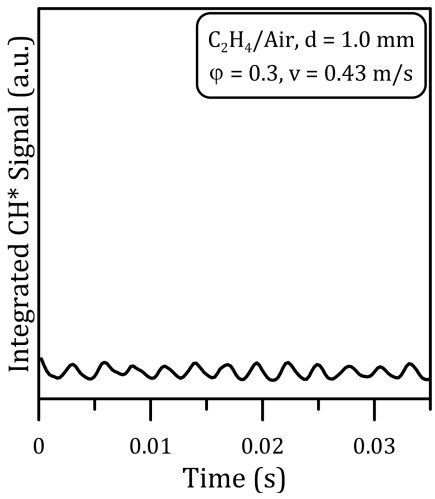

Figure 4.10: Temporal evolution of the CH* signal of ethylene/air oscillating weak flame (v = 0.43 m/s, $\varphi = 0.3$, Fr = 345.4 Hz).

As mentioned in Chapter 3, these unstable flames are comparable to FREI, but the initiation phase does not provide enough energy for the flame to propagate. In fact, the heat released by the reaction decreases with the inlet velocity, leading to a near blow-off configuration [31]. The flame front cannot travel upstream, but instead is locked in a high temperature zone where enhanced exothermic reactions at the wall sustain it [58, 65]. During the pulsations, the radical concentration fluctuates whereas the radical pool is totally depleted before re-ignition for a typical FREI [87].

The present data confirm the usefulness of the present experimental platform for

investigating combustion in ultra-lean conditions, and even below the flammability limits (0.4 – 8.0 for ethylene). Indeed, as highlighted by Aghalayam [65], the strong coupling between the flame and the wall can have a net stabilizing influence on weak flames.

4.1.2.2 Overview and Stable Flames

Figure 4.11 shows the evolution and the stabilization temperatures of ethylene/air flames as a function of the equivalence ratio (within 0.3 and 1.5) and inlet velocity. In line with the observations for methane, the stable flames settle at lower temperatures as the flow rate decreases. In the FREI regime, the mixture auto-ignites at high temperature ($> 1100\,\mathrm{K}$) and the flame then propagates upstream until extinction. Unlike the extinction locations, the ignition points are slightly affected by the equivalence ratio, except for very fuel-lean mixtures ($\varphi \leq 0.7$) for which the luminosity is particularly low. Weak flames are observed exclusively for the fuel-richest composition ($\varphi = 1.5$) while oscillating weak flames are observed only at $\varphi = 0.9$ and 1.0. Finally, oscillating FREIs are detected at $\varphi = 0.4$, at the interface between stable flames and FREIs. These oscillating flames and their behavior are thoroughly examined in the Section 4.1.2.3.

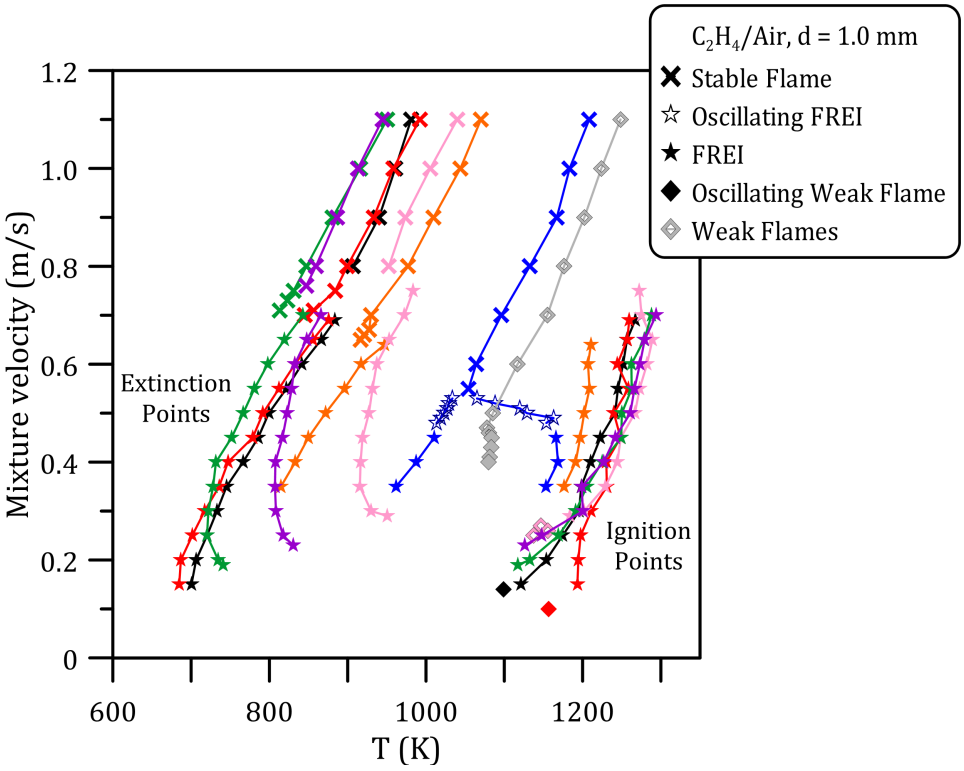

Figure 4.11: Ethylene/air flame position defined at the wall temperature as a function of the inlet mixture velocity for different equivalence ratios: 0.3 (grey), 0.4 (blue), 0.7 (orange), 0.9 (red), 1 (black), 1.1 (green), 1.3 (purple), 1.5 (pink).

Stable ethylene/air flames have similar characteristics than the corresponding methane/air flames (Chapter 3). They stabilize at higher wall temperature when the inlet velocity increases, but centerline stabilization temperatures do not change significantly for the reasons exposed in Chapter 3. Heat transfer efficiency from the wall to the gas is inversely proportional to the stream velocity: for high flow rates, the temperature of the fresh gases remains low and the incoming mixture must travel to a warmer channel section to enable flame ignition and anchoring. Conversely, at low velocities the centerline temperature rises much faster and the conditions for the flame stabilization are achieved further upstream.
Regarding the influence of the composition, the lowest stabilization temperatures are for fuel-rich mixtures, and more specifically at $\varphi = 1.1$ and 1.3. This equivalence ratio range corresponds to the maximum adiabatic temperature and laminar flame speed of ethylene/air mixtures [108]. Unlike methane/air flames, reporting the wall stabilization temperatures normalized by the adiabatic flame temperatures (T_{ad}/T) as a function of the laminar flame speed over the unburned gases velocity (S_l/v_{unb}) is not sufficient to fairly compare all the different flames. Indeed, the effect of the fuel diffusivity must be considered and is accounted for through the calculation of the reduced Lewis number, computed at the centerline stabilization temperature (Eq. 4.1).

$$Le = \frac{\alpha}{D} \tag{4.1}$$

where α is the thermal diffusivity [m^2 s^{-1}], computed at the flame stabilization temperature (Eq. 4.2):

$$\alpha = \frac{k}{\rho \times c_p} \tag{4.2}$$

and D is the mass diffusivity [m^2 s^{-1}] of the limiting reactant (l) in the specie j (Eq. 4.3):

$$D_{l \to mix} = \frac{\sum_{j \neq l}^{N} X_j \times M_j}{W \times \sum_{j \neq l}^{N} X_j / D_{lj}} \tag{4.3}$$

Where k, ρ and c_p are respectively the thermal conductivity [W m^{-1} K^{-1}], the density [kg m^{-3}], and the heat capacity at constant pressure [J kg^{-1} K^{-1}], W, X, M, N are the molecular weight [kg mol^{-1}], the mole fraction, the molar mass [kg mol^{-1}] and the number of species, respectively.
The effect of diffusivity is introduced in the normalized velocity term S_l/v_{unb}, and the resulting term is plotted as a function of the normalized adiabatic temperature in Fig. 4.12 for ethylene/air mixtures and methane/air mixtures. Laminar burning velocities, adiabatic flame temperatures, and thermal and mass diffusivities were calculated with the model of Xu and Konnov [108].

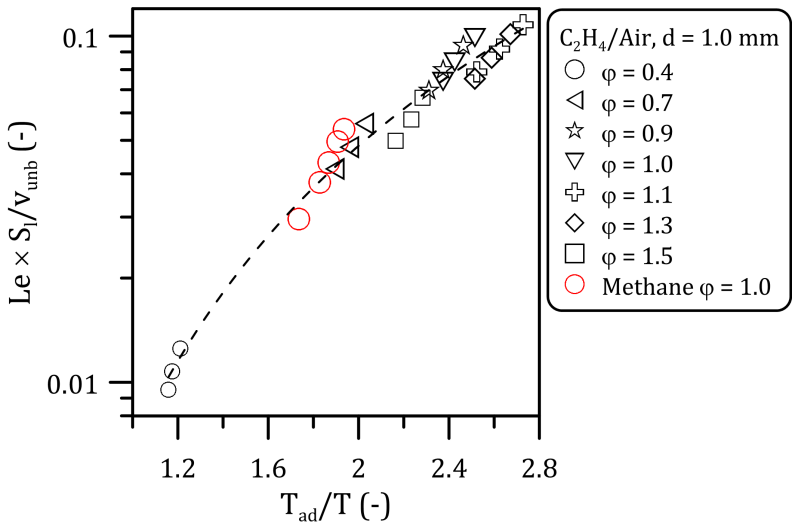

Figure 4.12: Correlation between T_{ad}/T and S_l/v_{unb} for ethylene/air mixtures.

The fuel-lean data are located in the region of low T_{ad}/T while mixtures with the highest energy content and thus flame speed, *i.e.* $T_{ad}/T = 1.1$ and 1.3, stabilize at high T_{ad}/T. As already observed for methane/air mixtures, a strong correlation is observed between the two normalized quantities, confirming the existence of a relation between the stabilization temperature, the adiabatic temperature and the laminar flame speed. The methane/air data points at $T_{ad}/T = 1.0$ are located near the ethylene/air data at $T_{ad}/T = 0.7$. For such equivalence ratios, the laminar burning velocities are comparable (36.47 cm/s for C_2H_4, 36.55 cm/s for CH_4) while the adiabatic flame temperature is higher for CH_4 (2260 vs. 1978 K for C_2H_4). But, as observed previously, the methane/air stable flames stabilize at wall temperatures ~300 K higher compared to ethylene. Thus, the data are located in the same region but the methane/air flames are set at a slightly lower T_{ad}/T.

4.1.2.3 FREI and oscillating flames

In Section 4.1.1.1 the time evolution of the CH^* signal during the propagation of stoichiometric ethylene/air FREIs has been investigated and multiple peaks were detected as a result of remaining unburned species behind the flame front. Similar CH^* progressions are reported at high (v = 0.60 m/s, Fig. 4.13a) and low (v = 0.30 m/s, Fig. 4.13b) inlet velocity for different equivalence ratios. The results obtained at $\varphi = 0.4$ are not presented, due to the low signal-to noise ratio, making difficult to unambiguously identify the multiple CH^* peaks. Moreover, as already mentioned for methane/air flames, the EM gain of the camera is adjusted for each mixture composition. Therefore the comparisons in Fig. 4.13 only support a qualitative discussion.

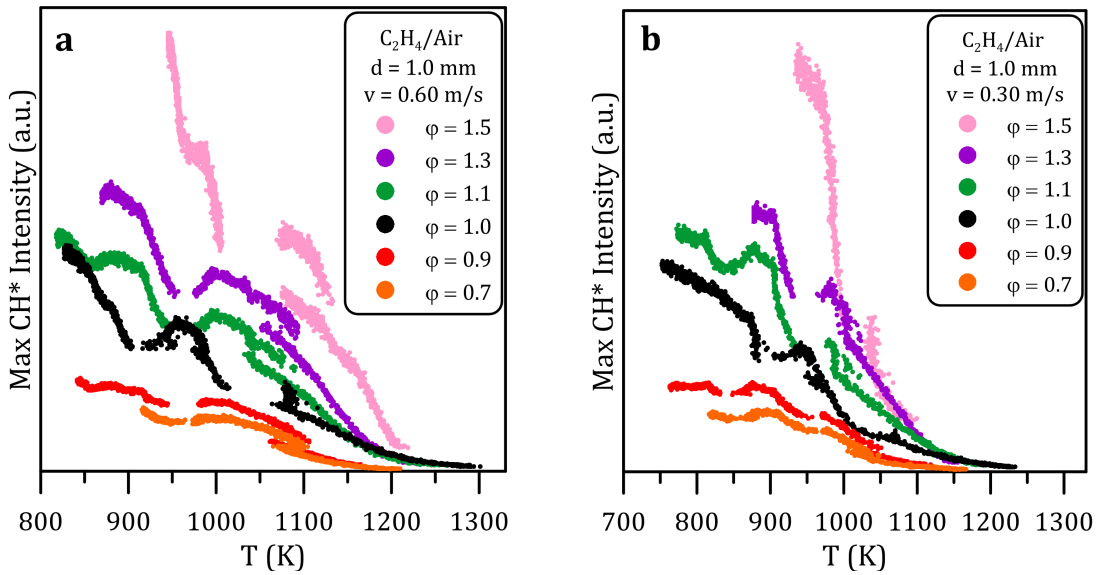

Figure 4.13: Maximum CH* progression with the equivalence ratio at a) high and b) low inlet velocity.

The discontinuities are present for all equivalence ratios, thus confirming that the multiple splitting is not specific to stoichiometric mixtures (Fig. 4.6 and Fig. 4.7), but is a more general feature of ethylene/air FREIs regardless of the equivalence ratio and the flow velocity. Spatially resolved CH* signal snapshots are given in the Annex E for each equivalence ratio.
Figure 4.14 shows the frequencies of the ethylene/air FREIs and oscillating flames. For sake of comparison, the frequencies for the stoichiometric methane/air flames in the 1.0 mm i.d. reactor are also displayed. The lowest frequencies are recorded at φ between 0.9 and 1.1, while the highest are in fuel-rich or to fuel-lean conditions. The frequency peaks correspond to the oscillating flames.

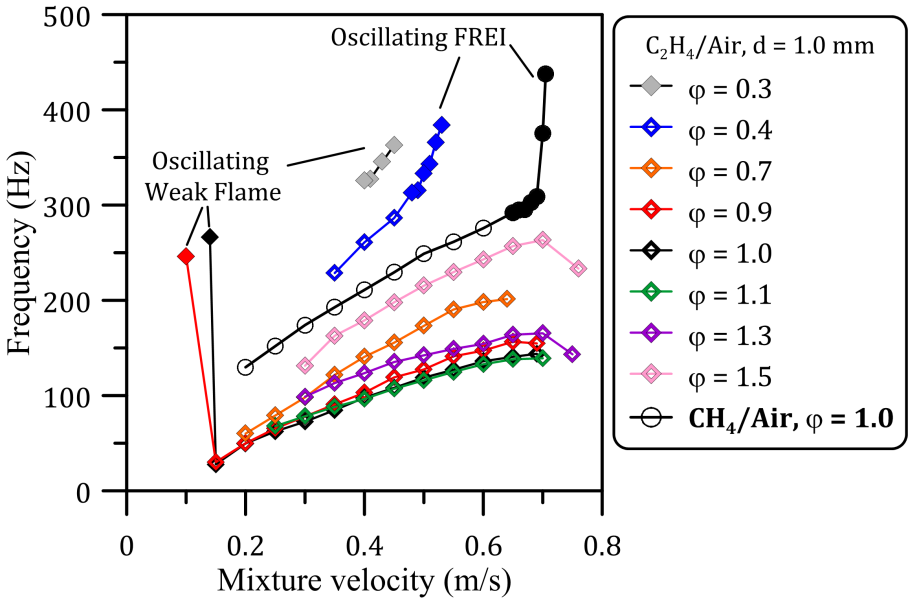

Figure 4.14: Flame frequencies obtained by varying the inlet velocity at different equivalence ratios.

As observed in Section 4.1.1.1 for ethylene/air mixtures, the time required to heat the cold fresh mixture up to the ignition temperature after the end of a previous cycle is considerably high because the FREI evolves in the low temperature region of the micro-reactor. For fuel-lean and fuel-rich compositions, the frequencies increase is the result of a flame propagating on shorter distances and extinguishing at higher wall temperatures; both characteristic times are thus lower.
In Fig. 4.11 one can notice that the extinction points have a different evolution with the equivalence ratio. In fuel-lean conditions, the wall temperature at the extinction location increases monotonously with the inlet velocity, while for fuel-rich mixtures a turning point is detected at low inlet velocity. Such a trend has already been observed for methane/air mixtures (Chapter 3) and can be explained by analyzing the characteristic times.
Figure 4.15 contains the FREI characteristic times of a fuel-lean ($\varphi = 0.7$, on the left) and a fuel-rich ($\varphi = 1.5$ on the right) ethylene/air mixture. Similar information for all the other equivalence ratios herein investigated is given in Annex E. In the lean condition, τ_{IE} (open symbol) is weakly impacted by the inlet velocity while τ_{EI} (closed symbols) decreases while increasing the mixture speed. The crossing point is observed for $v = 0.35\,m/s$. Above this inlet velocity, most of the cycle consists in the flame propagation. On the other hand, in the fuel-rich side τ_{IE} is smaller compared to the lean side, and it decreases with the inlet velocity. As already observed in Chapter 3, this means that the flame propagates faster thus resulting in a decrease of the convection time toward the fresh gases. As a consequence, the bulk temperature is lower and an earlier flame extinction occurs.

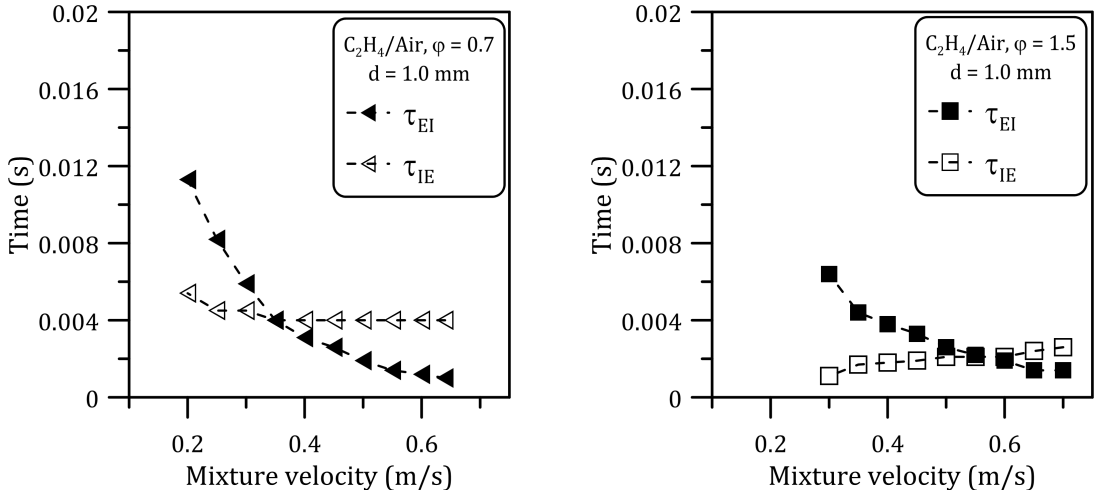

Figure 4.15: Characteristics times of ethylene/air mixtures at $\varphi = 0.7$ (on the left) and 1.5 (on the right).

Oscillating flames were observed at an equivalence ratio of 0.4 in the 0.53 – 0.48 m/s velocity range, at the interface between the stable flames and FREIs. These flames oscillate at high frequency but unlike FREIs they do not extinguish, i. e. the CH* signal does not go to zero, as illustrated in Fig. 4.16. The spatial amplitude of the oscillations increases as the inlet velocity approaches the FREI regime that emerges at v = 0.47 m/s. Methane/air flames exhibit the same oscillatory behavior in fuel-rich and fuel-lean conditions in a 1.85 mm i.d. micro-channel or at the stoichiometry in a 1.0 mm i.d. micro-reactor. As explained in Chapter 3, these flames result from diffusive-thermal instabilities and can lead to local overheating [87].

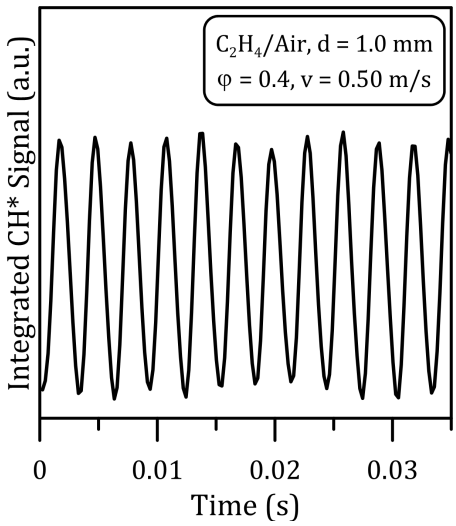

Figure 4.16: Oscillating flames observed at v = 0.5 m/s and $\varphi = 0.4$.

Frequencies of Fig. 4.14 were used to calculate the evolution of the Strouhal number

of ethylene/air mixtures with the equivalence ratio. Figure 4.17 displays this dependence, along with the corresponding data of methane/air mixtures (cf. Chapter 3). For both fuels, the Strouhal number is minimum for $\varphi = 1.1$ but it is twice smaller for ethylene than for methane (0.23 against 0.46).

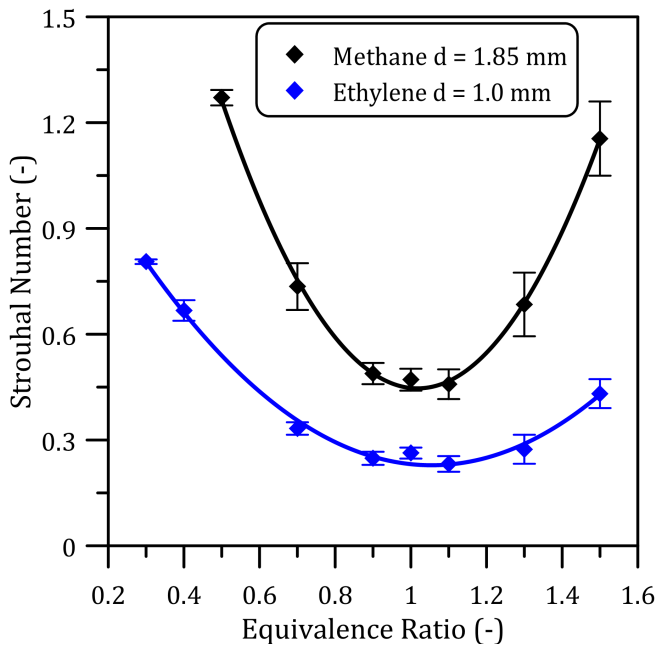

Figure 4.17: Strouhal Number for ethylene/air and methane/air mixtures.

The presence of a minimum Strouhal number indicates the existence of a preferred oscillating mode around $\varphi = 1.1$, that avoids or limits the development of hotspots that could damage the reactor wall.

4.1.3 Summary

Figure 4.18 gives an overview of the regions of existence of each flame regime with respect to the equivalence ratio and the inlet velocity.

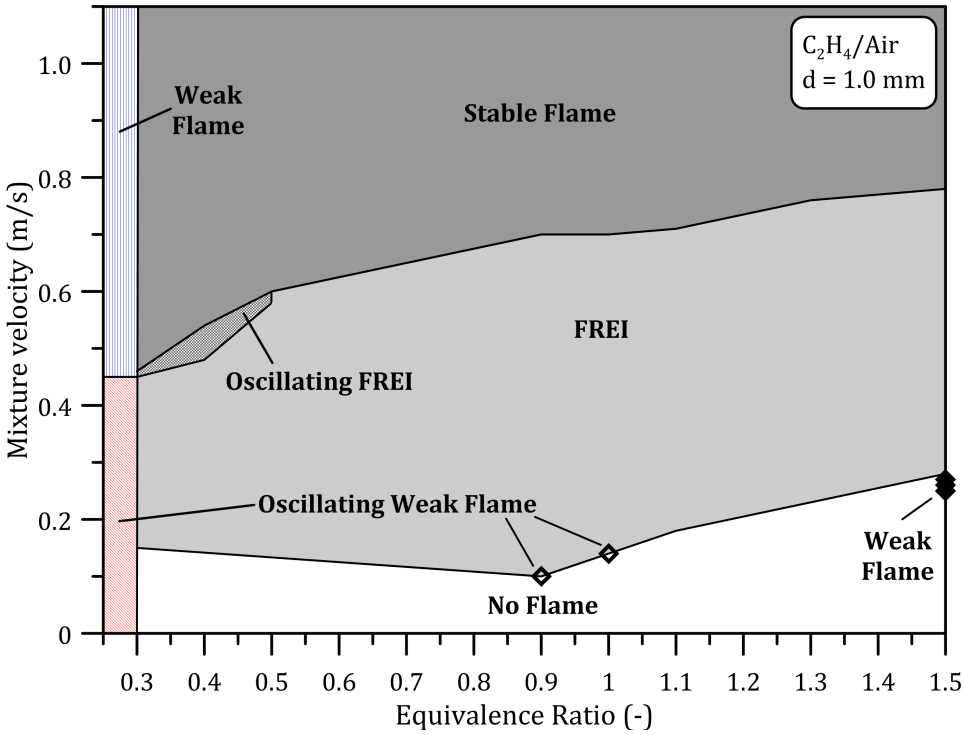

Figure 4.18: Map of different flame regimes for ethylene/air mixtures with the equivalence ratio as a function of the inlet velocity.

Stable flames, FREIs, weak flames, and oscillating weak flames were detected for $0.4 < \varphi \leq 1.5$. Stabilization temperatures of stable flames are linearly correlated to the adiabatic temperature and laminar flame speed, whereby the lowest stabilization wall temperatures are for mixtures with equivalence ratio between 1.1 and 1.3.
The FREI regime is pushed towards higher inlet velocities as the equivalence ratio increases, leading to a more unstable combustion mode. In this regime, a multiple flame splitting occurs in the propagation phase due to the presence of unburned gas behind the main front flame. Oscillating FREIs were not detected. In addition to the lower St, ethylene appears as a more suitable fuel than methane for combustion at micro-scale.
No weak flames were observed in the low velocity region, except at $\varphi = 1.5$, strengthening the assumption that those flames cannot be associated to the AIT.
Under ultra-lean conditions the combustion dynamics totally change. Oscillating flames were observed at $\varphi = 0.4$ between the stable flames and the FREI region whereas at $\varphi = 0.3$ the flames were limited to a weak flame and an oscillating weak flame regime. The present results confirm the existence of combustion at micro-scale in very lean conditions.

4.2 Acetylene/air mixtures

Acetylene (C_2H_2) is the simplest alkyne and has the highest heat of combustion and adiabatic flame temperature amid all common hydrocarbons, due to its triple bond structure. This fuel has been widely studied as it is a simple molecule, and for being a precursor of PAHs (Polycyclic Aromatic Hydrocarbons).
Therefore, experiments were conducted with acetylene in a 0.7 mm inner diameter micro-reactor [11, 12, 16] to study the effect of the inlet velocity and the equivalence ratio on the micro-combustion properties of this fuel. Unfortunately no experiments could be performed with methane and ethylene in a similar size micro-reactor because of the high frequency of their unstable flames and the low CH^* chemiluminescence. Nevertheless, acetylene data are compared to the results obtained in a 1 mm inner diameter micro-reactor with two other fuels. Moreover, a special attention is given to the combustion dynamics of acetylene/air mixtures in very-lean and rich conditions.

4.2.1 Effect of the inlet velocity

In Fig. 4.19 the results obtained with a stoichiometric acetylene/air mixture reacting in a 0.7 mm i.d. micro-channel are depicted. For comparison, the corresponding data for stoichiometric methane/air and ethylene/air mixtures in a 1.0 mm i.d. micro-reactor are also reported.

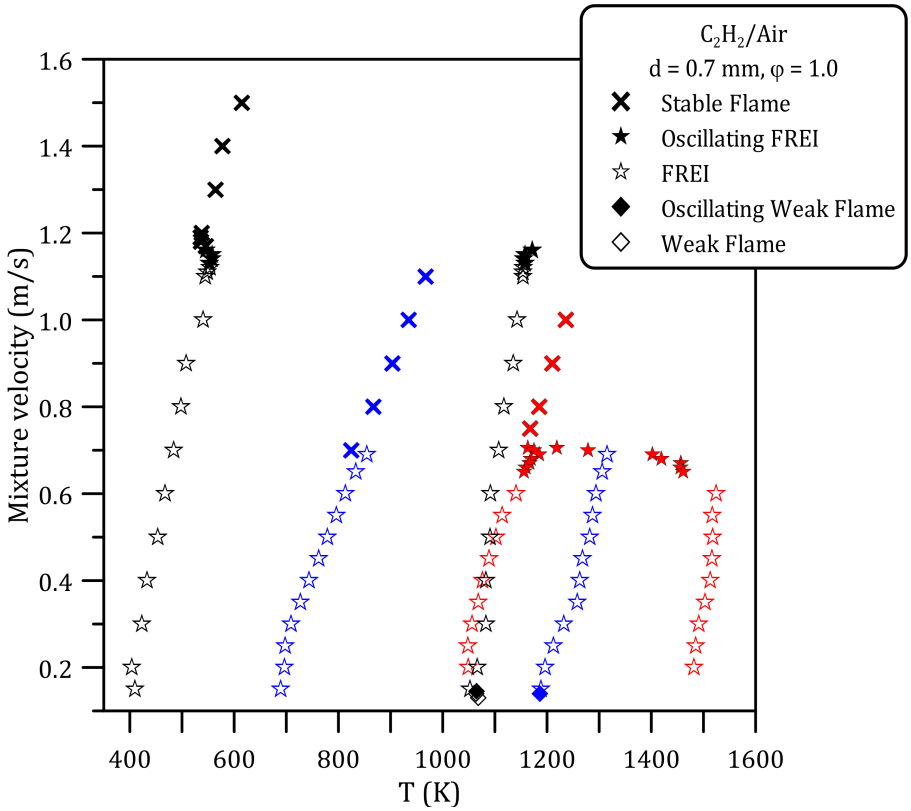

Figure 4.19: Flame position defined at the wall temperature as a function of the mixture flow velocity. Black = acetylene/air (d = 0.7 mm), blue = ethylene/air (d = 1.0 mm), red = methane/air mixtures (d = 1.0 mm).

All the flame regimes that were identified for methane in Chapter 3 are identified for acetylene/air mixtures, but the transitions occur at high inlet velocities. We observed stable flames for v $\geq$ 1.17 m/s, oscillating FREIs for 1.16 $\leq$ v (m/s) $\leq$ 1.13, FREIs for 1.12 $\leq$ v (m/s) $\leq$ 0.15, oscillating weak flame for v = 0.145 m/s, and weak flames for v $\leq$ 0.14 m/s.
Stabilization wall temperatures of stable and weak flames, as well as ignition and extinction temperatures, are systematically and significantly lower than those determined for ethylene and methane by about 150 and 400 K, respectively. This difference can be attributed to the higher heat of combustion and flame velocities of acetylene [109], but also to the narrower micro-reactor used for this fuel. Indeed, it was observed in Chapter 3 that the reactor diameter has an effect on the ignition and stabilization locations since the heat transfer efficiency from the wall is inversely proportional to the channel radius. However, the large difference herein observed between acetylene and the two other fuels suggests a predominance of the fuel effect over the size effect.

4.2.1.1 FREI and transitional regimes

The FREI regime of acetylene is spread over a larger range of inlet velocities compared to methane and ethylene. The FREIs are confined in a region of the microreactor located further upstream thus cooler, as demonstrated by the lower extinction and ignition wall temperatures (Fig. 4.19). The low wall temperatures encountered by the FREIs impact their dynamics through the heat transfer between the flame and the fresh gases.
The frequencies characterizing the stoichiometric acetylene/air FREIs and oscillating FREIs and weak flame are displayed in Fig. 4.20 (in black), along with those obtained for methane (in red) and ethylene (in blue).

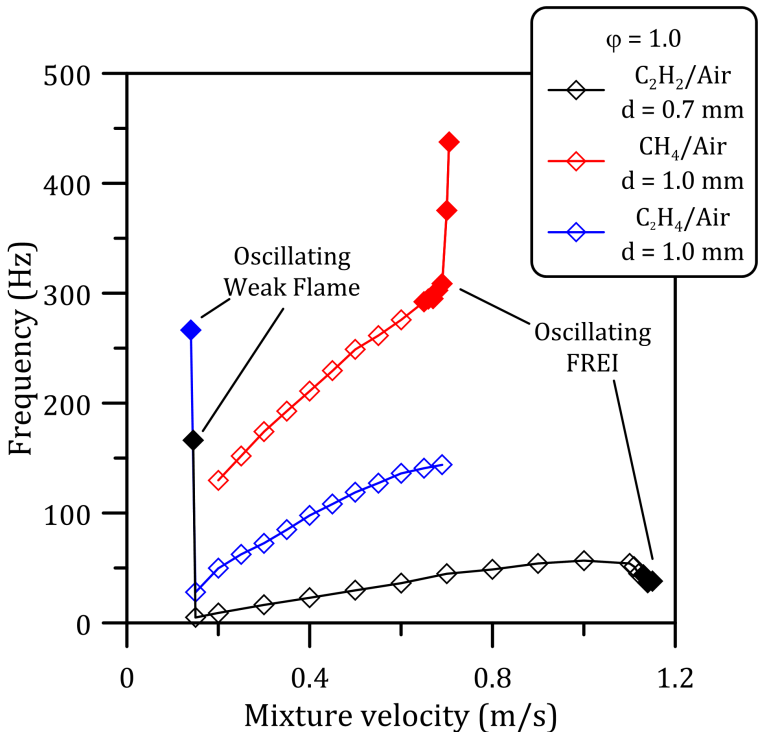

Figure 4.20: FREI frequency variation with inlet velocity for the three fuels investigated.

Frequencies are on average 68% lower compared to ethylene and 87% with methane. Regarding the transitional regimes, the frequencies decrease when switching to the FREI oscillating mode, unlike the previous observation for methane, while they increase once reaching the oscillating weak flame regime, which is similar to ethylene's behavior.
In order to understand those differences, the characteristic times τ_{IE} and τ_{EI} are presented in Fig. 4.21.

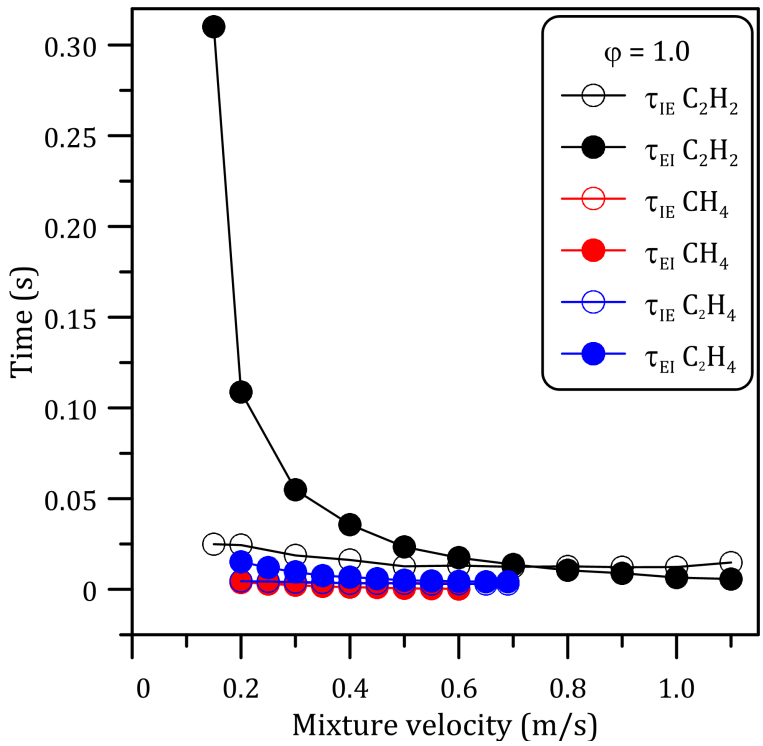

Figure 4.21: Comparison between τ_{IE} and τ_{EI} for acetylene (d = 0.7 mm, in black), ethylene (d = 1.0 mm, in blue) and methane (d = 1.0 mm, in red).

The time τ_{IE}, in other words the time between the flame ignition and extinction, is on average 77% higher compared to that of methane and ethylene. Indeed, even if the acetylene flame speed is higher [109], the τ_{IE} is higher because the flame travels over a longer distance and in a lower temperature region [58, 73]. Meanwhile, the time required to heat up and ignite the fresh mixture after the extinction and ignition positions also increases and is about twice the τ_{EI} determined for methane. This longer time is explained by the fact that the previous cycle ends in a cold reactor region and thus the mixture must travel a longer distance to reach the ignition location. The high characteristic times rationalize the low frequencies observed in Fig. 4.20.
The presence of multiple CH^* peaks during the FREI propagation is also investigated. Figure 4.22 displays the evolution of the maximum of CH^* intensity at high (v = 1.12 m/s) and low (v = 0.30 m/s) inlet velocity.

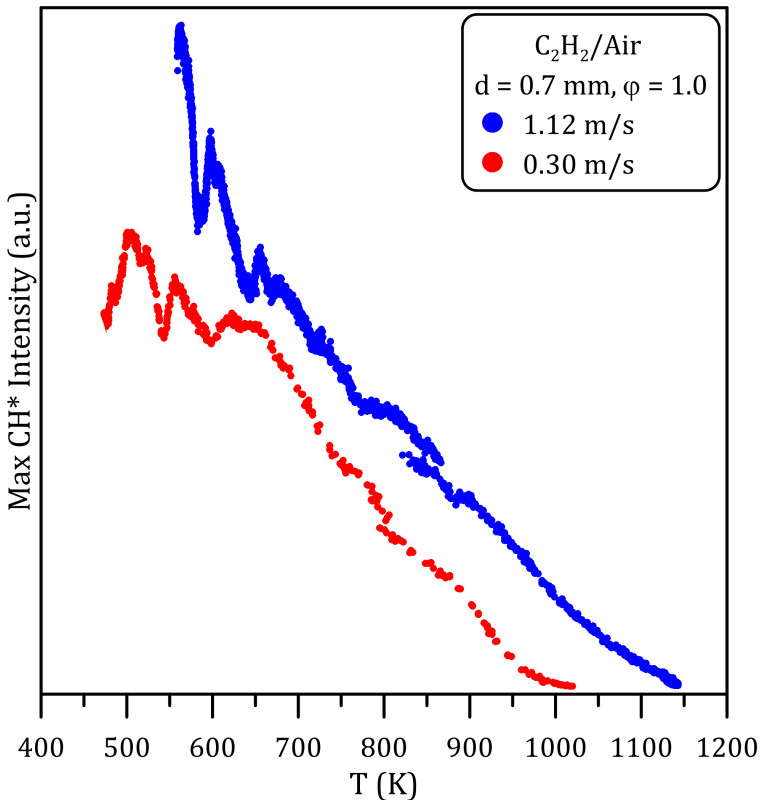

Figure 4.22: Maximum CH* progression in the FREI region at high (v = 1.12 m/s) and low (v = 0.30 m/s) inlet velocity.

For both inlet velocities, there is a jump in the experimental data: around 850 K and 780 K for v = 1.12 m/s and v = 0.30 m/s, respectively. Then the maximum of CH* signal progress irregularly, with a succession of increase and decrease of the signal, particularly pronounced at low wall temperatures. To analyze this behavior, spatially resolved snapshots of the CH* signal at successive instants are displayed in Fig. 4.23 and Fig. 4.24.

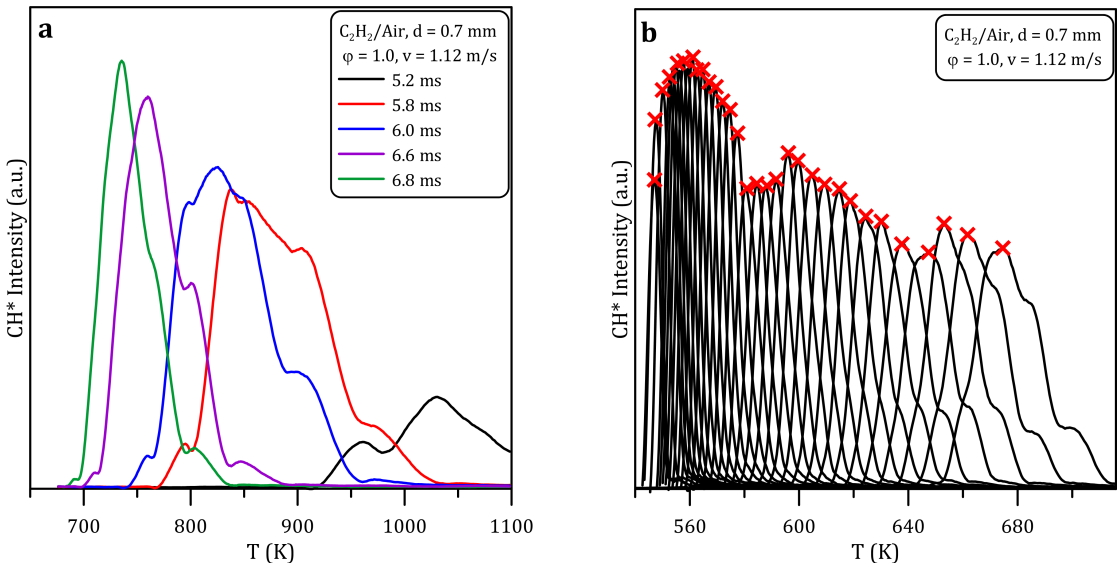

Figure 4.23: CH* emission at successive instants at v = 1.12 m/s. In a) the instant after the flame ignition are presented. In b) the successive instants until the flame extinction are reported.

The Fig. 4.23a shows the evolution of the CH* signal during the early stage of the flame propagation at v = 1.12 m/s. The mixture auto-ignites 5.0 ms after the end of the previous cycle. Immediately after, at 5.2 ms, a splitting in the CH* signal occurs (in black) between 960 and 1030 K. Then the brightness of the main flame rapidly increases, as visible at 5.8 ms (in red). At 6.0 ms (in blue) a new peak appears at 800 K, the luminosity of which quickly rises (at 6.6 ms, in purple). At 6.8 ms (in green) only one sharp peak remains, while the secondary flames extinguish.
In Fig. 4.23b the progression of the CH* signal is presented at successive instants until flame extinction. While multiple peaks were detected early in the propagation phase, the latter stages exhibit one single peak, the maximum intensity of which (red crosses) highly fluctuates over time. These fluctuations thus explain the irregular behavior previously detected in Fig. 4.22. It is noteworthy that these chaotic variations take place in the cooler section of the micro-reactor, at temperatures that neither ethylene nor methane FREIs encountered. It is thus reasonable to assume that the low reactor temperature affects the flame propagation, leading to a fluctuating CH* intensity.
At v = 0.30 m/s, despite the lower flame brightness, a similar overall behavior is observed. The flame ignites 55.0 ms after the end of the previous FREI cycle. The CH* signal is presented in Fig. 4.24a for four successive instants following the auto-ignition.

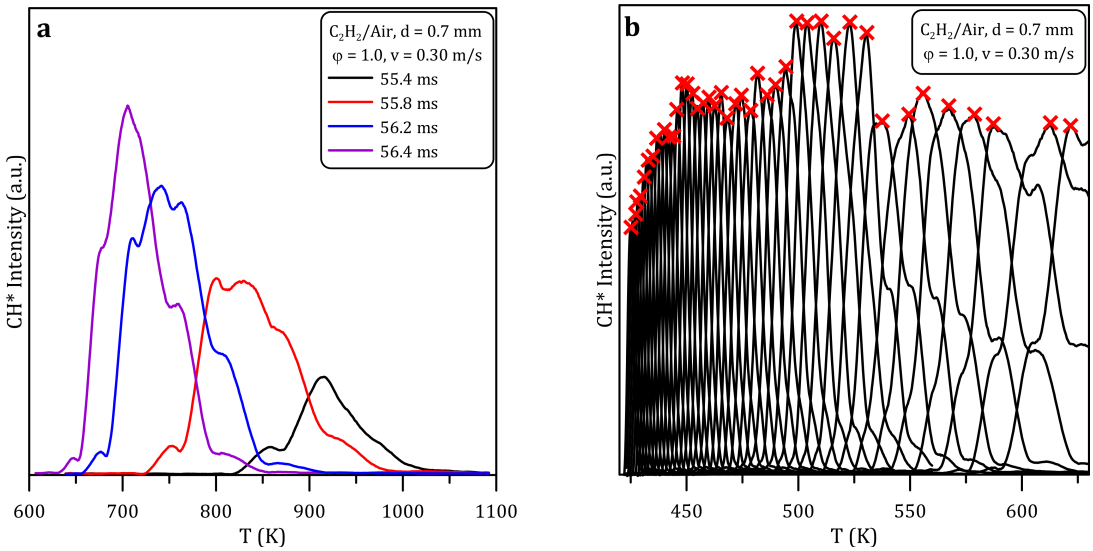

Figure 4.24: CH* emission at successive instants at v = 0.30 m/s. In a) the instant after the flame ignition are presented. In b) the successive instants until the flame extinction are reported.

After the occurrence of the first splitting at 55.4 ms (in black), the flame propagates further upstream between 55.8 (in red) and 56.2 ms (in blue) with the presence of three peaks whereas the front flame brightness increases during the flame propagation (56.4 ms, in purple). By looking at successive CH* signal snapshots before the flame extinction (Fig. 4.24b), it appears that the maximum of the CH* chemiluminescence fluctuates (red crosses), as already observed at v = 1.12 m/s.
This fluctuating behavior is visible also on the integrated CH* signals, shown in Fig. 4.25. It is important not to mix up these fluctuations with the oscillations that can be detected before extinction for an oscillating FREI (see Chapter 3).

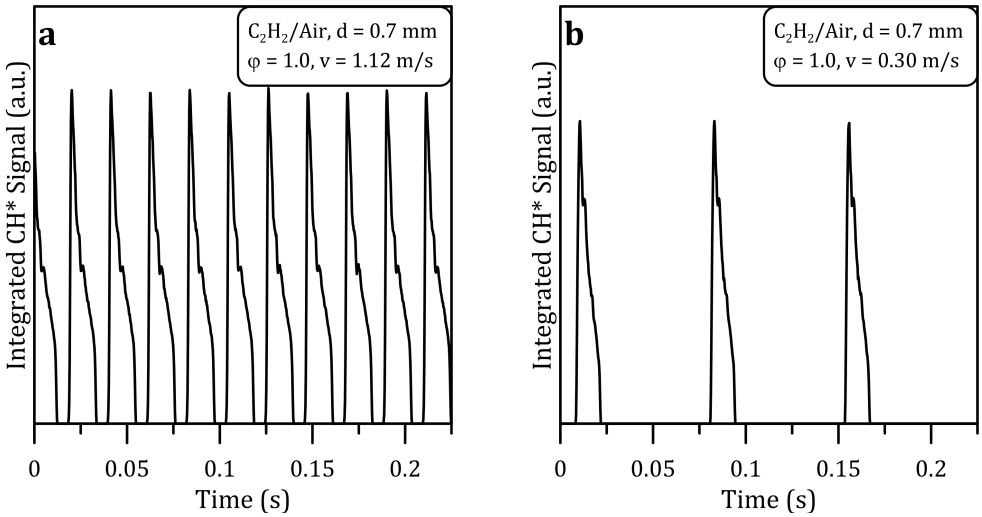

Figure 4.25: Integrated CH* signal for v = 1.12 and 0.30 m/s.

Regarding the oscillating regimes observed in the transition between the main flame regimes, integrated CH* signals of representative cases are presented in Fig. 4.19.

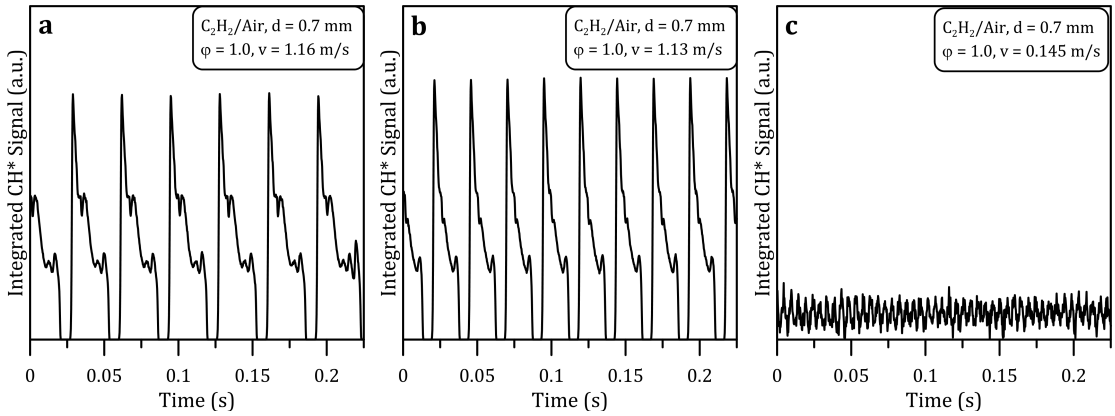

Figure 4.26: Integrated CH* signal of oscillating flames. a) v = 1.16 m/s (Oscillating FREI), b) v = 1.13 m/s (Oscillating FREI) Fr = 43.7 Hz, c) v = 0.145 m/s (Oscillating Weak Flame) Fr = 166.2 Hz.

At the interface between the stable flames and FREIs, the oscillating FREIs are characterized by the presence of multiple CH* oscillations before extinction. This behavior is in line with the previous observations for methane/air flames (near the stoichiometry) in larger reactor (see Chapter 3). These oscillations are due to pressure waves coupled to fluid density variations [31]. However, the number of oscillations is not fixed: while at v = 1.16 ms it changes from cycle to cycle (Fig. 4.19a), only one oscillation before the extinction is always observed at v = 1.13 m/s (Fig. 4.19b). The fluctuating CH* behavior discussed above for FREIs is also detected during the propagation phase, as illustrated by the discontinuities in the main oscillation.

The oscillating weak flame detected at 0.145 m/s (Fig. 4.19c), as observed earlier, is a flame that pulses with a very high frequency and presents a low CH^* emission [91]. The oscillation frequency is smaller with acetylene than with ethylene, 166.2 vs. 266.3 Hz, most likely because of the lower stabilization temperature.

4.2.2 Effect of the equivalence ratio

By adopting the same methodology as for methane and ethylene, acetylene micro-combustion has been investigated over a wide range of equivalence ratios. On the fuel-rich side, experiments were performed with equivalence ratios up to 1.7 whereas, on the fuel-lean side, equivalence ratios as low as 0.1 were investigated. The three main flame regimes (stable flame, FREI and weak flame) were observed. Oscillating FREIs were detected regardless of the equivalence ratio, but oscillating weak flames were only present at the stoichiometry. Unique and specific flame behaviors were identified under very lean condition (0.1 – 0.3) and are presented in the next section.

4.2.2.1 Flames in very-lean condition

Figure 4.27 displays the state mapping of acetylene/air flames at equivalence ratio of 0.1 (in red) and 0.3 (in black). For the leanest mixture, all the flames that are observed in the velocity region experimentally accessible are weak flames. Such a behavior is similar to that of ethylene/air mixtures at $\varphi = 0.3$ (see Section 4.1.2.1). The stabilization wall temperature of these flames decreases with the inlet velocity. As explained before, the high temperatures at which these flames stabilize enhance the wall effects [64, 65] and the exothermicity of the heterogeneous recombination reactions provide the energy for the flame to stabilize, even under very lean conditions, thus demonstrating the importance of the wall-fuel interaction in micro-systems.
Unlike what was observed for ethylene/air mixtures at the same equivalence ratio, different flame regimes are identified for an acetylene/air flames at $\varphi = 0.3$: stable flames ($v \geq 0.73$ m/s), oscillating FREI ($0.72 \leq v$ (m/s) ≤ 0.30) and FREI ($v \geq 0.2$ m/s).

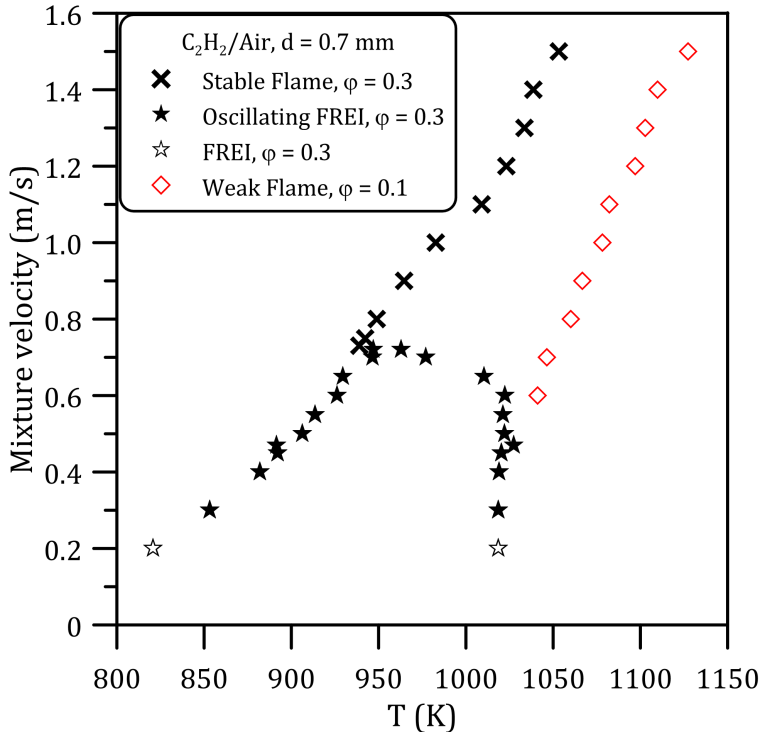

Figure 4.27: Flame position reported in terms of wall temperature for $\varphi = 0.1$ and 0.3.

The oscillating FREI regime at $\varphi = 0.3$ is spread over a wide range of inlet velocities. These flames pulse with a small amplitude and are due to thermo-diffusive instabilities [87], as already observed for fuel-lean or fuel-rich ethylene and methane mixtures. The dynamic of these flames is discussed below through the visualization of the integrated CH* signals at different inlet velocities in Fig. 4.28.

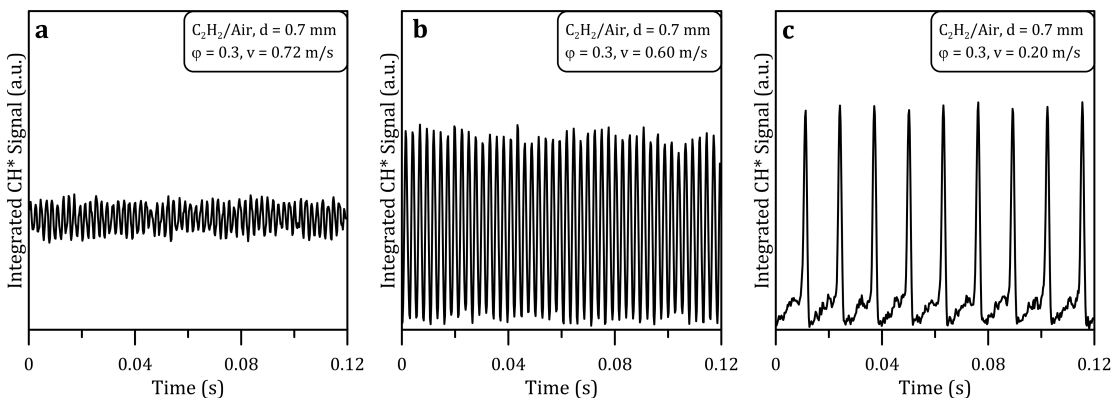

Figure 4.28: Spatially integrated CH* signals obtained at $\varphi = 0.3$. a) v = 0.72 m/s (Oscillating FREI), b) v = 0.60 m/s (Oscillating FREI), c) v = 0.20 m/s (FREI).

At v = 0.72 m/s (Fig. 4.28a), the upper bound of the oscillating FREI regime, the flame fluctuates quickly (∼480 Hz, Fig. 4.29) but with a very small amplitude and the CH^* signal never goes down to zero. By decreasing the inlet velocity, the amplitude increases (v = 0.60 m/s, Fig. 4.28b) while the frequency decreases (∼380 Hz, Fig. 4.29). When reaching v = 0.20 m/s (Fig. 4.28c), the flame switches to a normal FREI. In this latter case the CH^* signal rapidly fluctuates before the system evolves to the main propagation flame that rapidly moves upstream. The same behavior has been observed for methane/air flames in a 1.85 mm diameter reactor. There, the initial weak flame provides the energy for the main flame propagation [65, 73, 91].
In Fig. 4.29 oscillation frequencies of the normal and oscillating FREIs are displayed. The frequency increases with the inlet velocity, with a sharp onset at 0.65 m/s.

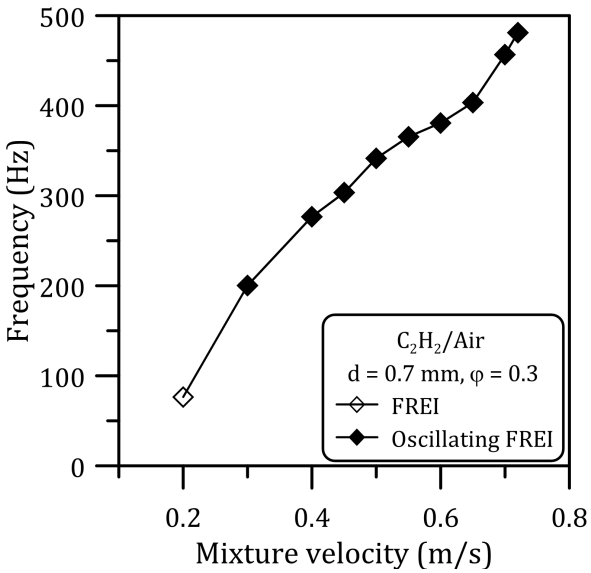

Figure 4.29: Frequencies of FREI and oscillating FREIs obtained at $\varphi = 0.3$.

4.2.2.2 Overview and Stable Flames

Figure 4.30 displays the experimental data collected for equivalence ratios between 0.5 and 1.7 regarding stabilization, ignition, and extinction temperatures.

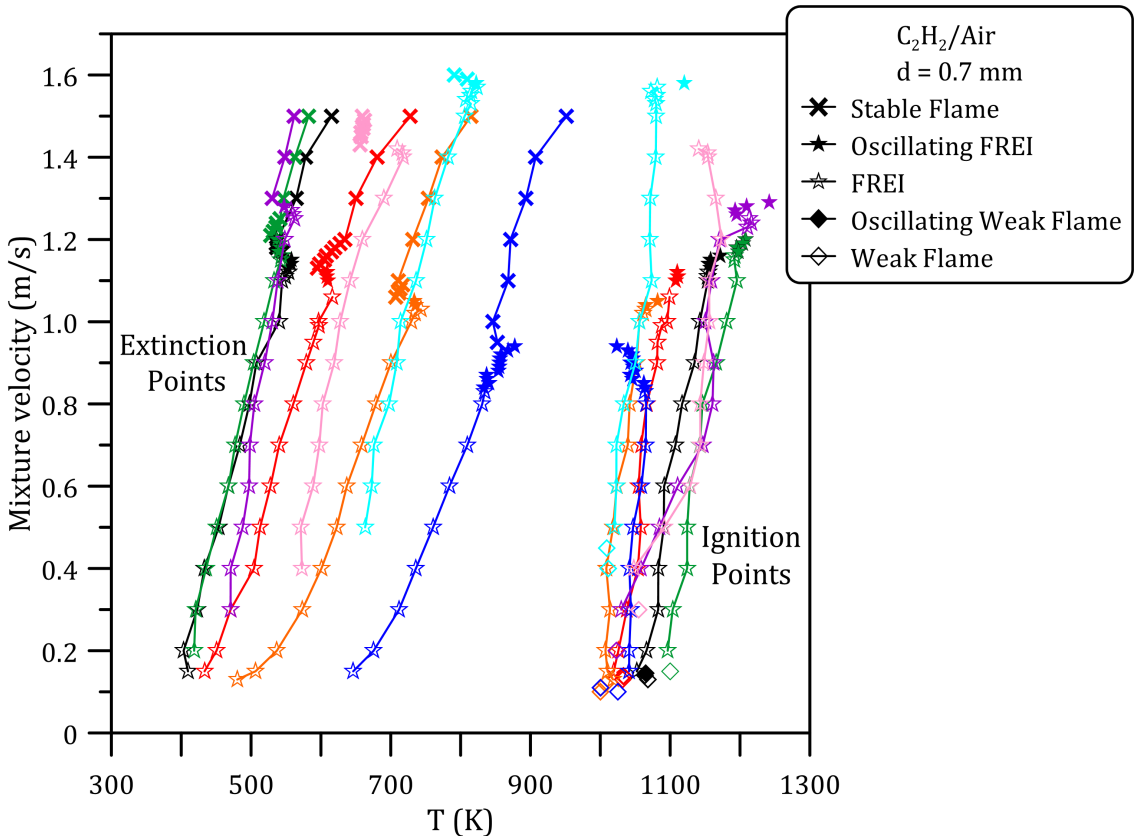

Figure 4.30: Flame position defined at the wall temperature as a function of the mixture velocity for different equivalence ratios: 0.5 (blue), 0.7 (orange), 0.9 (red), 1 (black), 1.1 (green), 1.3 (purple), 1.5 (pink), 1.7 (cyan).

For acetylene, the stable flame region is quite narrow and limited to very high flow rates. Indeed, unlike other fuels, instabilities appear for inlet velocities lower than 1.0 m/s. In the FREI regime, and in contrast with the previous observations for methane and ethylene, the ignition locations are particularly affected by the mixture equivalence ratio and seem to be pushed further downstream, towards higher temperature, as the equivalence ratio increases, although no clear trend can be derived from the present data. On the other hand, the extinction locations follow the usual trend: the flame extinguishes at lower temperatures around the stoichiometry than in fuel-lean or fuel-rich conditions. The transition between the stable flame and the FREI regimes goes through the formation of oscillating FREIs. The region of existence of such flames is narrower in the fuel-rich side (no oscillating flames were observed at $\varphi = 1.5$) but is particularly extended in the lean-side. Weak flames are observed at low inlet velocities (0.10 – 0.13 m/s) for both fuel-lean and slightly fuel-rich mixtures, but at much higher inlet velocities as the equivalence ratio further increases: ∼0.30 and ∼0.40 m/s at $\varphi = 1.5$ and 1.7, respectively. An oscillating weak flame is observed only at the stoichiometry, and has been discussed in detail in Section 4.2.1.1.

Regarding the stable flame region, the lowest stabilization temperatures are measured for $\varphi = 1.1$ and 1.3. For these equivalence ratios, the adiabatic laminar flame speed and temperature are maximum [109]. To check whether the correlation observed previously for methane and ethylene still hold, Figure 4.31 reports the reduced Lewis number and inlet velocities corrected laminar flame speeds ($Le \times S_l/v_{unb}$) as a function of the stabilization temperature normalized by the adiabatic flame temperature (T_{ad}/T) for the three fuels investigated.

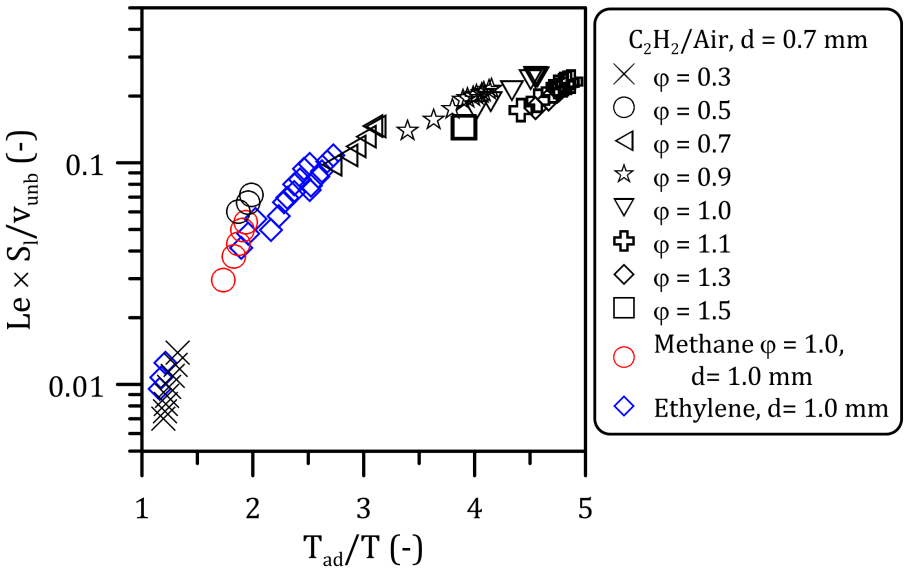

Figure 4.31: Correlation between T_{ad}/T and $Le \times S_l/v_{unb}$ for acetylene/air mixtures.

Despite the use of a narrower reactor, the acetylene data follow the trend previously outlined by ethylene and methane. In particular, on the lean side, the acetylene data collapse on those of ethylene/air mixtures. Globally, this progression confirms that the stabilization position of the stable flames is mainly the result of a balance between the flame temperature and speed, as well as the thermal and mass diffusivities. The reactor size also plays a crucial role in the heat transfer: this aspect has been highlighted by Zeldovich using the critical Peclet number [17]. However, the lack of information about the dependence of the quenching diameter on the temperature prevents the proposition of a formulation that would include the influence of the channel diameter.

4.2.2.3 FREI and oscillating flames

In the FREI regime, the slope relating the wall temperature at the extinction positions and the inlet velocities changes when switching from the fuel-lean to the fuel-rich side. As for methane and ethylene/air mixtures, this slope increase is due to the faster flame propagation in the rich side (decrease of τ_{IE}). The characteris-

tic times for each equivalence ratio and inlet velocities investigated are provided in Annex E.
Regarding the CH* emission and the front flame propagation, the splitting observed at the stoichiometry and discussed in Section 4.2.1.1 has been confirmed for all the other equivalence ratios. However, for $\varphi = 1.1$ and 1.3 the fluctuation amplitudes during the propagating phase are smaller because of the higher flame temperature that avoids the perturbations observed elsewhere. Progressions of the maximum CH* signal are reported in Annex E.
Nevertheless, a peculiar progression of the CH* signal is observed at $\varphi = 1.7$. Figure 4.32 displays these progressions for the upper (v = 1.54 m/s) and lower (v = 0.60 m/s) bounds of the FREI regime at this equivalence ratio.

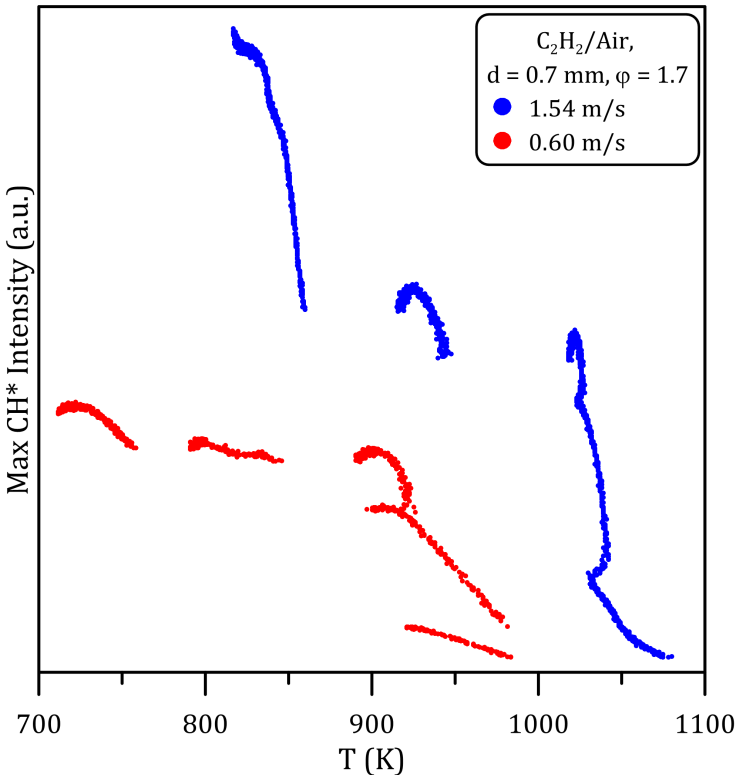

Figure 4.32: Maximum CH* progression at $\varphi = 1.7$ at high (v = 1.54 m/s) and low (v = 0.60 m/s) inlet velocity.

There are broad discontinuities for both inlet velocities. In order to elucidate this behavior, the CH* signals at successive instants are presented in Fig. 4.33 for the two cases considered.

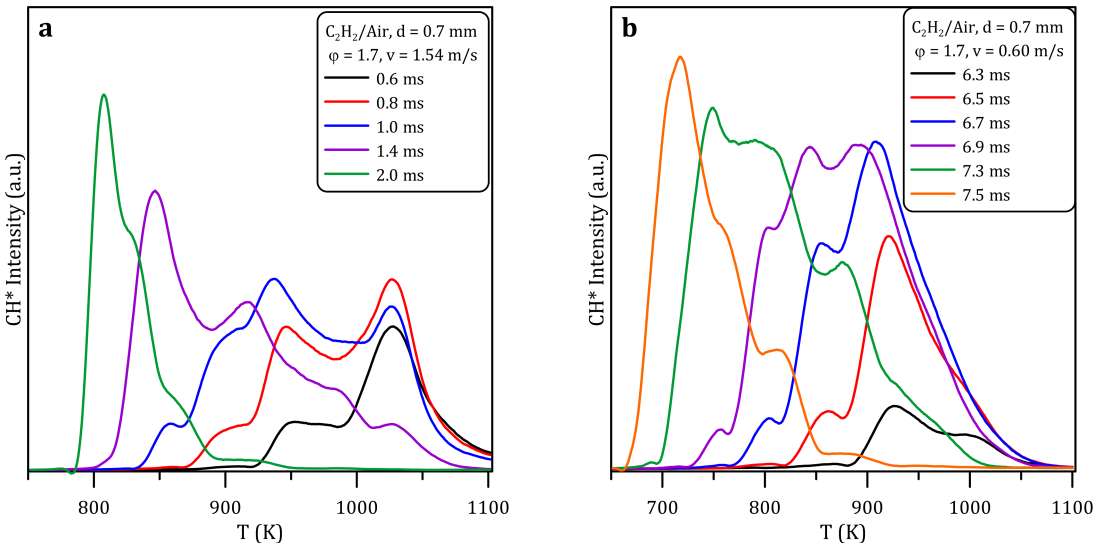

Figure 4.33: CH* signals at successive instants. a) v = 1.54 m/s, b) v = 0.60 m/s.

At v = 1.54 m/s, the mixture quickly auto-ignites after the extinction ($\tau_{EI} = 0.2$ ms). The flame then propagates over a small distance (4.1 mm) and a short time ($\tau_{IE} = 3.5$ ms). By looking at the CH* signal (Fig. 4.33a), it appears that after the flame ignition, a first splitting occurs at 0.6 ms (in black). During the early stage of the propagation phase (0.8 – 1.4 ms), the chemiluminescence signal remains broad with several peaks. When the flame reaches the extinction zone (at 2.0 ms, in green), the secondary peaks disappear and the reaction front gets thinner while the signal intensity increases.
At v = 0.60 ms (Fig. 4.33b) a similar behavior is observed: after a first early splitting, the flame propagates downstream with the presence of multiple CH* peaks before the formation of a sharper peak prior to flame extinction.
The excess of acetylene coupled to the fast flame propagation due to the high reactor temperature, is the reason, in both cases, of the multiple CH* emission peaks which are the markers of the oxidation of unburned species left behind the front flame.
In order to study the dynamics of the oscillating FREIs detected in the transition between the stable flame and FREI regimes, representative spatially integrated CH* signals are reported for each equivalence ratio in Fig. 4.34. Depending on the flame stoichiometry, different behaviors were identified.

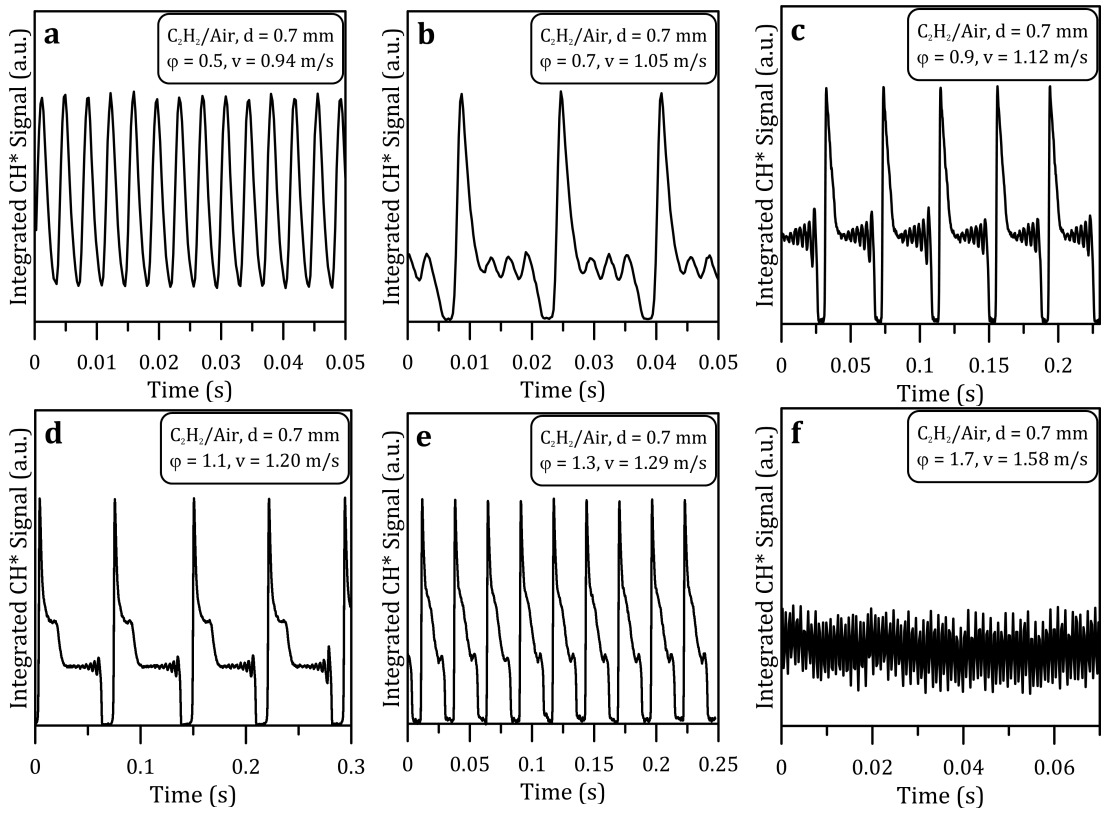

Figure 4.34: Oscillating flames observed for the transition from stable to FREI region at different equivalence ratios.

At $\varphi = 0.5$ (Fig. 4.34a) the CH^* signal fluctuates periodically but without going down to zero. This specific oscillating behavior has been numerically predicted by Miroshnichenko et al. [87] and is the outcome of thermo-diffusive instabilities. The amplitude of the fluctuation decreases with the inlet velocity until the flame evolves to a conventional FREI. When the equivalence ratio increases from 0.5 to 1.3, (Fig. 4.34b-e) periodic oscillations before the flame extinction are observed. This behavior is referred as a 'mixed mode' and as a 'periodic oscillatory behavior' in [87] and [31] respectively, and is due to pressure waves coupled to fluid density variations. In particular at $\varphi = 1.1$, a higher oscillation is observed then followed by oscillations of small amplitude. The number of these secondary fluctuations decreases with the inlet velocity before switching to a typical FREI. At $\varphi = 1.7$ and v = 1.58 m/s one oscillating flame is observed (Fig. 4.34f). This flame has the same characteristics as the oscillating flame at $\varphi = 0.5$, but with a smaller amplitude and a higher frequency.

Regarding the frequencies of the normal and oscillating FREIs, they are plotted for each equivalence ratio as a function of the inlet velocity in Fig. 4.35. For the sake of comparison, the frequencies of a stoichiometric methane/air mixture in a 1 mm i.d. micro-channel are also reported.

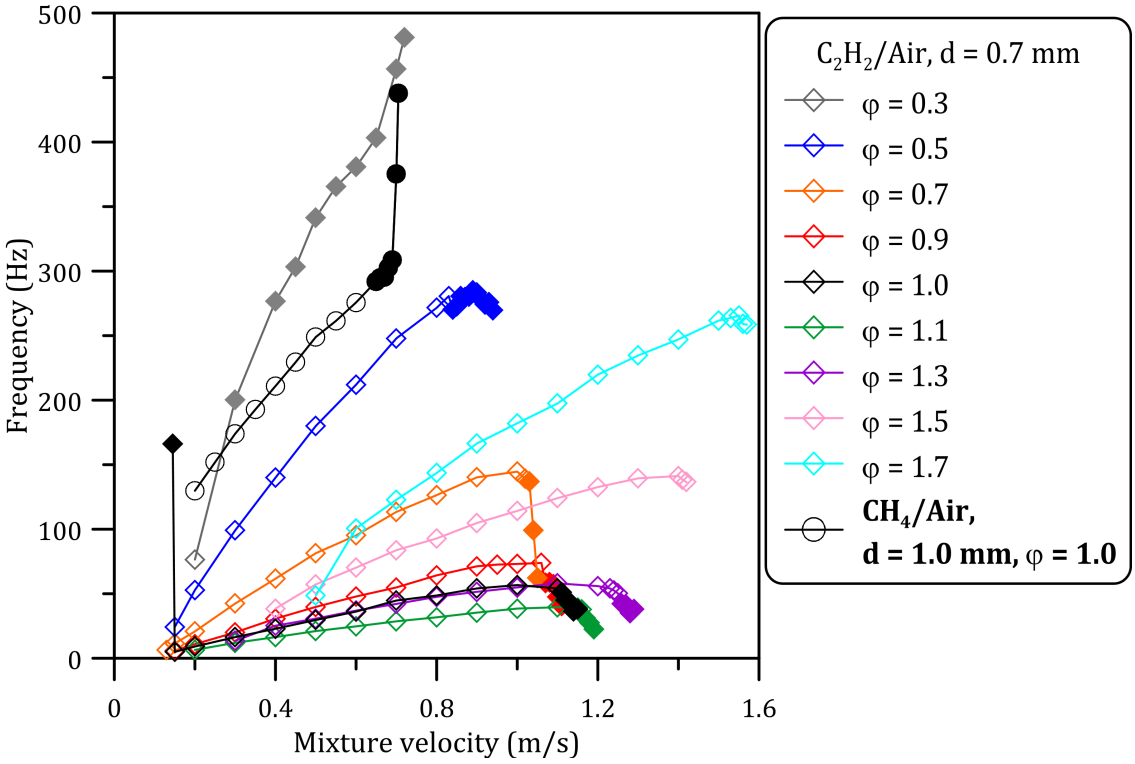

Figure 4.35: Flame frequencies obtained varying the inlet velocity at different equivalence ratios.

As observed previously for methane and ethylene, the FREI frequencies increase with the inlet velocity [30, 31, 93]. This dependence is more evident for fuel-rich and fuel-lean mixtures. Indeed, in these conditions, the flames move on a shorter distance and at a higher temperature (Fig. 4.30): temperature enhances the flame speed [58, 73] reducing the time available for the flame to propagate.
Therefore, the smallest frequencies are obtained for equivalence ratios in the range 1.0 – 1.3. Because of the high flame temperatures and velocities, the flames move over a longer distance and the characteristic times (τ_{EI} and τ_{IE}) thus increase consequently the frequencies decrease.
In the oscillating regimes, two different tendencies are observed with respect to the nature of the oscillating behavior. The frequencies drop down if periodic fluctuations before extinction are present ($0.7 \leq \varphi \leq 1.3$) while they increase if the flames are characterized by thermo-diffusive instabilities ($\varphi \leq 0.5$, $\varphi = 1.7$).
To push further the comparison between the three fuels investigated in the present work, the frequencies of Fig. 4.35 were used to calculate the Strouhal number of acetylene/air mixtures. The progression of this number with the equivalence ratio is depicted in Fig. 4.36, along with the corresponding information for methane and ethylene.

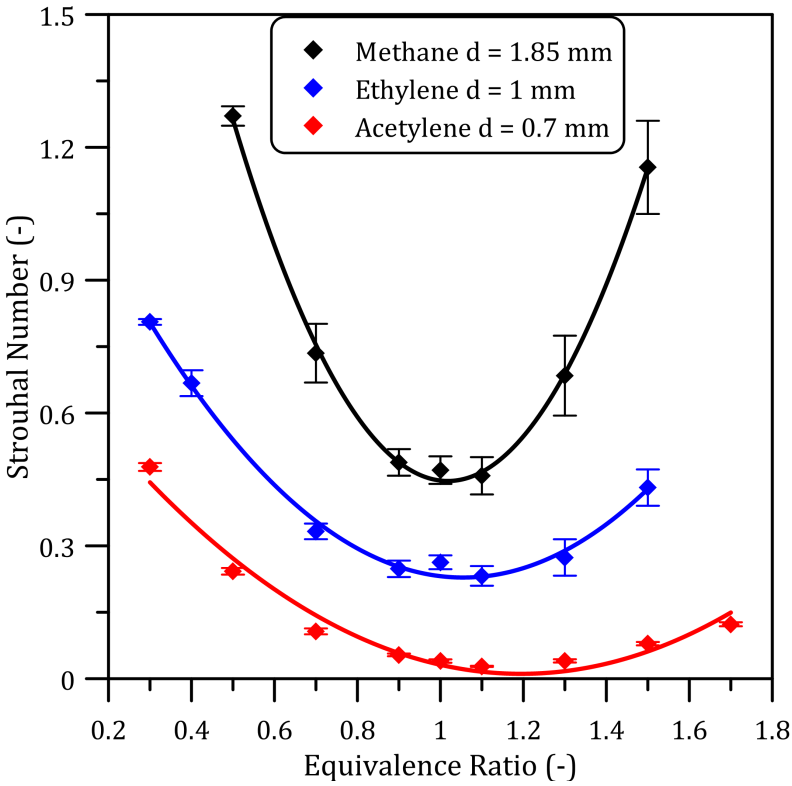

Figure 4.36: Strouhal number progression for the three fuels employed in the present work.

For acetylene, the Strouhal number is minimum at $\varphi = 1.1$ (St = 0.028), which is smaller than the minimum St calculated for methane and ethylene. The lower FREI frequencies of acetylene/air mixtures point this fuel as very suitable for micro-scale applications. However, the presence of a large oscillating FREI regime may make the thermal control more difficult and lead to safety issues.

4.2.3 Summary

Figure 4.37 summarizes the region of existence of each flame regime for acetylene/air mixtures reacting in a 0.7 mm internal diameter micro-channel.

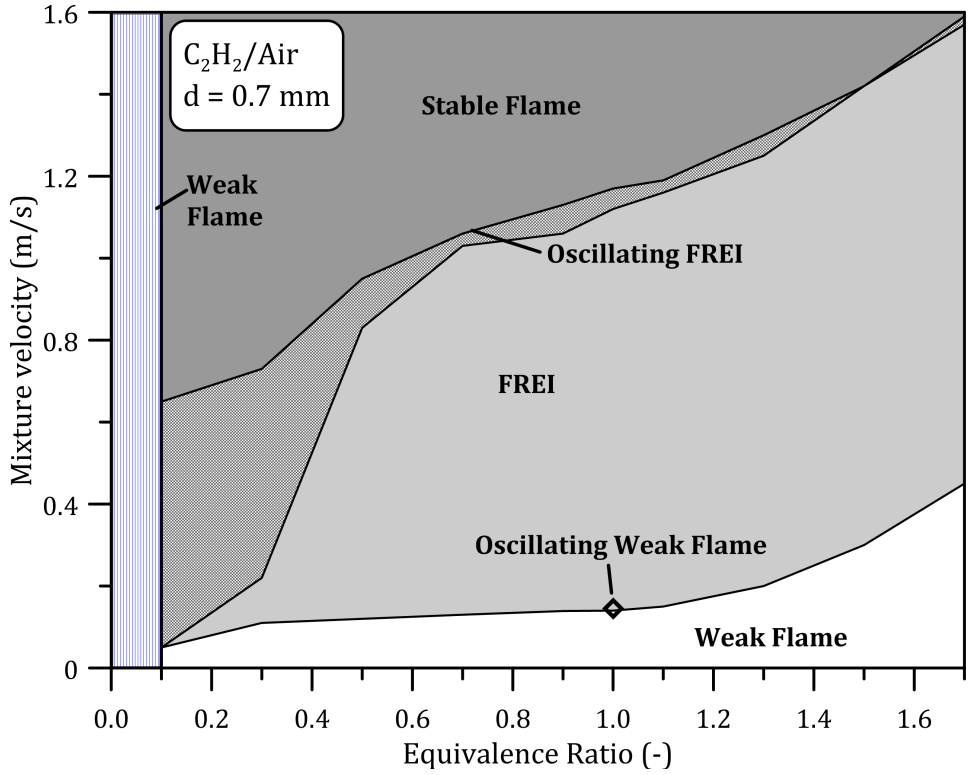

Figure 4.37: Map of different flame regimes for acetylene/air mixtures with the equivalence ratio as a function of the inlet velocity.

The stable flame region is particular narrow, compared with the other fuels examined, especially in the fuel-rich side. The FREI region is hence extended and characterized by low frequencies: the high flame temperature enhances the heat transfer between the reaction zone, the wall and the fresh gases, and the flame can propagate in a lower temperature region. The Strouhal number lower compared to methane and ethylene, allowing a more controllable combustion mode. However, the low temperatures encountered by the flame lead to fluctuations in the CH^* intensity during the propagating phase.
The oscillating FREI region is also extended, especially in fuel-lean conditions, and the oscillating flames are characterized by thermo-diffusive instabilities in the rich and lean side.
The high reactivity and luminosity of acetylene flames enabled experiments in very lean conditions, down to $\varphi = 0.1$, where only weak flames were observed. Like for ethylene, this result is promising for the application of this combustion mode in micro-combustors.

4.3 Conclusions

In order to investigate the combustion behavior of different fuels in micro-reactors, experiments were performed with ethylene and acetylene/mixtures over a wide range of equivalence ratios. The flame regimes observed in Chapter 3 were also observed, but their regions of existence were found to strongly depend on the fuel and the operating conditions.
For ethylene/air mixtures the high flame temperature and laminar speed allow the flames to propagate further downstream compared to methane, and the frequency of the FREIs are lower. After the FREI ignition, a flame splitting was observed and associated with the presence of unburned gases behind the main flame. An important characteristic was the absence of the oscillating FREI region for $\varphi > 0.5$. Weak flames were observed only at high equivalence ratio ($\varphi = 1.5$).
For acetylene/air mixture, the FREI region is spread on a wide range of the inlet velocity, and the same goes with the oscillating FREI regime. However, in the FREI region the frequencies recorded are particularly low: the mixtures auto-ignite at lower temperature than to methane and ethylene, and the flame is also quenched at very low temperature. The low reactor temperatures affect the flame propagation and cause fluctuations of the CH^* intensity. A flame splitting was also observed soon after the flame ignition, and a peculiar distribution of the CH^* signal with multiple peaks was spotted at $\varphi = 1.7$. In the oscillating flame region, diffusive-thermal oscillations were observed for very lean and very rich mixtures, while for the other equivalence ratios oscillations before extinction were detected.
For both fuels, the high flame chemiluminescence enabled the investigation of ultra-lean conditions, down to $\varphi = 0.3$ for ethylene and $\varphi = 0.1$ for acetylene. In such conditions only weak and oscillating weak flames were observed. These results confirm the capability of micro-combustion to extend the flammability limits and thus to achieve combustion in very lean conditions. Combustion in lean and very lean conditions is nowadays seen as a very promising technology for clean and high efficient combustion: indeed, the NO_x emission is reduced because of the low flame temperature. Furthermore, it ensures complete oxidation, reducing hydrocarbon and CO emissions.

Chapter 5

Numerical study of the ignition points

This chapter presents preliminary attempts to numerically investigate the ignition phase of the conventional FREIs experimentally observed. In particular, the influence of the inlet velocity, the reactor diameter and the fuel nature are considered. To do this, two numerical models, a two-dimensional (2D) and a homogeneous (0D) model, are employed with detailed chemistry. First, the 2D model is tested with methane/air mixtures reacting in channels of different diameters. Two detailed methane oxidation mechanisms (GRI-Mech 3.0 [90] and Konnov 0.5 [117]) are used. The computations are then compared to the experimental ignition temperatures and to those obtained with the 0D model. Finally, the computations are extended to ethylene and acetylene/air mixtures.

5.1 Numerical models

Two numerical models were used to perform the simulations: a 2D axisymmetric model with a wall temperature profile and a 0D model with a time-dependent temperature profile. In the next sections each model is described.

5.1.1 2D model

In this model, the coupled gas phase hydrodynamics and chemical kinetics in a channel is simulated. Boundary layer approximations for compressible flow are used since there is a dominant direction along the channel and since the diffusion flux dominates the convective flux in the radial (cross) flow direction. The parabolic na-

ture of the boundary layer equations allows employing an explicit method of lines for the integration [118]. An extended Von Misses transformation for which a stream function replaces the radial (cross) coordinate is also implemented [119, 120]. In the resulting transformed system of equations, the radial velocity component does not occur and the solution of the continuity equation is no more necessary since its validity is satisfied by the stream function. The computations are performed over 2D-axisymmetric solution domain for cylindrical channel flow-field. The solver discretizes the system of equations for momentum, energy and species using finite difference approximation over uniform grid which is clustered at the outer boundary. The flow rate, temperature and species concentrations at the channel inlet and the temperature profile at the channel wall are given as the boundary conditions. The temperature is set at the wall temperature profile measured during experiments (Chapter 2). Multicomponent molecular transport including thermal diffusion (Soret Effect) is considered when computing viscous fluxes since it has an effect on the species distribution [61, 62, 121], as shown in Fig. 5.1.

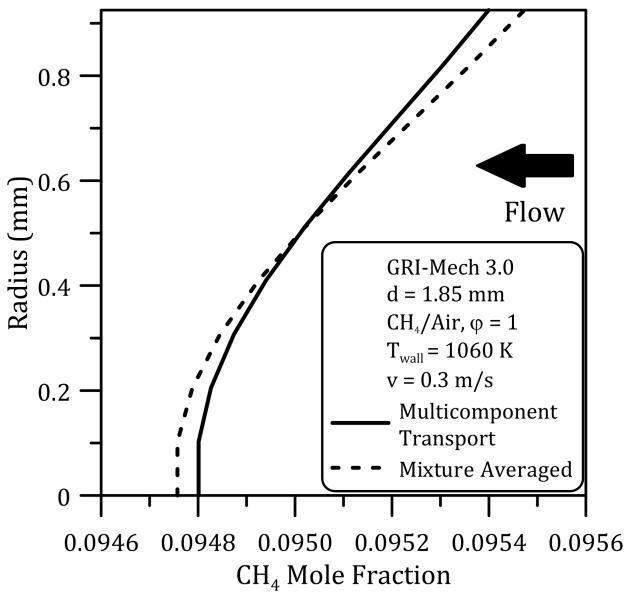

Figure 5.1: Effect of multicomponent transport and Soret effect on computed the CH_4 profile, compared to the mixture averaged simulations.

5.1.2 0D model

Simulations are performed with the SENKIN code [122] from the CHEMKIN package in a closed homogeneous batch reactor held at constant pressure. It consists of a simply perfectly-mixed, closed reactor with a time-dependent temperature profile. The time-temperature profiles are obtained through numerical simulations (detailed in Annex C). The distribution of the fluid velocity and temperature is computed

for a tubular reactor with respect to the experimental conditions: diameter, inlet velocity, and wall temperature profile. Then, the longitudinal velocity distribution is extracted at half of the radius in order to average the Poiseuille effect between the tube axis and the wall, as depicted in Fig. 5.2 (red line). Since previous numerical results showed that the mixture auto-ignites at the wall [31], simulations are also performed by extracting the velocity distribution at $^3/_4$ of the radius to take into account the flow deceleration at the boundary layer (blue line).

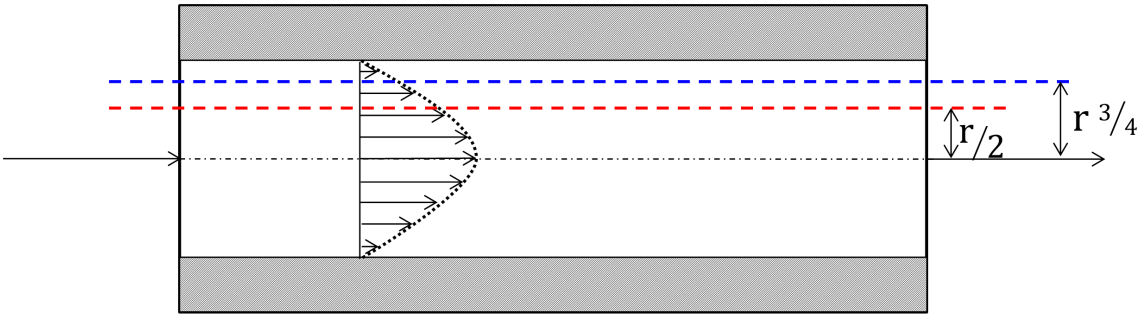

Figure 5.2: Sketch of the temperature profile extraction.

Combining the spatial wall temperature distribution and the integer of the inverse of the velocity distribution, the time-dependent temperature profile can be derived. Examples of such profiles are displayed in Fig. 5.3 for three different inlet velocities.

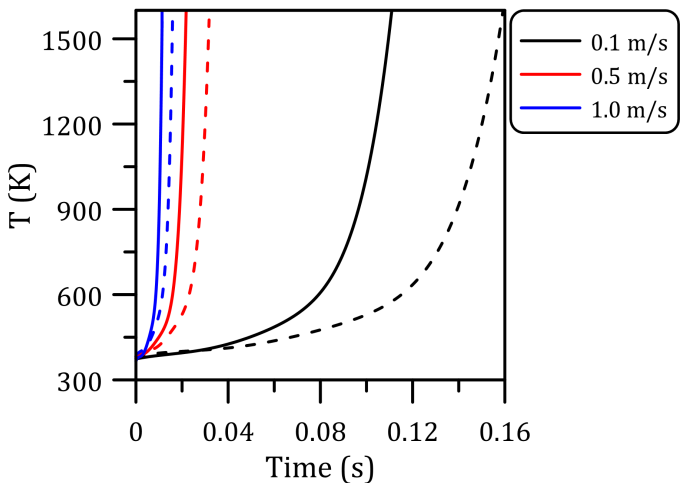

Figure 5.3: Time-varying temperature profiles employed in 0D simulations at half of the radius (solid line) and at $^3/_4$ of the radius (dashed line).

The other inputs required for the simulations are: the initial mixture composition, the pressure and the end time. The end time is set as the last time for which a temperature could be extracted.
Then CHEMKIN computes the species mole fractions as a function of time. Because

of the homogeneity assumption in these calculations, no transport contributions are included in the governing equations.

5.2 Reaction mechanisms

Two mechanisms are used, the GRI-Mech 3.0 [90] and the Konnov 0.5 [117]. The first one is a mechanism optimized for natural gas combustion. It contains 51 species and 325 reactions. The Konnov 0.5 mechanism consists of 125 species and 1200 reactions. It is based upon a methane combustion scheme extended to include ethylene oxide, methanol, acetaldehyde and ethanol oxidation.
The ignition location is defined as the spatial location for which the CH^* mole fraction is maximum on the reactor centerline, in line with the definition used in the experiments. To this end, a production and consumption subset for CH^* is added to both of the mechanisms as follows (Table 5.1). CH^* and CH share the same thermodynamic and transport properties.

Reactions	**A**	**n**	**E_a (cal/mol)**
$CH^* \rightarrow CH + h\nu$	1.90E+06	0.0	0.0
$CH^* + M \rightarrow CH + M$	4.00E+10	0.5	0.0
$CH^* + O_2 \rightarrow CH + O_2$	2.40E+12	0.5	0.0
$C_2H + O_2 \rightarrow CH^* + CO_2$	4.50E+15	0.0	25000

Table 5.1: Reactive chain and rate constants for the modified Arrhenius equation (k [cm^3, mol, s]) added to the mechanisms.

5.2.1 2D model: discretization and parameters effect

5.2.1.1 Spatial discretization

For the influence of the grid refinement on the results, simulations are performed in a 1.85 mm inner diameter tubular reactor. The gas-phase chemistry is described by the GRI-Mech 3.0 [90] and the flowing stream is methane/air stoichiometric mixture. The wall temperature and the inlet composition and flow rate are set as boundary conditions. The number of cells in the radial direction is changed from 3 to 20 with a 1 grid step while the axial resolution is varied from 5 up to 100 µm. The inlet velocity is varied with respect to the experimental conditions.

5.2.1.2 Radial discretization

Simulations are performed by changing separately the radial (3 to 20 cells) and axial (5, 10, 30, 50 and 100 µm) refinement. Figure 5.4 depicts the results obtained for an inlet velocity of 0.15 m/s.

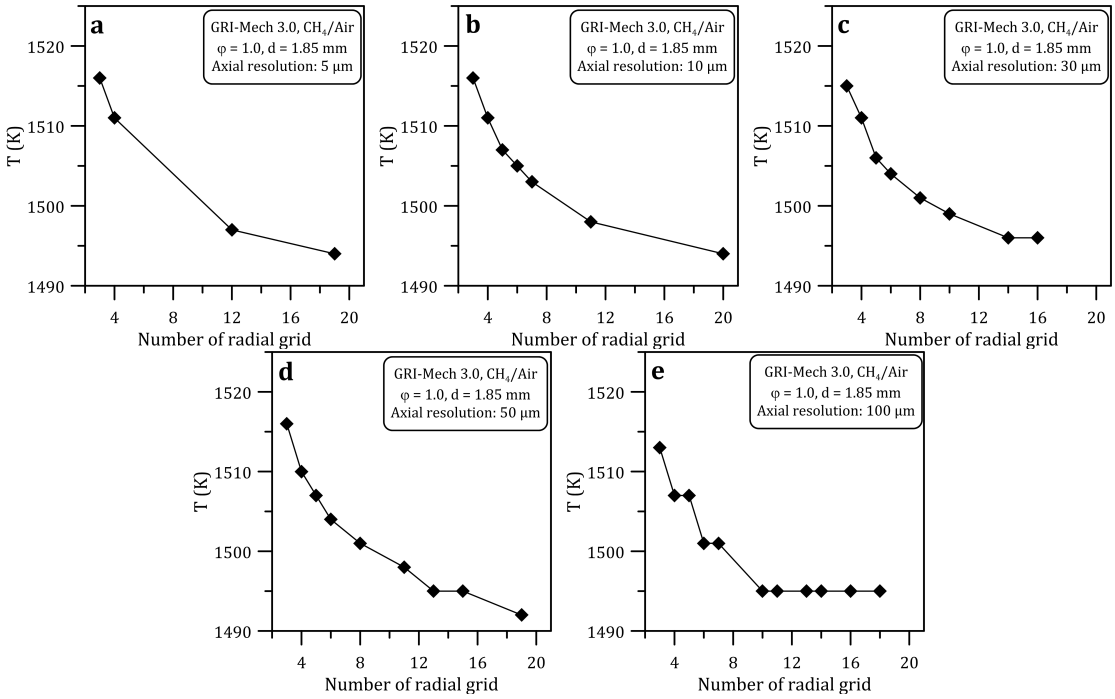

Figure 5.4: Results obtained at various axial refinements with varying the number of radial grid points.

When the axial resolution is high (5 µm, Fig. 5.4a), the computed temperature decreases toward an asymptotic value with the refinement of the radial component, but for a number of radial grid points higher than 12, the difference in temperature is only 3 K. However, convergence is not reached at each grid refinement because of the small axial mesh. Decreasing the axial resolution at 10 and 30 µm (Fig. 5.4b-c), the asymptotic value is reached with a coarser radial meshing: for an axial resolution of 30 µm, the temperature variation is less than 5 K between the 8 and 16 radial cell cases. Further decreasing the axial resolution, at 50 and 100 µm (Fig. 5.4d-e), the convergence is more chaotic but is achieved with fewer cells (10 for an axial resolution of 100 µm).

To summarize, regardless of the axial resolution, the same trend is observed: if the radial mesh is too large, the ignition temperatures are overestimated but this overestimation gets lower as the number of cells in the radial direction is increased. As a consequence, in the simulations performed hereafter, the number of radial grid points is set at the maximum for which the solution convergence is obtained.

Nevertheless, the results still depend on the axial refinement and this aspect is further analyzed in the next section.

5.2.1.3 Axial discretization

Figure 5.5 shows the effect of changing the grid axial resolution on the computed ignition points of stoichiometric methane/air mixtures when varying the inlet velocity.

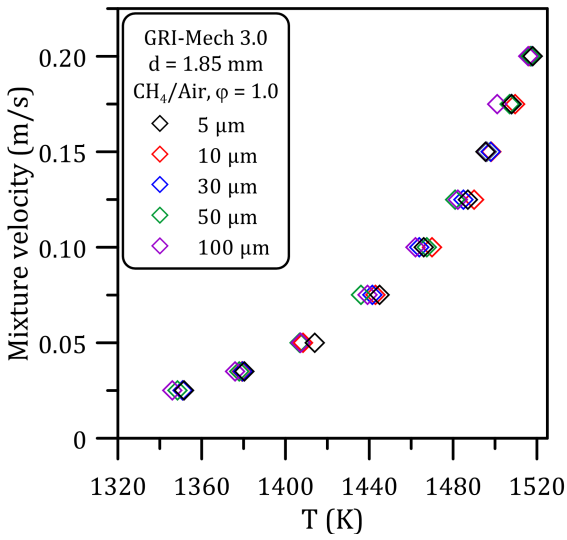

Figure 5.5: Results obtained with varying the axial refinement.

The ignition temperatures computed show a standard deviation less than 4 K, demonstrating a sufficient independence of the solution on the axial refinement. However, as observed in Section 5.2.1.2 a too large or a too small axial grid size leads to unsatisfactory results with changing the radial discretization.
Therefore, for the simulations performed hereafter the axial resolution was set between 10 and 30 µm, while the number of grid points is set at the maximum allowing solution convergence.

5.2.1.4 Temperature and transport effect

In the simulations, the experimental wall temperature profiles are given as boundary conditions. However, the temperature measurements have an overall error less than 3%, as explained in Chapter 2. In order to check the influence of this experimental uncertainty on the computed ignition temperatures, simulations were performed by perturbing uniformly the boundary wall temperature profile by ± 50 K. The results are shown in Fig. 5.6 for a stoichiometric methane/air mixture and compared to

those obtained with the experimental temperature profile (black line).

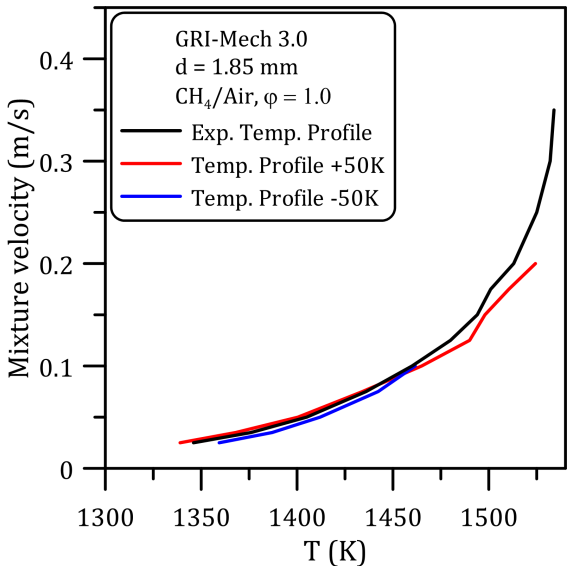

Figure 5.6: Effect of the temperature profile on the computed ignition temperature.

When the temperature profile is increased by 50 K (red line), the computed ignition temperature is weakly affected (deviation less than 11 K, mainly at high inlet velocity). The same observation holds for the opposite case (-50 K, blue line), but only when the inlet velocity remains below 0.10 m/s. Indeed, for larger flow rates, the mixture does not auto-ignite because of thermal effect: the reactor bulk is cooled by the fresh gases and the resulting temperature does not allow flame ignition. Thus, it can be concluded, excluding the extreme cases for which ignition is not observed, a 3% error in the temperature measurements does not affect significantly the computed ignition temperatures.
The effect of the transport properties is also tested. To this end, simulations are performed by varying the Lennard-Jones self-collision diameter of the reactants (CH_4, N_2, O_2) and the main chain carriers, namely H and OH. As previously, a stoichiometric methane/air mixture reacting in a 1.85 mm internal diameter reactor is considered (GRI-mech. 3.0). The inlet velocity is set at 0.15 m/s and the experimentally measured wall temperature profile given as boundary condition. Under this condition, the ignition temperature computed using the non-modified GRI-mech. 3.0 is 1521.19 K. Then, the scattering cross sections are changed independently by $\pm$ 0.5 Å. The results are shown in Fig. 5.7.

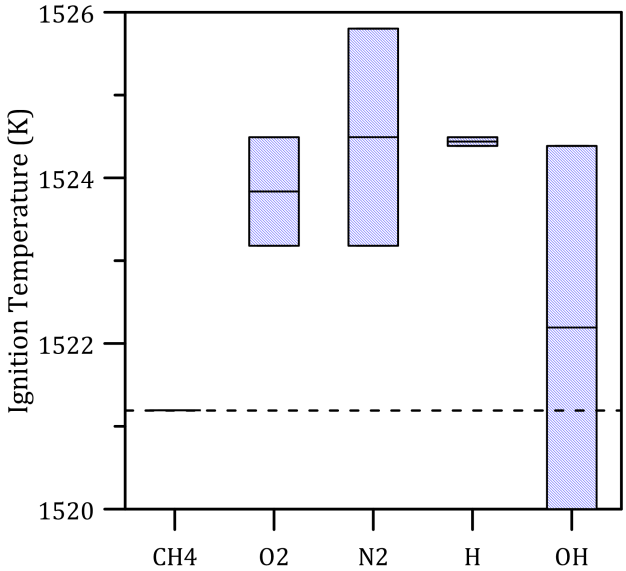

Figure 5.7: Transport properties effect on the ignition temperatures.

While a change in the CH_4 scattering cross section do not have an impact on the computed ignition temperature, for the other species the temperature increase or decrease with increasing or decreasing the scattering cross section respectively. In particular, for O_2, N_2 and H the temperatures are in average 2.64, 3.30 and 3.25 K higher than the computed ignition temperature (1521.19 K). A maximum deviation of 3.1 K is recorded for OH.
Therefore, it can be concluded that the results show a sufficient independence ($< 0.2\%$) on the scattering cross section. In the 2D axisymmetric simulations, the axial diffusion is neglected since overcome by convective transport.

5.3 Results

First, the 2D computation results obtained with the Konnov 0.5 and the GRI-Mech. 3.0 mechanisms are compared against the experimental data collected for methane/air mixtures in order to identify which mechanism performs better. Then, the impact of the dimensionality of the model on the ignition temperature is investigated. Finally, based on the conclusions drawn from the methane cases, numerical computations are extended to ethylene and acetylene/air mixtures.

5.3.1 Methane/Air

Figure 5.8 displays a comparison between the experimental and computed ignition temperatures of methane/air FREIs. Simulations were performed in a 1.85 mm

internal diameter channel and with the two mechanisms presented above.

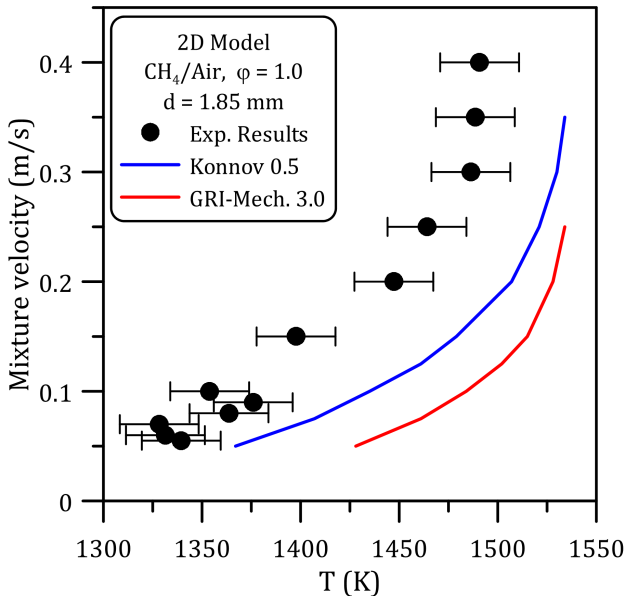

Figure 5.8: Ignition points obtained with Konnov 0.5 (blue) and GRI-Mech 3.0 (red) for methane/air mixtures (d = 1.85 mm).

Both mechanisms compute a decrease of the ignition temperature with the inlet velocity, consistently with the experimental observations (black circles). However, the Konnov 0.5 mechanism shows a better agreement with the experimental measurements than the GRI-Mech. 3.0 (red line), for which the temperatures are overestimated by about 100 K (7.0%). Furthermore, for inlet velocity higher than 0.25 m/s ignition is not observed. On the other hand, the gap between the experimental points and the Konnov 5.0 is in average 61 K (4.3%) and ignition is observed up to 0.35 m/s. The difference between experimental and numerical results is explained by several factors. First, the error of the experimental measurements: methane has a low chemiluminescence and, especially in the low velocity region, the ignition position is difficult to accurately localize. Second, during post-processing the ignition location is defined at the maximum of the CH^* signal: in average such signal is extended on 0.5 mm, which corresponds to a temperature variation of 30 K. Finally, the weakness of the numerical models (both physical and chemical) also has to be considered. Indeed the heat losses are not simulated in this model as well as the axial diffusion and the wall reactions. However, the Konnov 0.5 mechanism is able to reproduce the ignition point with an error of 4.3%.
Simulations were thus performed with the Konnov 0.5 changing the reactor diameter in order to confirm the conclusions achieved. According to the experiments, the diameters investigated are 1.0, 2.15 and 2.50 mm. The results are shown in Fig. 5.9.

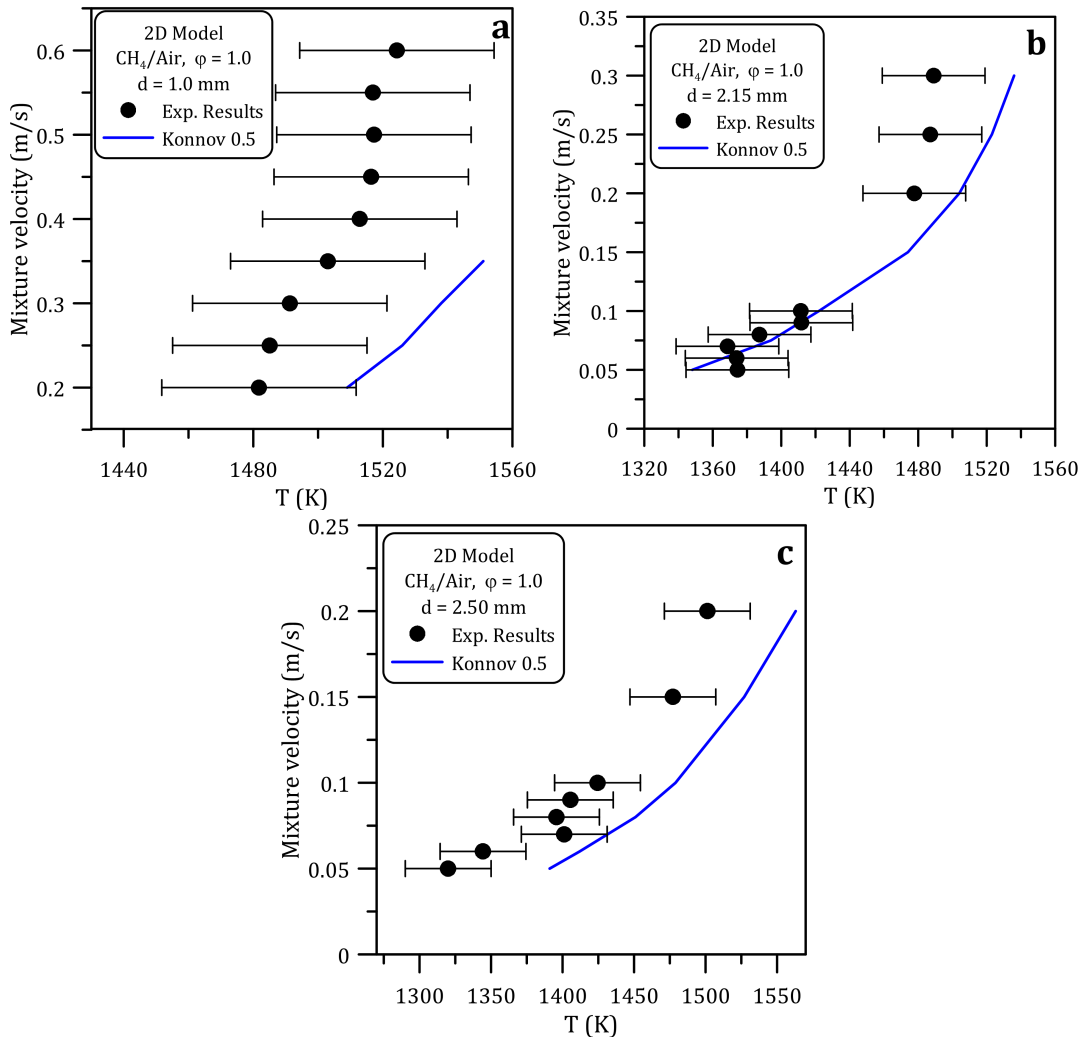

Figure 5.9: Ignition points obtained with changing the reactor diameter. a) d = 1.0 mm, b) d = 2.15 mm, c) d = 2.50 mm.

For d = 1.0 mm (Fig. 5.9a) mixture ignition was not observed for v > 0.35 m/s. However, the points obtained ($0.2 \leq$ v(m/s) ≤ 0.35) show an average deviation of 41 K (3%) as compared to the experimental results. At d = 2.15 at 2.50 mm (Fig. 5.9b-c) ignition was obtained for all the points investigated with an average error of 2% (30 K) and 3% (60 K) respectively, confirming the ability of the Konnov 0.5 mechanism to reproduce the ignition points with a small error.

5.3.2 Comparison between the numerical models

In Fig. 5.10 ignition temperatures computed with the 0D model are compared to those obtained with the 2D model. The simulations were performed using the profiles

extracted at half (purple) and at 3/4 of the radius (green). As done for the 2D model, the Konnov 0.5 (solid line) and the GRI-Mech 3.0 (dashed line) mechanisms are compared in order to confirm or not the conclusion achieved with the 2D model.

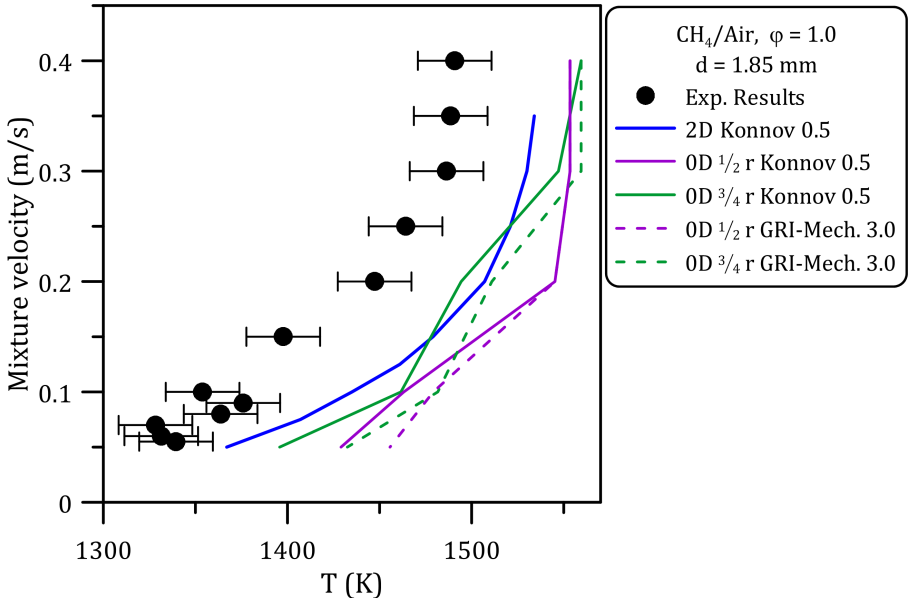

Figure 5.10: Comparison between the 0D and the 2D model.

While the ignition temperatures computed with the 2D model (blue line) decrease smoothly with the inlet velocity, the points obtained with the 0D model have a random distribution. For both time-temperature profile used (half and 3/4 radius), the points obtained with the GRI-Mech. 3.0 overestimate the ignition temperature (9.4%), likewise the results achieved with the 2D model (Section 5.3.1). Focusing on the points obtained with the Konnov 0.5 mechanism, the points computed with the 3/4 radius time-temperature profile are at slightly lower temperature compared to the half radius and close to the point obtained with the 2D model (maximum deviation 2%). However, the maximum deviation from the experimental results is of 8.0%, which corresponds to an overestimation of the ignition temperature by more than 108 K. These results demonstrate the importance of the model used to simulate the flame ignition in micro-reactors. Even if the results achieved with a simple 0D model (Konnov 0.5, 3/4 radius) are close to those obtained with the 2D model, the random distribution of the point proves that improvements are required to incorporate the hydrodynamics effects. Furthermore, as seen in Section 5.3.1, the reaction mechanism plays a fundamental role and has to be chosen carefully for simulations.

5.3.3 Ethylene/Air and Acetylene/Air

The 2D model is used to reproduce the ignition points of ethylene and acetylene/air mixtures reacting in a 1.0 and 0.7 mm i.d. channel respectively. The results obtained with GRI-Mech. 3.0 and Konnov 0.5 are compared. In Fig. 5.11 ignition temperatures obtained for ethylene/air mixtures are depicted.

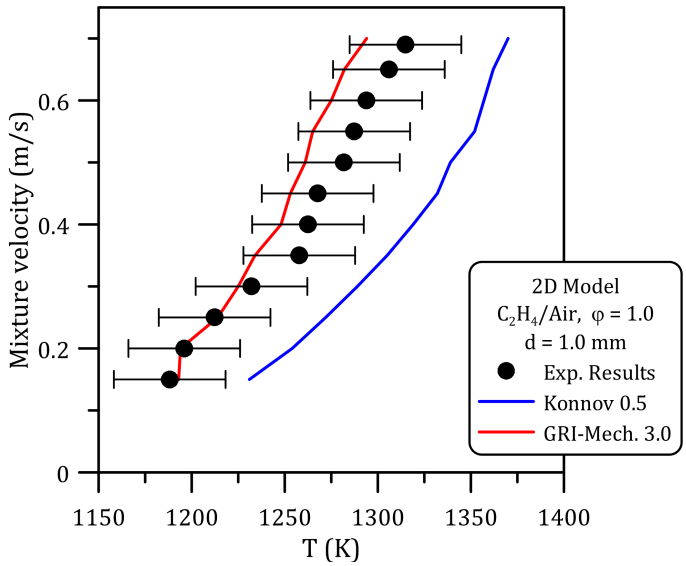

Figure 5.11: Results obtained with the 2D model for C_2H_4/air mixture (d = 1.0 mm).

Contrary to the observations for methane/air mixtures, for which the GRI-Mech. 3.0 overestimated ignition temperatures (Fig. 5.8), temperatures of ethylene/air mixtures are underestimated with an error of 2% (24 K) for $v \geq 0.3$ m/s. This confirms that this mechanism is not able to reproduce the ignition points well. The Konnov 0.5 mechanism gives better results: the error is on average 5%, which corresponds to 57 K. This deviation is smaller than the one observed for methane/air flames (Section 5.3.1): this is due to a better experimental determination of the ignition points, thanks to the high chemiluminescence of the ethylene flames.
For acetylene/air mixtures reacting in a 0.7 mm i.d. channel (Fig. 5.12) the results obtained have higher deviations. In this case the GRI-Mech. 3.0 overestimated the computed ignition temperature by 147 K (13%) and the points obtained at high inlet velocity ($v > 0.8$ m/s) have a more random distribution compared to those obtained at $v < 0.8$ m/s. Once again, the Konnov 0.5 mechanism shows a better agreement with the experimental points, but with an error of 8.4% (94 K), probably due to the reaction mechanism employed.

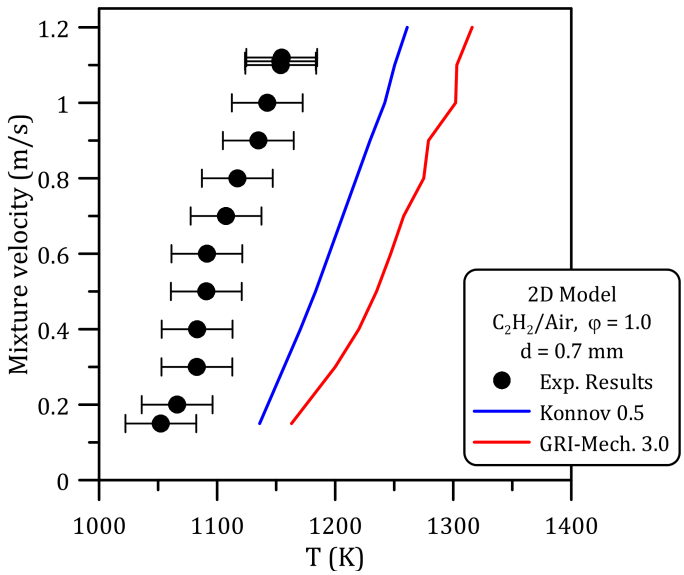

Figure 5.12: Results obtained with the 2D model for C_2H_2/air mixture (d = 0.7 mm).

Thus, the results achieved for methane/air mixtures are here extended to ethylene/air mixtures: the 2D model can reproduce the experimental results with an error less than 5% using the Konnov 0.5. For acetylene/air mixture, even if this mechanism gives better results compared to the GRI-Mech. 3.0, the error obtained is high (> 8%) and an optimized reaction mechanism is required.

5.4 Conclusions

Simulations were performed to compute the ignition points measured experimentally in the FREI region for the different operating conditions. Two numerical models were employed: a 2D model with a wall temperature profile (measured experimentally) set as a boundary condition, and a 0D model with user given time-temperature profiles extracted through numerical simulations at half and $^3/_4$ of the radius. Two reaction mechanisms were used during simulations: the GRI-Mech. 3.0 and the Konnov 0.5.

The results obtained with the 2D model for methane/air mixtures reacting in a 1.85 mm i.d. channel reveals that the Konnov 0.5 predicts the ignition points well with an error less than 4.3%. Such error is related to the experimental error and the approximation used during simulations (heat losses, axial diffusion and reaction to the wall neglected). This result is confirmed changing the reactor diameter. On the other hand, the GRI-Mech. 3.0 overestimates the ignition temperatures with an average of 100 K.

By comparing those results with the 0D model shows that the dimensionality plays a crucial role: the results obtained with the profile extracted at $^3/_4$ of the radius are

closer to the experimental results compared to the profile on the half radius, but with an overestimation of about 108 K.
The capability of the 2D model (Konnov 0.5) to reproduce the ignition points is hence confirmed for ethylene/air mixtures, for which the deviation from the experimental results is below 5%.
However, results with high deviation ($> 8\%$) are obtained for acetylene/air mixtures: in this latter case an optimized reaction mechanism is required.

Conclusions and Recommendations

This thesis aims at providing further insights on combustion behavior at micro-scale. The pioneering works in this field are from Maruta et al. [38], who developed an externally heated micro-reactor with a controlled temperature profile. This setup allowed the visualization of combustion modes exclusive to the micro-combustion and thus unseen at meso and macro-scale. Three main regimes with respect to the inlet velocity were identified: stable flames, FREI (Flames with Repetitive Extinction and Ignition) and weak flames. In the following experimental studies, a special consideration was given to the weak flame regime since these flames were early associated with the auto-ignition temperature (AIT) [42]. The other flame regimes and their dependence on the operating conditions received little or no attention. Thus, despite the efforts made over the last decade, there exists a huge lack of information that prevents the development and the application of micro-combustors (*i.e.* Swiss-roll combustors).

During this work a new experimental platform has been developed. It consists of a micro-reactor heated externally by three blowtorches. The flame dynamics are studied at high frequency using an EMCCD camera equipped with a band-pass filter at 430 nm (CH^* emission), while the temperature profile along the reactor wall is monitored continuously by an infrared camera.

After establishing the optimal experimental configuration, the new system has been benchmarked against and its reliability tested on methane/air mixtures. The existence of the three flame regimes previously observed by Maruta et al. [38] (stable flame, FREI, weak flames) has been confirmed. Furthermore, transitional flames have been detected between the main regimes and have been investigated experimentally for the first time.

Within the stable flame regime, the vulnerability of the flame depends on its shape: the higher the flow rate, the higher the heat losses [45]. As a consequence, the flame anchors at nearly the same centerline temperature for a given composition, regardless of the flow rate. This result has been confirmed for different channel diameters but the stabilization temperature increases with the diameter. Indeed, decreasing the reactor the heat flux within the wall is enhanced and thus the flames stabilize

at higher temperature to compensate the external losses. Moreover, through the study of the effect of the equivalence ratio on the stable flame regime, a correlation between the wall stabilization temperature, the mixture velocity, the adiabatic temperature and laminar flame speed has been obtained.
In the FREI region, the ignition and extinction positions depend on the inlet velocity. At high mixture speed the thermal effect is dominant: the reactor bulk is cooled by the fresh gases and the low temperature causes the flame extinction. On the contrary, low inlet velocity conditions have longer wall/fresh gas conduction time scales: the bulk temperature is higher, allowing the flame to further propagate downstream. Previous numerical works [64, 65] have also pointed out the contribution of the exothermicity of the heterogeneous reactions at the wall in the flame stabilization: this effect is more evident at low flow rate, when the radial gradients are negligible, and in lean conditions. The frequencies of all the FREIs have also been determined: they increase almost linearly with the inlet velocity, validating the numerical observations of Pizza et al. [93]. Alike stable flames, the adiabatic temperature and the laminar flame speed play a crucial role in the flame propagation: when these two parameters are low, in other words, in fuel-lean and fuel-lean conditions, the low flame temperature avoids an efficient heat exchange with the fresh gases. As a consequence, the flame propagates on a shorter section but with a higher frequency. A reduction of the channel diameter results in higher frequency because of a larger S/V ratio and thus heat losses: the flame is quenched.
Weak flames have been found not to be related to AIT: the position at which the reaction zone stabilizes is influenced by the flame temperature, enabling the flame to anchors at lower temperature for near stoichiometric mixtures.
Oscillating FREIs have been detected between the stable flame and the FREI regimes. Their behavior strongly depends on the operating conditions. For fuel-lean and fuel-rich mixtures the flames are affected by thermo-diffusive instabilities [87] and thus fluctuate at high frequency without extinguishing. Such a dynamic has been observed even in a narrow channel (d = 1.0 mm) albeit the unit Lewis number: as shown by Jackson et al. [91] those instabilities are the consequence of the heat flux within the wall. For larger reactors and near the stoichiometry the dynamic of the oscillating FREI evolves and multiple oscillations have been observed before the flame extinction. In this latter case the mixture reignites before the extinction thanks to the high wall temperature: the fluid density rapidly changes and pressure waves are hence associated [31].
Another transitional regime, called oscillating weak flame, has been detected between the FREI and the weak flame regions. In this case the flame fluctuates at high frequency and the CH^* signal never goes down to zero. However, these flames exist in a reduced velocity range and are very difficult to detect.
Experimental studies with ethylene and acetylene/air mixtures have confirmed the correlation derived from methane stable flames between the adiabatic flame temperature, the laminar flame speed, the stabilization temperature and the inlet speed, considering the mixture diffusivity. The higher reactivity of these two fuels also

allows the FREI to be quenched further downstream, leading to a reduction of the frequencies. However, different behaviors have been observed in the transitional regimes: while ethylene oscillating flames have been observed only in very lean condition, this transitional region is much extended for acetylene. The oscillating flames detected are characterized either by multiple oscillations before extinction (near the stoichiometry) or by diffusive-thermal instabilities (fuel-lean and fuel-rich side). Based on these observations and considering that these instabilities may lead to hotspots and thus to safety issues, we discourage the use of acetylene in micro-combustors.
However, the high chemiluminescence of these fuels has facilitated studies in very lean conditions (down to $\varphi = 0.3$ for ethylene and 0.1 for acetylene). Nevertheless, only stable flames with very low luminosity, thus associated with the weak flames, and oscillating weak flames have been observed. Micro-combustion enables extending the flammability range and thus offers the expectations of clean combustion in small-scale reactors.
Aside from the experimental studies, numerical computations have been carried out in order to study the ignition in the FREI regime. Two models, a 2D and a 0D, have been compared and the 0D model could not give satisfactory results. Two reaction mechanisms have been compared employing the 2D model: the Konnov 0.5 and the GRI-Mech. 3.0. Computations for methane and ethylene/air mixtures have shown that the Konnov 0.5 performed better, with an error less than 5% regarding the ignition points. This deviation can be ascribed to experimental uncertainties because of the weak flame luminosity at the ignition time, and to assumptions in the numerical model, since the axial diffusivity, the heat losses and wall reactions are neglected. Concerning acetylene, the computed ignition points did not match with the experimental ones and a dedicated acetylene reaction mechanism is required.
Thanks to the experimental platform developed and validated in this work, important results have been achieved towards the understanding of the dynamic of the unstable regimes at micro-scale and the phenomena involved in the flame stabilization. In future experimental work the use of smaller range mass flow controllers is needed in order to further explore flames at very low inlet velocities and very-fuel lean conditions. Furthermore the system developed can be adapted for the use of liquid fuels.
However, many unresolved problems remain. Indeed, the chemical effects must be considered when studying micro-combustion. The preliminary simulations confirmed that the dimensionality and the assumptions play a crucial role in the results [34, 39] and has to be carefully considered. Thus, a detailed numerical model with heterogeneous and complex gas phase chemistry is required to investigate the flame ignition and deeply understand the flame behavior in both stable and unstable regimes. The data provided in this thesis may be used for the validation and the improvement of these numerical models as well as of kinetic mechanisms. Furthermore they can allow the study of the wall effect on the flame stabilization: the current knowledge of radical quenching is deficient, but this mechanism cannot be neglected

at small scale.

Bibliography

[1] R. Ghodssi and P. Lin, *MEMS materials and processes handbook*. Springer Science & Business Media, 2011, vol. 1.

[2] Y. Ju and K. Maruta, "Microscale combustion: technology development and fundamental research", *Progress in Energy and Combustion Science*, 37 (6), pp. 669–715, 2011.

[3] N. S. Kaisare and D. G. Vlachos, "A review on microcombustion: fundamentals, devices and applications", *Prog. Energy Combust. Sci.*, 38 (3), pp. 321–359, 2012.

[4] D. C. Kyritsis, S. Roychoudhury, C. S. McEnally, L. D. Pfefferle, and A. Gomez, "Mesoscale combustion: a first step towards liquid fueled batteries", *Experimental Thermal and Fluid Science*, 28 (7), pp. 763–770, 2004.

[5] A. C. Fernandez-Pello, "Micropower generation using combustion: issues and approaches", *Proceedings of the Combustion Institute*, 29 (1), pp. 883–899, 2002.

[6] J. Vican, B. F. Gajdeczko, F. L. Dryer, D. Milius, I. A. Aksay, and R. A. Yetter, "Development of a microreactor as a thermal source for microelectromechanical systems power generation", *Proceedings of the Combustion Institute*, 29 (1), pp. 909–916, 2002.

[7] L. Sitzki, K. Borer, E. Schuster, P. D. Ronney, and S. Wussow, "Combustion in microscale heat-recirculating burners", in *The Third Asia-Pacific Conference on Combustion*, Seoul, Korea, vol. 6, 2001, pp. 11–14.

[8] B. Lewis and G. von Elbe, *Combustion, Flames and Explosives of Gases*. Academic Press, 1961.

[9] M. Gerstein and W. B. Stine, "Analytical criteria for flammability limits", in *Symposium (International) on Combustion*, Elsevier, vol. 14, 1973, pp. 1109–1118.

[10] D. B. Spalding, "A theory of inflammability limits and flame-quenching", in *Proceedings of the Royal Society of London A: Mathematical, Physical and Engineering Sciences*, The Royal Society, vol. 240, 1957, pp. 83–100.

[11] J. R. Grove, "The measurement of quenching diameters and their relation to the flameproof grouping of gases and vapours", in *Instutute of Chemical Engineering Symposium*, London, 1968.

[12] A. Gutkowski, "Laminar burning velocity under quenching conditions for propane/air and ethylene/air flames", *Archivum combustionis*, 26 (3–4), p. 163, 2006.

[13] A. L. Berlad and A. E. Potter, "Prediction of the quenching effect of various surface geometries", in *Symposium (International) on Combustion*, Elsevier, vol. 5, 1955, pp. 728–735.

[14] A. E. Potter and A. L. Berlad, "The effect of fuel type and pressure on flame quenching", in *Symposium (International) on Combustion*, Elsevier, vol. 6, 1957, pp. 27–36.

[15] I. Glassman, R. A. Yetter, and N. G. Glumac, *Combustion*. Academic press, 2014.

[16] J. Ducarme, M. Gerstein, and A. H. Lefebvre, *Progress in Combustion Science and Technology: International Series of Monographs in Aeronautics and Astronautics*. Elsevier, 2014, vol. 1.

[17] I. A. Zeldovich, G. I. Barenblatt, V. B. Librovich, and G. M. Makhviladze, "Mathematical theory of combustion and explosions", 1985.

[18] J. Jarosinski and B. Veyssiere, *Combustion phenomena: Selected mechanisms of flame formation, propagation and extinction*. CRC press, 2009.

[19] R. Friedman and W. C. Johnston, "The Wall–Quenching of Laminar Propane Flames as a Function of Pressure, Temperature, and Air-Fuel Ratio", *Journal of Applied Physics*, 21 (8), pp. 791–795, 1950.

[20] F. J. Weinberg, "Combustion temperatures: the future?", *Nature*, 233, pp. 239–241, 1971.

[21] T. Takeno, K. Sato, and K. Hase, "A theoretical study on an excess enthalpy flame", in *Symposium (International) on Combustion*, Elsevier, 1981, pp. 465–472.

[22] T. Takeno and K. Sato, "A theoretical and experimental study on an excess enthalpy flame", *Progress in Astronautics and Aeronautics*, 76 (4), pp. 596–607, 1981.

[23] D. R. Hardesty and F. J. Weinberg, "Burners producing large excess enthalpies", *Combustion Science and Technology*, 8 (5–6), pp. 201–214, 1973.

[24] V. K. Khanna, "A study of the dynamics of laminar and turbulent fully and partially premixed flames", PhD thesis, Virginia Polytechnic Institute and State University, 2001.

[25] K. T. Kim, D. H. Lee, and S. Kwon, "Effects of thermal and chemical surface–flame interaction on flame quenching", *Combustion and flame*, 146 (1), pp. 19–28, 2006.

[26] M. Katsuki and T. Hasegawa, "The science and technology of combustion in highly preheated air", in *Symposium (International) on combustion*, Elsevier, vol. 27, 1998, pp. 3135–3146.

[27] A. Cavaliere and M. de Joannon, "Mild combustion", *Progress in Energy and Combustion science*, 30 (4), pp. 329–366, 2004.

[28] S. A. Lloyd and F. J. Weinberg, "A burner for mixtures of very low heat content", *Nature*, 251, pp. 47–49, 1974.

[29] S. A. Lloyd, "Limits to energy release and utilisation", *Nature*, 257, 1975.

[30] J. Li, S. K. Chou, W. M. Yang, and Z. W. Li, "A numerical study on premixed micro-combustion of ch4-air mixture: effects of combustor size, geometry and boundary conditions on flame temperature", *Chemical engineering journal*, 150 (1), pp. 213–222, 2009.

[31] D. G. Norton and D. G. Vlachos, "Combustion characteristics and flame stability at the microscale: a CFD study of premixed methane/air mixtures", *Chemical Engineering Science*, 58 (21), pp. 4871–4882, 2003.

[32] N. I. Kim, S. Kato, T. Kataoka, T. Yokomori, S. Maruyama, T. Fujimori, and K. Maruta, "Flame stabilization and emission of small swiss-roll combustors as heaters", *Combust. Flame*, 141 (3), pp. 229–240, 2005.

[33] N. I. Kim, S. Aizumi, T. Yokomori, S. Kato, T. Fujimori, and K. Maruta, "Development and scale effects of small swiss-roll combustors", *Proceedings of the Combustion Institute*, 31 (2), pp. 3243–3250, 2007.

[34] F. Bianco, S. Chibbaro, and G. Legros, "Low-dimensional modeling of flame dynamics in heated microchannels", *Chemical Engineering Science*, 122, pp. 533–544, 2015.

[35] F. Bianco, "Theoretical and numerical analysis of the interaction between dynamics and chemistry in reactive flows", PhD thesis, Paris 6, 2013.

[36] D. Norton and D. Vlachos, "A CFD study of propane/air microflame stability", *Combustion and Flame*, 138 (1–2), pp. 97–107, 2004.

[37] A. Veeraragavan and C. P. Cadou, "Flame speed predictions in planar micro/mesoscale combustors with conjugate heat transfer", *Combustion and Flame*, 158 (11), pp. 2178–2187, 2011.

[38] K. Maruta, T. Kataoka, N. I. Kim, S. Minaev, and R. Fursenko, "Characteristics of combustion in a narrow channel with a temperature gradient", *Proceedings of the Combustion Institute*, 30 (2), pp. 2429–2436, 2005.

[39] G. P. Gauthier, G. M. G. Watson, and J. M. Bergthorson, "An evaluation of numerical models for temperature-stabilized CH4/air flames in a small channel", *Combustion Science and Technology*, 184 (6), pp. 850–868, 2012.

[40] A. Kazakov and M. Frenklach, *DRM19*, http://www.me.berkeley.edu/drm/, 1994.

[41] G. M. G. Watson and J. M. Bergthorson, "The effect of chemical energy release on heat transfer from flames in small channels", *Combustion and Flame*, 159 (3), pp. 1239–1252, 2012.

[42] Y. Tsuboi, T. Yokomori, and K. Maruta, "Lower limit of weak flame in a heated channel", *Proceedings of the Combustion Institute*, 32 (2), pp. 3075–3081, 2009.

[43] Y. Tsuboi, T. Yokomori, and K. Maruta, "Study on ignition and weak flame in heated meso-scale channel", in *ASME 2007 International Mechanical Engineering Congress and Exposition*, American Society of Mechanical Engineers, 2007, pp. 155–158.

[44] A. Di Stazio, C. Chauveau, G. Dayma, and P. Dagaut, "Combustion in microchannels with a controlled temperature gradient", *Experimental Thermal and Fluid Science*, 73, pp. 79–86, 2016.

[45] J. Daou and M. Matalon, "Influence of conductive heat-losses on the propagation of premixed flames in channels", *Combustion and Flame*, 128 (4), pp. 321–339, 2002.

[46] D. R. Ballal and A. H. Lefebvre, "Ignition and flame quenching in flowing gaseous mixtures", in *Proceedings of the Royal Society of London A: Mathematical, Physical and Engineering Sciences*, The Royal Society, vol. 357, 1977, pp. 163–181.

[47] N. I. Kim and K. Maruta, "A numerical study on propagation of premixed flames in small tubes", *Combustion and flame*, 146 (1), pp. 283–301, 2006.

[48] K. Maruta, J. K. Parc, K. C. Oh, T. Fujimori, S. S. Minaev, and R. V. Fursenko, "Characteristics of microscale combustion in a narrow heated channel", *Combustion, Explosion and Shock Waves*, 40 (5), pp. 516–523, 2004.

[49] F. Richecoeur and D. C. Kyritsis, "Experimental study of flame stabilization in low reynolds and dean number flows in curved mesoscale ducts", *Proceedings of the Combustion Institute*, 30 (2), pp. 2419–2427, 2005.

[50] Y. Fan, Y. Suzuki, and N. Kasagi, "Experimental study of micro-scale premixed flame in quartz channels", *Proceedings of the Combustion Institute*, 32 (2), pp. 3083–3090, 2009.

[51] Y. Fan, Y. Suzuki, and N. Kasagi, "Quenching mechanism study of oscillating flame in micro channels using phase-locked oh-plif", *Proceedings of the Combustion Institute*, 33 (2), pp. 3267–3273, 2011.

[52] A. Fan, S. S. Minaev, E. V. Sereshchenko, Y. Tsuboi, H. Oshibe, H. Nakamura, and K. Maruta, "Dynamic behavior of splitting flames in a heated channel", *Combustion, Explosion, and Shock Waves*, 45 (3), pp. 245–250, 2009.

[53] S. S. Minaev, E. V. Sereshchenko, R. V. Fursenko, A. Fan, and K. Maruta, "Splitting flames in a narrow channel with a temperature gradient in the walls", *Combustion, Explosion, and Shock Waves*, 45 (2), pp. 119–125, 2009.

[54] H. Nakamura, A. Fan, S. S. Minaev, E. V. Sereshchenko, R. Fursenko, Y. Tsuboi, and K. Maruta, "Bifurcations and negative propagation speeds of methane/air premixed flames with repetitive extinction and ignition in a heated microchannel", *Combustion and Flame*, 159 (4), pp. 1631–1643, 2012.

[55] A. Alipoor and K. Mazaheri, "Studying the repetitive extinction-ignition dynamics for lean premixed hydrogen-air combustion in a heated microchannel", *Energy*, 73, pp. 367–379, 2014.

[56] E. Miyata, N. Fukushima, Y. Naka, M. Shimura, M. Tanahashi, and T. Miyauchi, "Direct numerical simulation of micro combustion in a narrow circular channel with a detailed kinetic mechanism", *Proceedings of the Combustion Institute*, 35 (3), pp. 3421–3427, 2015.

[57] J. F. Griffiths and J. A. Barnard, *Flame and combustion*. CRC Press, 1995.

[58] B. Bai, Z. Chen, H. Zhang, and S. Chen, "Flame propagation in a tube with wall quenching of radicals", *Combustion and Flame*, 160 (12), pp. 2810–2819, 2013.

[59] Y. Ju and B. Xu, "Theoretical and experimental studies on mesoscale flame propagation and extinction", *Proceedings of the Combustion Institute*, 30 (2), pp. 2445–2453, 2005.

[60] P. Popp and M. Baum, "Analysis of wall heat fluxes, reaction mechanisms, and unburnt hydrocarbons during the head-on quenching of a laminar methane flame", *Combustion and Flame*, 108 (3), pp. 327–348, 1997.

[61] H. Bongers and L. P. H. De Goey, "The effect of simplified transport modeling on the burning velocity of laminar premixed flames", *Combustion science and technology*, 175 (10), pp. 1915–1928, 2003.

[62] A. Ern and V. Giovangigli, "Thermal diffusion effects in hydrogen-air and methane-air flames", *Combustion Theory and Modelling*, 2 (4), pp. 349–372, 1998.

[63] A. Korsakova, V. Gubernov, V. Bykov, and U. Maas, "The effect of soret diffusion on stability of rich premixed hydrogen–air flames", *International Journal of Hydrogen Energy*, 41 (39), pp. 17 670–17 675, 2016.

[64] S. Raimondeau, D. Norton, D. G. Vlachos, and R. I. Masel, "Modeling of high-temperature microburners", *Proceedings of the Combustion Institute*, 29 (1), pp. 901–907, 2002.

[65] P. Aghalayam, P. A. Bui, and D. G. Vlachos, "The role of radical wall quenching in flame stability and wall heat flux: hydrogen-air mixtures", *Combustion Theory and Modelling*, 2 (4), pp. 515–530, 1998.

[66] V. V. Gubernov, S. S. Minaev, V. I. Babushok, and A. V. Kolobov, "The effect of depletion of radicals on freely propagating hydrocarbon flames", *Journal of Mathematical Chemistry*, 53 (10), pp. 2137–2154, 2015.

[67] Y. Kizaki, H. Nakamura, T. Tezuka, S. Hasegawa, and K. Maruta, "Effect of radical quenching on CH4/air flames in a micro flow reactor with a controlled temperature profile", *Proceedings of the Combustion Institute*, 35 (3), pp. 3389–3396, 2015.

[68] Y. Saiki and Y. Suzuki, "Effect of wall surface reaction on a methane-air premixed flame in narrow channels with different wall materials", *Proceedings of the Combustion Institute*, 34 (2), pp. 3395–3402, 2013.

[69] C. M. Miesse, R. I. Masel, C. D. Jensen, M. A. Shannon, and M. Short, "Submillimeter-scale combustion", *AIChE Journal*, 50 (12), pp. 3206–3214, 2004.

[70] K. L. Wray and T. J. Connolly, "Thermal conductivity of clear fused silica at high temperatures", *Journal of Applied Physics*, 30 (11), pp. 1702–1705, 1959.

[71] M. De Joannon, A. Cavaliere, T. Faravelli, E. Ranzi, P. Sabia, and A. Tregrossi, "Analysis of process parameters for steady operations in methane mild combustion technology", *Proceedings of the combustion institute*, 30 (2), pp. 2605–2612, 2005.

[72] P. Sabia, "Experimental and numerical studies of mild combustion processes in model reactors", PhD thesis, Università degli Studi di Napoli Federico II, 2006.

[73] S. S. Minaev, K. Maruta, and R. Fursenko, "Nonlinear dynamics of flame in a narrow channel with a temperature gradient", *Combustion Theory and Modelling*, 11 (2), pp. 187–203, 2007.

[74] H. Oshibe, H. Nakamura, T. Tezuka, S. Hasegawa, and K. Maruta, "Stabilized three-stage oxidation of DME/air mixture in a micro flow reactor with a controlled temperature profile", *Combustion and Flame*, 157 (8), pp. 1572–1580, 2010.

[75] S. Suzuki, M. Hori, H. Nakamura, T. Tezuka, S. Hasegawa, and K. Maruta, "Study on cetane number dependence of diesel surrogates/air weak flames in a micro flow reactor with a controlled temperature profile", *Proceedings of the Combustion Institute*, 34 (2), pp. 3411–3417, 2013.

[76] M. Hori, A. Yamamoto, H. Nakamura, T. Tezuka, S. Hasegawa, and K. Maruta, "Study on octane number dependence of prf/air weak flames at 1–5 atm in a micro flow reactor with a controlled temperature profile", *Combustion and Flame*, 159 (3), pp. 959–967, 2012.

[77] M. Hori, H. Nakamura, T. Tezuka, S. Hasegawa, and K. Maruta, "Characteristics of n-heptane and toluene weak flames in a micro flow reactor with a controlled temperature profile", *Proceedings of the Combustion Institute*, 34 (2), pp. 3419–3426, 2013.

[78] A. Yamamoto, H. Oshibe, H. Nakamura, T. Tezuka, S. Hasegawa, and K. Maruta, "Stabilized three-stage oxidation of gaseous n-heptane/air mixture in a micro flow reactor with a controlled temperature profile", *Proceedings of the Combustion Institute*, 33 (2), pp. 3259–3266, 2011.

[79] H. H. Freytag and F. Boberg, *Handbuch der Raumexplosionen*. Verlag Chemie, 1965.

[80] R. D. Coffee, "Cool flames and autoignitions: two oxidation processes", *Loss Prev AIChE Tech Manual*, 13, pp. 74–82, 1980.

[81] Chemsafe, *Database for evaluated safety characteristics*, 2006.

[82] F. Norman, "Influence of process conditions on the auto-ignition temperature of gas mixtures", PhD thesis, Katholieke Universiteit Leuven, 2008.

[83] W. A. Affens and R. S. Sheinson, "Autoignition: the importance of the cool flame in the two-stage-process", *Loss Prev*, 13, pp. 83–88, 1980.

[84] N. P. Setchkin, "Self-ignition temperatures of combustible liquids", *Journal of Research of the National Bureau of Standards*, 53 (1), pp. 49–66, 1954.

[85] N. N. Semenov, "Chemical kinetics and chain reactions", *Oxford University Press*, 1935.

[86] Y. Tsuboi, T. Yokomori, and K. Maruta, "Extinction characteristics of premixed flame in heated microchannel at reduced pressures", *Combustion Science and Technology*, 180 (10–11), pp. 2029–2045, 2008.

[87] T. Miroshnichenko, V. Gubernov, K. Maruta, and S. Minaev, "Diffusive–thermal oscillations of rich premixed hydrogen–air flames in a microflow reactor", *Combustion Theory and Modelling*, 20 (2), pp. 313–327, 2016.

[88] V. Gubernov, A. Kolobov, V. Bykov, and U. Maas, "Investigation of rich hydrogen–air deflagrations in models with detailed and reduced kinetic mechanisms", *Combustion and Flame*, 168, pp. 32–38, 2016.

[89] A. Korsakova, V. Gubernov, A. Kolobov, V. Bykov, and U. Maas, "Stability of rich laminar hydrogen–air flames in a model with detailed transport and kinetic mechanisms", *Combustion and Flame*, 163, pp. 478–486, 2016.

[90] P Gregory, D. M. G. Smith, M. Frenklach, N. W. Moriarty, B. Eiteneer, and M. Goldenberg, *Gri 3.0*, http://www.me.berkeley.edu/gri_mech/.

[91] T. L. Jackson, J. Buckmaster, Z. Lu, D. C. Kyritsis, and L. Massa, "Flames in narrow circular tubes", *Proceedings of the Combustion Institute*, 31 (1), pp. 955–962, 2007.

[92] M. A. Bucci, J.-C. Robinet, and S. Chibbaro, "Global stability analysis of 3d micro-combustion model", *Combustion and Flame*, 167, pp. 132–148, 2016.

[93] G. Pizza, C. E. Frouzakis, J. Mantzaras, A. G. Tomboulides, and K. Boulouchos, "Dynamics of premixed hydrogen/air flames in microchannels", *Combustion and Flame*, 152 (3), pp. 433–450, 2008.

[94] A. Alipoor and K. Mazaheri, "Combustion characteristics and flame bifurcation in repetitive extinction-ignition dynamics for premixed hydrogen-air combustion in a heated micro channel", *Energy*, 109, pp. 650–663, 2016.

[95] H. Nakamura, R. Tanimoto, T. Tezuka, S. Hasegawa, and K. Maruta, "Soot formation characteristics and pah formation process in a micro flow reactor with a controlled temperature profile", *Combustion and Flame*, 161 (2), pp. 582–591, 2014.

[96] A. K. Dubey, T. Tezuka, S. Hasegawa, H. Nakamura, and K. Maruta, "Sooting behavior of ethane in a micro flow reactor with a controlled temperature profile", *25th ICDERS*, 2015.

[97] M. Sánchez-Sanz, D. Fernández-Galisteo, and V. N. Kurdyumov, "Effect of the equivalence ratio, Damkohler number, Lewis number and heat release on the stability of laminar premixed flames in microchannels", *Combustion and Flame*, 161 (5), pp. 1282–1293, 2014.

[98] C. Robinson and D. B. Smith, "The auto-ignition temperature of methane", *Journal of hazardous materials*, 8 (3), pp. 199–203, 1984.

[99] C. A. Naylor and R. V. Wheeler, "The ignition of gases. Part VI. ignition by a heated surface. mixtures of methane with oxygen and nitrogen, argon, or helium", *Journal of the Chemical Society (Resumed)*, pp. 2456–2467, 1931.

[100] L. Ye, Y. Pan, J. Jiang, and W. Zhang, "A numerical study of the auto-ignition temperatures of CH4/air, C3H8/air, CH4/C3H8/air and CH4/CO2/air mixtures", *Journal of Loss Prevention in the Process Industries*, 29, pp. 85–91, 2014.

[101] N. S. Kaisare and D. G. Vlachos, "Optimal reactor dimensions for homogeneous combustion in small channels", *Catalysis Today*, 120 (1), pp. 96–106, 2007.

[102] V. N. Kurdyumov and C. Jiménez, "Propagation of symmetric and non-symmetric premixed flames in narrow channels: Influence of conductive heat-losses", *Combustion and Flame*, 161 (4), pp. 927–936, 2014.

[103] G. P. Gauthier, G. M. G. Watson, and J. M. Bergthorson, "Burning rates and temperatures of flames in excess-enthalpy burners: a numerical study of flame propagation in small heat-recirculating tubes", *Combustion and Flame*, 161 (9), pp. 2348–2360, 2014.

[104] S. C. Crow and F. H. Champagne, "Orderly structure in jet turbulence", *Journal of Fluid Mechanics*, 48 (03), pp. 547–591, 1971.

[105] T. Kamada, H. Nakamura, T. Tezuka, S. Hasegawa, and K. Maruta, "Study on combustion and ignition characteristics of natural gas components in a micro flow reactor with a controlled temperature profile", *Combustion and Flame*, 161 (1), pp. 37–48, 2014.

[106] S. Kikui, H. Nakamura, T. Tezuka, S. Hasegawa, and K. Maruta, "Study on combustion and ignition characteristics of ethylene, propylene, 1-butene and 1-pentene in a micro flow reactor with a controlled temperature profile", *Combustion and Flame*, 163, pp. 209–219, 2016.

[107] X. Li, L. Jia, H. Nakamura, T. Tezuka, S. Hasegawa, and K. Maruta, "Study on flame responses and ignition characteristics of CH4/O2/CO2 mixture in a micro flow reactor with a controlled temperature profile", *Applied Thermal Engineering*, 84, pp. 360–367, 2015.

[108] C. Xu and A. A. Konnov, "Validation and analysis of detailed kinetic models for ethylene combustion", *Energy*, 43 (1), pp. 19–29, 2012.

[109] G Jomaas, X. Zheng, D. Zhu, and C. Law, "Experimental determination of counterflow ignition temperatures and laminar flame speeds of c 2–c 3 hydrocarbons at atmospheric and elevated pressures", *Proceedings of the Combustion Institute*, 30 (1), pp. 193–200, 2005.

[110] J. Kariuki and R. Balachandran, "Experimental investigation of dynamics of premixed acetylene–air flames in a micro-combustor", *Experimental Thermal and Fluid Science*, 34 (3), pp. 330–337, 2010.

[111] P. Instrument, *ProEM EMCCD Camera System*, 2012.

[112] R. M. Sova, M. J. Linevsky, M. E. Thomas, and F. F. Mark, "High-temperature infrared properties of sapphire, alon, fused silica, yttria, and spinel", *Infrared physics & technology*, 39 (4), pp. 251–261, 1998.

[113] P. Conte, "Utilizzo delle bande dell'infrarosso termico in tecniche di remote sensing per applicazioni in ambito urbano", PhD thesis, Alma Mater Studiorum Universitá di Bologna, 2012.

[114] A. B. FLIR, *The Ultimate Infrared Handbook for R&D professionals.*

[115] A. E. Lutz, F. M. Rupley, and R. J. Kee, *EQUIL: A Chemkin implementation of Stanjan for computing chemical equilibria*, 1998.

[116] R. J. Kee, J. F. Grcar, M. D. Smooke, and J. A. Miller, *A Fortran Program for Modelling Steady Laminar One-dimensional Premixed Flames*, 1985.

[117] A. A. Konnov, "Detailed reaction mechanism for small hydrocarbons combustion", *Release 0.5*, 2000.

[118] R. J. Kee, M. E. Coltrin, and P. Glarborg, *Chemically reacting flow: theory and practice*. John Wiley & Sons, 2005.

[119] M. E. Coltrin, R. J. Kee, and J. A. Miller, "A mathematical model of the coupled fluid mechanics and chemical kinetics in a chemical vapor deposition reactor", *Journal of The Electrochemical Society*, 131 (2), pp. 425–434, 1984.

[120] S. Ostrach and F. K. Moore, "Theory of laminar flows", *Section F, FK Moore (Ed.) Princetown University Press, Princeton*, 1964.

[121] M. E. Coltrin, R. J. Kee, and J. A. Miller, "A Mathematical Model of Silicon Chemical Vapor Deposition Further Refinements and the Effects of Thermal Diffusion", *Journal of The Electrochemical Society*, 133 (6), pp. 1206–1213, 1986.

[122] A. E. Lutz, R. J. Kee, and J. A. Miller, "SENKIN: a FORTRAN program for predicting homogeneous gas phase chemical kinetics with sensitivity analysis", Sandia National Labs., Livermore, CA (USA), Tech. Rep., 1988.

[123] A. Savitzky and M. J. E. Golay, "Smoothing and differentiation of data by simplified least squares procedures.", *Analytical Chemistry*, 36 (8), pp. 1627–1639, 1964.

[124] H. G. Weller, G. Tabor, H. Jasak, and C. Fureby, "A tensorial approach to computational continuum mechanics using object-oriented techniques", *Computers in physics*, 12 (6), pp. 620–631, 1998.

[125] F. Contino, H. Jeanmart, T. Lucchini, and G. D'Errico, "Coupling of in situ adaptive tabulation and dynamic adaptive chemistry: an effective method for solving combustion in engine simulations", *Proceedings of the Combustion Institute*, 33 (2), pp. 3057–3064, 2011.

[126] ANSYS, *Academic research release 16.0 help system. FLUENT user guide*, ANSYS, Inc., 2015.

[127] V. K. Bityukov and V. A. Petrov, "Optical quartz glass as a reference substance for the thermal conductivity coefficient of partially transparent materials", *High Temperature*, 38 (2), pp. 293–299, 2000.

Appendices

Appendix A

Emission Spectroscopy Diagnostic

The flame emission spectroscopy (FES) of stoichiometric oxygen-enriched CH_4/air flames (25% oxygen, 75% nitrogen) was investigated. The aim of these experiments was to determine the flame spectrum and thus to choose an adapted bandpass filter for the EMCCD camera.
A 2.15 mm inner diameter reactor was employed to this end. It was placed vertically and a high mixture velocity was set (10 m/s). The flame was ignited at the reactor outlet.
A HR4000 Fiber Optic Spectrometer (Ocean Optics), with a focal length of 101 mm and 14–grating, was employed to detect the flame chemiluminescence at the exact focus point. This device allows the expansion of a 200 – 1100 nm wavelength region on 3648 pixels. The entrance aperture used is 5 µm, giving a spectral resolution of 1 nm. A silica lens with a 60 mm focal length was used.
The spectrometer calibration was operated using a He lamp and two emission lines were considered, 501 and 667 nm. The device function was determined from the line half-height width and found equal to 0.3600 ± 0.0085 nm. The He spectrum obtained is presented in Fig. A1.

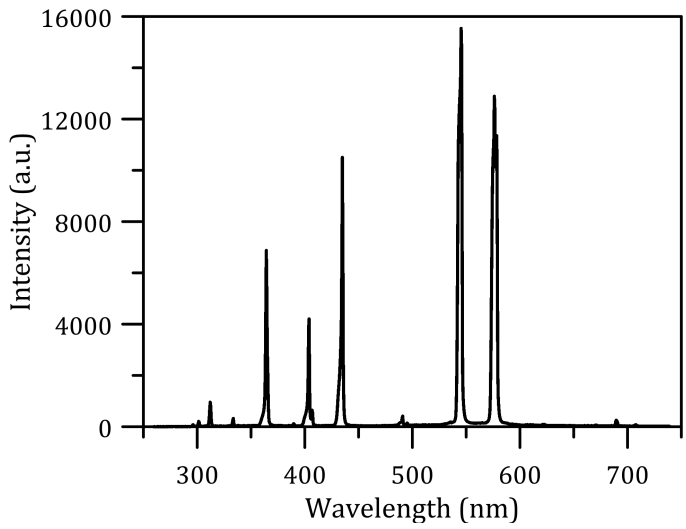

Figure A1: He spectrum.

A typical flame emission spectrum observed with this experimental setting is shown in Fig. A2.

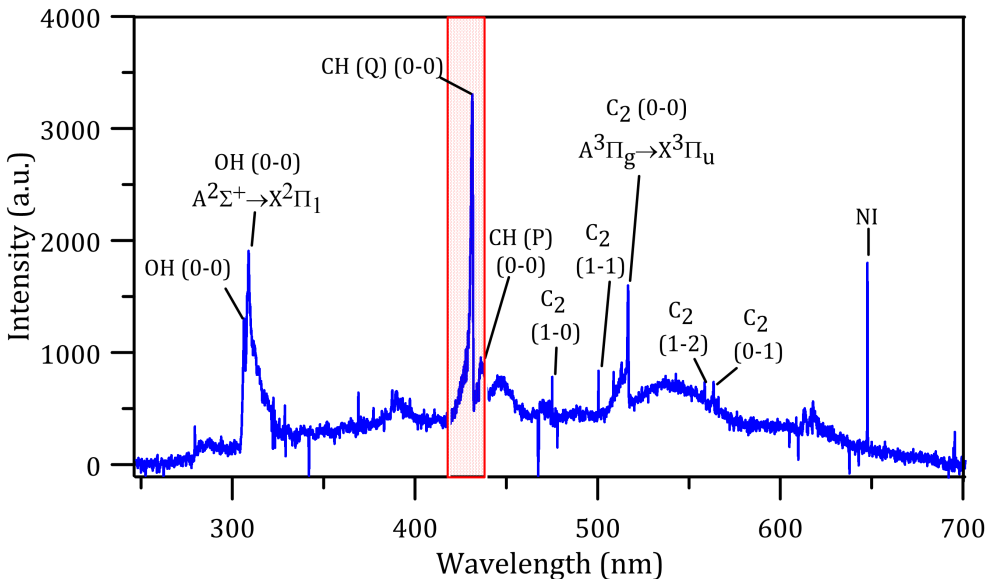

Figure A2: Emission spectrum of an oxygen-enriched methane/air flame.

Several bands are clearly visible, and in particular those of OH ($A^2\Sigma^+ \rightarrow X^2\Pi_1$, 308.9 nm) and CH ($A^2\Delta \rightarrow X^2\Pi$, 431.5 nm). Other bands correspond to C_2 and NI. As described in Chapter 3, the system used to heat up the micro-reactor relies on H_2/O_2 flames. These flames produce OH^*, so as the flames inside the reactor. Thus, in order to study the flame chemiluminescence without perturbation from the external heat sources, CH^* emission was preferred to follow the flame dynamics.

Therefore, and for all experiments, a band-pass filter (20BF10–430) was used to detect the signal at 430 nm. This filter bandwidth is shown in Fig. A3 and depicted as a red box in Fig. A2: the P and Q branches of CH^* emission are well visualized.

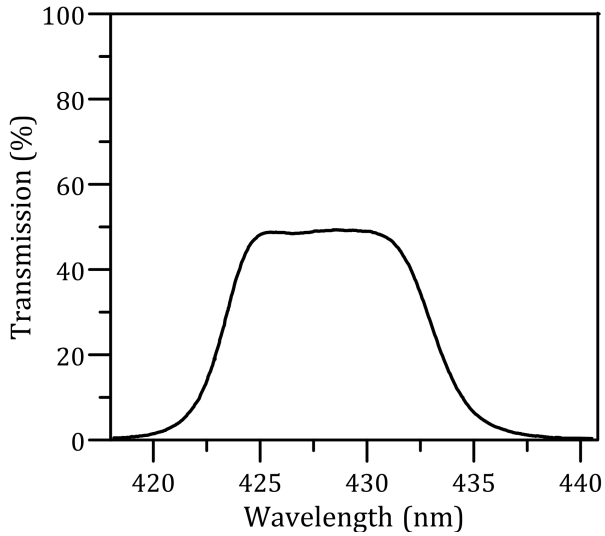

Figure A3: Bandwidth of the filter used in the present work.

Appendix B

Post-processing procedure

FREI frequency and characteristic times

The regularity over time of FREI allows performing a frequency analysis of the collected CH* signal and thus determining the flame characteristic times. To this end, a cross-section is operated on the CH* signal: for every single frame, the signal of all pixels (1648 ×8 domain) is summed up and averaged onto one pixel, as illustrated in Fig. B1.

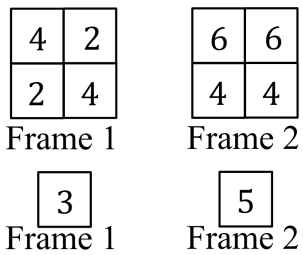

Figure B1: Example of averaged cross-section on a 2×2 domain.

The time evolution of the overall CH* signal, that is to say over the entire FREI zone, can then be visualized on successive frames. An example of such a graph is presented in Fig. B2.

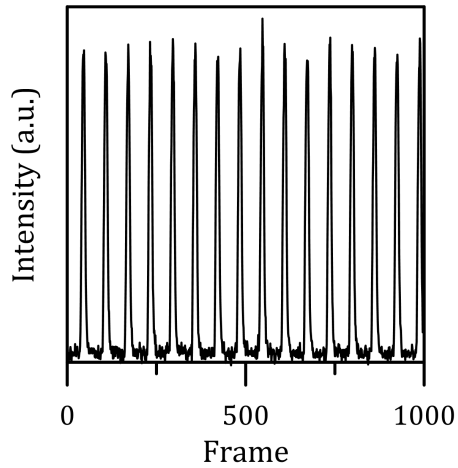

Figure B2: Example of cross-section on 1000 frames. The recording frequency is 4260 Hz.

Performing a Fourier Transform analysis on the spectral cross-section of CH^* signal, the characteristic frequency of flames in FREI regime can be extracted.
In order to explain the characteristic frequency dependence on several parameters, the characteristic times between ignition and extinction must also be determined. In this case the cross-section is operated on a specific ROI (region of interest), which is the reactor section in which the flame ignites and extinguishes. Figure B3 displays an example of such cross-section. The time between ignition and extinction (τ_{IE}, time required for the flame to propagate upstream, from ignition to extinction) and the time between the extinction and ignition (τ_{EI}, time required to heat up and ignite the fresh mixture) are also shown.

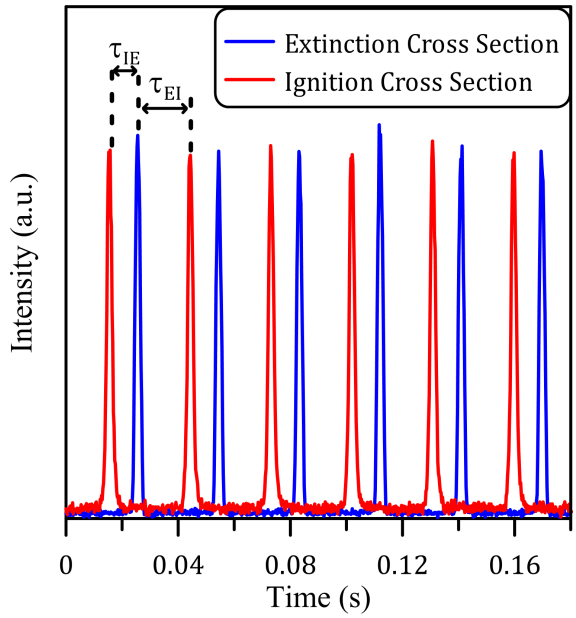

Figure B3: Determination of characteristic times.

Evolution of CH* intensity

In order to study the flame evolution in the FREI regime, an analysis of the time evolution of the CH* signal is performed. The aim of this post-processing step is to track the CH* evolution during the flame propagation: it is then possible to compare the FREI characteristics when varying the operating conditions, and to detect the eventual presence of multiple CH* peaks.
The post-processing sequence is as follows. First, a background subtraction is operated to reduce the noise. A Savitzky-Golay filter [123] is then applied: it consists in a low-pass filter, based on a local least-squares polynomial approximation (order 2 typically), that smooths the signal without distorting it. The maximum of the CH* signal, *i.e.* the height of the CH* peak, is thus determined from the smoothed signal. An example of the result obtained is shown in Fig. B4.

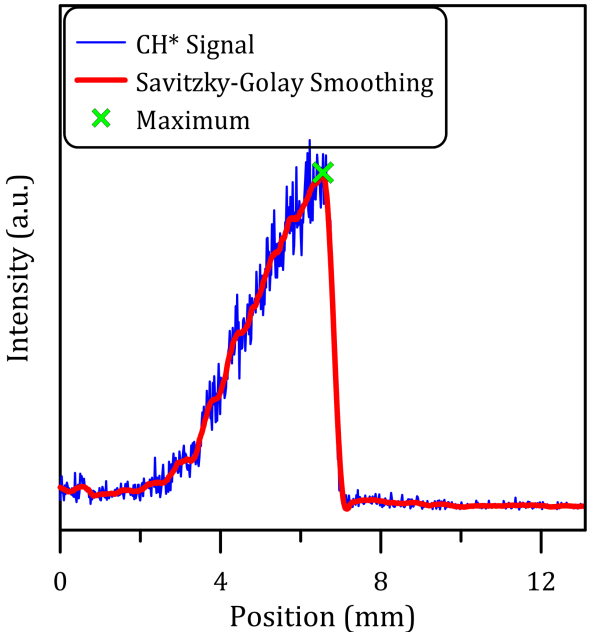

Figure B4: Example of post-processing applied on a single instant.

Applying this algorithm on each frame, the time evolution of the maximum of the CH* signal is obtained. The result is shown in Fig. B5: after the flame ignition (initial increase of CH* intensity) the signal intensity increases sharply during the flame propagation and reaches a maximum. Then the intensity decreases and falls down to zero when the flame extinguishes.

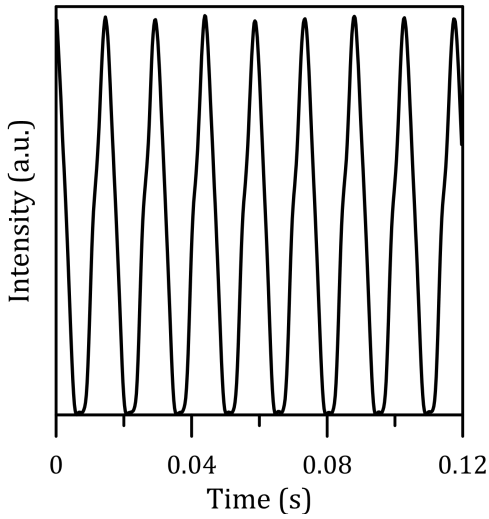

Figure B5: Temporal evolution of maximum CH* peaks (CH_4/air, $\varphi = 1$, d = 2.15 mm, v = 0.32 m/s).

To analyze the flame evolution during the propagation phase (between the ignition and the maximum of CH* intensity), only the frames between the ignition time and

the time for which the signal reaches its maximum (within a cycle) must be selected. To identify those frames, the first derivative has been calculated. Indeed, during the buildup of the CH* signal, the local first derivative is positive, and can thus be a criterion of selection. An example of application of this method is illustrated in Fig. B6: the time evolution of maximum CH* signal and the points selected using this method on several FREI cycles can be observed.

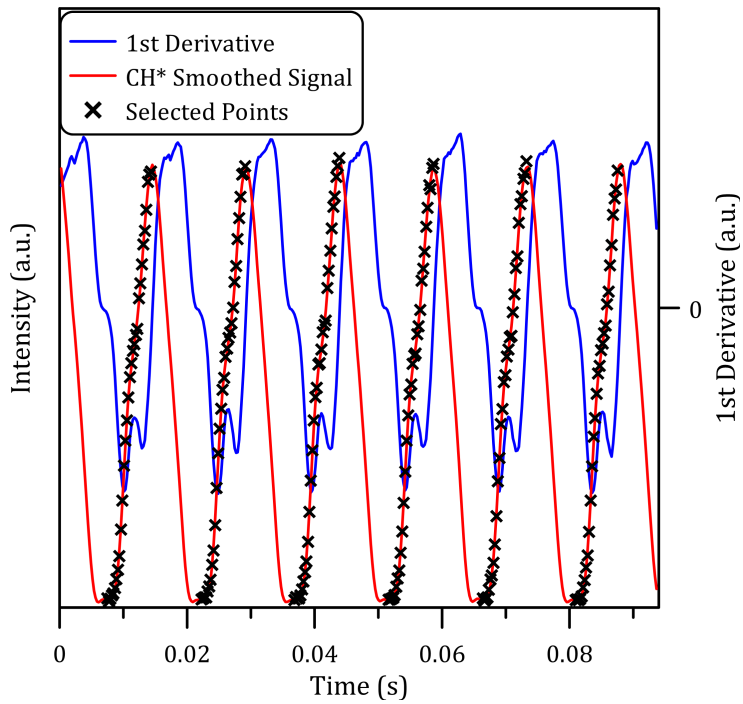

Figure B6: Point selected during propagation phase (CH_4/air, $\varphi = 1$, d = 2.15 mm, v = 0.32 m/s).

Then the points obtained for each single FREI cycle are collapsed onto one plot and reported in term of spatial coordinate to clearly visualize the displacement of the flame front. Such a plot is shown in Fig. B7: the blue crosses represent the maximum CH* peaks (of each frame, Fig. B4) obtained over several cycles after filtering, while the red squares represent the points extracted by applying the first derivative (thus corresponding to the propagation phase). Then a running average is applied on these points.

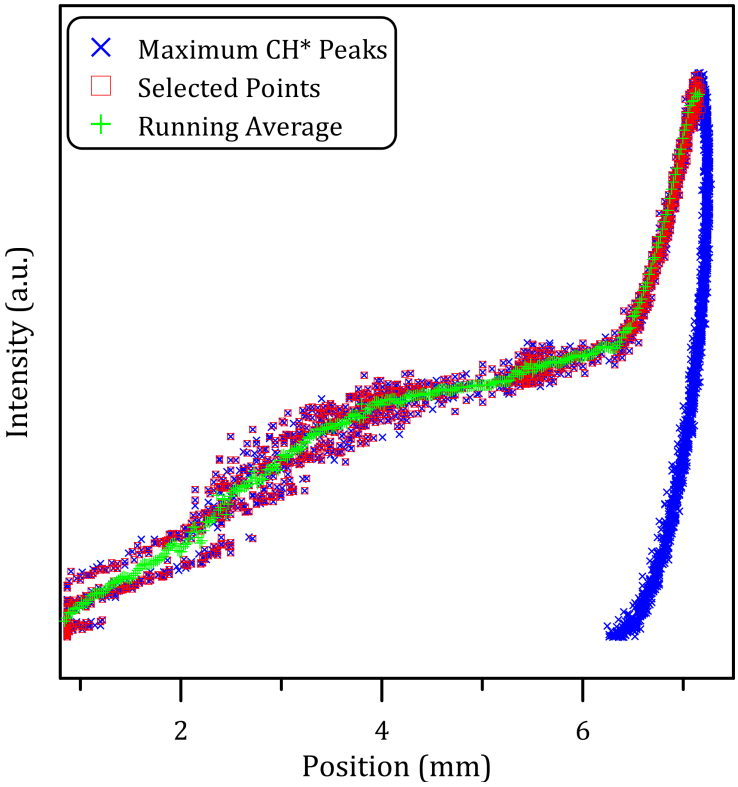

Figure B7: Points selected during the propagation phase over several cycles (CH_4/air, $\varphi = 1$, d = 2.15 mm, v = 0.32 m/s).

This post processing also allows to check the eventual presence of multiple CH^* peaks. As explained in [52–55], the presence of multiple reactive peaks is due to the combustion of remaining unburned species. By way of example, the CH^* signal of an ethylene/air FREI flame is presented in Fig. B8. In Fig. B8a the running average of the flame progression is depicted: one can notice discontinuities, especially at 4.8 and 6.5 mm. Stepping back and visualizing the CH^* signal at different instants, in Fig. B8b, multiple peaks are visible. The flame ignition (in red), characterized by a low CH^* emission, occurs 9.15 ms after the end of the previous cycle. Then the flame propagates and the CH^* intensity increases. During the propagation, the flame splits into two reactive peaks at 9.85 ms (in blue). The brightest peak corresponds to the ordinary flame that keeps propagating upstream, whereas the other one is a secondary peak probably due to the combustion of unburned gases. While the flame keeps moving forward, a new splitting occurs at 10.09 ms (in green), between 6 and 7 mm. These two successive splitting are in line with the discontinuities observed in Fig. B8a and thus highlight the importance of following the progression over time of the flame considered.

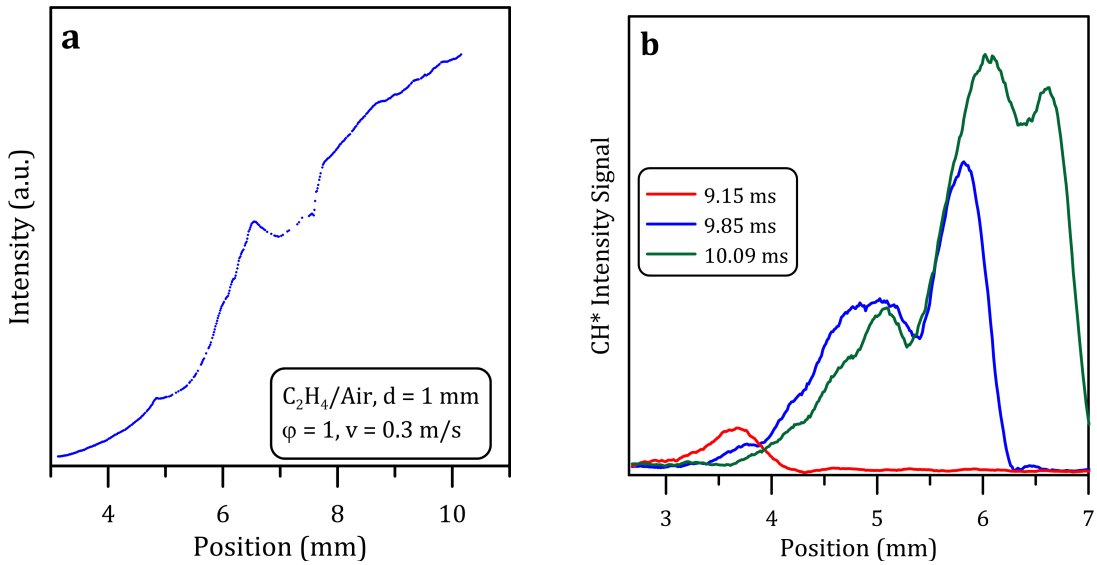

Figure B8: Progression of a stoichiometric ethylene/air flame: a) flame progression, b) CH* emission at successive instants.

These post-processing methods were only devoted to the visualization of the flame front. It may also be interested to analyze the flame as a whole and to this end a spatial integration of the CH* signal acquired at each instant is operated. Figure B9 illustrates such an integration.

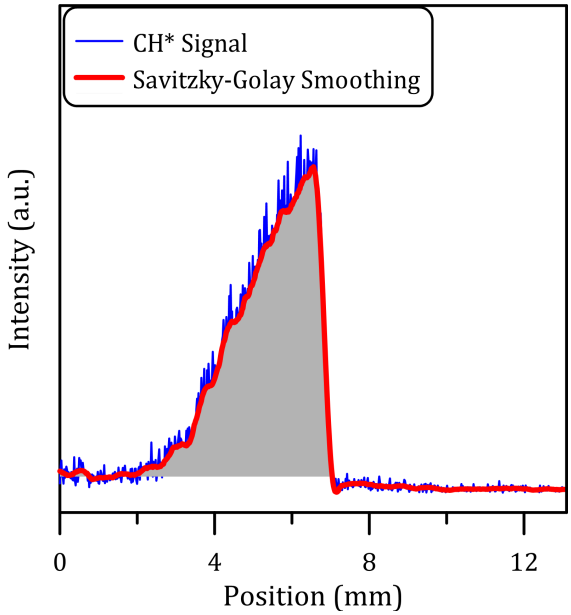

Figure B9: Example of spatially integration on the CH* signal (grey area).

By doing so, the time evolution of the integrated CH* signal can be constructed for each point of the FREI domain as a function of time, as illustrated in Fig. B10. The

spatial integrated CH* signals are thus used to study the dynamics of the unstable flames and the eventual presence of multiple oscillations (oscillating FREI).

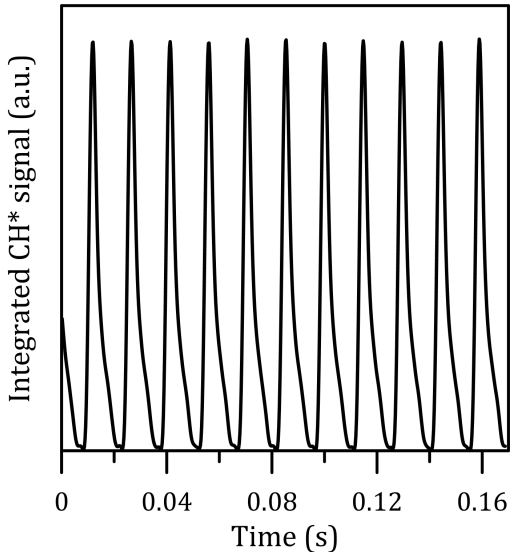

Figure B10: Spatially integrated CH* signal at v = 0.32 m/s (CH_4/air, $\varphi = 1$, d = 2.15 mm).

Appendix C

Numerical Simulation with non-reactive mixtures

In parallel with the experimental study carried out in the present thesis, numerical works were also performed. The aim of such works was to reproduce the results obtained experimentally (flame position, FREI frequency,...). The first attempt was carried out during the thesis of Charles Endouard, who developed a numerical model using OpenFoam [124]. It consisted of a 2D axisymmetric microchannel with detailed chemistry associated with the TDAC (Tabulation and Dynamic Adaptive Chemistry) method, developed by F. Contino [125]. Unfortunately, this model was not completed within the prescribed time, and not all the objectives were met despite the achievement of first encouraging results.
A second attempt was carried out during the master II of Geetesh Waghela, using the software package Ansys (Fluent, [126]) and a simple kinetic model (2-step reaction mechanism). However, the numerical results achieved were unsatisfactory.
Although these numerical models have failed, they provided us some important information that cannot be overlooked when modeling micro-combustion. As already discussed in Chapter 1, a 2D axisymmetric model, or a 3D one, is essential to take into account the Poiseuille flow field inside the tube, in order to get all the other profiles (species, temperature,...). Also, in order to reproduce the heat transfer between the fluid, the flame and the reactor wall, a model with constant Nusselt is not sufficient, as already demonstrated by several works [31, 34, 39]. In addition, the nature of the reactor wall has to be taken into account [2, 68, 69]. Indeed, the heat transfer takes place from outside the channel inwards, as the reactor is heated externally by the blowtorches. The interaction between the flame and the wall needs also to be carefully considered. Moreover, we believe that the use of an adaptive mesh that could represent an advantage when simulating the FREI dynamics.
Thereafter we used these models in the non-reactive cases to extract useful data about the flow characteristic in micro-channels. They are used for the analysis of

the experimental results achieved in the present work.
To this end we modeled the flow characteristics in micro-reactors varying the channel diameter and the inlet velocity in line with the experimental conditions. 3D simulations were performed considering only a 90° section of the tube (Fig. C1). The mixture considered was CH_4/air in stoichiometric condition, and we observed that the mixture composition does not impact the results obtained. The external diameter was set to 6 mm, while the internal diameter was varied accordingly to the experimental conditions (0.7, 1.0, 1.85, 2.0, 2.15 and 2.5 mm). The tube length was set to 100 mm. A Cartesian grid was used and the total cell number was 568639, of which 443790 cells were used to model the fluid. The reactor wall was modeled as quartz (fused silica) and its heat transfer characteristics were introduced following the literature available on the subject [70, 127]. Thermal conduction through the wall was considered while radiation and gravitational effects were neglected. The humidity of the gas has not been taken into account and the roughness of the inner wall either. The temperature profile, measured experimentally, was imposed on the outer surface of the tube: to this end a temperature law was introduced (T vs Z, Fig. C2). In Figs. C3 and C4 the results obtained are depicted. Figure C3 shows the temperature contours for a 1.85 mm inner diameter reactor and v = 0.6 m/s. Figure C4 depicts the evolution of the fluid velocity with the temperature in a 1.85 mm inner diameter reactor.

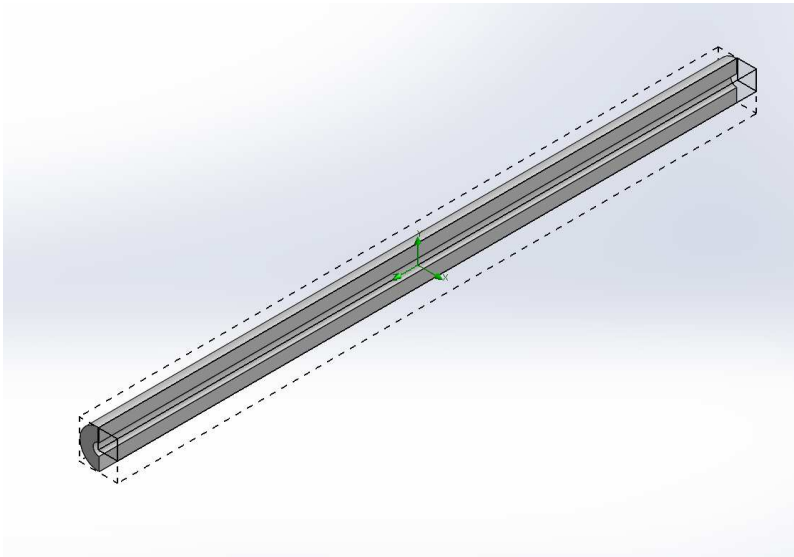

Figure C1: 3D model.

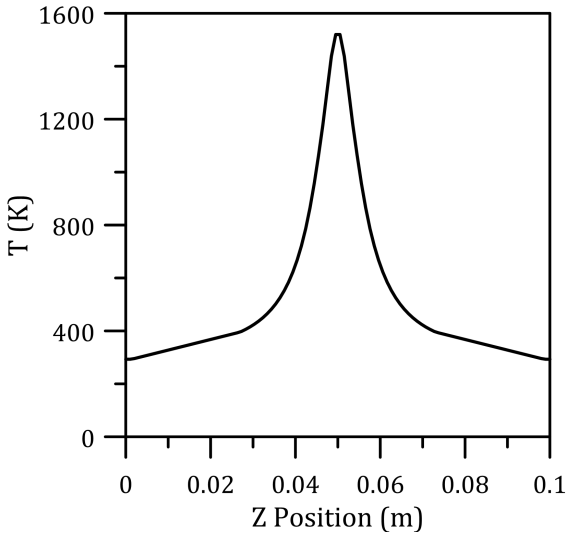

Figure C2: Temperature profile at the wall.

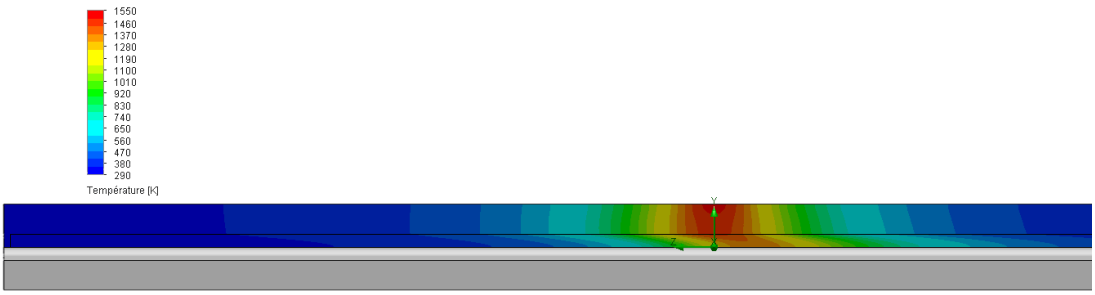

Figure C3: Temperature contours for methane/air mixture, d = 1.85 mm, v = 0.6 m/s.

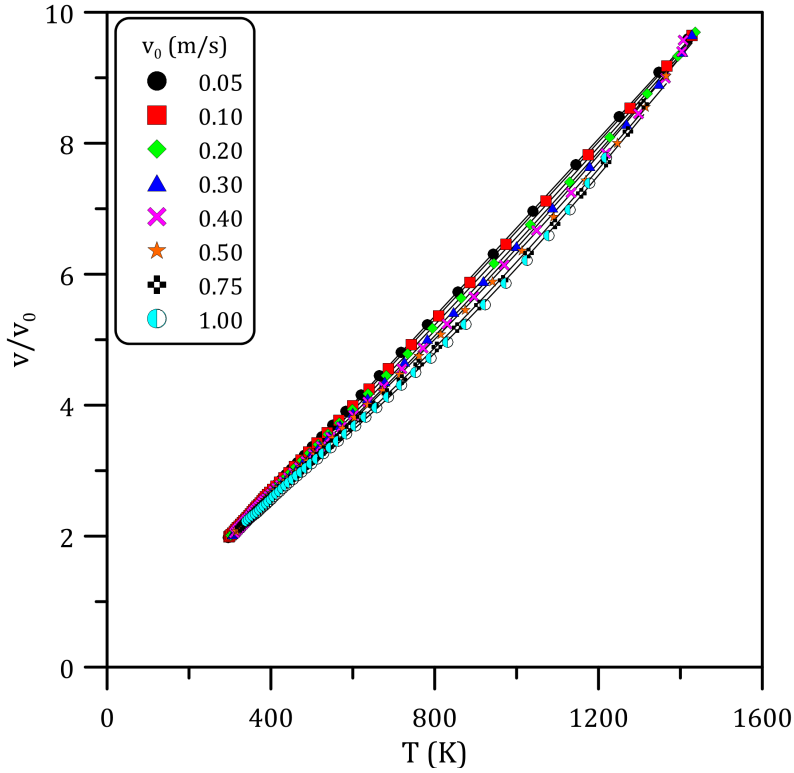

Figure C4: Evolution of v/v_0 with the wall temperature (v_0 = inlet velocity, d = 1.85 mm).

Appendix D

Results: Methane/Air mixtures

The time evolutions of the spatially integrated CH* signals are presented for CH_4/air mixtures at $\varphi = 0.7$ (Fig. D1) and 1.5 (Fig. D2).

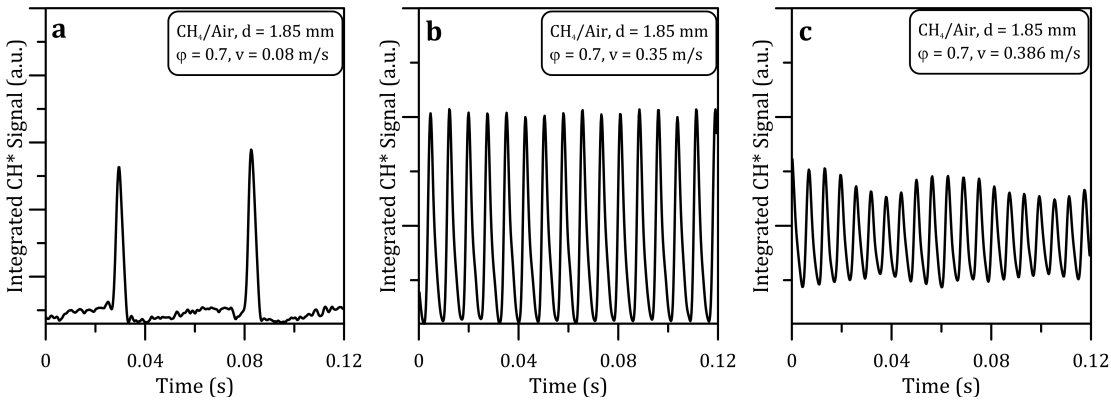

Figure D1: Temporal evolution of CH_4/Air unstable flames at $\varphi = 0.7$. a) v = 0.08 m/s, Fr = 19.8 Hz (FREI), b) v = 0.35 m/s, Fr = 131.1 Hz (FREI), c) v = 0.386 m/s, Fr = 160.0 Hz (Oscillating FREI).

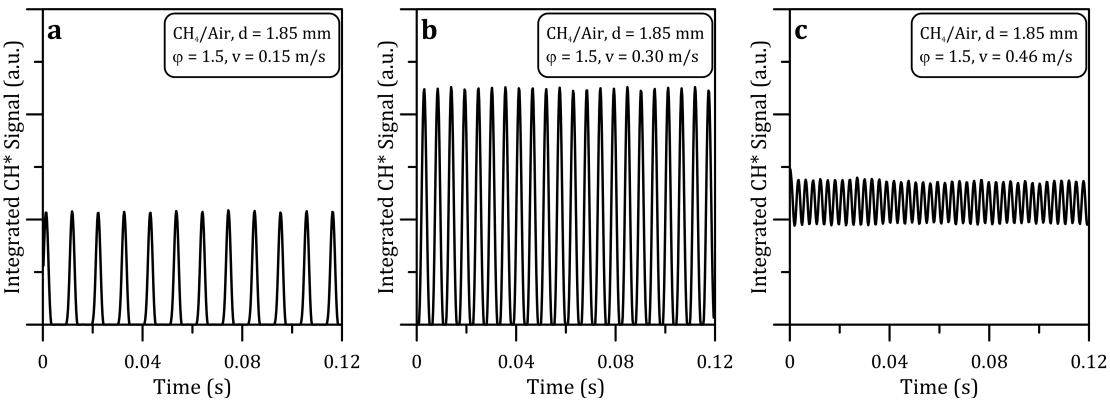

Figure D2: Temporal evolution of CH_4/Air unstable flames at $\varphi = 1.5$. a) v = 0.15 m/s, Fr = 95.7 Hz (FREI), b) v = 0.30 m/s, Fr = 183.1 Hz (FREI), c) v = 0.46 m/s, Fr = 336.1 Hz (Oscillating FREI).

Appendix E

Results: Ethylene and Acetylene/Air mixtures

Characteristic Times

In Figs. E1 and E2 the characteristic times τ_{IE} and τ_{EI} are presented for C_2H_4/air and C_2H_2/air mixtures at different equivalence ratios.

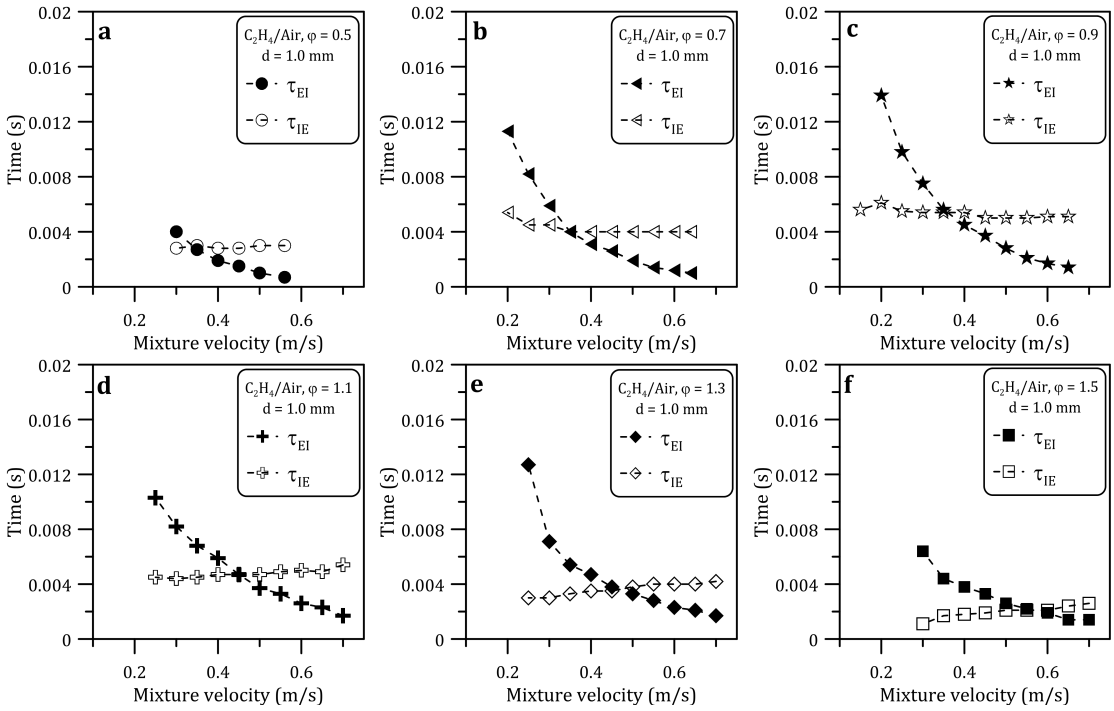

Figure E1: Characteristic times of C_2H_4/Air unstable flames at different equivalence ratios. a) $\varphi = 0.5$, b) $\varphi = 0.7$, c) $\varphi = 0.9$, d) $\varphi = 1.1$, e) $\varphi = 1.3$, f) $\varphi = 1.5$.

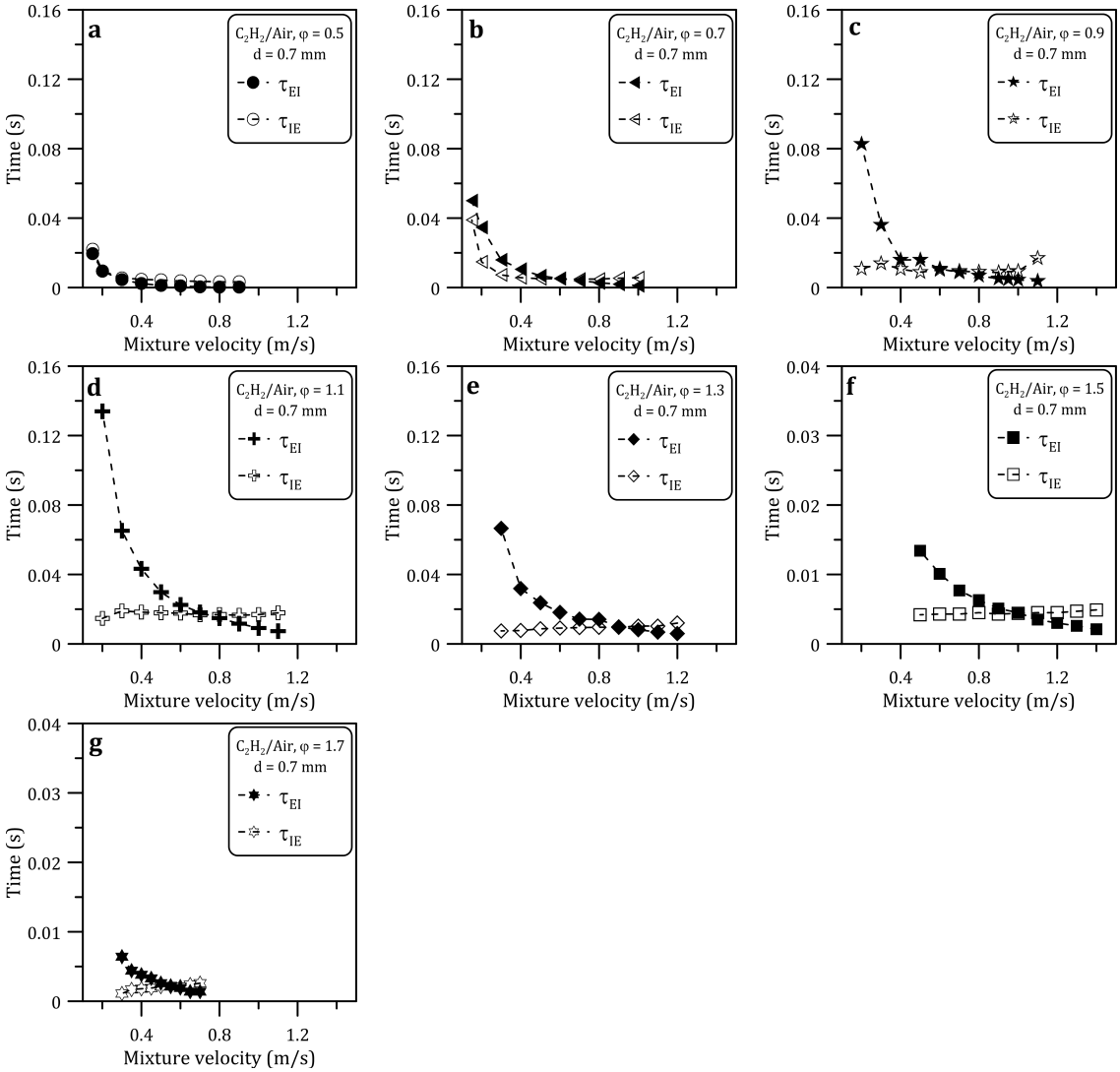

Figure E2: Characteristic times of C_2H_2/Air unstable flames at different equivalence ratios. a) $\varphi = 0.5$, b) $\varphi = 0.7$, c) $\varphi = 0.9$, d) $\varphi = 1.1$, e) $\varphi = 1.3$, f) $\varphi = 1.5$, g) $\varphi = 1.7$.

Time Evolutions and Mamimum CH* progression

The time evolutions of the spatially integrated CH* signals are presented for C_2H_4/air and C_2H_2/air mixtures at different equivalence ratios (Figs. E3-E13). If oscillating flames are not present, the signals are presented at the low and the high limit of the FREI region.

Then, in Figs. E14 and E15 the maximum of CH* of C_2H_4/air and C_2H_2/air mixtures are displayed at different equivalence ratios with changing the inlet velocity.

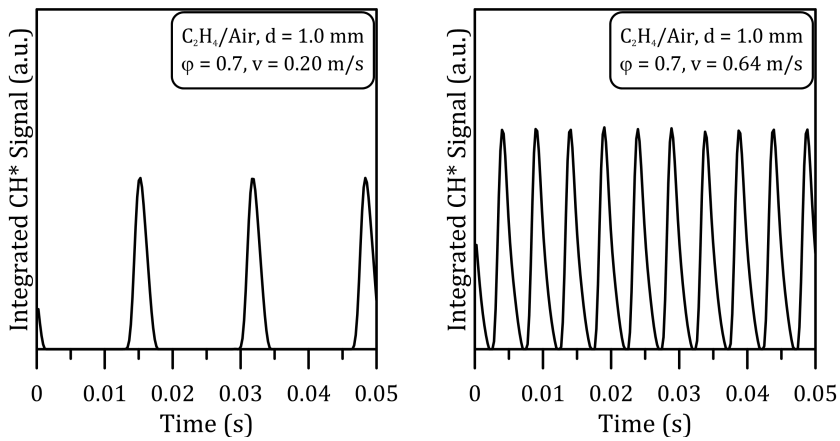

Figure E3: Temporal evolution of C_2H_4/Air unstable flames at $\varphi = 0.7$. Only ordinary FREI were observed at low (at v = 0.20 m/s, Fr = 60.1 Hz, on the left) and high (v = 0.64 m/s, Fr = 201.3 Hz, on the right) inlet velocity.

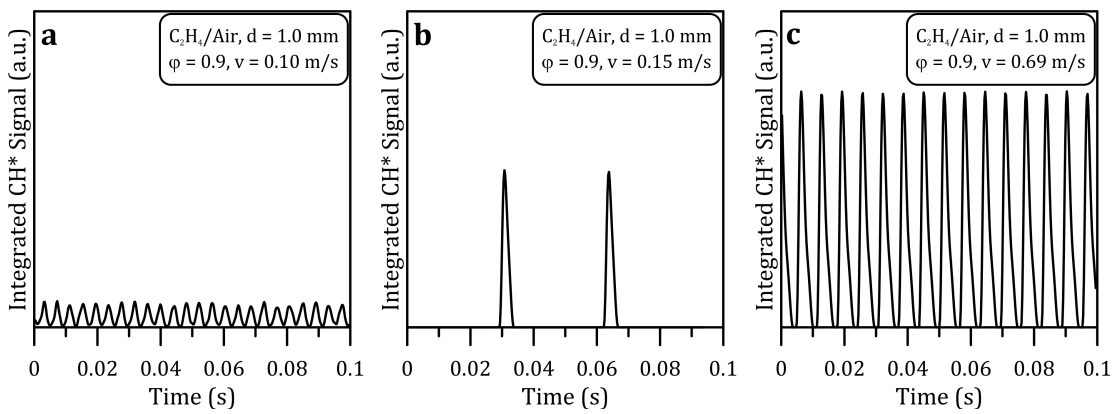

Figure E4: Temporal evolution of C_2H_4/Air unstable flames at $\varphi = 0.9$. a) v = 0.10 m/s, Fr = 246.1 Hz (Oscillating weak flame), b) v = 0.15 m/s, Fr = 30.2 Hz (FREI), c) v = 0.69 m/s, Fr = 154.8 Hz (FREI).

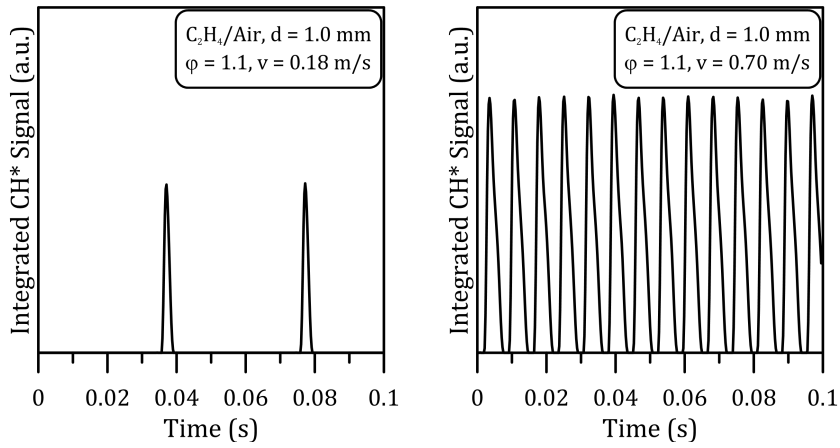

Figure E5: Temporal evolution of C_2H_4/Air unstable flames at $\varphi = 1.1$. Only ordinary FREI were observed at low (at v = 0.18 m/s, Fr = 25.1 Hz, on the left) and high (v = 0.70 m/s, Fr = 139.1 Hz, on the right) inlet velocity.

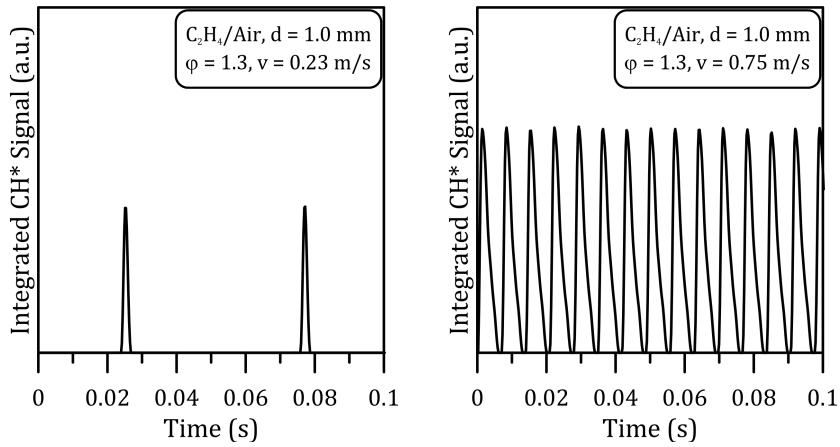

Figure E6: Temporal evolution of C_2H_4/Air unstable flames at $\varphi = 1.3$. Only ordinary FREI were observed at low (at v = 0.23 m/s, Fr = 18.7 Hz, on the left) and high (v = 0.75 m/s, Fr = 143.3 Hz, on the right) inlet velocity.

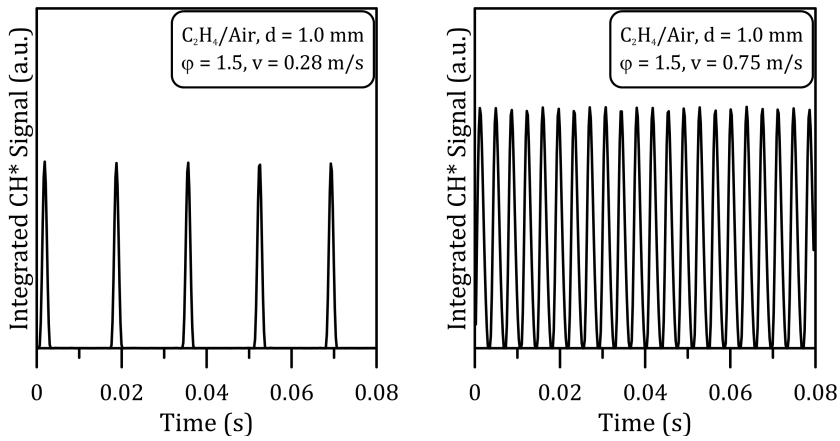

Figure E7: Temporal evolution of C_2H_4/Air unstable flames at $\varphi = 1.5$. Only ordinary FREI were observed at low (at v = 0.28 m/s, Fr = 42.1 Hz, on the left) and high (v = 0.75 m/s, Fr = 233.3 Hz, on the right) inlet velocity.

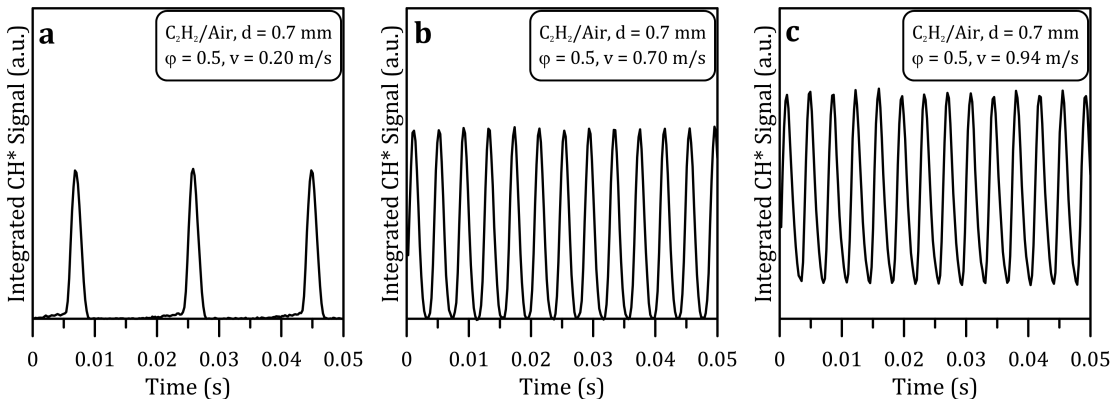

Figure E8: Temporal evolution of C_2H_2/Air unstable flames at $\varphi = 0.5$. a) v = 0.20 m/s, Fr = 52.8 Hz (FREI), b) v = 0.70 m/s, Fr = 247.9 Hz (FREI), c) v = 0.94 m/s, Fr = 269.7 Hz (Oscillating FREI).

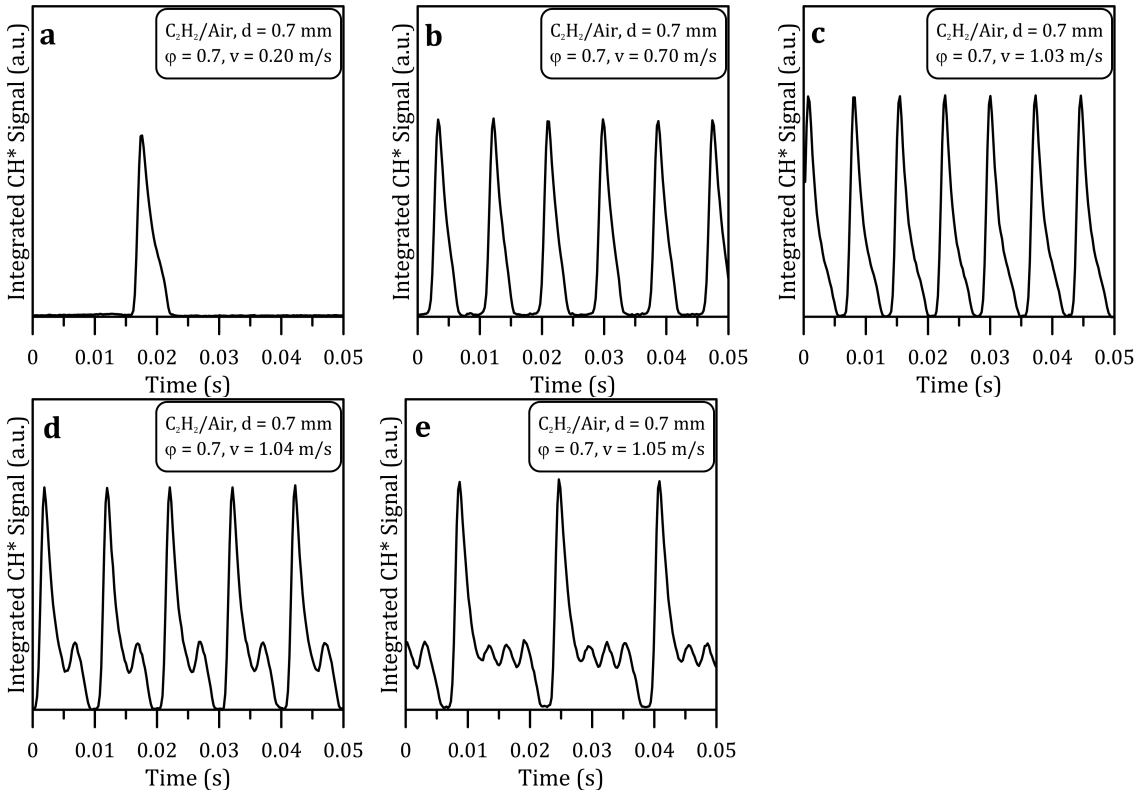

Figure E9: Temporal evolution of C_2H_2/Air unstable flames at $\varphi = 0.7$. a) v = 0.20 m/s, Fr = 20.8 Hz (FREI), b) v = 0.70 m/s, Fr = 113.4 Hz (FREI), c) v = 1.03 m/s, Fr = 137.1 Hz (FREI), d) v = 1.04 m/s, Fr = 99.1 Hz (Oscillating FREI), e) v = 1.05 m/s, Fr = 62.2 Hz (Oscillating FREI).

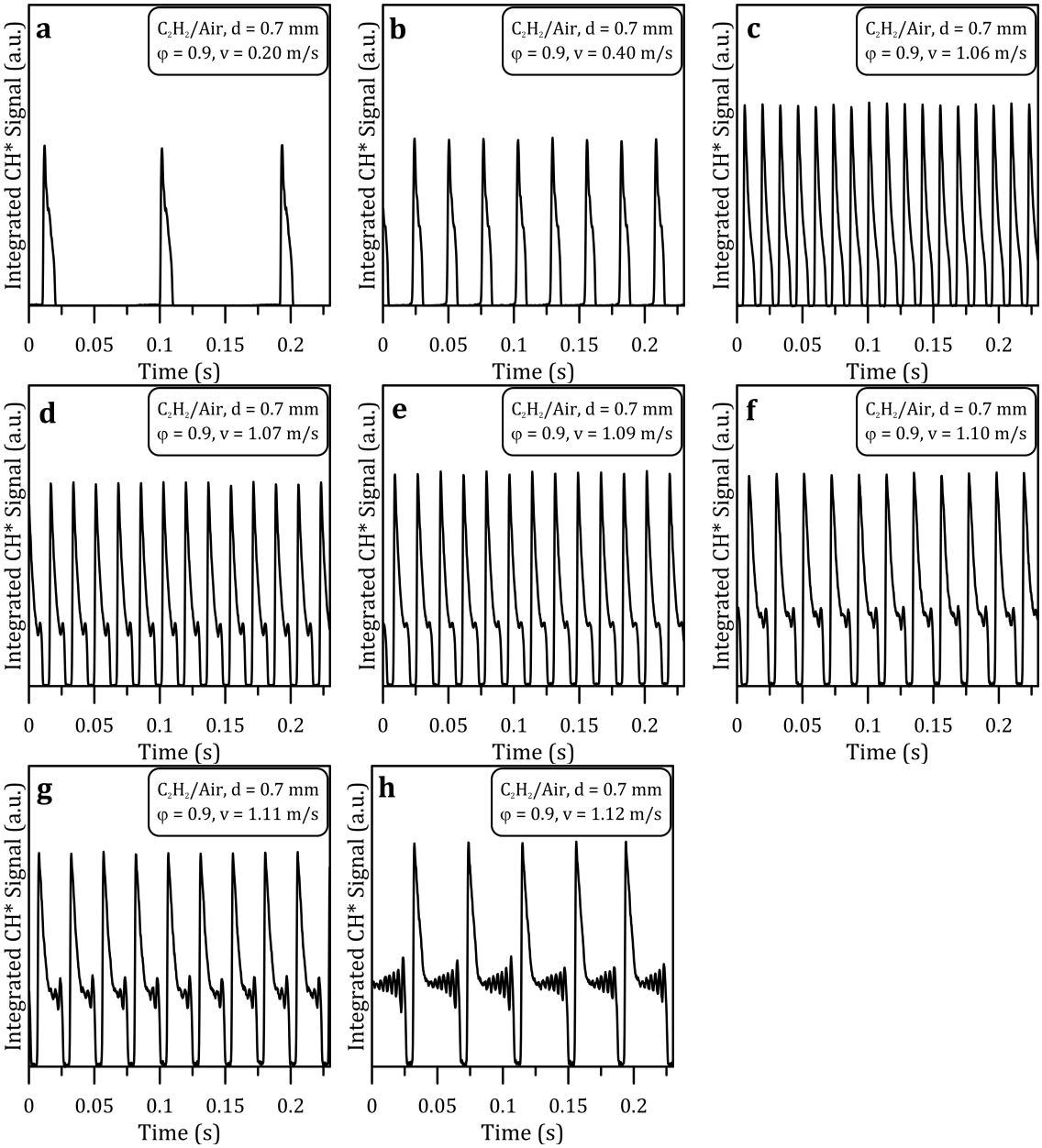

Figure E10: Temporal evolution of C_2H_2/Air unstable flames at $\varphi = 0.9$. a) v = 0.20 m/s, Fr = 10.9 Hz (FREI), b) v = 0.40 m/s, Fr = 30.7 Hz (FREI), c) v = 1.06 m/s, Fr = 73.9 Hz (FREI), d) v = 1.07 m/s, Fr = 58.3 Hz (Oscillating FREI), e) v = 1.09 m/s, Fr = 57.2 Hz (Oscillating FREI), f) v = 1.10 m/s, Fr = 47.6 Hz (Oscillating FREI), g) v = 1.11 m/s, Fr = 40.6 Hz (Oscillating FREI), h) v = 1.12 m/s (Oscillating FREI).

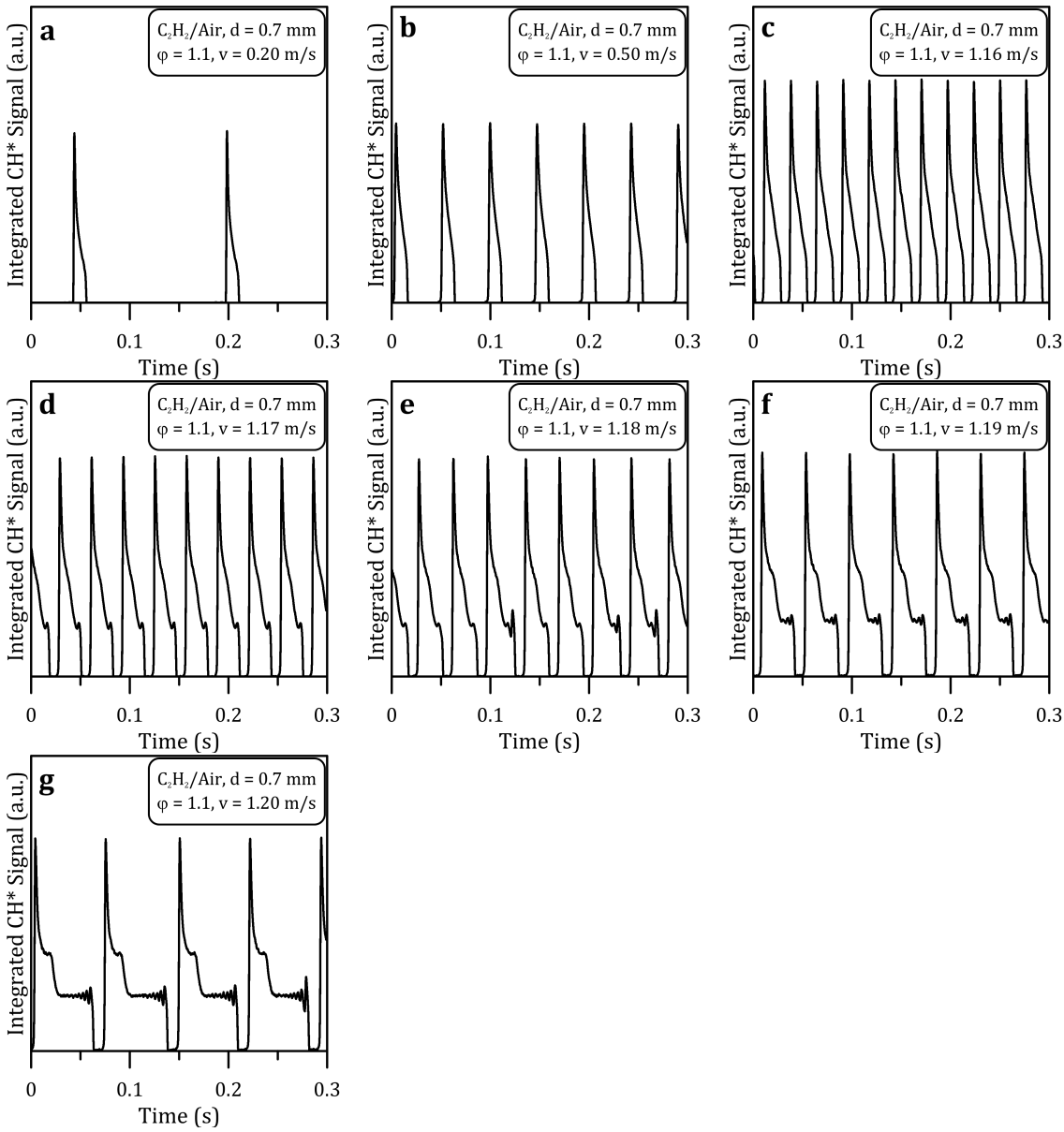

Figure E11: Temporal evolution of C_2H_2/Air unstable flames at $\varphi = 1.1$. a) v = 0.20 m/s, Fr = 6.5 Hz (FREI), b) v = 0.50 m/s, Fr = 21.1 Hz (FREI), c) v = 1.16 m/s, Fr = 37.7 Hz (FREI), d) v = 1.17 m/s, Fr = 31.2 Hz (Oscillating FREI), e) v = 1.18 m/s, Fr = 27.6 Hz (Oscillating FREI), f) v = 1.19 m/s, Fr = 22.6 Hz (Oscillating FREI), g) v = 1.20 m/s (Oscillating FREI).

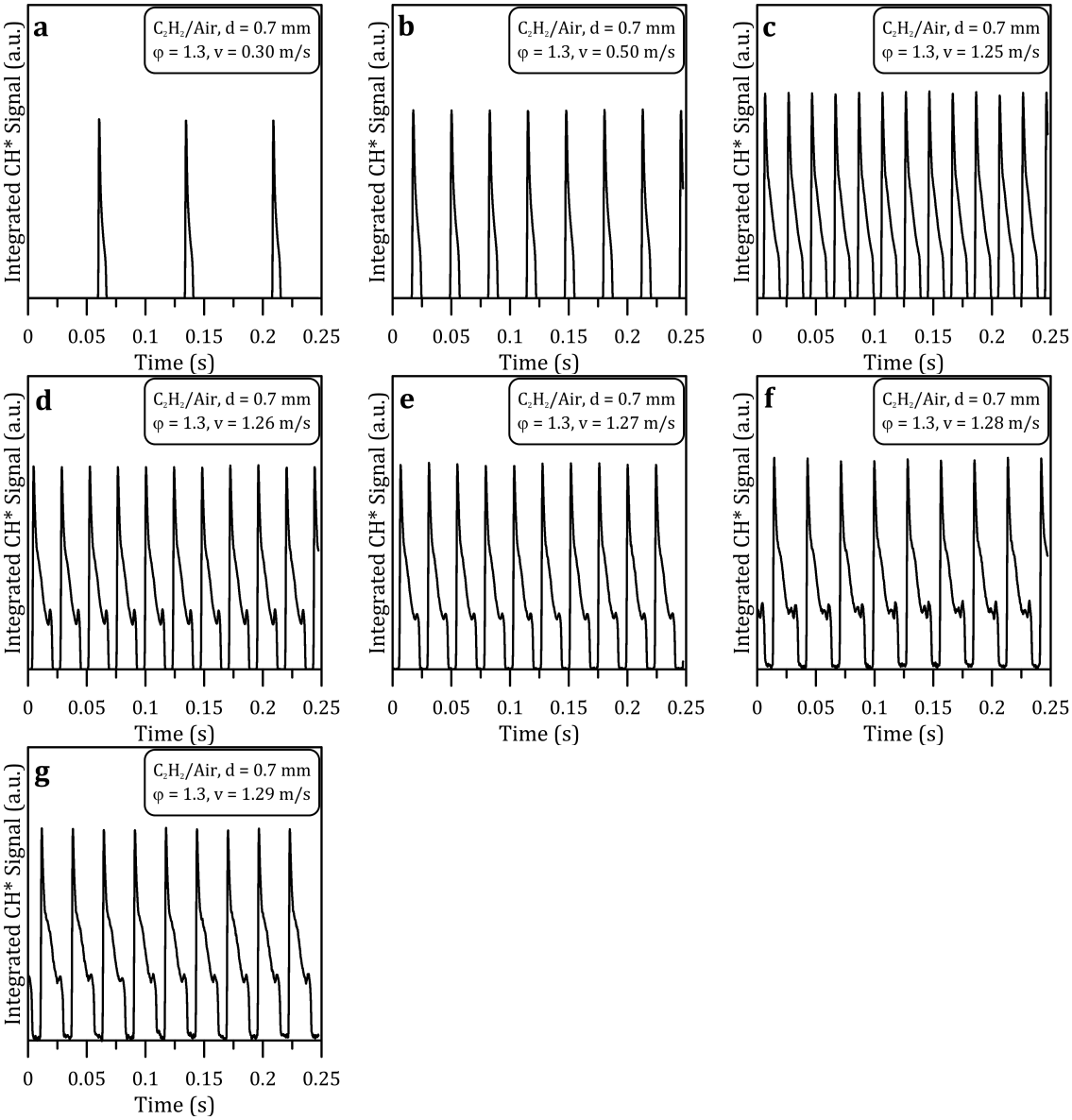

Figure E12: Temporal evolution of C_2H_2/Air unstable flames at $\varphi = 1.3$. a) v = 0.30 m/s, Fr = 13.5 Hz (FREI), b) v = 0.50 m/s, Fr = 30.7 Hz (FREI), c) v = 1.25 m/s, Fr = 50.2 Hz (FREI), d) v = 1.26 m/s, Fr = 42.1 Hz (Oscillating FREI), e) v = 1.27 m/s, Fr = 41.3 Hz (Oscillating FREI), f) v = 1.28 m/s, Fr = 31.1 Hz (Oscillating FREI), g) v = 1.29 m/s, Fr = 38.0 Hz (Oscillating FREI).

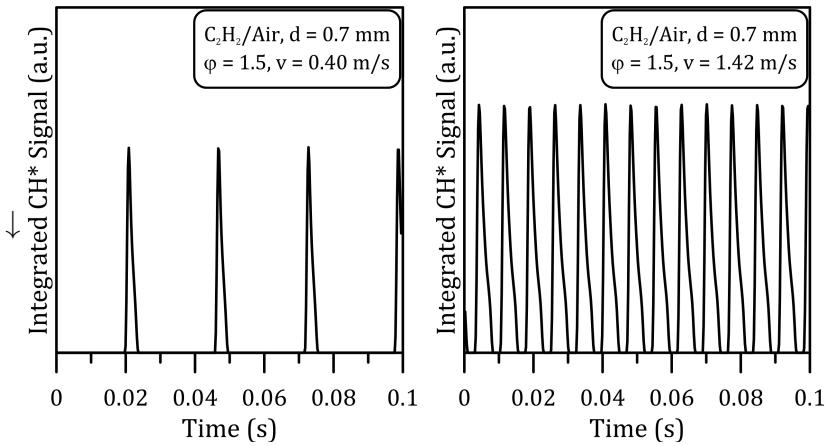

Figure E13: Temporal evolution of C_2H_2/Air unstable flames at $\varphi = 1.5$. Only ordinary FREI were observed at low (at v = 0.40 m/s, Fr = 38.5 Hz, on the left) and high (v = 1.42 m/s, Fr = 136.5 Hz, on the right) inlet velocity.

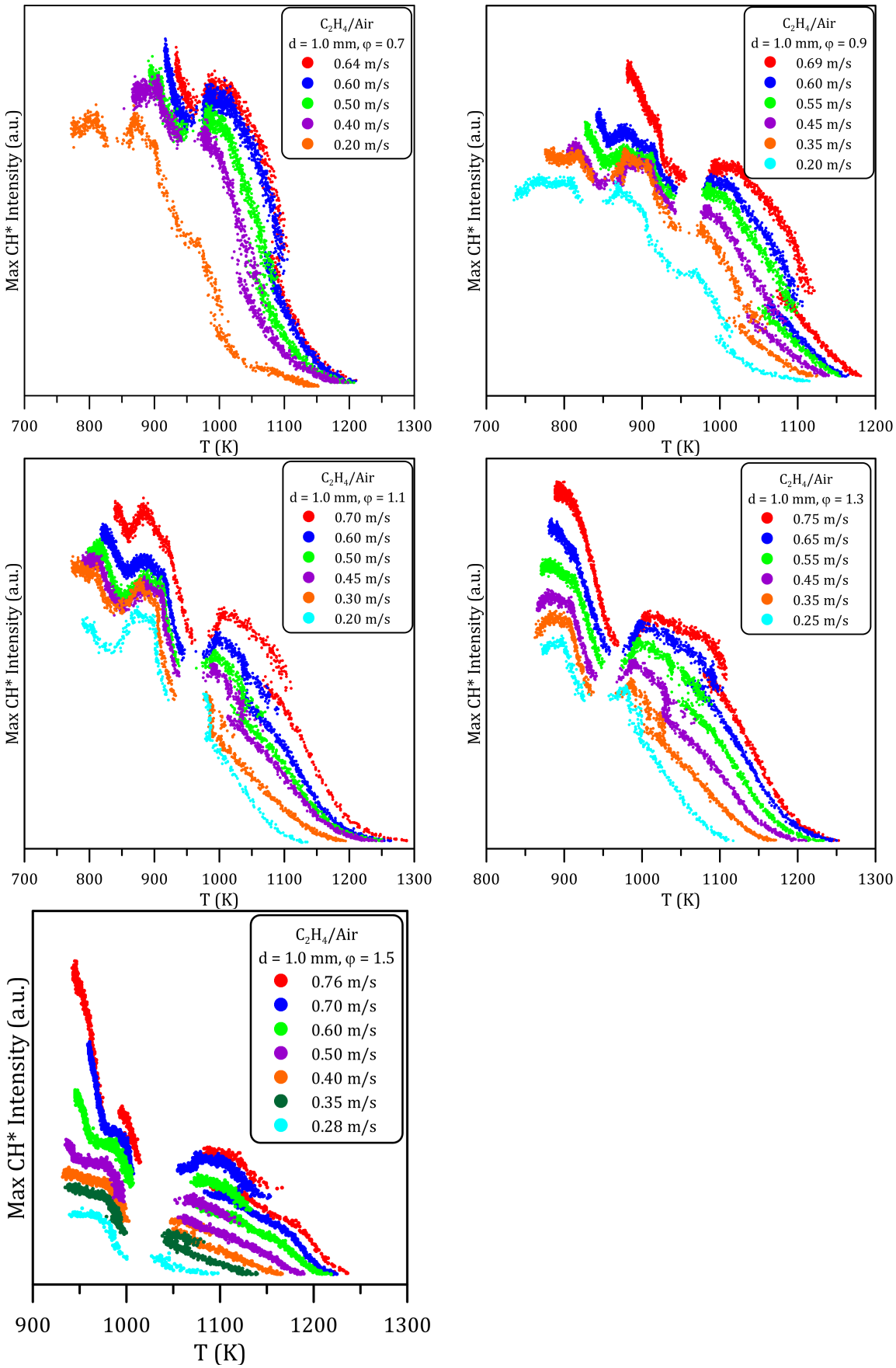

Figure E14: Mamimum CH* progression for C_2H_4/Air flames at different equivalence ratios.

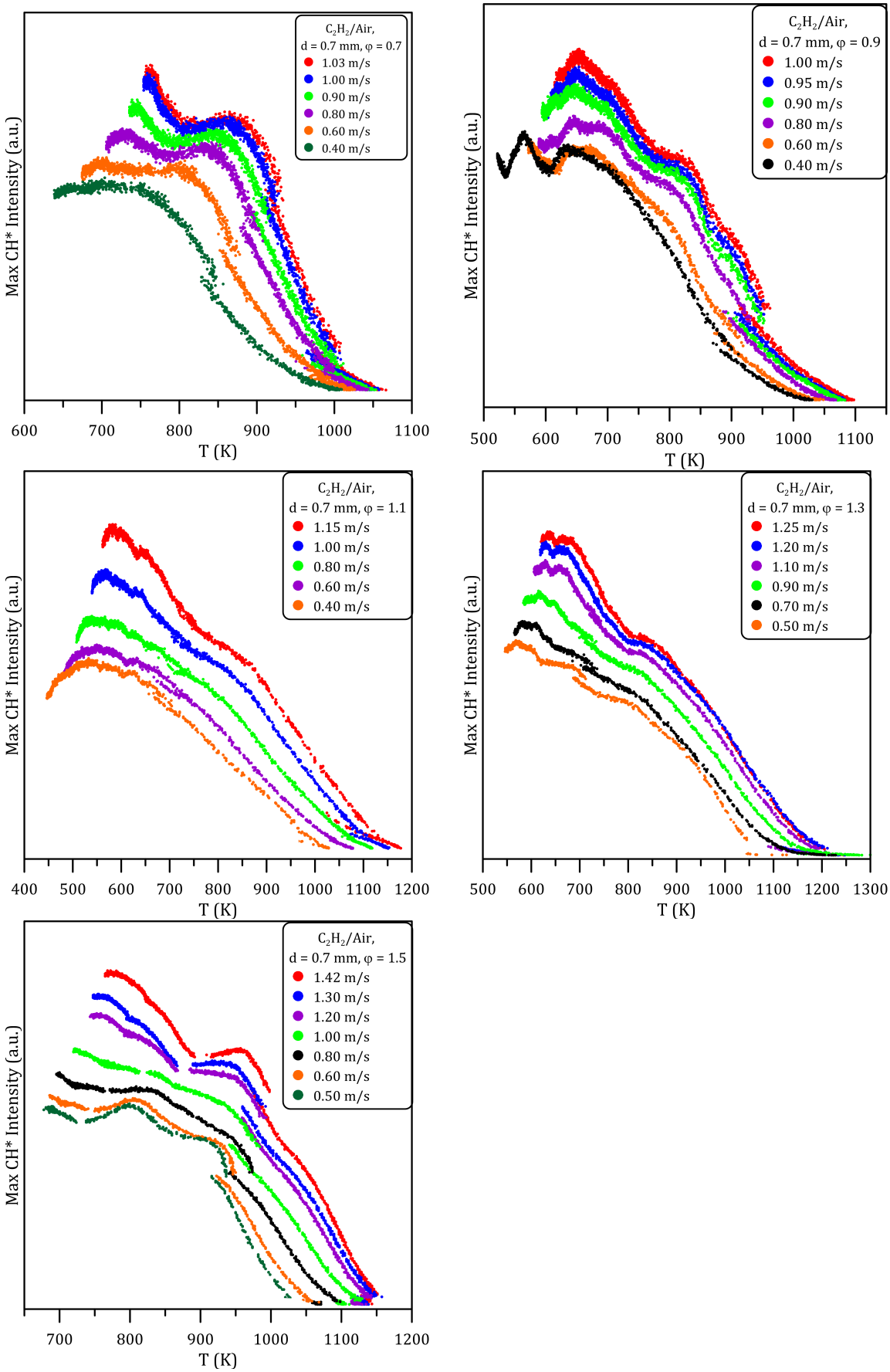

Figure E15: Mamimum CH* progression for C_2H_2/Air flames at different equivalence ratios.

Annalisa DI STAZIO

Caractérisation expérimentale de la dynamique de la combustion à micro-échelle

Résumé :

Aujourd'hui, avec la demande de systèmes à haute efficacité, les microsystèmes électromécaniques (MEMS) ont connu un développement croissant, car ceux-ci peuvent générer plus d'énergie que les batteries modernes. Dans ce contexte,une étude expérimentale sur la dynamique de la combustion à microéchelle a été conduite. Un nouveau dispositif expérimental a été mis au point. Il se compose d'un microréacteur tubulaire avec un profil contrôlé de la température imposée sur sa face externe. La température élevée du gaz permet l'auto-allumage du mélange combustible circulant à l'intérieur de ce microréacteur et elle permet aussi la stabilisation de flammes dans des réacteurs de diamètre intérieur inférieur au diamètre de coincement.
Le profil de température le long du tube est mesuré en continu par une caméra infrarouge, alors qu'une caméra EMCCD est utilisée pour enregistrer l'émission de CH^* de la flamme.
Cette étude expérimentale sur des mélanges carburant/air dans un réacteur de faible diamètre a été entreprise pour fournir des informations détaillées sur la combustion à microéchelle. Trois régimes de flamme ont été observés : (i) des flammes stables et lumineuses pour les écoulements à vitesse élevée, (ii) des flammes avec extinction et allumage répétitif (FREI) pour des débits de milieu de gamme, et (iii) des flammes faibles pour les écoulements à très faible vitesse. La présence de régimes transitoires oscillants a également été étudiée et une analyse détaillée des régimes instables (détermination des fréquences et des temps caractéristiques) a été réalisée. Trois combustibles ont été utilisés, c.-à-d., , le méthane, l'éthylène et l'acétylène. Les effets des différents paramètres ont été étudiés: la vitesse débitante, la richesse et la taille du réacteur. Des simulations numériques ont également été conduites pour étudier les caractéristiques d'allumage des flammes instables.

Mots clés : Microcombustion, Stabilisation de flamme, FREI, Flammes oscillatoires, Flammes faibles, Méthane, Éthylène, Acétylène, Allumage.

Experimental characterization of the combustion dynamics at micro-scale

Abstract:

Nowadays with the demand for high efficiency systems, there is growing development and application of micro electro-mechanical systems (MEMS devices) which may generate more energy than the modern batteries. In this context, a new experimental device has been developed. It consists of a micro tubular reactor with a controlled external temperature profile. The high gas temperature allows auto-ignition of the mixture and the flame stabilization in reactors with inner diameter smaller than the ordinary quenching diameter.
The temperature profile along the tube is measured continuously using an infrared camera while an EMCCD camera is used to collect the CH^* emission from the flame.
The present experimental study on fuel/air mixtures reacting in narrow channels has been undertaken to provide detailed information on flame combustion at micro-scale. Three kinds of flame behavior were observed: (i) bright and stable flames under high flow velocity, (ii) flames with repetitive extinction and ignition (FREI) in the middle flow rate range, and (iii) weak flames at low flow rates. The presence of oscillating transitional regimes was also investigated and a detailed analysis of the unstable regimes (determination of frequencies and characteristic times) was carried out. Three fuels were used, namely methane, ethylene, and acetylene. The effect of different parameters was investigated: inlet velocity, equivalence ratio, and reactor size. Numerical simulations were also conducted to study the ignition characteristics of unstable flames.

Keywords: Micro-combustion, Flame stabilization, FREI, Oscillating Flames, Weak flames, Methane, Ethylene, Acetylene, Flame Ignition.

Institut de Combustion Aérothermique Réactivité et Environnement
UPR 3021 du CNRS
1C, avenue de la Recherche Scientifique
45071 Orléans, Cedex 2